

EXPLORE/OC: A PHOTOMETRIC SEARCH FOR TRANSITING  
EXTRASOLAR PLANETS IN SOUTHERN OPEN CLUSTERS

by

Brian Leverett Lee

A thesis submitted in conformity with the requirements  
for the degree of Doctor of Philosophy  
Graduate Department of Astronomy and Astrophysics  
University of Toronto

Copyright © 2007 by Brian Leverett Lee

# Abstract

EXPLORE/OC: A Photometric Search for Transiting Extrasolar Planets in Southern  
Open Clusters

Brian Leverett Lee

Doctor of Philosophy

Graduate Department of Astronomy and Astrophysics

University of Toronto

2007

Extrasolar Planets Occultation Research in Open Clusters (EXPLORE/OC) is a monitoring survey of eight Southern open clusters, designed to detect transits of close-in extrasolar giant planets. In total, the survey produced a sample of approximately 32000 stars with 2-10 mmag photometric precision (rms). For stars both in clusters and the Galactic field, we discriminate between planet transits and other sources that vary with amplitudes of a few percent by combining this excellent precision with high time-sampling (1000-2000 measurements per star, spread over three weeks).

The survey employs special techniques to measure and characterize the tens of thousands of sources. The data reduction pipeline incorporates neighbour subtraction and a generalized aperture photometry approach for mitigation of common observational systematic errors. We evaluate distances and spectral types for our sources by spectral energy distribution fitting. Armed with distance estimates, we are able to assign robust cluster membership probabilities to our sources.

In each cluster field, we find of order one transit-like variable, and dozens of eclipsing binary stars and pulsators. This number of planet candidates is in line with the expected frequency of planet occurrence derived from other planet searches.

Our eclipsing binary sample is large enough to offer a statistical view on the evolution of the fraction of eclipsing binaries in open clusters. Using our cluster contact binaries, we find evidence that the fraction of contact binaries increases on a timescale of Gyr,

consistent with previous work. Extending those previous results to detached binaries, we find that detached binaries in clusters are destroyed on Gyr timescales. Pooling our detached binary detections from both clusters and the field, we find no support for the hypothesis that the binary mass ratio distribution is peaked towards equal masses.

## Acknowledgements

This thesis could not exist without the endless dedication of my supervisor, Howard Yee. He is nothing less than a treasure trove of great ideas. Thanks, Howard!

Thanks to Kaspar von Braun for sharing so many long nights with me at Swope. Here's to our continuing collaboration. Thanks also to my other EXPLORE Project collaborators for all their help- Gabriela Mallén-Ornelas, Sara Seager, and Mike Gladders. And of course, I am very grateful to all the excellent staff at Las Campanas Observatory for their outstanding technical and logistical support

My supervisory committee has been dedicated to seeing me through my degree, providing me with very helpful science advice. Thanks Marten and Yanqin! I also appreciate having had useful discussions on binary stars with two experts in our department, Slavek Rucinski and Stefan Mochnecki.

Thanks so much to all my fellow grad students for enriching my years in Toronto. In particular, I have been blessed by frequent discussions and engaging conversations, scientific and otherwise, with Kris Blindert, Carrie Bridge, Luke Chamandy, Caroline D'Angelo, Parandis Khavari, Preethi Nair, Duy Nguyen, and Marija Stankovic. Thanks to our crack administrative team and our magnificent departmental computer support for making life so much easier. Hugh, Ross, Marc, Toni, and Angela- your tireless efforts over so many of my years here are much appreciated!

To my good friend Dawn Patterson, thanks for your counsel and your unique perspective on school, jobs, and life. Keep that fabulous epistolary ability in shape!

My family has supported me from thousands of miles away, but the telephone lines have kept us close. I'm glad you were always there to keep me from getting homesick. Lastly, I want to remember my late aunt Linda and my late landlady Zenta. I wish you could have been here with me today.

This material is based upon work supported by the National Science Foundation under Grant No. 0206278, the Natural Sciences and Engineering Research Council of Canada, the Government of Ontario, the Estate of Walter John Helm, the Walter C. Sumner Foundation, and the University of Toronto.

# Contents

<b>List of Tables</b>	<b>viii</b>
<b>List of Figures</b>	<b>x</b>
<b>1 Introduction</b>	<b>1</b>
1.1 Frequency of Planet Occurrence . . . . .	2
1.2 Transit Searches . . . . .	3
1.3 Transit Searches in Open Clusters . . . . .	4
1.4 Ancillary science . . . . .	5
1.5 Outline of Thesis . . . . .	6
<b>2 A Southern Open Cluster Planet Transit Survey</b>	<b>8</b>
2.1 Introduction . . . . .	8
2.2 The Open Cluster Sample . . . . .	9
2.2.1 EXPLORE/OC . . . . .	9
2.2.2 Selection Criteria . . . . .	10
2.3 Observing Strategy and Data . . . . .	11
2.3.1 Photometric Strategy and Observations . . . . .	11
2.3.2 Supplementary Low-resolution Spectroscopy: Strategy and Observations . . . . .	29
2.4 Data Reduction . . . . .	30
2.4.1 Photometric frames . . . . .	30
2.4.2 Spectroscopic frames . . . . .	33
2.5 Photometric catalogue . . . . .	35
<b>3 Time Series Photometry</b>	<b>43</b>
3.1 Introduction . . . . .	43
3.1.1 Two Common Approaches to Relative Photometry . . . . .	43

3.1.2	EXPLORE Project Time-series Photometry: Preliminary Pipeline	44
3.2	Generalized aperture photometry	45
3.2.1	Normalization by empirical PSF division	48
3.2.2	Selection of reference stars and pixels	48
3.3	DAOphot neighbour subtraction	49
3.4	Performance tests	50
<b>4</b>	<b>Cluster membership analysis</b>	<b>75</b>
4.1	Introduction	75
4.2	Reddening along the line of sight	76
4.2.1	Spectroscopic Determination	76
4.2.2	Red Clump Determination with Bootstrapping	77
4.3	Algorithm for Determining Photometric Spectral Types	80
4.4	Verification	82
4.5	The Results: Cluster Membership Probabilities	84
4.5.1	NGC 2447	86
4.5.2	NGC 2660	88
4.5.3	NGC 5316	89
4.5.4	NGC 6134	91
4.5.5	NGC 6208	107
4.5.6	NGC 6253	107
4.5.7	IC 2714	118
4.5.8	IC 4651	118
<b>5</b>	<b>Planet Transit Candidates and Statistics</b>	<b>129</b>
5.1	Introduction	129
5.2	Algorithms for variable finding	130
5.2.1	Lomb-Scargle periodogram	130
5.2.2	Phase Dispersion Minimization	130
5.2.3	Box-fitting Least Squares	130
5.2.4	Correlation	131
5.3	Visual examination	132
5.4	Detection threshold	133
5.5	Relative performance of automated algorithms	133
5.6	Planet Transit Candidates	136

5.6.1	NGC 6134, star 18882 . . . . .	144
5.6.2	NGC 2447, star 11724 . . . . .	146
5.6.3	NGC 2447, star 17417 . . . . .	147
5.6.4	NGC 6208, star 12407 . . . . .	147
5.6.5	NGC 6253, star 13404 . . . . .	148
5.7	Statistical significance . . . . .	149
<b>6</b>	<b>Binary Star Statistics</b>	<b>161</b>
6.1	Introduction . . . . .	161
6.2	The sample . . . . .	161
6.2.1	Variable star properties . . . . .	161
6.2.2	Catalogue of binaries: properties and light curves . . . . .	162
6.3	Results . . . . .	184
6.3.1	Period distribution . . . . .	184
6.3.2	Colour distribution . . . . .	185
6.3.3	Estimated spectral type and $M_V$ distribution . . . . .	186
6.3.4	Primary eclipse amplitude distribution . . . . .	187
6.3.5	Secondary eclipses and the mass ratio distribution . . . . .	192
6.3.6	Evolution of contact and detached binaries in clusters . . . . .	194
<b>7</b>	<b>Conclusion</b>	<b>201</b>
7.1	The Survey . . . . .	202
7.2	Results . . . . .	202
7.2.1	Planets . . . . .	202
7.3	Binary Stars . . . . .	204
7.3.1	Global Properties . . . . .	204
7.3.2	Mass Ratios . . . . .	204
7.3.3	Evolution of the Binary Fraction . . . . .	205
7.4	Future Work . . . . .	205
	<b>References</b>	<b>207</b>

# List of Tables

2.1	Open cluster targets with basic data from the WEBDA database and references therein. . . . .	12
2.2	Journal of monitoring observations . . . . .	17
2.3	Journal of observations on photometric nights for NGC 6208, NGC 2660, IC 2714, NGC 5316, NGC 6253, and their flanking control fields . . . . .	27
2.4	Journal of observations on photometric nights for NGC 2447, NGC 6134, IC 4651, and their flanking control fields . . . . .	28
2.5	Journal of spectroscopic observations . . . . .	30
2.6	Photometric calibration transformation equations . . . . .	34
2.7	Sample of NGC 2447 photometric catalogue . . . . .	36
2.8	Quantity of objects overall, and quantity with sensible photometry . . . . .	38
3.1	Quantities of well-measured stars yielded by relative photometry: single nights . . . . .	56
3.2	Quantities of well-measured stars yielded by relative photometry: entire runs . . . . .	58
4.1	Reddening-distance fit coefficients . . . . .	80
4.2	Spectral type analysis of simulated binaries at the reddening of NGC 2447 . . . . .	85
5.1	Performance of automated detection algorithms for contact binaries in NGC 6208 . . . . .	136
5.2	Performance of automated detection algorithms for detached eclipsing binaries in NGC 6208 . . . . .	136
5.3	Performance of automated detection algorithms for low-amplitude eclipsing objects in NGC 6208 . . . . .	137
5.4	Application of unique solution equations to low-amplitude eclipses in IC 2714, IC 4651, and NGC 2447 . . . . .	151



5.5	Application of unique solution equations to low-amplitude eclipses in NGC 2660, NGC 5316, and NGC 6134 . . . . .	152
5.6	Application of unique solution equations to low-amplitude eclipses in NGC 6208 and NGC 6253 . . . . .	153
5.7	Star yields after applying cuts 1, 2, and 3abcd, outlined in §5.7, with and without additional early-type cuts. . . . .	157
5.8	Planet candidate yields in cuts 1, 2, and 3abcd, as outlined in §5.7, with and without additional early-type cuts. . . . .	158
6.1	Properties of the contact binaries (part 1) . . . . .	164
6.2	Properties of the contact binaries (part 2) . . . . .	165
6.3	Properties of the contact binaries (part 3) . . . . .	166
6.4	Properties of the contact binaries (part 4) . . . . .	167
6.5	Properties of the contact binaries (part 5) . . . . .	168
6.6	Properties of the contact binaries (part 6) . . . . .	169
6.7	Properties of the contact binaries (part 7) . . . . .	170
6.8	Properties of the detached binaries (part 1) . . . . .	171
6.9	Properties of the detached binaries (part 2) . . . . .	172
6.10	Properties of the detached binaries (part 3) . . . . .	173
6.11	Properties of the detached binaries (part 4) . . . . .	174
6.12	Properties of the detached binaries (part 5) . . . . .	175
6.13	Properties of the detached binaries (part 6) . . . . .	176
6.14	Properties of the detached binaries (part 7) . . . . .	177
6.15	Properties of the detached binaries (part 8) . . . . .	178
6.16	Properties of the detached binaries (part 9) . . . . .	179
6.17	Properties of the detached binaries (part 10) . . . . .	180
6.18	Properties of the detached binaries (part 11) . . . . .	181
6.19	Properties of the detached binaries (part 12) . . . . .	182
6.20	Properties of the detached binaries (part 13) . . . . .	183

# List of Figures

2.1	Average $P_{vis}$ and observing run efficiency . . . . .	14
2.2	Images of NGC 2660 and control fields . . . . .	18
2.3	Images of NGC 6208 and control fields . . . . .	19
2.4	Images of IC 2714 and control fields . . . . .	20
2.5	Images of NGC 5316 and control fields . . . . .	21
2.6	Images of NGC 6253 and control fields . . . . .	22
2.7	Images of NGC 2447 and control fields . . . . .	23
2.8	Images of NGC 6134 and control fields . . . . .	24
2.9	Images of IC 4651 and control fields . . . . .	25
2.10	$P_{vis}$ for NGC 2447, NGC 2660, NGC 5316, and NGC 6134 . . . . .	26
2.11	$P_{vis}$ for NGC 6208, NGC 6253, IC 2714, and IC 4651 . . . . .	37
2.12	Sample output mask design for NGC 2447 . . . . .	38
2.13	Quality of PPP object finding . . . . .	39
2.14	MK classification for two typical multi-object spectra . . . . .	40
2.15	$I$ magnitude distributions for NGC 2447, NGC 2660, NGC 5316, and NGC 6134 . . . . .	41
2.16	$I$ magnitude distributions for NGC 6208, NGC 6253, IC 2714, and IC 4651	42
3.1	DAOphot subtraction on a crowded pair . . . . .	46
3.2	Generalized aperture photometry on a saturated star . . . . .	47
3.3	Sample of DAOphot subtraction . . . . .	51
3.4	DAOphot light curve improvement in the field of IC 2714 . . . . .	53
3.5	IC 2714: single night performance of new relative photometry . . . . .	59
3.6	IC 4651: single night performance of new relative photometry . . . . .	60
3.7	NGC 2447: single night performance of new relative photometry . . . . .	61
3.8	NGC 2660: single night performance of new relative photometry . . . . .	62
3.9	NGC 5316: single night performance of new relative photometry . . . . .	63

3.10	NGC 6134: single night performance of new relative photometry . . . . .	64
3.11	NGC 6208: single night performance of new relative photometry . . . . .	65
3.12	NGC 6253: single night performance of new relative photometry . . . . .	66
3.13	IC 2714: whole run performance of new relative photometry . . . . .	67
3.14	IC 4651: whole run performance of new relative photometry . . . . .	68
3.15	NGC 2447: whole run performance of new relative photometry . . . . .	69
3.16	NGC 2660: whole run performance of new relative photometry . . . . .	70
3.17	NGC 5316: whole run performance of new relative photometry . . . . .	71
3.18	NGC 6134: whole run performance of new relative photometry . . . . .	72
3.19	NGC 6208: whole run performance of new relative photometry . . . . .	73
3.20	NGC 6253: whole run performance of new relative photometry . . . . .	74
4.1	Spectroscopic and red clump reddening-distance data . . . . .	79
4.2	Red clump locus on the NGC 2447 $J - K$ CMD . . . . .	81
4.3	Photometric estimate of spectral type as a function of true spectroscopic MK classification . . . . .	83
4.4	Recovery of spectral types from simulated photometry . . . . .	86
4.5	NGC 2447 CMD . . . . .	87
4.6	NGC 2447 spatial clustering . . . . .	88
4.7	NGC 2447 spatial clustering with cluster cut . . . . .	89
4.8	NGC 2447 spatial clustering with non-cluster cut . . . . .	90
4.9	NGC 2447 background subtraction . . . . .	91
4.10	NGC 2660 CMD . . . . .	92
4.11	NGC 2660 spatial clustering . . . . .	93
4.12	NGC 2660 spatial clustering with cluster cut . . . . .	94
4.13	NGC 2660 spatial clustering with non-cluster cut . . . . .	95
4.14	NGC 2660 background subtraction . . . . .	96
4.15	NGC 5316 CMD . . . . .	97
4.16	NGC 5316 spatial clustering . . . . .	98
4.17	NGC 5316 spatial clustering with cluster cut . . . . .	99
4.18	NGC 5316 spatial clustering with non-cluster cut . . . . .	100
4.19	NGC 5316 background subtraction . . . . .	101
4.20	NGC 6134 CMD . . . . .	102
4.21	NGC 6134 spatial clustering . . . . .	103
4.22	NGC 6134 spatial clustering with cluster cut . . . . .	104

4.23	NGC 6134 spatial clustering with non-cluster cut . . . . .	105
4.24	NGC 6134 background subtraction . . . . .	106
4.25	NGC 6208 CMD . . . . .	108
4.26	NGC 6208 spatial clustering . . . . .	109
4.27	NGC 6208 spatial clustering with cluster cut . . . . .	110
4.28	NGC 6208 spatial clustering with non-cluster cut . . . . .	111
4.29	NGC 6208 background subtraction . . . . .	112
4.30	NGC 6253 CMD . . . . .	113
4.31	NGC 6253 spatial clustering . . . . .	114
4.32	NGC 6253 spatial clustering with cluster cut . . . . .	115
4.33	NGC 6253 spatial clustering with non-cluster cut . . . . .	116
4.34	NGC 6253 background subtraction . . . . .	117
4.35	IC 2714 CMD . . . . .	119
4.36	IC 2714 spatial clustering . . . . .	120
4.37	IC 2714 spatial clustering with cluster cut . . . . .	121
4.38	IC 2714 spatial clustering with non-cluster cut . . . . .	122
4.39	IC 2714 background subtraction . . . . .	123
4.40	IC 4651 CMD . . . . .	124
4.41	IC 4651 spatial clustering . . . . .	125
4.42	IC 4651 spatial clustering with cluster cut . . . . .	126
4.43	IC 4651 spatial clustering with non-cluster cut . . . . .	127
4.44	IC 4651 background subtraction . . . . .	128
5.1	Variable finding by Lomb-Scargle and PDM . . . . .	138
5.2	Variable finding by Lomb-Scargle and BLS box-fitting . . . . .	139
5.3	Variable finding by Lomb-Scargle and correlation . . . . .	140
5.4	Lomb-Scargle sorting performance . . . . .	141
5.5	PDM sorting performance . . . . .	142
5.6	BLS sorting performance . . . . .	143
5.7	Correlation sorting performance . . . . .	144
5.8	Histogram of the inferred radii of planet candidates . . . . .	145
5.9	The phased light curve of star 18882 in the field of NGC 6134 . . . . .	146
5.10	The phased light curve of star 11724 in the field of NGC 2447 . . . . .	147
5.11	The phased light curve of star 17417 in the field of NGC 2447 . . . . .	148
5.12	The phased light curve of star 12407 in the field of NGC 6208 . . . . .	149

5.13	The phased light curve of star 13404 in the field of NGC 6253 . . . . .	150
5.14	Predicted probabilities for finding planets: no cluster cuts . . . . .	156
5.15	Predicted probabilities for finding planets: cluster stars in cluster aperture cut . . . . .	159
5.16	Predicted probabilities for finding planets: field stars in cluster aperture cut	160
6.1	Sample light curves of contact, possibly semi-detached or detached, and detached binaries . . . . .	163
6.2	The period distribution of contact eclipsing binaries . . . . .	185
6.3	The period distribution of detached eclipsing binaries . . . . .	186
6.4	The $(B - V)_0$ colour distribution of contact eclipsing binaries . . . . .	187
6.5	The $(B - V)_0$ colour distribution of detached eclipsing binaries . . . . .	188
6.6	The $M_V$ distribution for contact binaries . . . . .	188
6.7	The $M_V$ distribution for detached eclipsing binaries . . . . .	189
6.8	The numerical spectral type distribution for contact binaries . . . . .	189
6.9	The numerical spectral type distribution for detached eclipsing binaries .	190
6.10	The primary eclipse depth distribution for contact binaries . . . . .	191
6.11	The primary eclipse depth distribution for detached eclipsing binaries . .	191
6.12	Secondary eclipse depth/primary eclipse depth for contact binaries . . . .	194
6.13	Secondary eclipse depth/primary eclipse depth for detached eclipsing binaries	195
6.14	Evolution of the contact binary fraction . . . . .	198
6.15	Evolution of the detached binary fraction- raw fractions . . . . .	198
6.16	Evolution of the detached binary fraction- all stars . . . . .	199
6.17	Evolution of the detached binary fraction- late types only . . . . .	200

# Chapter 1

## Introduction

For many years, searching for planets was an exercise confined to the solar system. Yet, astronomers have thought deeply about the possibility of extrasolar planets- planets orbiting other stars- for decades. The detection of a planet is quite similar in principle to detecting a binary star, only requiring much greater observational precision. Struve (1952) anticipated several aspects (including three present-day planet search techniques: radial velocity searches, transit searches, and direct imaging) of today's work on extrasolar planets- an emerging field which, although awaited for many years, did not seriously emerge from the realm of theory until twenty years ago.

The 1980's saw developments in spectrograph technology, such as calibration by HF absorption cells, which improved the accuracy of spectroscopy in determining the radial velocities of stars to  $\sim 13$  m/s (Campbell et al. 1988). Pushing far below the radial velocity precision (km/s) that was required to detect binary companions, this precision is approximately the radial velocity variation induced in the Sun by the gravitational tug of Jupiter. Walker et al. (1995) applied the technology in an attempt to discover Jupiter analogues orbiting at several AU from their host stars, but they did not report any discoveries.

Ironically, the first extrasolar planets were discovered in orbit around the pulsar PSR 1257+12, not by a radial velocity search, but by timing of the pulsar (Wolszczan & Frail 1992). However, since then, many groups have successfully employed the technique of Campbell et al. (1988) to discover scores of planets circling ordinary main sequence stars. The first planet discovered in orbit around a main sequence star was 51 Peg b, a gas giant in a surprisingly short-period orbit of only 4.23 days (Mayor & Queloz 1995). These close-in extrasolar giant planets are popularly referred to as "Hot Jupiters" (HJ). Popular theory asserts that these do not form in place on short orbits, but rather are

formed at large radius orbits beyond the snowline (inside of which radius the temperatures are too high for volatile gases to coalesce), and migrate inwards by interactions with the protoplanetary disk (Raymond et al. 2006, and references therein).

As of the end of November 2006, the tally of extrasolar planets is at 209, distributed over 171 host stars (Schneider 2006). These planets have been discovered in a variety of ways, but the majority have been detected using the radial velocity technique, which has been refined such that surveys now achieve precisions as fine as  $\sim 1$  m/s (Sato et al. 2005). Since high mass planets have larger physical effects on their host stars, most planets detected are of order Jupiter mass, although radial velocity searches have found objects of a few Earth masses (e.g., Rivera et al. 2005), and the pulsar planets are also of terrestrial mass. Most surprisingly, over 50 planets have been discovered with orbital semi-major axes  $< 0.1$  AU and periods of a few days (Schneider 2006)!

## 1.1 Frequency of Planet Occurrence

One of the most enduring questions regarding extrasolar planets is how frequently they occur. This number is a key that can truly open doors for cross-disciplinary fields such as astrobiology and comparative planetology. Radial velocity searches in the solar neighbourhood have yielded a relatively high frequency of planet occurrence. On average,  $\sim 10\%$  of stars searched by radial velocity surveys play host to extrasolar planets. The number of these in HJ orbits is significant-  $0.7\%$  of stars searched host an HJ (Marcy et al. 2004). It has been found that metallicity has a marked influence on the overall frequency of occurrence of planets (Fischer et al. 2004). As one might intuitively expect, higher system metallicity translates to a higher likelihood of finding planets (Fischer & Valenti 2005). This may be due to “pollution” of the star by high metallicity infalling planetary system material (Murray & Chaboyer 2002), but more likely due to primordial metal enhancement (Gonzalez 2006, and references therein).

No detection techniques other than radial velocity searches have been able to accumulate a competitive number of planet detections yet. However, such a cross-check would be extremely useful, as radial velocity searches experience difficulties in probing massive stars and very faint stars. In general, these magnitude-limited surveys search main sequence FGKM stars; for example, the California-Carnegie group imposes sample cuts  $V < 8.5$ ,  $(B - V) > 0.5$ , and  $M_V > 3.0$  (Butler et al. 2006). Recently some searches have focussed on K giant stars (Hatzes et al. 2006). Stars of spectral type A and earlier are difficult to measure with high precision because they have relatively few spectral lines.

## 1.2 Transit Searches

Just as binaries can be discovered by looking for the eclipse of a star by a companion, so can planets be discovered by watching them eclipse their host stars. Since searches for transits of planets are photometric rather than spectroscopic, they can target very large samples of stars, and can target much fainter magnitudes than radial velocity searches.

Eclipses are complementary to radial velocity information, because the presence of eclipses constrains the system inclination to near  $i \sim 90$  degrees. Knowing the orbital inclination, one can fold in radial velocity measurements to derive the true mass of the planet without the  $\sin i$  mass ambiguity of radial velocity data alone. In addition, in visible light, the planet is virtually black compared to the star, so the depth of the eclipse establishes the relative radii of the planet and star. Only transits and direct imaging are able to infer radii for extrasolar planets, and thus derive their densities. The radii and masses of the transiting planets are important for constraining models of the structure of planets, and the evolutionary processes that may influence those models (see, e.g., Burrows et al. 2000, Guillot & Showman 2002, Baraffe et al. 2003, and references therein).

Over 20 transit searches have been conducted or are underway (Horne 2003). There are now a total of 16 transiting planets known: five discovered by the OGLE survey (Konacki et al. 2003, Bouchy et al. 2004, Konacki et al. 2004, Pont et al. 2004), two by the TrES survey (Alonso et al. 2004, O’Donovan et al. 2006), two by the WASP survey (Collier Cameron et al. 2006), two by the SWEEPS survey (Sahu et al. 2006), one by the HAT project (Bakos et al. 2006), one by the XO Project (McCullough et al. 2006), and three by photometric follow-up of previously known planets discovered using radial velocity searches (Charbonneau et al. 2000, Sato et al. 2005, Bouchy et al. 2005b). All are short-period planets.

Let us consider the probability that a given star will host a transiting HJ, assuming that the overall chance of a star having an HJ at all is given by the  $f_{HJ} = 0.7\%$  fraction of Marcy et al. (2004), scaled up or down according to the metallicity of the star by a factor  $\frac{f([\text{Fe}/\text{H}]_{\text{targetstar}})}{f([\text{Fe}/\text{H}]_{\text{Marcy}})}$ . For a planet with orbital semi-major axis  $a$  and a star of radius  $R_*$ , the probability  $p_{\text{geometric}}$  that the planet’s orbit is sufficiently inclined so that the planet transits the face of the star is given in, Heacox (e.g., 1996):

$$p_{\text{geometric}} = \frac{R_*}{a}. \quad (1.1)$$

The knowledge that close-in giant planets exist therefore makes transit searching a feasi-



ble enterprise, because the probability of transit is 1 in 10 for a planet with  $a = 0.05\text{AU}$  orbiting a star of radius  $1R_{\odot}$ .

Thus, the probability of a star hosting a transiting HJ is the joint probability between the overall frequency of occurrence of HJ at a given metallicity, and the geometric probability of a favourable orientation.

$$p = f_{HJ} \frac{f([\text{Fe}/\text{H}]_{\text{targetstar}}) R_*}{f([\text{Fe}/\text{H}]_{\text{Marcy}}) a}. \quad (1.2)$$

Using typical numbers of  $\frac{f([\text{Fe}/\text{H}]_{\text{targetstar}})}{f([\text{Fe}/\text{H}]_{\text{Marcy}})} \approx 0.5$  (for an average metallicity star,  $[\text{Fe}/\text{H}]=-0.1$ , in the solar neighbourhood), and  $p_{\text{geometric}} \approx 0.1$ , we find that 1/3000 stars should host a transiting HJ.

Furthermore, the probability of actually seeing a transiting HJ will be affected by gaps in the observations. In particular, a survey from the ground cannot operate during the daytime or during bad weather, and thus will miss roughly 50% of visible transits (although over a very long time baseline, there will be multiple opportunities to eventually recover the repeating transit signal). This fraction can be expressed more precisely as a window function  $P_{\text{vis}}$ , which we discuss in §2.3.

Hence, depending on observing run length and conditions, we would expect to find fewer than one HJ for every 3000 stars surveyed. So, to conduct a search for transiting planets, one must be able to monitor many thousands of stars simultaneously for transit events. The searches in operation achieve this either by observing ultra wide fields of several degrees in diameter with small telescopes, including the HAT (Bakos et al. 2004), WASP (Pollacco et al. 2006), and TrES (Alonso et al. 2004) surveys, or wide fields, tens of arcminutes in diameter, with telescopes of 1-4 metres in diameter, such as the St. Andrews planet search (Street et al. 2002) and the EXPLORE Galactic field survey (Mallén-Ornelas et al. 2003), upon which the EXPLORE/OC survey (von Braun et al. 2005) in this thesis is based).

### 1.3 Transit Searches in Open Clusters

The advantages of monitoring open clusters for transiting planets were originally presented in Janes (1996), and updated during the the EXPLORE/OC survey von Braun et al. (2005). Open clusters provide a tool for examining the effects of stellar age, metallicity, and the local environment on planet frequency. Every star in a cluster shares the same metallicity, age, distance, and reddening, properties which are relatively easily

derived, and are sometimes already catalogued in the literature. This thesis presents a planet transit search in open clusters (von Braun et al. 2005; Lee et al. 2004; von Braun et al. 2004) in order to leverage these uniform properties.

In particular, the property of metallicity is expected, from radial velocity search results, to influence the frequency of occurrence of planets. Planets belonging to stars in open clusters would provide robust data points to verify this trend using a completely different strategy. They will also provide data with which to correlate other intrinsic cluster star properties, such as age or evolutionary history, with the planet frequency. The evolutionary history of stars in open clusters versus globular clusters or the Galactic field may influence planet frequency via dynamical interactions or via formation mechanisms. It has been suggested that UV photons from O and B stars in clusters could evaporate protoplanetary disks and inhibit planet formation (e.g., Adams et al. 2004; Adams et al. 2006). Also, Gilliland et al. (2000) and Wel Drake et al. (2005) have conducted transit searches in the globular cluster 47 Tuc, and have reported no detections. This may be due to the low metallicity of 47 Tuc, or also to the high stellar density, which will lead to close encounters and possible planetary system disruptions. Open cluster samples provide a more uniform set of stars than Galactic field searches and a less dynamically active set of stars than globular cluster searches, so offer an opportunity to separate the effects of dynamics and metallicity on the frequency of planet occurrence.

In addition to the survey presented in this thesis, there are three planet transit surveys under way in open clusters. Planets in Stellar Clusters Extensive Search (PISCES) targeted the open clusters NGC 6791 (Mochejska et al. 2002) and NGC 2158 (Mochejska et al. 2004). University of St. Andrews Planet Search (UStAPS) targeted NGC 6819 (Street et al. 2002) and NGC 7789 (Bramich et al. 2004). The Survey for Transiting Extrasolar Planets in Stellar Systems (STEPSS) is described in Burke et al. (2003) and Gaudi et al. (2002), and targeted NGC 1245 (Burke et al. 2004), NGC 2099, and M67. None of these searches have discovered any transiting planets. Analysis of STEPSS data is still ongoing. The survey presented in this thesis, EXPLORE/OC (von Braun et al. 2005), is the only transit search operating in southern open clusters, and has the largest sample of both clusters and number of stars of any open cluster transit search to date.

## 1.4 Ancillary science

One of the products of any sky monitoring project is the detection of variable stars, including eclipsing binaries and pulsating stars. For example, the OGLE project has

catalogued over 200 000 variable objects in the Galactic bulge (Wozniak et al. 2002). The ASAS-3 variability search (Pojmanski 2002) has catalogued 50 000 variable objects.

Just one example of the utility of these giant variability catalogues is in a field closely related to planet statistics- the field of binary star research. Rucinski (1998) has used the OGLE catalogue to perform a definitive analysis of the properties of a large sample of contact binary systems in the direction of Baade’s Window in the Galactic bulge. Among other results, the papers derived the frequency of occurrence of contact binaries relative to main sequence stars, showed the utility of contact binaries as distance indicators, and ascertained that the distribution of mass ratios in the sample climbs steeply towards very unequal masses. Rucinski (1998) has also performed an analysis of contact binary properties in open clusters, including a demonstration of the evolution of frequency of occurrence as a function of age.

## 1.5 Outline of Thesis

In this thesis, we present a more extensive open cluster planet transit search than any attempted so far. We monitor eight southern open clusters with a range of metallicities from  $[\text{Fe}/\text{H}]=-0.18$  to  $[\text{Fe}/\text{H}]=+0.36$  (mainly supersolar), and a range of ages, from 150 Myr to 5 Gyr. We achieve high-precision time series photometry of better than 1% rms scatter on stars of  $14 < I < 17$ , with a high time-sampling of  $\sim 7$  min., over observing runs typically three weeks in duration. In total, we have collected light curves of over 30000 stars with better than 1% photometric precision, with  $\sim 1000 - 2000$  epochs per light curve. We use the same telescope and detector for all our observations. This allows us to apply uniform techniques across the whole data set, permitting direct internal comparisons within the data and limiting the potential for systematic errors.

Our main scientific goal is to detect transiting planets in open clusters in order to investigate the frequency of occurrence of the Hot Jupiter class of extrasolar planets. This number has been established only for the solar neighbourhood, and using only the radial velocity search technique. We seek to leverage the uniformity of open cluster stars to provide robust statistics on the occurrence of planets as a function of metallicity.

Our secondary goal is to evaluate the properties of binary stars in open clusters. We seek to compare our contact binary statistics to previous work, and extend the discussion to detached binaries.

This data set is the largest monitoring survey of open cluster fields to date. In Chapter 2, we present our observations. We describe the specific strategy required to perform

an efficient open cluster planet transit search, and use established tools to create basic catalogues for our sample. In Chapter 3, we introduce novel techniques for high-precision relative photometry. We compare the results produced by our newest techniques to previous work. Chapter 4 presents our algorithm for determining the cluster membership probabilities of stars in our sample. Using the high-precision photometry derived in Chapter 3, we present algorithms for finding variable stars in Chapter 5. After cataloguing the potential planets among the variables, we use the spectral type information from Chapter 4 both to examine whether the inferred properties of our planet candidates are completely self-consistent, and to examine the frequency of occurrence of planet candidates in open clusters. In Chapter 6, we analyze the properties of the binary stars in our sample, in particular addressing the distribution of mass ratios and the evolution of the binary fraction.

# Chapter 2

## A Southern Open Cluster Planet Transit Survey

### 2.1 Introduction

This chapter presents EXPLORE/OC (EXtrasolar PLANet Occultation REsearch in Open Clusters), a photometric, high time-sampling variability survey in open clusters. Our survey provides the largest southern open cluster planet transit search data set at present, with a total of thousands of epochs and tens of thousands of well-measured stars. Our campaign is designed to compare the frequency of occurrence of close-in extrasolar giant planets in open clusters to their frequency of occurrence in the solar neighbourhood and galactic field.

The majority of successful planet detections to date have sampled the solar neighbourhood; these are results from radial velocity searches in the nearest tens of pc (e.g. Butler et al. 2006), which require bright targets with many spectral lines in the visible for precision of order a few m/s. The large numbers of planets detected by radial velocity searches indicate that planets occur preferentially around metal-rich stars (Santos et al. 2004). The planet sample enjoys its best statistics for late-type dwarfs high in metals. Both transit and radial velocity searches have revealed many orbiting with extremely short periods (Hot Jupiters).

To date, no planets have been found in open clusters, since at their distances, solar-type dwarf stars are relatively faint to attack with radial velocity searches. Yet, the discovery of planets around stars in open clusters would be extremely valuable because of their common evolutionary history. The members of a cluster share a single isochrone-

fit age, metallicity, and dynamical environment, so clusters are tantamount to a controlled laboratory for gathering statistics on rates of planet occurrence, where the properties of a large number of stars can be varied in unison, and the outcomes computed for comparison with expectations extrapolated from other surveys.

We present our cluster selection strategy in §2.2. These open clusters are mostly metal-rich and lie near the Galactic Plane at moderate distances along the line of sight. This sample maximizes both our chances of finding transiting planets and our complementarity with existing knowledge.

In §2.3, we explain our observing strategy and summarize our observations. Our strategy is built around efficient use of observing time and high rejection of astrophysical mimics of transiting planets. In addition, our highly uniform technique minimizes systematic biases from instrumentation, when we compare results within our own data set.

Section 2.4 describes our preprocessing for all images. Routine colour calibration reduction is also addressed here. The more sophisticated reductions necessary for high precision time series photometry are addressed in Chapter 3. We show some sample photometric catalogue data in §2.5.

## 2.2 The Open Cluster Sample

### 2.2.1 EXPLORE/OC

We have designed the EXPLORE/OC planet transit survey in order to compare planet occurrence in a well defined open cluster sample with existing radial velocity search statistics and with statistics from Galactic field planet transit searches (in particular, the parent EXPLORE survey, Mallén-Ornelas et al. 2003, hereafter M03, which shares many techniques in common with EXPLORE/OC). In order to accomplish this comparison, we must maximize the number of well-measured stars (both temporally and photometrically) that we observe, in regions of stellar parameter space that overlap with the parameters explored by radial velocity searches.

Following M03, we note that only about 1 in 3000 stars can be expected to possess a transiting Hot Jupiter with  $a < 0.05\text{AU}$ , and at a typical open cluster field richness of a few thousand bright stars, we require a sample of several open clusters to build even minimal comparison statistics. Therefore, we present here a sample of eight open cluster targets that we have observed.

### 2.2.2 Selection Criteria

Our exploration of the most useful way to find planets in open clusters are exposted in von Braun et al. (2005). We draw our candidate clusters from the WEBDA database of open clusters (Mermilliod 1996). We considered four cluster field properties for ranking candidates to be observed, and list them below.

1. **Observability.** Our metric of observability is the quantity  $P_{vis}$ , defined as the probability of detecting at least two transits of an extant transiting planet given a certain block of observing time, explained more fully in §2.3 and M03. Our survey was conducted from the LCO Swope 1-m Telescope, located in the south at 70.700° W longitude, 29.002° S latitude. The geographical location of the observatory limits the months of the year when we can achieve  $P_{vis}$  of at least 50% with three week observation runs for open clusters in the Galactic Plane. Typically, the exact telescope time allocation granted narrows the available targets with expected  $P_{vis} > 0.5$  (for a perfect run of  $\sim 3$  weeks) to a window of about 2 hours in Right Ascension (depending on Declination).
2. **Richness.** We must image a few thousand bright stars on which we can achieve at least 1% relative photometric precision (the size of the canonical photometric signal caused by the eclipse of a Sun-like star by a Jupiter radius planet) because of the expected 1/3000 presence of transiting Hot Jupiters. Therefore, we define richness of a field as the number of stars within the magnitude interval that will deliver 1% relative photometric precision. In fields harbouring large populations of red giant stars (visible in colour-magnitude diagrams as a distinct sequence at brighter apparent magnitudes and redder colours than the main sequence stars), we also make a colour cut to exclude giants from the richness estimate. This cut is made because planets around giants will not be detectable with 1% relative photometric precision. The colour cut varies depending on the reddening and stellar population of each field .
3. **Distance and reddening.** The light-collecting power of the instrument, combined with a high time-sampling survey strategy (see §2.3), define a window of apparent magnitudes (between the saturation limit and large photon noise) where relative photometric precision better than 1% can be reached. These apparent magnitudes span a certain range of main sequence spectral types at a given cluster's distance and reddening. Since the best targets for this campaign are F, G, K, and M-dwarfs

(for comparison with radial velocity surveys, and maximization of the photometric signal of a  $1R_J$  planet), clusters at a modest range of distance moduli are acceptable. Also, we demand sufficiently distant clusters to match the clusters' angular sizes with the telescope's field of view.

4. Age. A mild consideration is that younger stars exhibit higher surface activity, adding extra noise to photometric measurements and radial velocity follow-ups. In practice, application of the three more important criteria listed above almost always dictates the choice of cluster for a given observing run.

These criteria were not applied to our pilot cluster, NGC 2660, but did result in the following criteria for selection of the remainder of our cluster sample. For good Southern Hemisphere observability, many of our candidates were chosen from the ranges  $7^{\text{h}} < \alpha < 9^{\text{h}}$  and  $16^{\text{h}} < \alpha < 18^{\text{h}}$ , and  $\delta < 0$ . We did choose IC 2714 and NGC 5316 from outside this range, since they were the best observable candidates for their respective observing runs; they had good observability because of their high southern declinations. Based on our pilot cluster, we found we could achieve 1% relative photometric precision using Swope for  $I$  magnitudes  $14 < I < 17$ , so to target FGKM dwarfs, we picked cluster distances of about 700-1500 pc. The fields' richnesses are typically 2000-4000 stars with final relative photometric precision of  $< 1\%$ . For the purpose of cluster selection, richnesses were usually estimated at the telescope with a quick and dirty photometric calibration in the first couple of hours (for an observing run with more than one candidate cluster target), since the richnesses estimated from literature (Cox 2000; Lynga 1987) are not necessarily similar to our own definition of richness. Our quick calibration at the telescope used only exposures in  $V$  and  $I$  of the cluster and a Landolt standard field, taken at nearly the same airmass to minimize error in case we suspected periods of only marginally photometric conditions on our first observing night. Using this quick calibration at the telescope, we counted typically 2000 – 4000 stars of magnitudes  $14 < I < 17$ . The resulting sample of clusters we observed is presented in Table 2.1.

## 2.3 Observing Strategy and Data

### 2.3.1 Photometric Strategy and Observations

We quantify the usefulness of one proposed night of observations using the  $P_{vis}$  of M03—the probability that a detectable planet transit occurs at least twice within the time



Table 2.1: Open cluster targets with basic data from the WEBDA database and references therein.

Cluster	$D$ (pc)	$E_{B-V}$	$M_{I_{limit}}^a$	$\alpha_{2000}$	$\delta_{2000}$	$(l, b)$	[Fe/H]	$\log(\text{age})$	1% rms stars <sup>b</sup>	$\langle P_{\text{vis}} \rangle^c$
NGC 2447	1037	0.046	6.83	07 44 29.2	-23 51 11	(240.0, 0.1)	$+0.03 \pm 0.10$	8.588	1900	0.30
NGC 2660	2826	0.313	4.14	08 42 38.0	-47 12 00	(265.9, -3.0)	$-0.18 \pm 0.06$	9.033	2750	0.27
IC 2714	1238	0.341	5.87	11 17 27.3	-62 43 30	(292.4, -1.8)	$-0.01 \pm 0.04$	8.542	2750	0.57
NGC 5316	1215	0.267	6.06	13 53 57.2	-61 52 00	(310.2, 0.1)	$+0.13 \pm 0.07$	8.202	2800	0.58
NGC 6134	913	0.395	6.43	16 27 46.5	-49 09 04	(334.9, -0.2)	$+0.18 \pm 0.03$	8.968	2850	0.64
NGC 6208	939	0.210	6.73	16 49 28.1	-53 43 42	(333.8, -5.8)	$+0.00 \pm 0.04$	9.069	3250	0.62
NGC 6253	1510	0.200	5.22	16 59 05.1	-52 42 31	(335.5, -6.3)	$+0.36 \pm 0.20$	9.70	3400	0.61
IC 4651	888	0.116	7.03	17 24 42.0	-49 57 00	(340.1, -7.9)	$+0.09 \pm 0.02$	9.057	3200	0.23

<sup>a</sup>Faintest absolute  $I$  magnitude which we can observe with photometric precision better than 1% at the Swope 1-m telescope, derived assuming  $I = 17$  is the faintest apparent  $I$  magnitude for which photometric precision better than 1% will be reached, and  $A_i = 1.94E_{B-V}$

<sup>b</sup>Number of stars measured with photometric precision better than 1% on a clear night

<sup>c</sup>Average (over 1 to 5 day periods) of the window function, which is described in §2.3.1

windows during which that star is being monitored. Using  $P_{vis}$  as a metric of performance of a given observing strategy, we ask the question, “On average, will a night of observing add more new planet detections than the previous night did?” Figure 2.1, adapted from M03, shows a plot that tracks the rise in  $P_{vis}$  (averaged over an even distribution of planet phases and periods  $1d < P < 5d$ ) as a hypothetical perfect observing run of 10.8 hour nights increases in length. It also shows the same plot but divided by the number of nights elapsed, thus measuring the average nightly probability of detecting an extant planet, which is, in effect, the planet-finding efficiency of the run, peaking near three weeks. Thus, we typically schedule a cluster to be observed over 3-6 weeks in time baseline, with actual run lengths dictated by the size of holes within the schedule due to other observing programs and weather losses.

Following the prescription of M03, we monitor only a single target field per run (rather than increasing the number of stars monitored by alternating between targets during the night) so that we may take high cadence observations, and to maximize  $P_{vis}$  without introducing period aliasing. Our high time-sampling of the light curve, 300 sec. exposure and 130 sec. readout, provides definition of the light curve shape during ingress and egress. The durations of the ingress and egress of the light curve are required for determining the physical parameters of a planet-star system from photometry alone (Seager & Mallén-Ornelas 2003), and provide power to discriminate between likely planet candidates and astrophysical false positives with similar light curve morphologies. To further improve the discriminating power of the light curve, we observe in  $I$ -band, to minimize the softening effects of limb-darkening on the sharp detail of any transit light curve.

Monitoring in  $I$ -band yields further benefits. Choosing such a red band minimizes extinction losses, which can be important when we observe open clusters close to the Galactic plane. It allows us to monitor redder dwarfs, which have smaller radii and so yield deeper transits for planets of Jupiter radius. For dwarfs of type M0V or later, the very red colour ( $R - I \sim 0.91$ ) compensates for the lower quantum efficiency of our CCD (36% in  $I$  compared to 55% in  $R$ ).

We manually fine-tune the telescope autoguiding to keep the target cluster stable on the chip, typically to within 0.435 arcsec, throughout the course of an observing run. This reduces the complexity of the pipeline reduction, since objects are then readily matched from frame to frame.

On a photometric night, we observe the cluster in  $BVRI$ , plus Landolt (1992) photometric standard stars with a range of colours and airmasses. We also use the colours

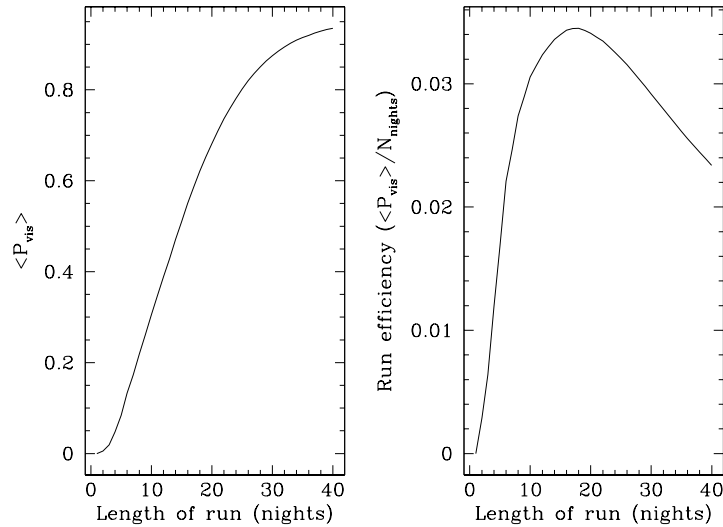


Figure 2.1: **Left:** Average of  $P_{\text{vis}}$  over periods of  $1d < P < 5d$  and random phases, as a function of run length. For this calculation, we assume 10.8 hour nights, sufficiently perfect that the planet transit is detected 100% of the time if it falls within the observing window. The rollover at long run lengths occurs as detections of short period planets saturate at 100%; as we continue to pick up longer period planets, the  $\langle P_{\text{vis}} \rangle$  asymptotically approaches 100%. **Right:** Mean  $P_{\text{vis}}$  as in left panel, but normalized by the length of the run. This illustrates how, due to saturation on short periods, a point of diminishing returns is reached, where only a few new (phase, period) combinations become detectable each night. Therefore, assuming random (phase, period) distributions, we can maximize the number of planets detected by switching to a fresh target field (assuming the same number of transiting planets are present in both old and new target fields) after the equivalent of  $\sim 18$  perfect nights of observing.

of each star to narrow down its possible spectral type, in the absence of a spectrum; this technique is calibrated using a small sample of spectroscopic observations, outlined in §2.3.2. Since the open clusters are several arcminutes in angular diameter, we cannot accurately ascertain the background population using only the cluster-centred images. Therefore, we observe two off-cluster control fields in a minimum of  $VI$ ; in half the cases, we had sufficient time to observe them in  $BR$  also.

Photometric observations were all performed using the SITE#3 CCD imager on the Swope 1.0 metre telescope at Las Campanas Observatory. The chip is  $2048 \times 4096$ , with camera plate scale 0.435 arcsec/pixel, gain  $2.5 \text{ e}^-/\text{ADU}$ , and read noise  $6.6 \text{ e}^-$ . However,

it is vignetted at the top, so we only use a subraster of  $2048 \times 3350$ , corresponding to a field of view  $15' \times 23.5'$ .

From Mar. 5-Apr. 9, 2004, an alternate mounting base and guider camera were substituted, during a telescope upgrade. The substitute guider exhibited flexure of order 1 arcsec per five minute exposure. However, the filters used remained the same.

Each open cluster was monitored for a single run. We observed our eight cluster targets during over 190 allocated nights less 38 nights of weather losses and instrument problems.

The LCO Swope Telescope is not staffed by a telescope operator. Therefore, all telescope calibration is the responsibility of the user. Our standard observing procedure is as follows.

1. We take series of  $\sim 10 - 20$  biases and domeflats in the afternoon. The computer clock drifts by  $\sim 5$  seconds per day, so we synchronize it with the USNO master clock each afternoon to ensure good timings on our light curves. Extra domeflats are taken if the observing run is broken up every two nights by other telescope users, since dust patterns on the filters may change when other users swap out filters; we aim to produce at least 100 domeflats per observed filter, for each undisturbed string of nights allocated to us. An hour before the beginning of the night, conditions permitting, we open the dome shutter and turn on telescope mirror fans to bring the telescope to thermal equilibrium. At twilight, if the sky is photometric, we collect skyflats of an empty field passing near zenith. Because of the two-min. CCD readout time, we are limited to approximately five skyflats in each of two filters. We aim for average flatfield count levels of 5000-15000 ADU, well below the CCD saturation level of 32768 ADU.
2. The maximum exposure time we allow for a skyflat is five minutes, at which point the sky is dark enough to begin calibrating the telescope pointing and focussing. We use the fast-readout TV guider (typical refresh time 0.25 seconds, zoomable field of view  $\sim 2' \times 2'$ ) to locate a bright star and calibrate the telescope encoders. We then slew to our target field, low in the East at the beginning of the night. The slew is generally accurate to a fraction of an arcminute, allowing us to use the TV guider to locate a target field we have previously observed and picked a guide star for. If we are observing the field for the first time, we must use the slow-readout SITE#3 CCD to verify positional accuracy, then choose a bright but unsaturated guide star in the guider field of view. We position the guider in the same place

relative to the imager at the beginning of each night, then move the telescope to always place the guide star on the same TV guider pixel. This allows us to set up the telescope on the field with a repeatability of  $\sim 4$  arcsec from night to night, at which point the SITE#3 CCD itself must be used to fine-tune the pointing.

3. We use the target field itself to focus the telescope at the beginning of the night. We estimate a focus setting (position of the secondary mirror) by examining the ellipticities and peak fluxes of stars in a CCD focus strip, based on the last setting from the previous night, and add an offset based on the difference in the telescope cell temperature. As the night proceeds, the focus is finely adjusted in between exposures if the average PSF becomes elliptical (ellipticity  $> 0.1$ ). In the first hour of the night, the temperature often changes quickly enough that the focus must be adjusted on a timescale of  $\sim 10$  min.
4. During the course of a typical night, we collect between one and one hundred 300 second *I*-band monitoring images, depending on weather and target observability. While collecting the images, we try to maintain the telescope pointing to a precision of  $\pm 1$  pixel= $0.435''$  (the guider software allows the user to move the telescope reliably in steps of 0.1 arcsec at best). We maintain precise pointing by comparing the CCD frames to a good reference frame taken during the first night, using an IRAF script written by G. Mallén-Ornelas. For hand-picked stars, the script measures the centroid offsets between the most recent CCD frame and the reference frame, the integrated counts, and the seeing values. In between frames, we adjust the guider according to the reported centroid offsets. Fine guiding adjustments of order 0.2 arcsec must be made on timescales of  $\sim 30$ min., while a couple of times per night, large-scale adjustments of order 1 arcsec are necessary due to more sudden flexures in the telescope.
5. On a photometric night during a run, we also collect images of the cluster in other filters, typically 300 sec. in *R* and *V*, and 500 sec. in *B*. We attempt to collect these images when the cluster is at low airmass, and follow them up with images of fields offset plus and minus one degree in Galactic longitude at the same Galactic latitude. These non-cluster “control fields” are observed for 300 sec. in *V* and *I*, and, time permitting, for 300 sec. in *R* and 500 sec. in *B*. Over the course of the night, we attempt to observe up to six Landolt standard fields at a range of airmasses: two fields at the beginning of the night, two in the middle, and two in

morning twilight.

Sample *I*-band images of our target fields and their flanking one-degree-offset control fields are shown in Figures 2.2 through 2.9. We typically obtained 1000-2000 epochs for each cluster, with best seeing 0.9", worst seeing  $\gtrsim 2.5''$ , and typical seeing at low airmass in good conditions 1.2". This coverage was sufficient to generate an average  $P_{vis} \sim 0.5$ , and, given a typical in-transit Hot Jupiter duty cycle of  $\sim 5\%$ , to secure an average of at least 20 data points per transit. As will be discussed in §5.X, our sample is large enough to yield multiple planet detections. A summary of our photometric observing runs is presented in Table 2.2, listing the exact number of 300 sec. *I*-band monitoring frames obtained, along with the amount of observing time required to obtain them (we can lose up to a third of our nights in bouts of southern winter weather). A journal of the photometric night calibration observations, including imaging of cluster, control, and Landolt fields, is presented in Tables 2.3 – 2.4. If a cluster and its control fields could not be photometrically calibrated during the cluster's monitoring run, they were calibrated during a later run. We typically observe 4 Landolt standard fields per science target, and calibrate the science target with  $\gtrsim 20$  Landolt standard stars in opportune positions spanning airmasses of 1.2 to 2.0. Plots of the window functions we achieved for each cluster are shown in Figures 2.10 and 2.11. These show that for our best observing runs, we are sensitive to nearly 100% of possible planet phases at periods less than two days, and still maintain coverage of 40% of possible phases out to five day periods.

Table 2.2: Journal of monitoring observations

Target	Run dates	#Nights allocated	#Usable I frames	Comments
NGC 2660	Feb. 10-28, 2003	16	932	$\sim 1$ night lost due to weather
NGC 6208	May 16-Jun. 19, 2003	32	1678	$\sim 11$ nights lost due to weather
IC 2714	Mar. 5-Apr. 4, 2004	26	1616	$\sim 3$ nights lost due to weather, $\sim 1$ night to instrument issues.
NGC 5316	Apr. 5-Apr. 26, 2004	22	1516	$\sim 3$ nights lost due to weather
NGC 6253	Jun. 3-24, 2004	22	1724	$\sim 3$ nights lost due to weather
NGC 2447	Nov. 24, 2004-Jan. 8, 2005	22	1138	Mostly clear; no nights lost
NGC 6134	May 1-Jun. 5, 2005	32	1888	$\sim 10$ nights lost due to weather
IC 4651	Jul. 3-Jul. 29, 2005	18.5	929	$\sim 6$ nights lost due to weather

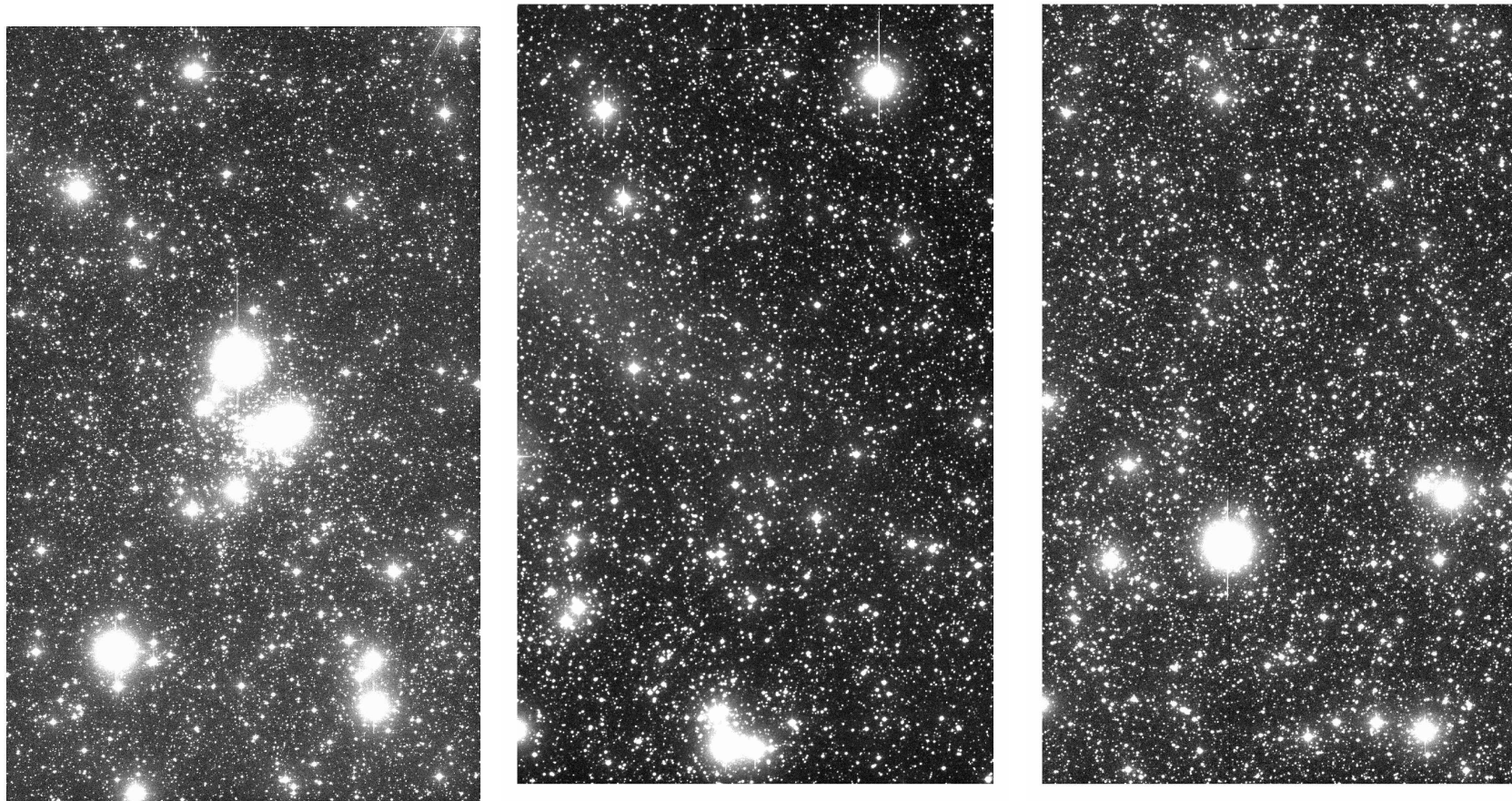


Figure 2.2: **Left:** NGC 2660. **Middle:** NGC 2660 flanking control field at Galactic coordinates  $(l, b) = (264.9, -3.0)$ . **Right:** NGC 2660 flanking control field at  $(l, b) = (266.9, -3.0)$ . All images are 300 seconds in  $I$ -band. For the Swope CCD, north is down; east is right. The  $2048 \times 3350$  subraster used corresponds to a field size  $15' \times 23.5'$ .

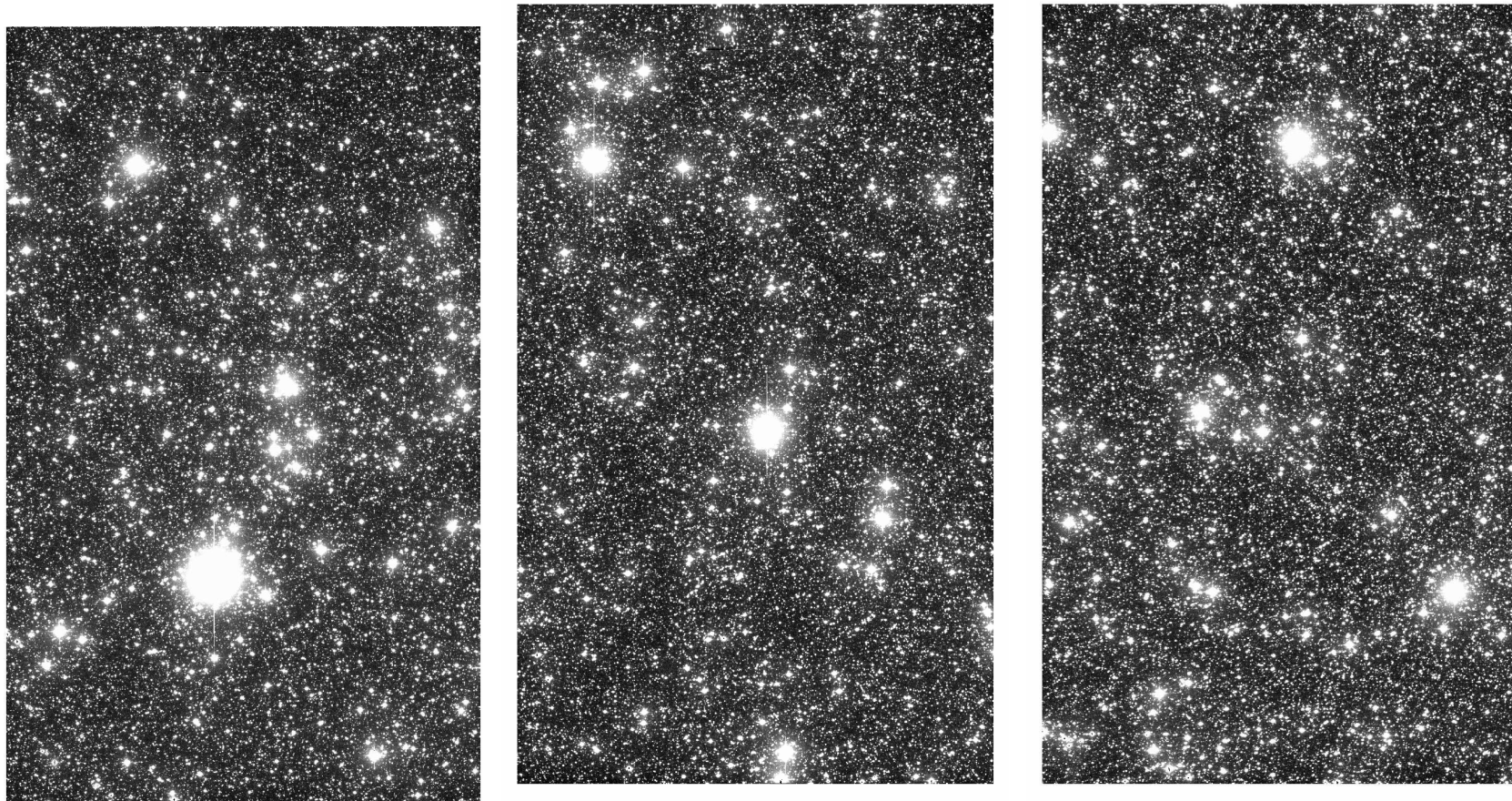


Figure 2.3: **Left:** NGC 6208. **Middle:** NGC 6208 flanking control field at  $(l, b) = (334.8, -5.8)$ . **Right:** NGC 6208 flanking control field at  $(l, b) = (332.8, -5.8)$ . All images are 300 seconds in  $I$ -band. For the Swope CCD, north is down; east is right. The  $2048 \times 3350$  subraster used corresponds to a field size  $15' \times 23.5'$ .



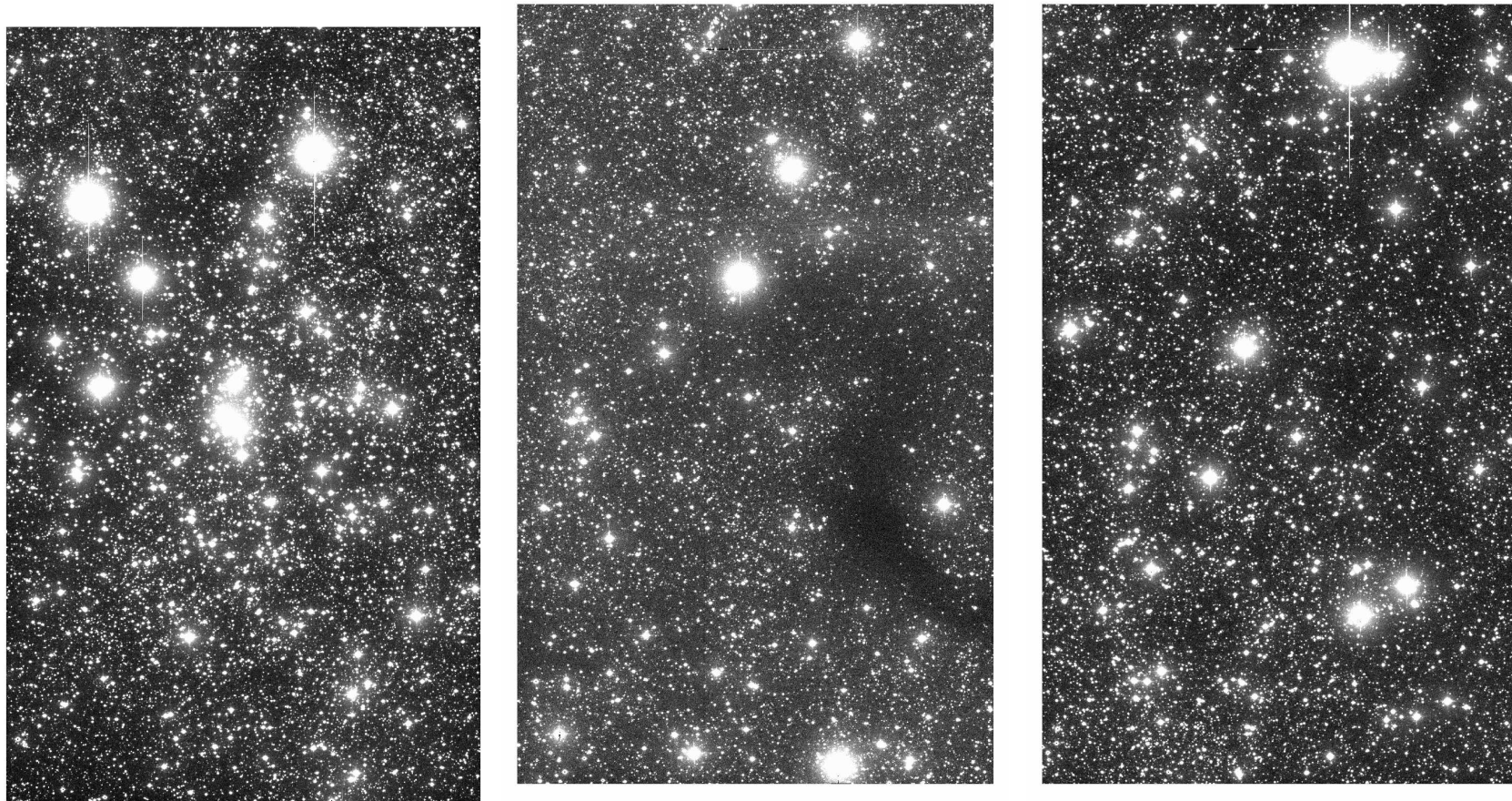


Figure 2.4: **Left:** IC 2714. **Middle:** IC 2714 flanking control field at  $(l, b) = (291.4, -1.8)$ . **Right:** IC 2714 flanking control field at  $(l, b) = (293.4, -1.8)$ . All images are 300 seconds in  $I$ -band. For the Swope CCD, north is down; east is right. The  $2048 \times 3350$  subrastrer used corresponds to a field size  $15' \times 23.5'$ .

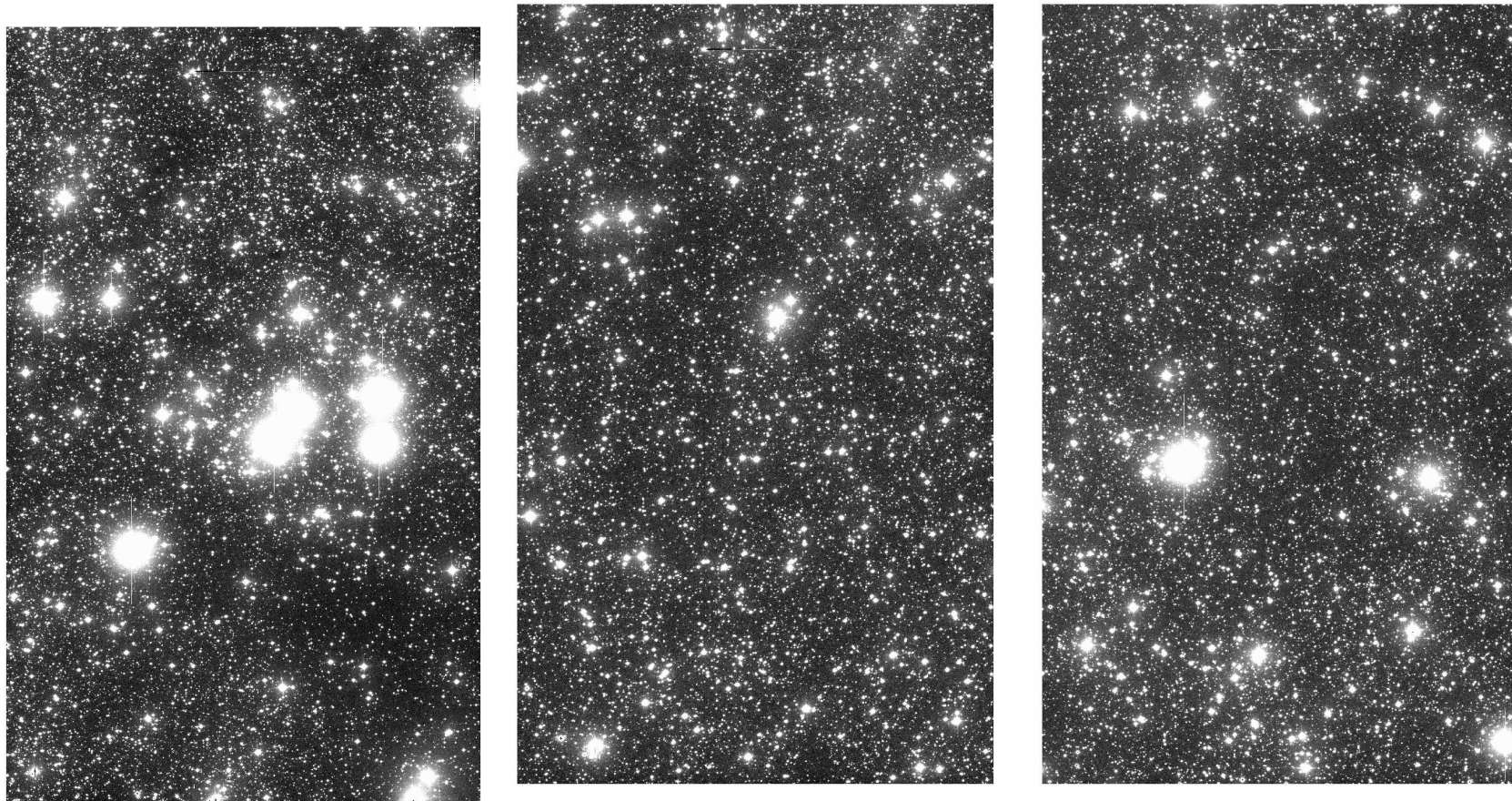


Figure 2.5: **Left:** NGC 5316. **Middle:** NGC 5316 flanking control field at  $(l, b) = (311.2, 0.1)$ . **Right:** NGC 5316 flanking control field at  $(l, b) = (309.2, 0.1)$ . All images are 300 seconds in  $I$ -band. For the Swope CCD, north is down; east is right. The  $2048 \times 3350$  subraster used corresponds to a field size  $15' \times 23.5'$ . Dust lanes are visible in the field of NGC 5316.

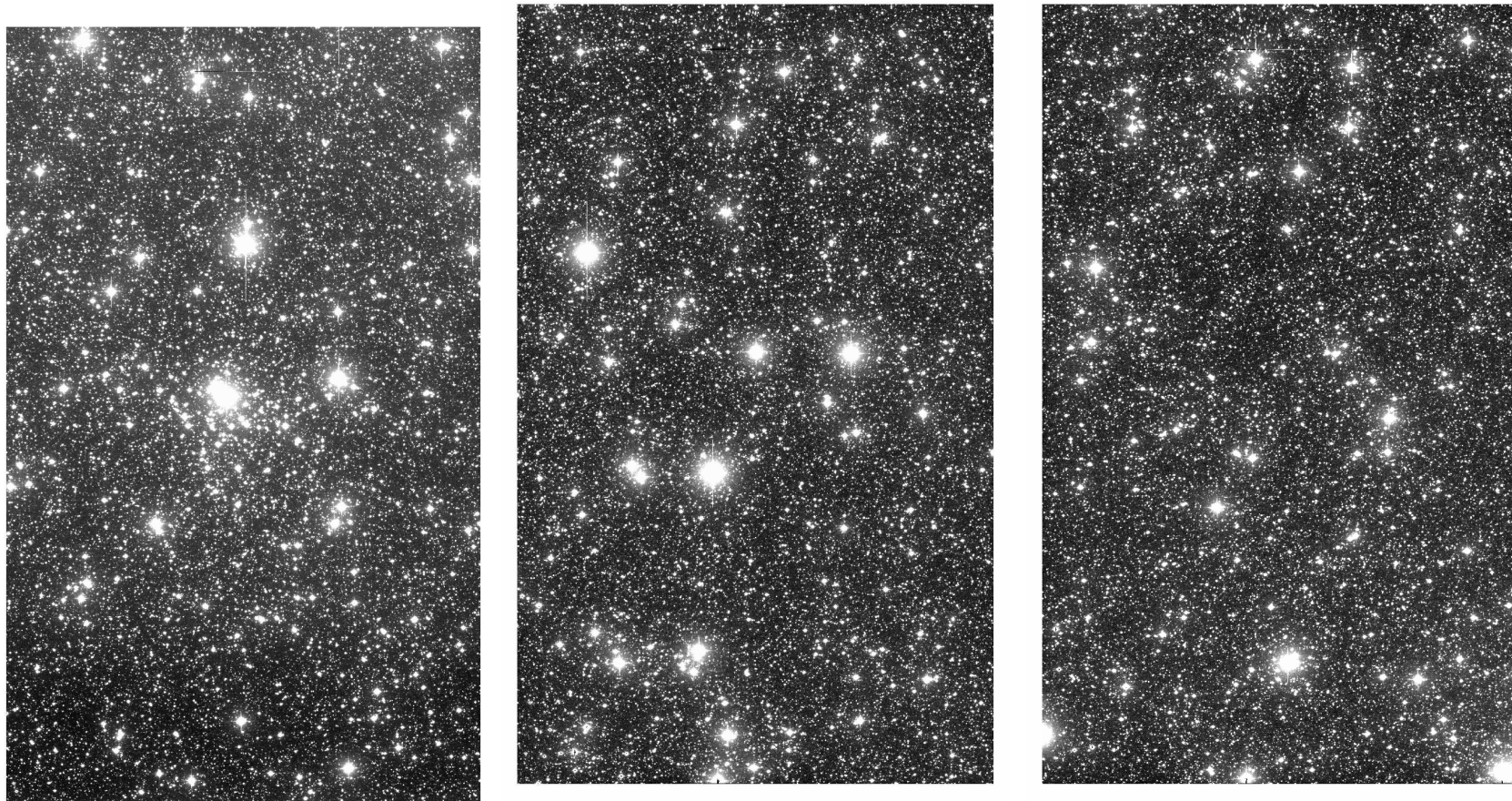


Figure 2.6: **Left:** NGC 6253. **Middle:** NGC 6253 flanking control field at  $(l, b) = (334.5, -6.3)$ . **Right:** NGC 6253 flanking control field at  $(l, b) = (336.5, -6.3)$ . All images are 300 seconds in  $I$ -band. For the Swope CCD, north is down; east is right. The  $2048 \times 3350$  subraster used corresponds to a field size  $15' \times 23.5'$ .

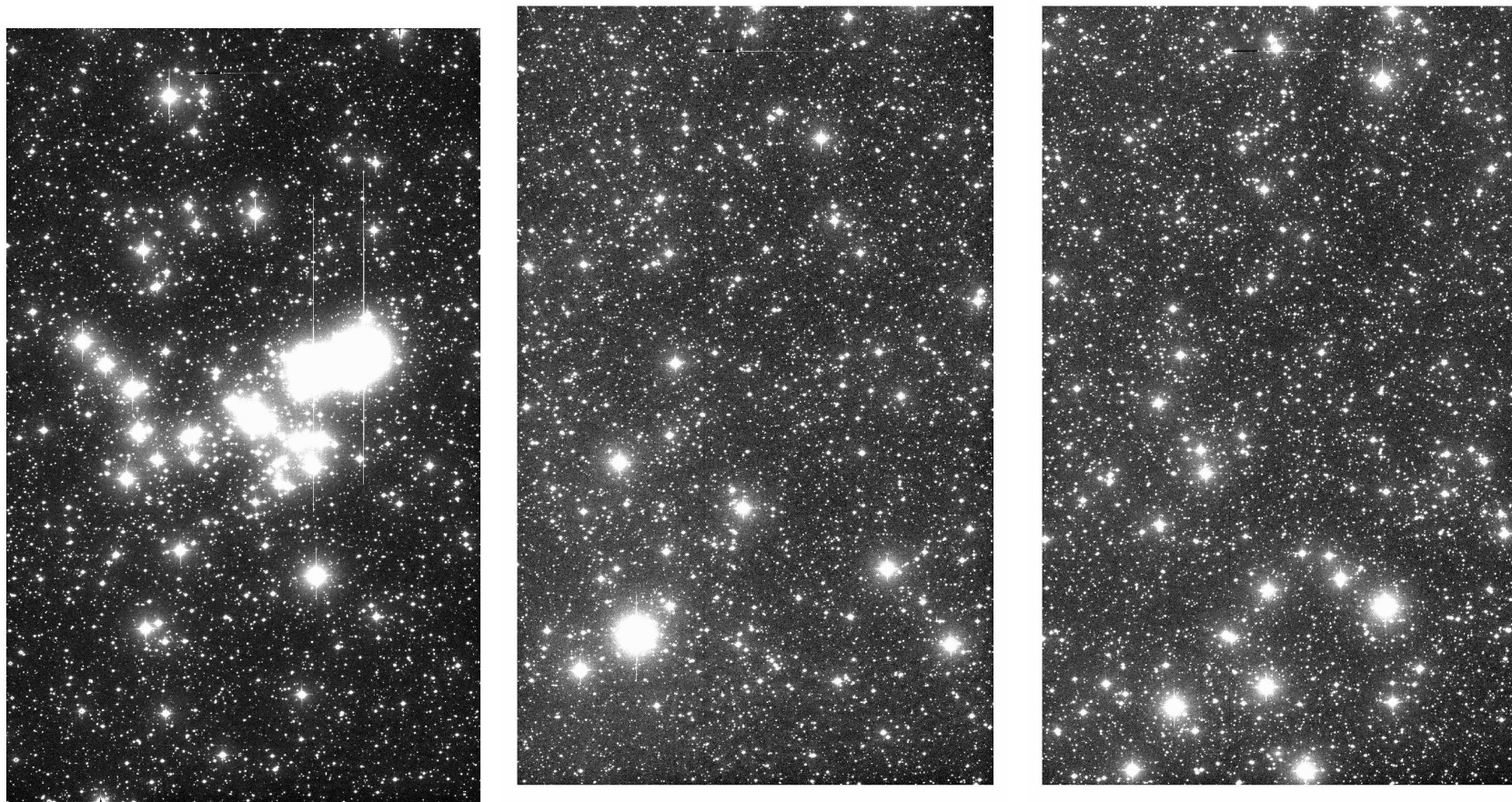


Figure 2.7: **Left:** NGC 2447. **Middle:** NGC 2447 flanking control field at  $(l, b) = (239.0, 0.1)$ . **Right:** NGC 2447 flanking control field at  $(l, b) = (241.0, 0.1)$ . All images are 300 seconds in  $I$ -band. For the Swope CCD, north is down; east is right. The  $2048 \times 3350$  subraster used corresponds to a field size  $15' \times 23.5'$ .

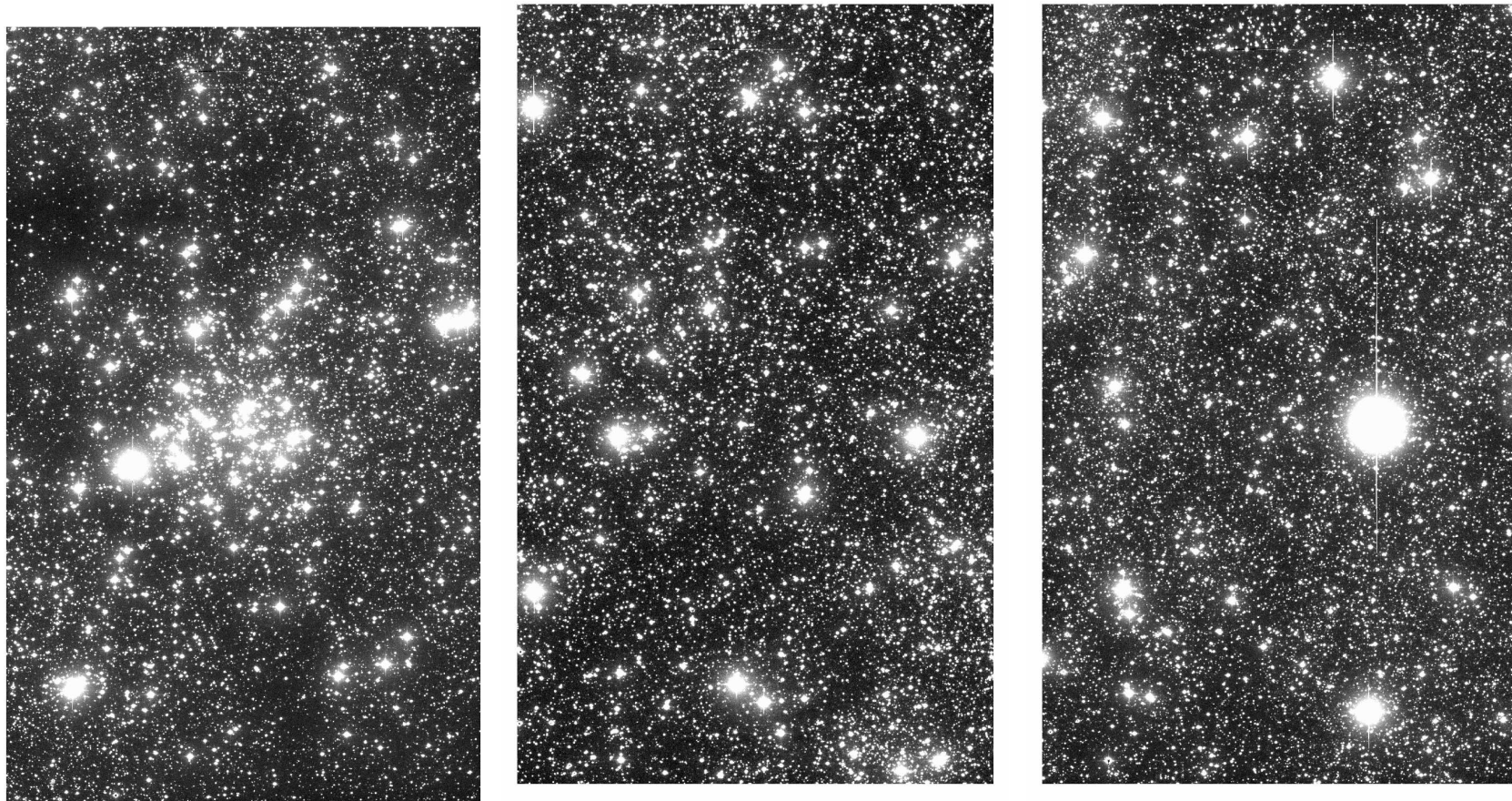


Figure 2.8: **Left:** NGC 6134. **Middle:** NGC 6134 flanking control field at  $(l, b) = (333.9, -0.2)$ . **Right:** NGC 6134 flanking control field at  $(l, b) = (341.9, -0.2)$ . All images are 300 seconds in  $I$ -band. For the Swope CCD, north is down; east is right. The  $2048 \times 3350$  subrastrer used corresponds to a field size  $15' \times 23.5'$ . The field of NGC 6134 contains prominent dust lanes.

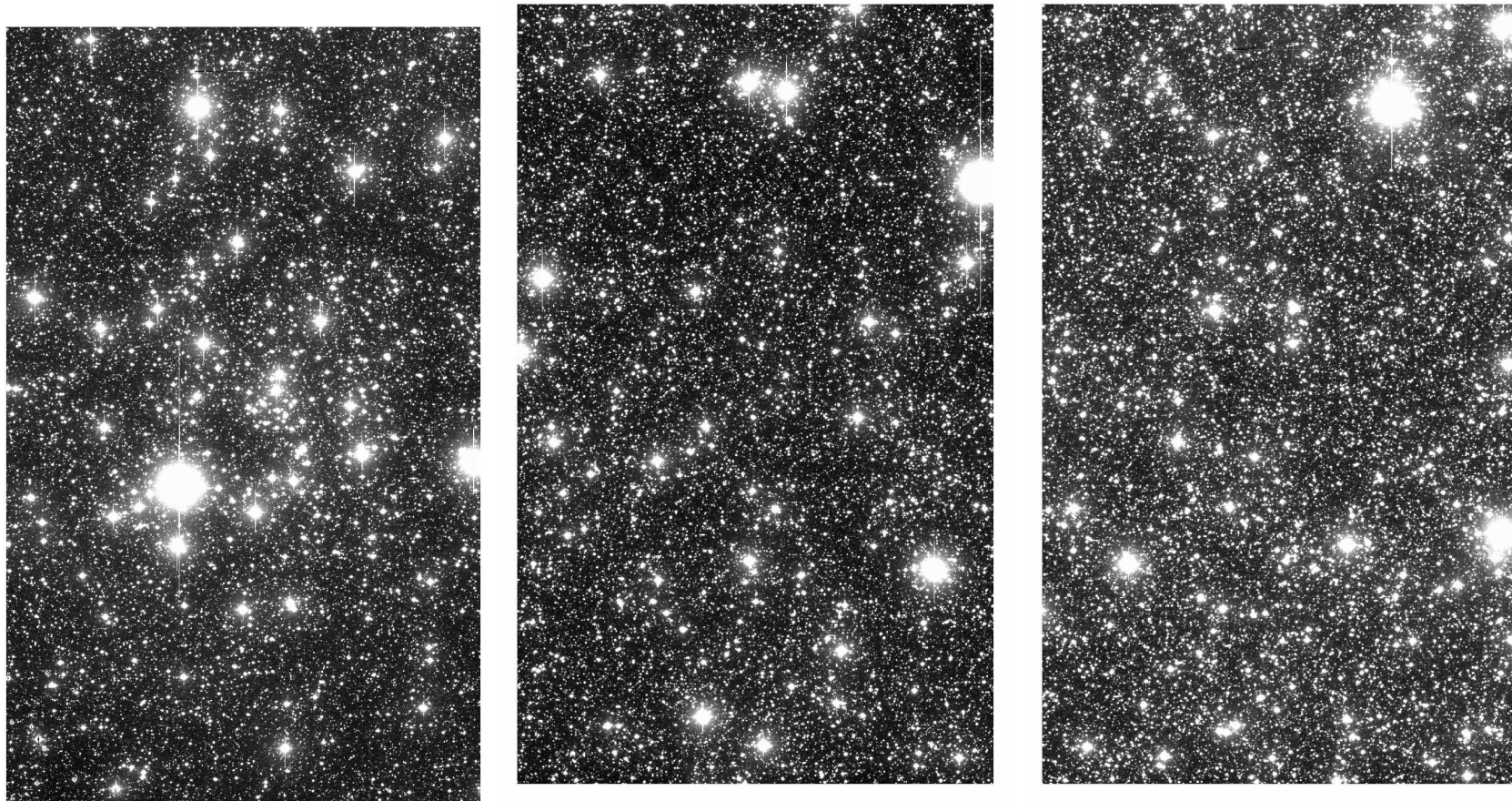


Figure 2.9: **Left:** IC 4651. **Middle:** IC 4651 flanking control field at  $(l, b) = (339.1, -7.9)$ . **Right:** IC 4651 flanking control field at  $(l, b) = (341.1, -7.9)$ . All images are 300 seconds in  $I$ -band. For the Swope CCD, north is down; east is right. The  $2048 \times 3350$  subrastrer used corresponds to a field size  $15' \times 23.5'$ .

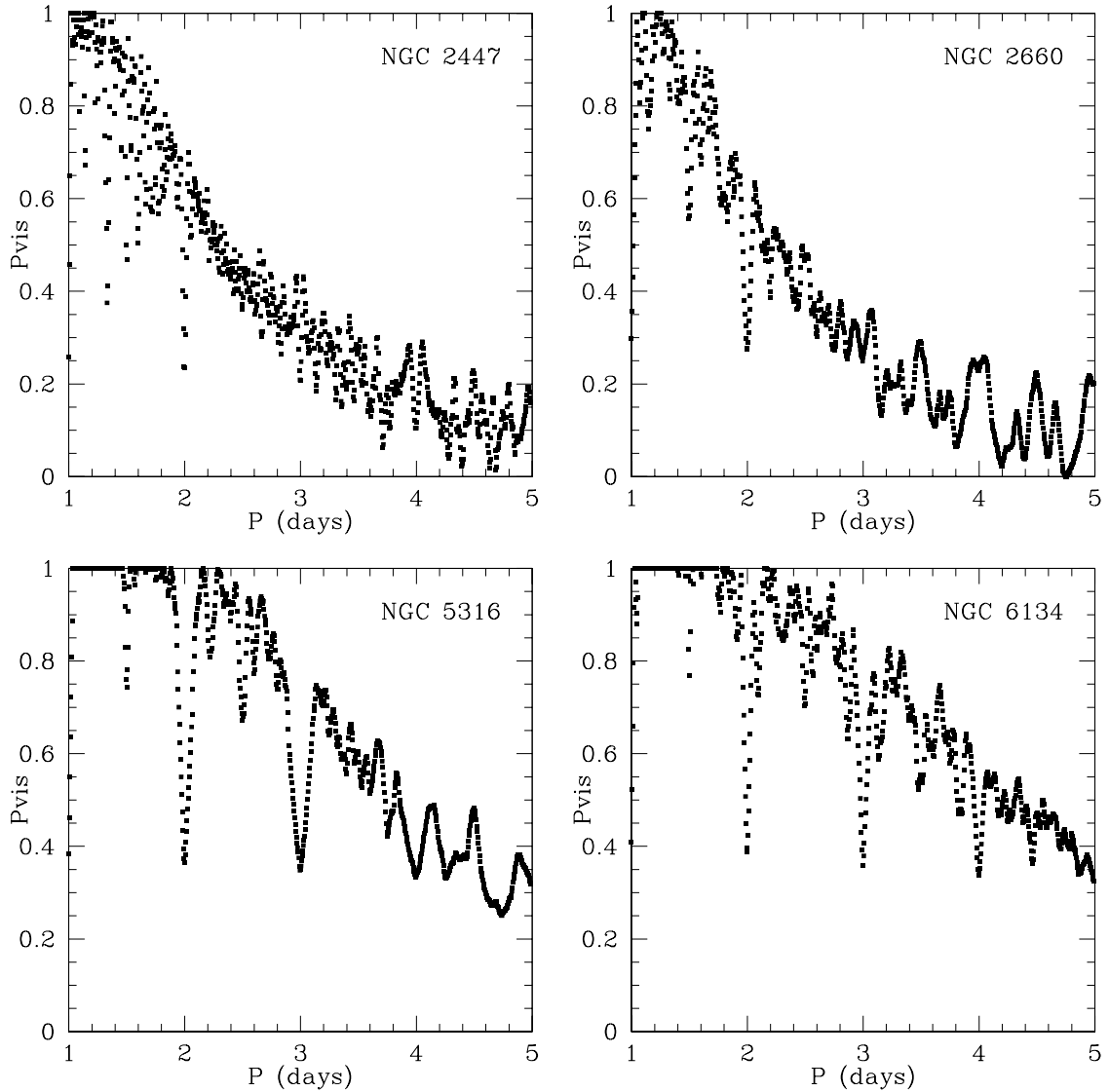


Figure 2.10: Probability  $P_{vis}$  of two extant transits falling within the observing windows, as a function of hypothetical planet periods, for our observations of NGC 2447, NGC 2660, NGC 5316, and NGC 6134. At precisely integral periods,  $\sim 50\%$  of all phases of planet transits will never occur during the nighttime, causing  $\sim 50\%$  drops in  $P_{vis}$ .

Table 2.3: Journal of observations on photometric nights for NGC 6208, NGC 2660, IC 2714, NGC 5316, NGC 6253, and their flanking control fields

Date of calibration	List of science fields with filters observed	Exposure times <i>B, V, R, I</i> (sec.)	List of Landolt fields observed	Exposure times <i>B, V, R, I</i> (sec.)	Landolt field airmasses <i>B, V, R, I</i>	# of standard stars in Landolt field
May 24, 2003	NGC 6208 <i>BVRI</i>	500, 300, 300, 300	SA 104	45, 20, 20, 20	1.24, 1.23, 1.21, 1.22	11
	NGC 6208 control fields <i>BVRI</i>	500, 300, 300, 300	SA 107	45, 20, 20, 20	2.09, 1.85, 2.03, 1.98	11
			SA 110	90, 20, 20, 20	1.71, 1.63, 1.65, 1.60	11
Mar. 7, 2004	NGC 2660 <i>BVRI</i>	500, 300, 300, 300	SA 95	120, 20, 10, 10	1.52, 1.46, 1.56, 1.58	6
	NGC 2660 control fields <i>BVRI</i>	500, 300, 300, 300	SA 98	25, 10, 10, 10	2.66, 2.74, 2.59, 2.50	39
	IC 2714 <i>BVRI</i>	500,300,300,300	SA 110	60, 30, 15, 10	1.46, 1.49, 1.48, 1.53	5
	IC 2714 control fields <i>VI</i>	-,300,-,300	RU 149	60, 20, 15, -	1.14, 1.14, 1.14, -	8
			PG 1323	60, 25, 25, 20	1.07, 1.07, 1.07, 1.07	5
Apr. 6, 2004	NGC 5316 <i>BVRI</i>	500, 300, 300, 300	SA107	80, 30, 30, 30	1.20, 1.18, 1.19, 1.18	11
	NGC 5316 control fields <i>BVI</i>	500, 300, -, 300	SA107	80, 30, 10, 10	1.63, 1.61, 1.54, 1.53	11
			SA 113	20, 10, 10, 10	1.81, 1.91, 1.84, 1.87	10
			RU 149	25, 10, 10, 10	1.15, 1.14, 1.15, 1.14	8
Jun. 6, 2004	NGC 6253 <i>BVRI</i>	500, 300, 300, 300	SA 101	30, 20, 20, 20	1.21, 1.20, 1.21, 1.19	11
	NGC 6253 control fields <i>BVRI</i>	500, 300, 300, 300	SA 104	30, 20, 20, 20	1.21, 1.20, 1.21, 1.20	13
			SA 110	30, 10, 10, 10	1.33, 1.37, 1.34, 1.35	11
			SA 110	30, 10, 10, 10	2.09, 1.96, 2.05, 2.01	11
			SA 113	30, 10, 10, 10	1.21, 1.20, 1.20, 1.19	15



Table 2.4: Journal of observations on photometric nights for NGC 2447, NGC 6134, IC 4651, and their flanking control fields

Date of calibration	List of science fields with filters observed	Exposure times <i>B, V, R, I</i> (sec.)	List of Landolt fields observed	Exposure times <i>B, V, R, I</i> (sec.)	Landolt field airmasses <i>B, V, R, I</i>	# of standard stars in Landolt field
Nov. 25, 2004	NGC 2447 <i>BVRI</i>	500, 300, 300, 300	TPHE	30, 10, 10, 10	1.15, 1.13, 1.14, 1.11	7
	NGC 2447 control fields <i>VI</i>	-, 300, -, 300	SA 92	45, 15, 15, 10	1.30, 1.33, 1.30, 1.32	12
			SA 98	60, 40, 20, 20	1.90, 2.04, 1.94, 1.99	35
			SA 98	120, 30, 20, 30	1.86, 1.76, 1.64, 1.68	35
			SA 98	90, 60, 20, -	1.58, 1.72, 1.60, -	35
May 21, 2005	NGC 6134 <i>BVRI</i>	500, 300, 300, 300	PG 1047	20, 20, 10, 10	1.15, 1.15, 1.15, 1.16	4
	NGC 6134 control fields <i>BVRI</i>	500, 300, 300, 300	PG 1047	20, 20, 10, 10	2.08, 2.04, 2.12, 2.00	4
			RU 149	10, 10, 8, 8	1.96, 1.92, 1.99, 1.88	8
			PG 1323	20, 20, 10, 10	1.14, 1.13, 1.14, 1.13	5
Jul. 7, 2005	IC 4651 <i>BVRI</i>	500, 400, 300, 300	PG 1323	30, 10, 15, 10	1.07, 1.07, 1.07, 1.07	5
	IC 4651 control fields <i>VI</i>	-, 400, -, 300	G93	45, 20, 20, 10	1.32, 1.31, 1.32, 1.30	1
			SA 112	45, 20, 20, 10	1.88, 1.79, 1.85, 1.82	5
			SA 114	45, 20, 20, 10	1.27, 1.29, 1.26, 1.28	3
			SA 114	30, 15, 10, 10	1.35, 1.34, 1.36, 1.37	4
			PG 2336	10, 10, 5, 10	1.29, 1.26, 1.28, 1.27	3

### 2.3.2 Supplementary Low-resolution Spectroscopy: Strategy and Observations

Four of our open clusters, IC 2714, NGC 2447, NGC 5316, and NGC 6253, were targeted with multi-object spectroscopy for MK stellar classification purposes. Our spectroscopic observations were performed using the WFCCD multi-object spectrograph on the duPont 2.5 metre telescope at Las Campanas Observatory. The chip is  $2048 \times 2048$ , with camera plate scale 0.774 arcsec/pixel, gain  $1.0 \text{ e}^-/\text{ADU}$ , and read noise  $5.6 \text{ e}^-$ . We use the H&K grism, unfiltered, with a central wavelength of  $3700 \text{ \AA}$  and a dispersion of  $1.3 \text{ \AA}/\text{pixel}$ . Although the clear field of view is 25 arcmin in diameter, we only place slits on north half of the telescope's field of view when collecting spectra, in order to span a wavelength range  $\sim 2000 \text{ \AA}$  redwards of the central wavelength. We offset the telescope pointing 5 arcmin. to the south of the cluster coordinates to compensate for the northerly slit placement.

We sample approximately 50 random stars from each cluster field, in the magnitude range  $14 < I < 15.5$ . Since the dispersion axis is north-south, highest priority is given to stars within a 10 arcmin. wide strip in declination, distributed in a single tier across the centre of each open cluster field. This facilitates spectral coverage from  $\sim 3800 \text{ \AA} < \lambda < 5000 \text{ \AA}$  at an MK classification resolution of  $1.3 \text{ \AA}$  per pixel. On each mask, four bright alignment stars are chosen from a magnitude bin  $13.5 < I < 14.0$ . We required a minimum slit length of 10 arcsec (to ensure we sample a few arcsec of sky background in typical seeing conditions), a slit separation of 3 arcsec (the minimum required to ensure non-overlapping spectra, considering the optical distortions in the duPont+WFCCD system), and a 0.9 arcsec separation between the object and the end of the slit (to allow for seeing up to  $\sim 2$  arcsec). Within these magnitude and spatial sampling constraints, targets were automatically selected from our photometric catalogues (augmented with an astrometric calibration tied to the USNO system, supplied by M. Gladders) by the mask design software provided at Las Campanas Observatory. The software first maximized the number of targets, then maximized the slit lengths. Our multi-object slit masks were fabricated by Las Campanas Observatory with the minimum available slit width of 1.941 arcsec, and the holes for the alignment stars were 12 arcsec square. A sample mask layout is shown in Figure 2.12. We endeavour to achieve extracted spectra with  $\text{SNR} > 10$  at the blue end, typically requiring between 2400 and 7200 sec. of exposure time on duPont+WFCCD.

In order to do the best possible classification, an atlas of MK templates for this

particular instrument and slit size must be built. To this end, we observed  $\sim 10$  MK standard stars on each night of our observing run. These observations were conducted using a mask in which a long slit (also of width 1.941 arcsec) was cut on the north half of the mask, to provide red coverage matching that obtained for the multi-object spectra. Exposure times on the order of tens of seconds were sufficient to yield average  $\text{SNR} > 100$ .

Wavelength calibration is provided by HeArNe arc lamp spectra. We take at least one arc lamp and one quartz flat spectrum in place before or after each exposure to minimize error due to telescope flexure. Darks and biases are taken at the beginning or end of the night.

One four-night run was allocated for the spectroscopic observations. A summary of our spectroscopic observing runs is presented in Table 2.5.

Table 2.5: Journal of spectroscopic observations

Observation date	Cluster observed	Exposures	Comments
May 14, 2004	NGC 2447	$2 \times 1200$ sec.	
May 15, 2004	NGC 5316	$2 \times 1200$ sec.	
May 16, 2004	NGC 6253	$2 \times 1200$ sec.	
May 17, 2004	IC 2714	$2 \times 2400$ sec.	Light cloud cover

## 2.4 Data Reduction

### 2.4.1 Photometric frames

Here, we outline the standard preliminary steps in reducing our images, both to generate catalogues of stars captured in our surveys, and in preparation for more advanced analyses. These standard steps include preprocessing, object finding, and colour photometry. Since these steps are performed using existing software not specifically developed for this thesis, only a brief overview is provided. The intricacies of performing non-standard, high-precision relative photometry on our time-series of  $I$ -band observations are detailed in Chapter §3.

## Preprocessing

Image preprocessing was performed in a standard manner using IRAF (Tody 1986). We conducted overscan subtraction, bias subtraction, and flatfielding using the standard IRAF combine algorithms.

We collected sets of bias and domeflat images on almost every night. For many of our observing runs, the camera was untouched and stable over the whole run. In those cases, we could combine calibration frames from all nights to produce a single, high signal-to-noise master frame of each type. For observing runs interrupted by filter swaps or other instrument changes, separate master frames were made for calibrating each stretch of uninterrupted camera operation.

Note that while we collected twilight flats on several photometric evenings each run, we noticed little difference between these and the domeflats. Hence, we opted to calibrate using the higher signal-to-noise master domeflats.

The Swope CCD chip was maintained at a temperature  $\sim -95$  degrees C by liquid nitrogen, so dark current was negligible over our typical  $\sim 300$  sec. exposures, and no dark subtraction was necessary. The chip is not thinned, and so we did not notice significant fringing in any observed band. Thus, we did not defringe the images. The mild nonlinearity in counts near saturation (measured over the course of the 2005 season by the Carnegie Supernova Project, and expressed by the polynomial approximation in equation 2.1) was incorporated into the photometry codes, rather than in preprocessing.

$$ADU_{corrected} = ADU_{raw} \left[ 1 - 0.133722 \left( \frac{ADU_{raw}}{32767} \right) + 0.0498351 \left( \frac{ADU_{raw}}{32767} \right)^2 \right] \quad (2.1)$$

## Object finding

Object finding was performed using PPP (Yee 1991). We conduct the object search on a reference frame with moderately good seeing ( $\sim 1.3''$ ), such that the stars are well sampled by the  $.435''$  pixels, and so the brightest stars of interest are not saturated. The object finding image was masked to exclude bad columns and a region of bad charge transfer. An initial list of candidate objects was formed by including all peaks  $0.7\sigma$  above the sky background. Objects were rejected as cosmic rays if the peak pixel value was over ten times any surrounding pixel value. The PPP connectivity test was applied over a diameter of two pixels around each candidate object, to check whether those pixels were higher than  $1/20$  of the sky sigma. The PPP check for false detections within haloes

of bright stars was applied by smoothing candidates over a box size of three pixels and rejecting candidates that vanished after smoothing. Double detections were eliminated by merging any objects within one pixel of each other. A random  $\sim 4' \times 5'$  sample field of IC 2714 showing the typical quality of the object finding using these parameters is shown in Figure 2.13.

### Derivation of calibration coefficients

We correct our photometry for atmospheric absorption using first-order transformation equations together with our images of Landolt standards. For stars in the science and Landolt fields, we perform photometry for a sequence of apertures using the package PPP. PPP uses a curve of growth technique to extrapolate or interpolate the instrumental magnitude of each star from the aperture with minimum photometric noise to a large, common aperture size. We extract magnitudes corrected to an aperture radius of  $7''$ . Then, using the standard IRAF photcal package (partially automated by the snphot scripts written by M. Hamuy especially for the Swope telescope), we calculate the photometric calibration transformation coefficients using the Landolt fields. The transformation equations used by IRAF were:

$$B = b - k_b X_b + a_b(b - v) + \xi_b \quad (2.2)$$

$$V = v - k_v X_v + a_v(v - i) + \xi_v \quad (2.3)$$

$$R = r - k_r X_r + a_r(v - r) + \xi_r \quad (2.4)$$

$$I = i - k_i X_i + a_i(v - i) + \xi_i \quad (2.5)$$

where  $BVRI$  are the calibrated apparent magnitudes,  $bvri$  are the instrumental magnitudes,  $k_j$  are the airmass coefficients,  $X_j$  are the airmasses,  $a_j$  are the colour terms, and  $\xi_j$  are the zeropoints. The fitted airmass coefficients, colour terms, and zeropoints we derived on each photometric calibration night are listed in Table 2.6, for each of the  $B$ ,  $V$ ,  $R$ , and  $I$  transformation equations (Eqs. 2.2-2.5).

Fitting the coefficients using  $\gtrsim 20$  Landolt standard stars spread over airmasses from 1.2 to 2.0, we find average airmass coefficients of  $k_B \sim 0.23$ ,  $k_V \sim 0.12$ ,  $k_R \sim 0.09$ , and  $k_I \sim 0.05$ , with typical errors  $\pm 0.02$ . Our average colour terms are  $a_B \sim 0.07$ ,  $a_V \sim -0.06$ ,  $a_R \sim 0.02$ , and  $a_I \sim 0.04$ , with typical errors  $\pm 0.02$ . Our zero points

vary over ranges  $21.87 \leq \xi_B \leq 22.18$ ,  $21.94 \leq \xi_V \leq 22.18$ ,  $22.10 \leq \xi_R \leq 22.38$ , and  $21.60 \leq \xi_I \leq 21.86$ , with typical error  $\pm 0.03$ .

Once we have our transformation coefficients, we apply them to the PPP-derived science frame instrumental magnitudes, using EXPLORE project scripts to ensure uniform catalogue formats. A sample of the resulting catalogue is presented in §2.5.

## 2.4.2 Spectroscopic frames

We use the standard IRAF combine tasks to perform bias subtraction, dark subtraction, and flatfielding on each spectroscopic frame. Then, prior to extraction of individual spectra, we transform our multi-object spectra of cluster stars into a batch of single long-slit equivalent spectra. Using our Swope photometric catalogue positions plus a catalogue of positions from the same-night field alignment snapshots on du Pont WFCCD, we use IRAF's standard geometric transform tasks to map our catalogue target positions onto our multi-object spectral frame. For each spectroscopic target, we copy a rectangular strip around the target position, with sufficient width to encompass the spectrum (40 pixels' width along the spatial axis for multi-object slits from cluster fields, and 100 pixels' width for MK standard stars which were observed through a single slit); we also copy the corresponding regions from the arc spectra.

Each rectangular strip is then treated as a longslit spectrum. We use IRAF's `noao.twodspec` package to identify HeArNe lamp lines. For each spectrum, a few arc lines are identified by hand along a single row, and the identification propagated automatically to identify the lines in the other rows. For each row, we fit a Chebyshev polynomial of order 4 for the dispersion relation, apply the dispersion relation to the spectrum, manually select object and sky apertures, trace the spectrum with a polynomial of order 3 to 5, and finally extract this two-dimensional wavelength-calibrated spectrum to one dimension.

Finally, we visually compare the extracted, unknown multi-object spectra to our MK standard spectra. We assign a classification to each unknown spectrum based on the closest available standard spectrum. In cases where the unknown clearly falls halfway between two standards, the unknown may be classified with an intermediate type, but in general, the SNR of the unknown spectra is not sufficient to make such a distinction. Hence, we estimate our classification error as the typical spacing between the standard spectrum bins:  $\pm 3$  spectral subtypes. Sample comparisons between two unknowns and their closest standard matches are shown in Figure 2.14.

Table 2.6: Photometric calibration transformation equations

Calibration date (clusters calibrated)	Transformation equation	$k_j$	$a_j$	$\xi_j$
and number of Landolt standards in fit				
May 03 (NGC 6208)	B	$0.25 \pm 0.02$	$0.11 \pm 0.02$	$21.87 \pm 0.03$
	V	$0.11 \pm 0.02$	$-0.05 \pm 0.01$	$21.94 \pm 0.04$
	R	$0.08 \pm 0.02$	$0.03 \pm 0.02$	$22.10 \pm 0.03$
	I	$0.07 \pm 0.02$	$0.08 \pm 0.01$	$21.62 \pm 0.03$
33 points in fit	B	$0.24 \pm 0.01$	$0.05 \pm 0.01$	$22.12 \pm 0.01$
	V	$0.14 \pm 0.01$	$-0.06 \pm 0.01$	$22.18 \pm 0.02$
	R	$0.09 \pm 0.01$	$0.02 \pm 0.01$	$22.31 \pm 0.01$
	I	$0.05 \pm 0.01$	$0.04 \pm 0.01$	$21.80 \pm 0.02$
Mar. 04 (NGC 2660 and IC 2714)	B	$0.18 \pm 0.02$	$0.08 \pm 0.02$	$21.96 \pm 0.03$
	V	$0.12 \pm 0.02$	$-0.07 \pm 0.01$	$22.07 \pm 0.03$
	R	$0.10 \pm 0.02$	$-0.01 \pm 0.02$	$22.27 \pm 0.03$
	I	$0.08 \pm 0.02$	$0.03 \pm 0.01$	$21.78 \pm 0.03$
58 points in fit	B	$0.20 \pm 0.02$	$0.08 \pm 0.01$	$21.93 \pm 0.02$
	V	$0.12 \pm 0.02$	$-0.05 \pm 0.01$	$22.02 \pm 0.02$
	R	$0.07 \pm 0.01$	$0.03 \pm 0.01$	$22.16 \pm 0.02$
	I	$0.03 \pm 0.02$	$0.06 \pm 0.01$	$21.66 \pm 0.02$
Apr. 04 (NGC 5316)	B	$0.23 \pm 0.01$	$0.06 \pm 0.01$	$21.94 \pm 0.02$
	V	$0.10 \pm 0.01$	$-0.06 \pm 0.01$	$21.97 \pm 0.02$
	R	$0.09 \pm 0.01$	$0.01 \pm 0.01$	$22.14 \pm 0.02$
	I	$0.01 \pm 0.01$	$0.03 \pm 0.01$	$21.60 \pm 0.02$
124 points in fit	B	$0.26 \pm 0.02$	$0.06 \pm 0.02$	$22.18 \pm 0.03$
	V	$0.11 \pm 0.02$	$-0.07 \pm 0.02$	$22.17 \pm 0.04$
	R	$0.11 \pm 0.02$	$0.03 \pm 0.03$	$22.38 \pm 0.04$
	I	$0.04 \pm 0.02$	$0.03 \pm 0.02$	$21.86 \pm 0.04$
May 05 (NGC 6134)	B	$0.23 \pm 0.02$	$0.08 \pm 0.02$	$22.11 \pm 0.03$
	V	$0.13 \pm 0.02$	$-0.04 \pm 0.01$	$22.16 \pm 0.03$
	R	$0.09 \pm 0.02$	$0.06 \pm 0.03$	$22.29 \pm 0.04$
	I	$0.05 \pm 0.02$	$0.04 \pm 0.01$	$21.85 \pm 0.03$
21 points in fit	B	$0.23 \pm 0.02$	$0.08 \pm 0.02$	$22.11 \pm 0.03$
	V	$0.13 \pm 0.02$	$-0.04 \pm 0.01$	$22.16 \pm 0.03$
	R	$0.09 \pm 0.02$	$0.06 \pm 0.03$	$22.29 \pm 0.04$
	I	$0.05 \pm 0.02$	$0.04 \pm 0.01$	$21.85 \pm 0.03$
Jul. 05 (IC 4651)	B	$0.23 \pm 0.02$	$0.08 \pm 0.02$	$22.11 \pm 0.03$
	V	$0.13 \pm 0.02$	$-0.04 \pm 0.01$	$22.16 \pm 0.03$
	R	$0.09 \pm 0.02$	$0.06 \pm 0.03$	$22.29 \pm 0.04$
	I	$0.05 \pm 0.02$	$0.04 \pm 0.01$	$21.85 \pm 0.03$

## 2.5 Photometric catalogue

We produce catalogues of objects for both our cluster and control fields. A sample of data extracted from one of our photometric catalogues is shown in Table 2.7. The column labels are largely self-explanatory, giving each object’s catalogue number, position on the chip, magnitudes and errors. The classifier flag is meant for distinguishing extended objects, but here, virtually all our objects are stars. Therefore, we only take notice of the classifier flag if it has a value of 4, which means the object was saturated in one or more filters. Unreliable source detections are indicated either by a magnitude flagged by a value higher than 98, or by photometric errors larger than 1 mag.

The raw numbers of objects detected in object finding are in the tens of thousands for each cluster field. Some of these sources turn out to be false detections on blank patches of sky. Table 2.8 lists the raw numbers of detections in each field, and the numbers excluding objects with  $I > 98$  or with  $\sigma_I > 1$  mag. The fraction of such questionable detections is of order 10%, which is an acceptably small detriment to computational speed.

We use our catalogues to generate colour-magnitude diagrams of our clusters. Examples of these CMDs in  $V$  and  $V - I$  can be seen in Chapter 4.

Figures 2.15 and 2.16 show histograms of the  $I$  magnitudes of the catalogued stars, on a log scale. Our calibrated photometric catalogues become incomplete as the histograms turn over at faint magnitudes. We find the turn over is between  $I \sim 19$  and  $I \sim 19.5$  for NGC 6208, NGC 6253, and IC 4651, turn over is at  $I \sim 20$  for NGC 2660, NGC 5316, NGC 6134, and IC 2714, and turn over for NGC 2447 is at  $I \sim 21$ . While our monitoring images vary in depth depending on the observing conditions, the standard monitoring exposure time of 300 sec. is the same as the calibration image taken on a photometric night, so we expect conservatively that the monitoring images are incomplete past  $I \sim 19$ .



Table 2.7: Sample of NGC 2447 photometric catalogue

Object ID	x pixel position	y pixel position	$B$	$\sigma_B$	$V$	$\sigma_V$	$R$	$\sigma_R$	$I$	$\sigma_I$	Classifier flag
12800	1678.00	1910.00	134.23	1.46	22.62	0.66	21.11	0.21	19.62	0.24	2
12801	1696.00	1911.00	14.60	0.00	13.39	0.00	12.77	0.00	12.01	0.00	4
12802	1724.60	1911.90	127.45	9.00	120.46	0.75	22.31	0.18	22.45	0.13	1
12803	690.80	1912.50	22.18	0.75	22.60	1.06	21.69	0.40	20.15	0.25	2
12804	1718.00	1911.00	23.72	9.00	23.65	9.00	21.04	0.28	19.81	0.18	1
12805	1728.80	1911.20	127.45	9.00	120.55	2.95	24.68	9.00	23.98	0.29	2
12806	593.80	1912.60	134.20	0.69	23.12	0.67	22.06	0.27	21.39	0.46	1
12807	422.70	1913.30	18.21	0.00	17.46	0.02	17.06	0.00	16.28	0.02	0
12808	526.00	1912.00	127.45	9.00	120.75	1.52	127.25	9.00	27.09	9.00	0
12809	1193.00	1912.00	20.69	0.02	20.68	0.33	19.38	0.34	19.66	0.62	2
12810	1731.10	1912.00	26.00	9.00	22.83	0.80	22.36	0.45	19.53	0.30	1
12811	132.20	1913.00	134.06	1.27	25.18	9.99	22.87	0.57	21.36	0.34	0
12812	784.40	1912.50	14.38	0.00	13.95	0.00	13.75	0.00	13.43	0.00	1
12813	1222.60	1912.90	13.43	0.00	13.28	0.00	13.09	0.00	12.85	0.00	1
12814	839.60	1913.80	134.26	9.00	22.19	0.40	21.27	0.19	20.36	0.18	3
12815	504.80	1914.10	20.83	0.11	19.25	0.03	18.45	0.02	17.64	0.03	3
12816	891.30	1914.30	134.26	9.00	22.22	0.51	20.76	0.15	19.99	0.18	3
12817	1063.10	1913.00	16.96	1.88	120.65	1.32	127.25	9.00	25.46	9.00	0
12818	1402.00	1911.00	22.73	9.00	22.87	9.00	22.20	9.00	18.79	0.47	1
12819	968.00	1913.00	23.91	9.00	23.17	9.00	21.43	0.22	21.56	0.65	0
12820	631.30	1914.60	24.81	4.19	20.55	0.12	19.65	0.05	18.48	0.04	3

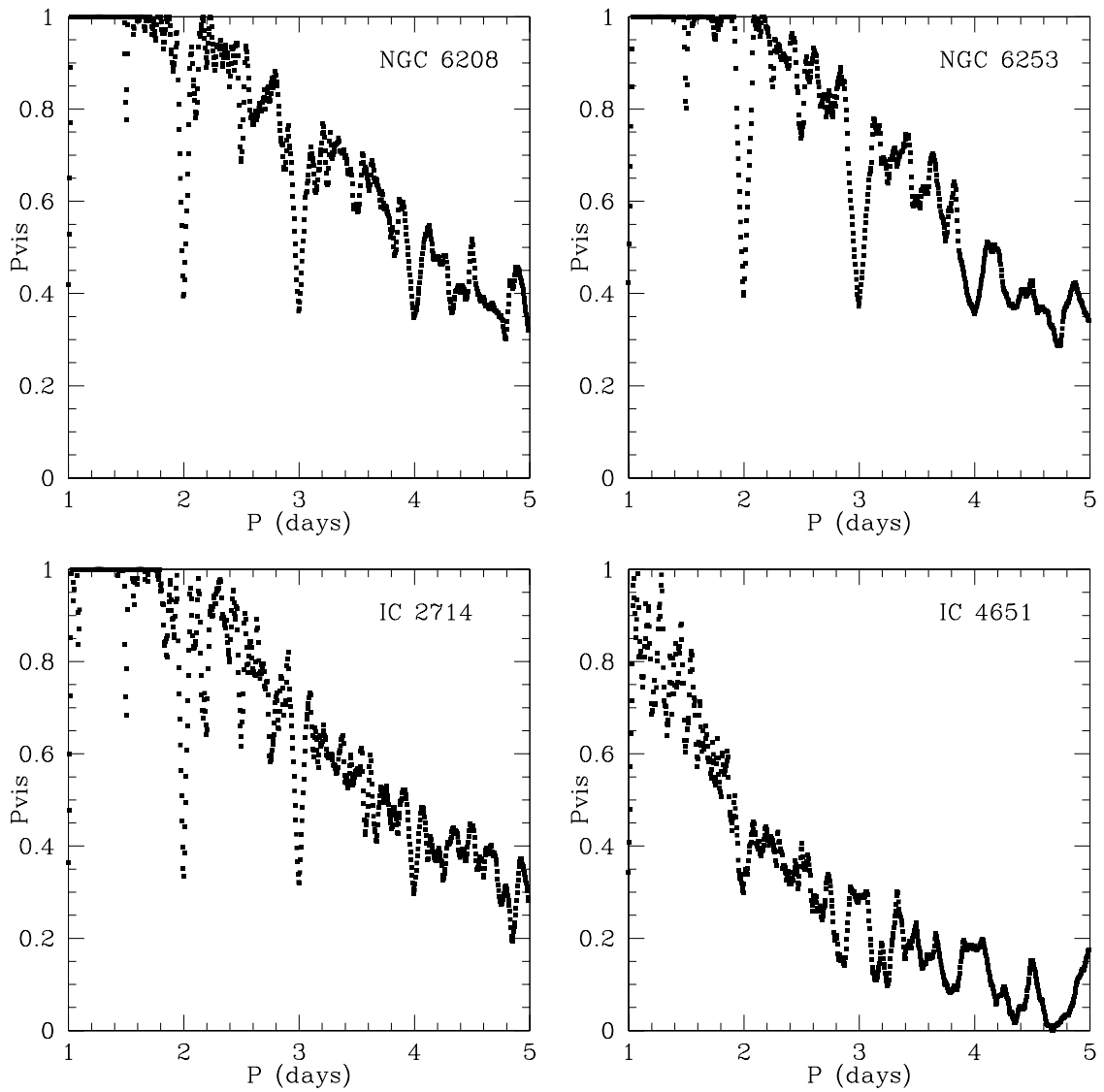


Figure 2.11: Probability of two extant transits falling within the observing windows, as a function of hypothetical planet periods, for our observations of NGC 6208, NGC 6253, IC 2714, and IC 4651.

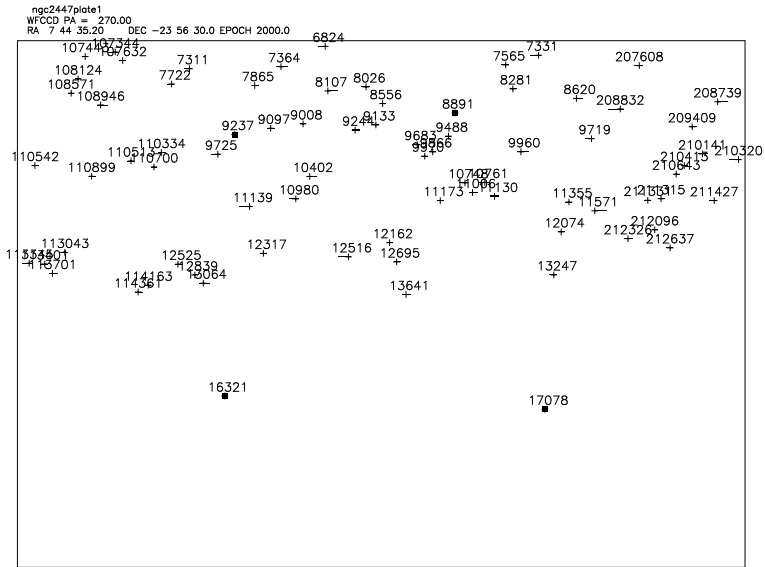


Figure 2.12: Sample output mask design for NGC 2447 as generated by the LCO duPont mask design software. Square boxes are alignment holes. Crosses mark locations of selected targets, and horizontal bars through the crosses show the lengths of the slits. Notice the placement of all slits on the north half of the mask, to enhance redward coverage.

Table 2.8: Quantity of objects overall, and quantity with sensible photometry

Cluster name	Raw number of objects detected	Objects with $I < 98$ and $\sigma_I < 1$ mag
IC 2714	35563	27754
IC 4651	41824	38176
NGC 2447	21851	17541
NGC 2660	30272	25104
NGC 5316	26562	31954
NGC 6134	28170	23367
NGC 6208	55967	48828
NGC 6253	48295	42953

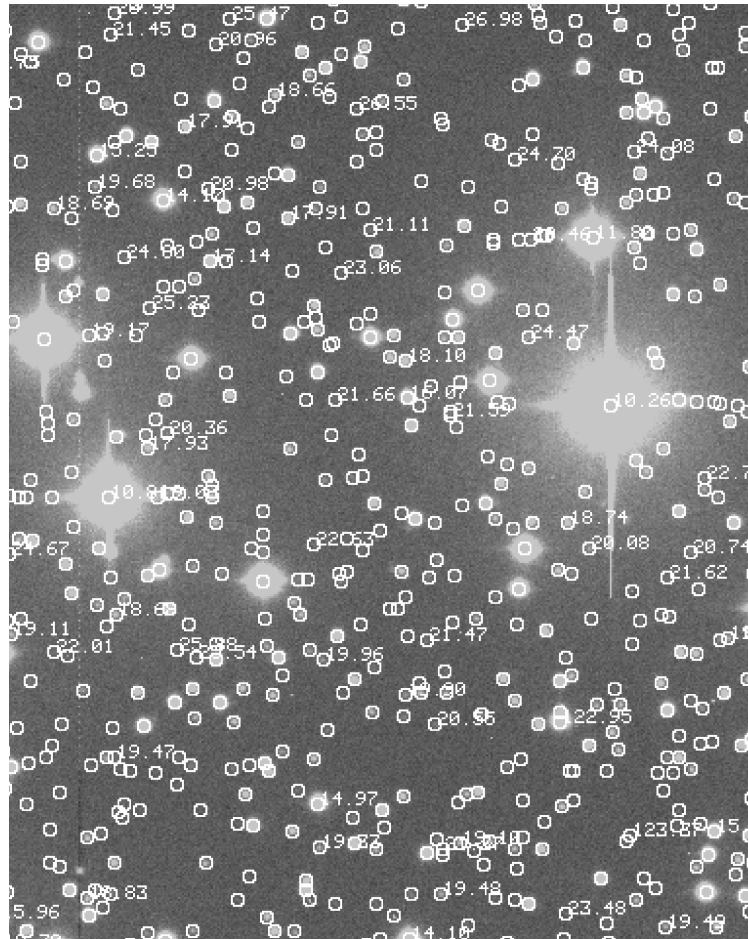


Figure 2.13: Quality of PPP object finding on a  $\sim 4' \times 5'$  sample field from IC 2714. Every tenth object has been labelled to its upper right with its  $I$  magnitude, demonstrating nearly 100% detection of objects to beyond  $I = 20$  (but note that magnitudes brighter than  $I = 13$  or fainter than  $I = 22$  are beyond the range of reliable photometry).

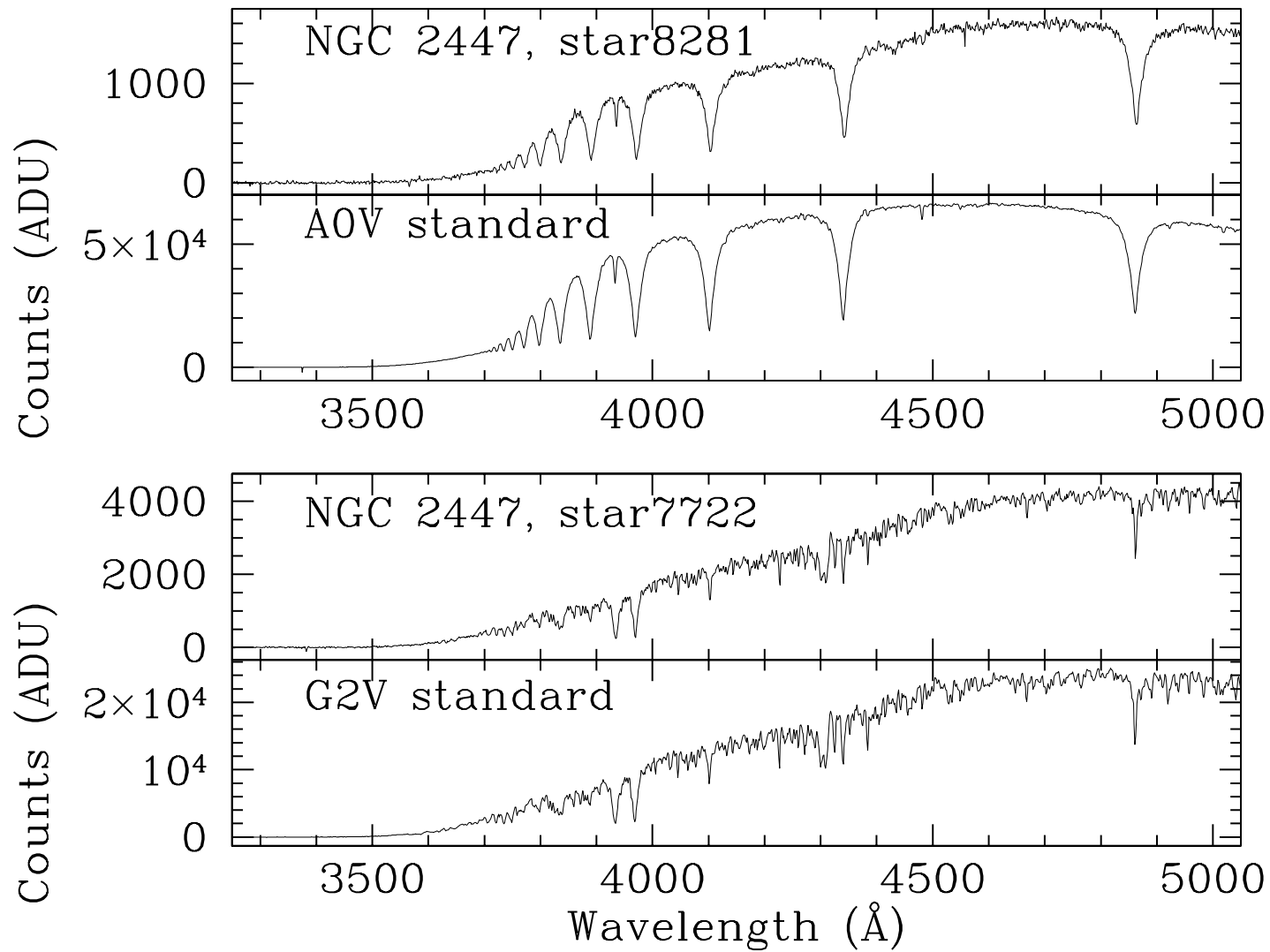


Figure 2.14: MK classification for two typical multi-object spectra. Two sample stellar spectra from the NGC 2447 multi-object mask are shown. Star 8281 best matches an A0V star, and star 7722 best matches a G2V star.

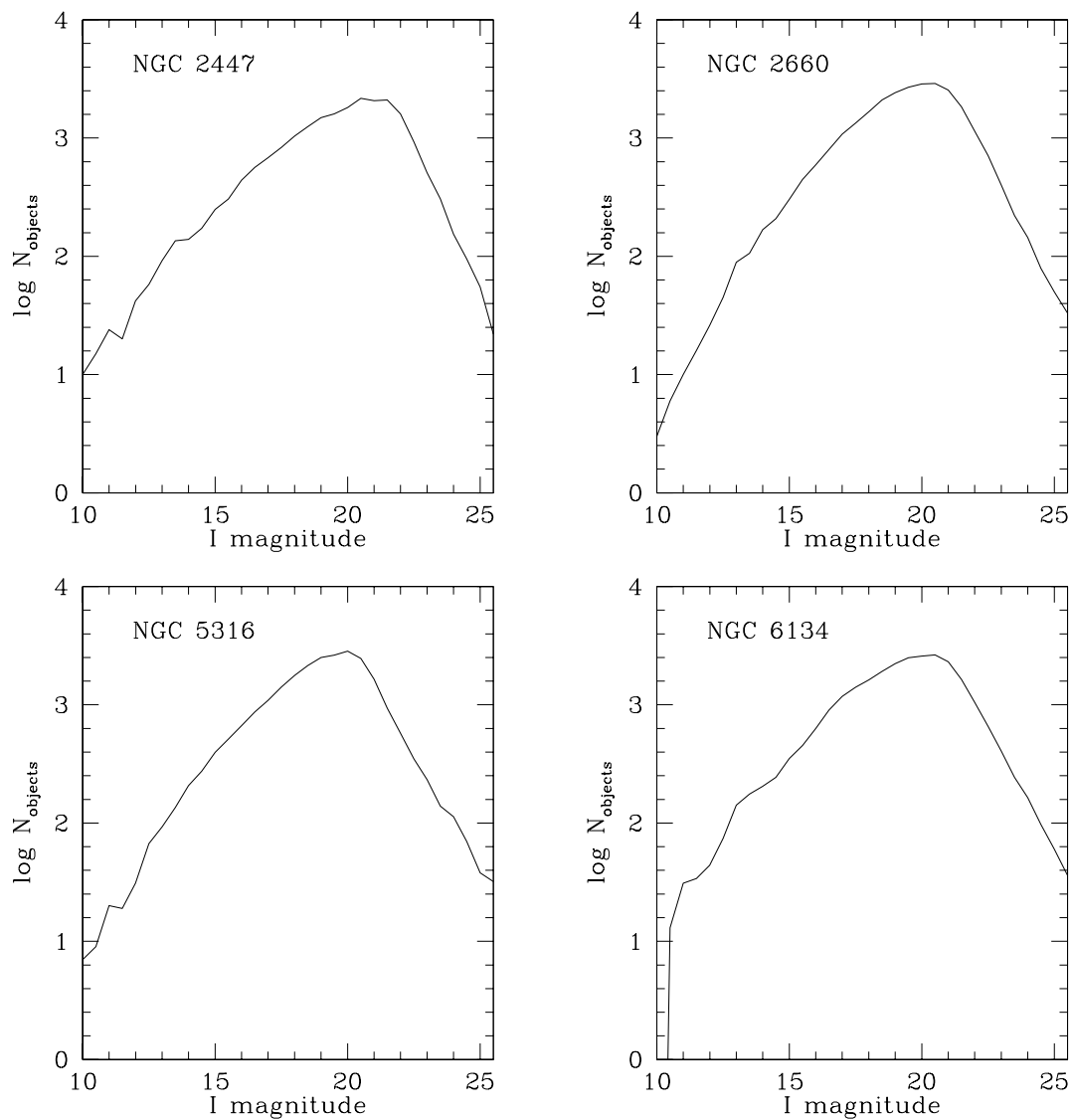


Figure 2.15: Histograms of object counts as a function of  $I$  magnitude for NGC 2447, NGC 2660, NGC 5316, and NGC 6134.

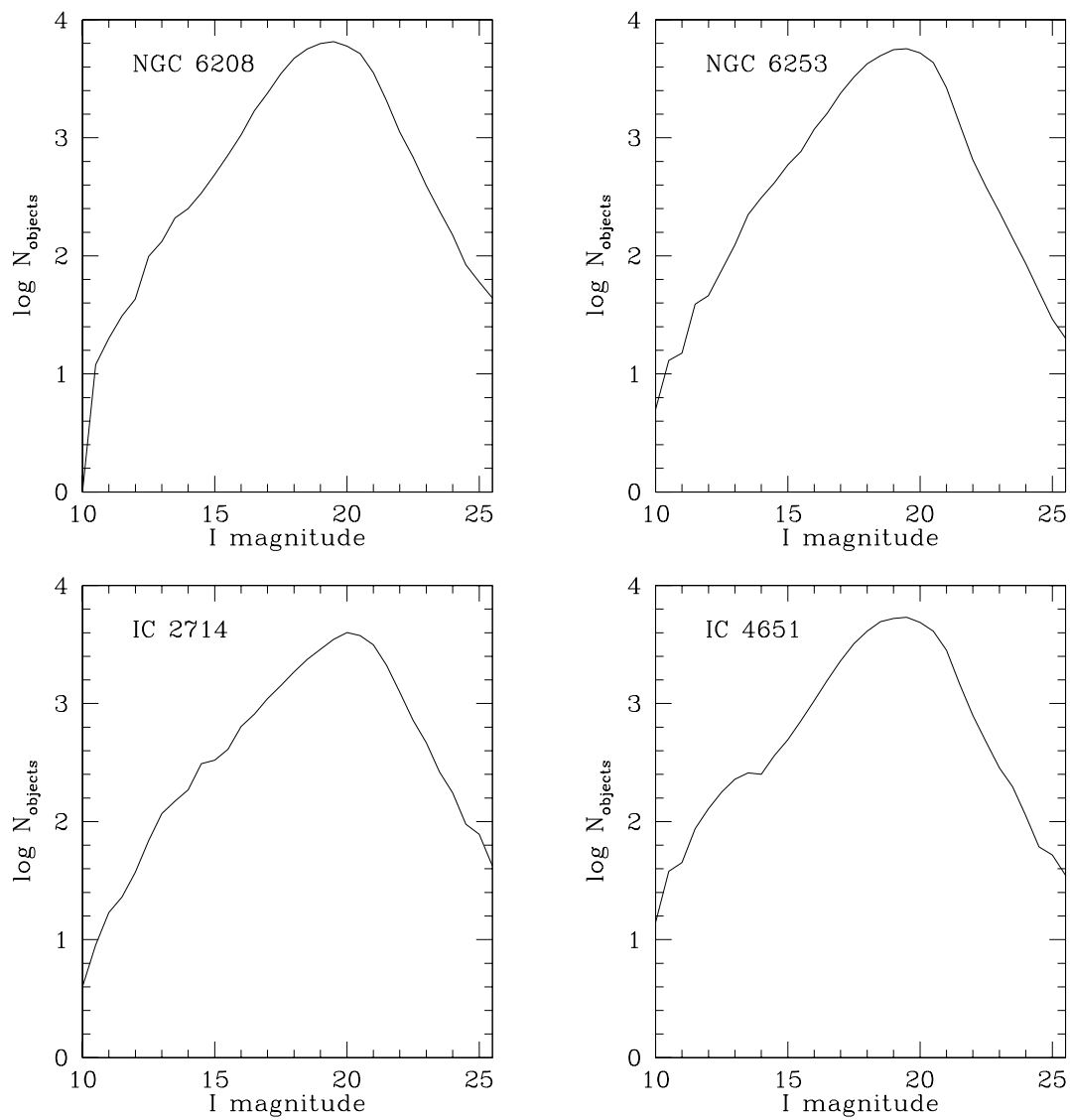


Figure 2.16: Histograms of object counts as a function of  $I$  magnitude for NGC 6208, NGC 6253, IC 2714, and IC 4651.

# Chapter 3

## Time Series Photometry

### 3.1 Introduction

Good relative photometry is essential for pushing the detection sensitivity of a transit search to as small a companion radius as possible. Having observed a statistically significant number of stars with sufficiently broad and dense time coverage, we must detect the smallest possible drops in the light curve (stellar flux as a function of time). We cannot rely on an absolute flux calibration to standard flux references in other fields on any partly cloudy nights. Therefore, we must perform a relative flux calibration using flux references in the same image.

#### 3.1.1 Two Common Approaches to Relative Photometry

Relative photometry attempts to quantify and remove non-astrophysical decrements in flux, caused by atmospheric or instrumental effects. These drops are computed by referencing the flux of the target to the flux of an ensemble of stars. The accuracy of the computation is limited by the quality of the choice of stars that go into the ensemble. This choice determines the constancy and signal-to-noise ratio of the ensemble. Poor choices of flux references include stars that are variable, blended into nearby stars, hit by cosmic rays, affected by hot pixels or bad columns, or saturated.

One common strategy to form the astrophysically constant ensemble is to iteratively pick a set of bright stars, each with low root mean square scatter about the mean of the light curve. The flux of the ensemble is divided out of all the light curves. The makeup of the ensemble is adjusted by sigma-clipping out poor stars revealed after the correction, and the process is repeated until the corrected light curves have converged.



This bare-bones strategy is computationally inexpensive, since it starts with integrated fluxes (instrumental magnitudes), and does not need to address the original image pixels.

Another relative photometry strategy, especially common in microlensing and planet transit searching, is difference image analysis (DIA, also called image subtraction; see Alard and Lupton 1998, Alard 2000, Wozniak 2000). In DIA, the entire field is used to compute a least squares solution for transforming a reference image to the seeing and flux scale of a program image. Pixels from poor quality stars are removed by sigma-clipping. The difference between the program image and the transformed image contains only the variable portion of the flux. The variables are relatively easy to detect and measure off of the difference frame, because crowding due to constant sources is eliminated. The variable part of the flux is then calibrated to a relative scale after matching variable sources with their underlying counterparts on the reference image.

### 3.1.2 EXPLORE Project Time-series Photometry: Preliminary Pipeline

The EXPLORE/OC Project was initially jump-started using an existing data processing pipeline inherited from the EXPLORE Galactic field transit search on 4-metre telescopes, and is described in (Mallén-Ornelas et al. 2003). This preliminary photometry pipeline was designed with the aim of minimizing the sky noise for faint stars not significantly brighter than the sky. Therefore, the initial photometry pipeline employed small apertures (typically 2-3 times larger than the seeing disk) for determination of instrumental magnitudes. The EXPLORE small aperture photometry is combined with a high-precision iterative sinc-shift centroiding algorithm in the PPP software package (Yee et al. 1988; Yee 1991; Yee et al., in prep.; Mallén-Ornelas et al. 2003). While EXPLORE/OC's target magnitude window is not as faint, it is still useful to minimize sky noise, especially during bright time.

The instrumental magnitudes were put on a relative system using the fast algorithm of iteratively choosing a reference ensemble. The algorithm was sufficiently fast that we could perform quick-look next-night reduction of our data at the telescope. However, this simple approach was quite prone to two systematic errors.

1. In the course of the 4-metre searches, it was discovered that in crowded Galactic plane fields, it is not uncommon for a target star's small aperture to be contaminated with light from a nearby star. This introduces systematic error that varies

with seeing. Even worse, for poor observing conditions and high crowding, the centroid may be miscalculated by so much that a nearby bright star may be measured instead of the target star. Real examples from our data for both of these effects are shown in Figure 3.1.

2. Light saturation of stars was the most insidious systematic when we searched for planet transits in this preliminary photometry. Temporary saturation is caused by periods of good seeing. A star which might not normally saturate will begin to lose flux in the central pixel when the PSF narrows and sharpens. Since periods of good seeing often occur during the middle of a night when the target is being tracked through low airmass, the timescale of the flux loss is typically hours. This small loss of flux for two to three hours is the systematic effect which most closely mimics a planet transit signal. A real example from our data is shown in Figure 3.2.

Neither this preliminary method nor the difference image analysis method will mitigate the effects of slight saturation on the light curve, since both methods create the light curve based on the stellar flux integrated over the whole stellar image. Therefore, to improve on our first generation pipeline, we introduce two improvements that specifically address the problems we discovered. To resist saturation systematics and other effects which contaminate only a segment of the PSF, we use a generalized aperture photometry technique, described in §3.2. We outline our use of DAOPhot for reducing photometric errors due to crowded fields in §3.3. We evaluate how much better the new photometry performs over the old photometry in §3.4.

## 3.2 Generalized aperture photometry

Generalized aperture photometry works to excise bad pixels from measurements while retaining the good pixels, thus extending the regime of good photometric precision to lightly saturated stars. Instead of using a round aperture, we allow the aperture to take on the best shape for each individual star, for each measurement epoch. The pixels to be rejected from the aperture are selected by a sigma-clipping algorithm. The information from the pixels selected for a target star and multiple reference stars is combined to derive the value of the light curve.

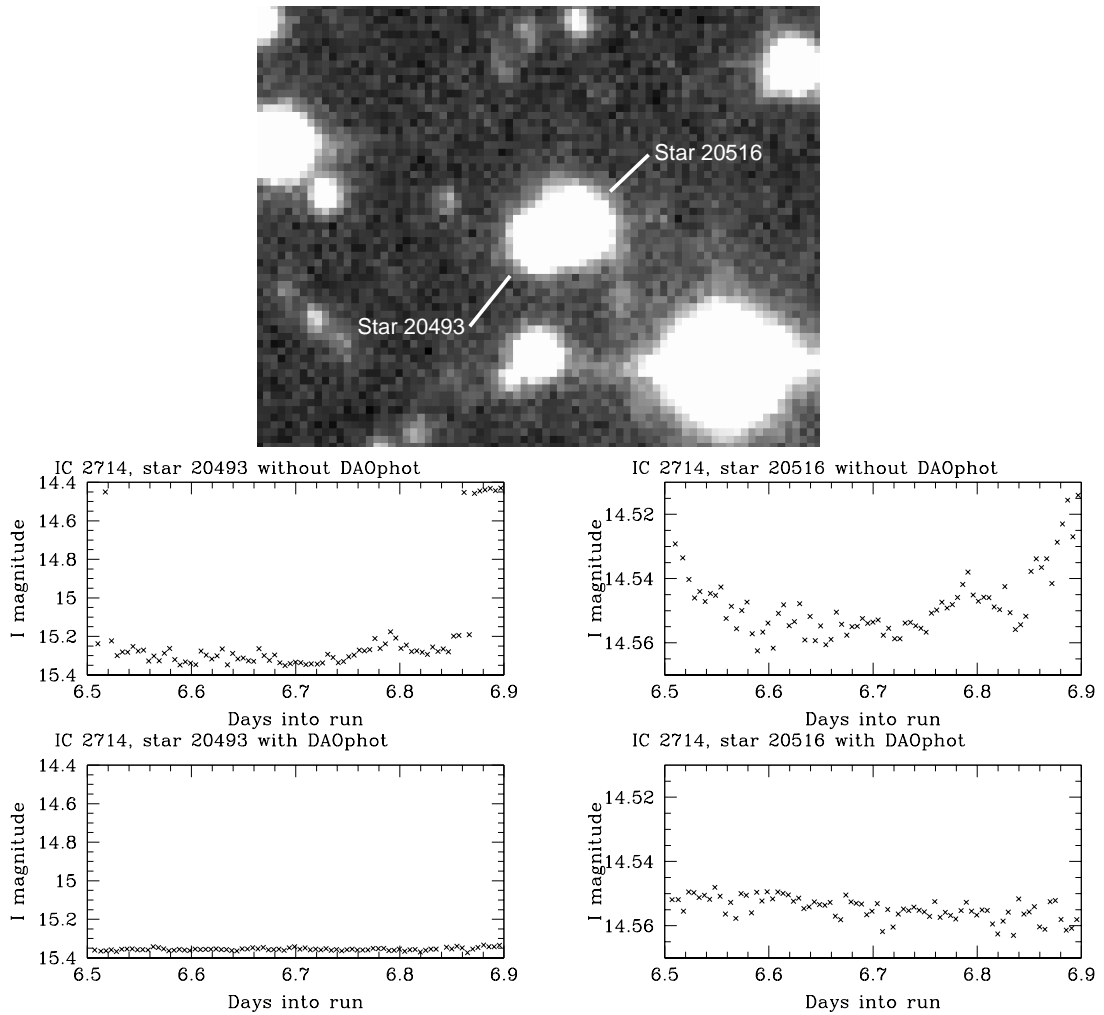


Figure 3.1: **Top:** 300 sec.  $I$  image of a  $35'' \times 25''$  portion of the field of IC 2714, showing a close pair of stars, star 20516 and star 20493, which severely contaminate each other's photometry apertures. **Bottom left:** Light curve of the fainter star 20493, before and after turning on the DAOPhot neighbour subtraction feature in the data reduction. Before correction for the contamination from the PSF of the bright star 20516, the light curve shows beginning and end of night jumps to the brightness of star 20516. After correction, the light curve becomes quite stable, with an improvement of almost ten times in rms scatter between 6.6 and 6.8 days. **Bottom right:** Light curve of the brighter star 20516 before and after neighbour subtraction. Before correction, the light curve gradually moves from a minimum in the middle of the night (when the seeing is best and the leakage of light from the neighbour is minimized) to maxima 4% brighter at the ends of the night. After correction, the subtraction of the light leakage shaves the overall trend in the light curve over the course of the night to less than 1%, and the rms scatter over the whole night is improved by a factor of three.

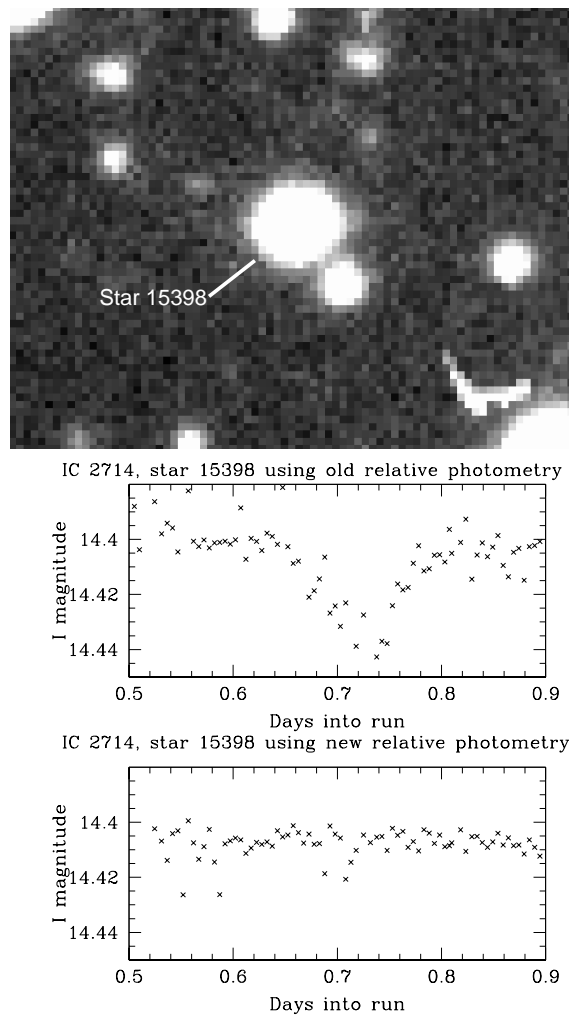


Figure 3.2: **Top:** 300 sec.  $I$  image of a  $35'' \times 25''$  portion of the field of IC 2714, showing the very bright, relatively isolated star 15398. (The sickle-shaped feature in the lower right is a cosmic ray hit.) **Bottom:** Light curve of star 15398 on night 1, before and after turning on the new, generalized aperture photometry (but in both cases using DAOPhot neighbour subtraction). This star is so bright that the core becomes saturated during periods of good seeing. The saturation shows up as a flux loss in the light curve using the old photometry, mimicking here a 3% deep eclipse event. Observe how the bad pixel clipping algorithms in the new relative photometry significantly clean up the flux loss due to saturation, so that it is no longer similar to an eclipse signal. Overall, the light curve rms scatter improves from 1.5% to 0.5%.

### 3.2.1 Normalization by empirical PSF division

Arbitrary apertures are not supported in typical relative photometry algorithms because of changes in the PSF from frame to frame (for example, due to seeing changes). Under a change of PSF, the percentage-wise frame-to-frame variation in integrated stellar flux will be different for different apertures. As a result, any relative photometry algorithm that operates on integrated fluxes must maintain a constant aperture for the entire length of the run, in order for the seeing-induced flux changes to divide out.

Variable apertures are only allowed if the pixels are appropriately normalized in a seeing-independent fashion. The seeing can be removed on the pixel scale (instead of the integrated aperture scale) by dividing one stellar image (the target star) by another stellar image (a reference star, appropriately registered).

The registration of one image on top of the other is accomplished using the iterative sinc-shift resampling technique in the PPP software (Yee et al. 1988; Yee 1991; Yee et al., in prep.; Mallén-Ornelas et al. 2003). We use the sinc-shift resampling to generate a 9x9 postage stamp of each star on each frame, with the stamp resampled such that the peak is in the centre pixel, and so that the adjacent pixels in the vertical and horizontal directions are symmetric. In cases where the star is too noisy to centre by this definition, PPP finds the centre by a simple iterated intensity centroid. By resampling our stars onto postage stamp images, we ensure that the PSF is transformed to the same coordinate grid for each star, where the origin of the PSF is taken to lie at its peak pixel. At present, we use a 5x5 pixel subset for all further calculations to preserve CPU resources, since the outermost pixels will contribute less additional signal but increased sky noise.

Dividing a target star's postage stamp by a reference star's postage stamp empirically divides out the PSF, and so the resulting array is populated by estimates of the flux ratio of the two stars. The flux ratio will stay the same from frame to frame if neither star varies. So, one can deduce the actual variation in flux by dividing out the flux ratio between the two stars (as measured off of a reference frame). In this manner, one produces a light curve for a target star-reference star pair. The process may be repeated using multiple reference stars, to yield a very large aggregate of measurements of the target star's light curve: one measurement for each pixel, for each reference star.

### 3.2.2 Selection of reference stars and pixels

Each target star's own set of reference stars is chosen empirically at each epoch. We rank the brightnesses of all unsaturated stars near the target star (within 250 pixels' radius)

to form a list of potential reference stars. Beginning with the brightest ten unsaturated stars, we sum up the stellar fluxes within each postage stamp image, and compute the shot noise. We then proceed down the brightness-ranked list of candidate reference stars, adding each candidate’s flux and noise into the ensemble. As fainter candidates contribute more and more sky noise, the SNR of the ensemble eventually reaches a maximum, indicating that the membership of the reference ensemble is optimal.

For each target star pixel, outlier reference star measurements are discarded by five iterations of  $3\sigma$  clipping. This automatically discards pixels noticeably affected by spatial or temporal anomalies such as cosmic ray hits, bad pixels, crowding, variability, or saturation. The rms scatter on the light curve measurement, per target star pixel, can be estimated since the light curve value for that pixel has been measured relative to hundreds of reference stars. This scatter represents the statistical and systematic uncertainty on the measurement. Armed with these measurements of the uncertainty, we can calculate a weighted average of the pixelwise light curve values, which is our best estimate for the value of the light curve.

Note that generalized aperture photometry does not rely on selection of reference stars by analyzing the entire time series. The rejection process is based only upon the current frame and the reference frame. Thus, it is a nearly time-independent method of picking the ensemble flux necessary for relative photometry. An iterated time-dependent implementation might improve the makeup of the reference ensemble, but at a currently prohibitive CPU cost. Generalized aperture photometry is also unique in permitting a per-frame estimate of statistical plus systematic error on the light curve.

### 3.3 DAOPhot neighbour subtraction

Aperture photometry, no matter how sophisticated, cannot tease apart crowded stars. A secondary technique must be applied to alleviate photometry errors introduced by flux leakage from nearby objects into the target aperture. We use the neighbour subtraction algorithm from the DAOPhot package (Stetson 1992) to preclean each target star just before we apply generalized aperture photometry to it.

The DAOPhot package is a PSF-fitting photometry program. Given an ensemble of high signal-to-noise ratio stars in an image, it computes the PSF as a function of pixel position. It then performs a chi-squared fit of the PSF to each source of interest, such that the total counts for that source are the integral under the fit. One of the data products is a “residual image” where DAOPhot returns the image with all fitted sources

subtracted out. A sample residual image is shown beside the original image in Figure 3.3.

Because the bulk of DAOPhot CPU time is expended in fitting the sources and subtracting them from the image, we opt not to run an instance of DAOPhot for each target star. Rather, we run DAOPhot once per frame and save two data products in memory: the residual image, and the catalogue of fit parameters. When we seek to measure, or retrieve a postage stamp for, a given target star, we retrieve its fit parameters and the residual image, and add that single star back into the residual frame. Given  $N$  stars per frame, this algorithm reduces the number of star subtractions and additions required from  $N^2$  to  $2N$ - an essential CPU savings since our frames contain tens of thousands of stars.

We initialize our DAOPhot subtractions using automated scripts inside PPP. This includes automatic selection of DAOPhot PSF reference stars (a few dozen are desired for good DAOPhot PSF construction). Reference stars that do not have point-like PSFs are rejected by requiring that at every pixel on the candidate reference star, the reference star PSF profile (normalized to a peak value of 1) be no more than 25% deviant from the the average PSF profile. We perform a preliminary photometry run of fast PPP iterative intensity centroiding on all sources to create the input catalogue for DAOPhot, which DAOPhot employs as first guesses when performing PSF fits.

While we use a variable PSF in DAOPhot to express the variation of PSF as a function of pixel position, we find that the PSF of the Swope telescope varies too much over the field of view to be accommodated by the highest (second) order variable PSF in DAOPhot. Hence, we divide the frame into nine subframes for the purpose of computing the PSF. We provide an overlap region of 100 pixels around each subframe so that the PSF can be interpolated from both sides along the edge of each subframe.

### 3.4 Performance tests

We have checked the performance of our photometry algorithms by running different algorithmic setups on common sets of actual observations. Some metrics for improvements in the photometry of a target field are as enumerated below.

1. Does the rms scatter about the mean improve for most stars?
2. Does the number of stars with rms less than a certain level (0.5%, 1%, 1.5%, 2%) increase?

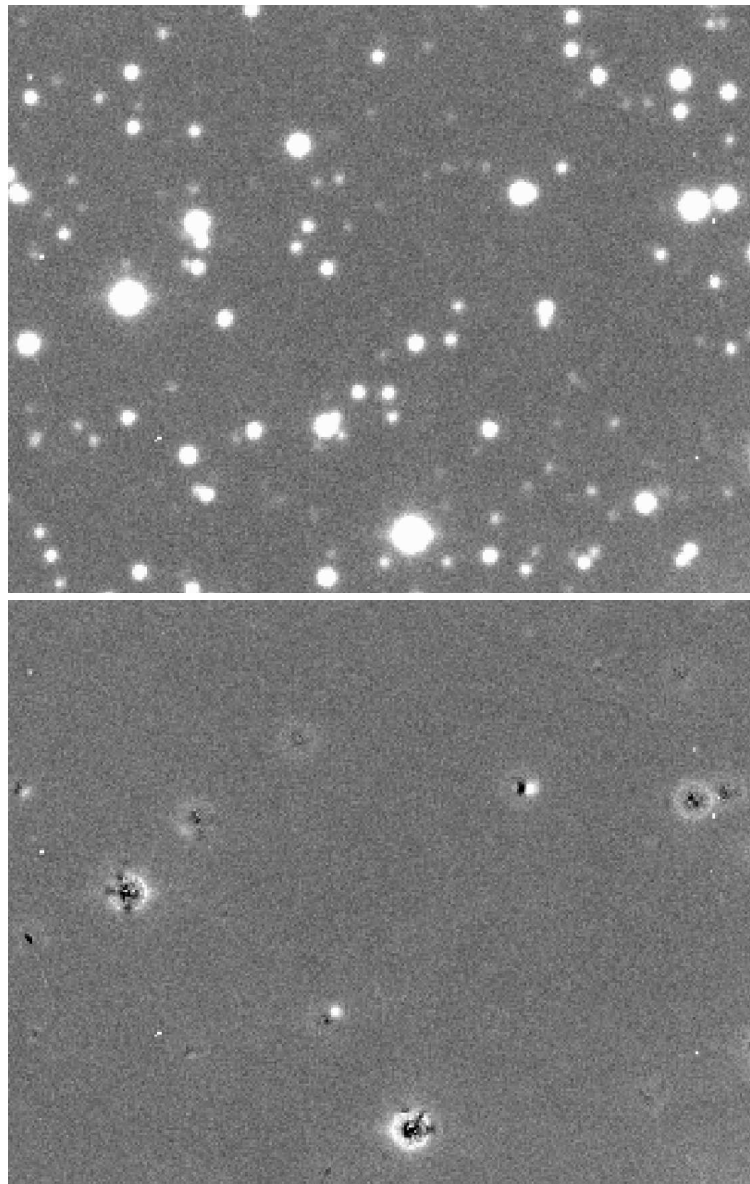


Figure 3.3: **Top:**  $2.2' \times 1.75'$  sample region from an NGC 2447 monitoring frame. **Bottom:** The sample region after DAOPhot source subtraction. Fainter stars are well-fit, and their profiles subtract cleanly. Saturated stars do not subtract well because their PSFs do not conform to the computed profile.



### 3. Do the improvements reduce systematic errors in the light curves?

In Figure 3.4, we show how the distribution of the rms scatter of the light curves is improved by the use of DAOphot neighbour subtraction. We show the light curve quality- rms as a function of  $I$ - for a single night, before and after neighbour subtraction (but in both cases using the old relative photometry algorithm). Percentagewise, one expects neighbour subtraction will yield the greatest improvement for the photometry of faint stars in the haloes of much brighter stars. We expect so for two reasons. Firstly, seeing variations cause haloes of close neighbours to variably contaminate the relative photometry. Secondly, the photocentre of the target can sometimes be shifted enough by a nearby bright star that the photometry program mistakenly measures the bright contaminating star instead of the faint target.

Both of these effects are visible in the bottom panel of Figure 3.4. We see how DAOphot subtraction addresses the first effect by tracking the main population of measured stars across the plot. Calculating and plotting up the median improvement in 0.5 magnitude bins, we see the percentage improvement in rms rises for fainter stars, up to a 10% improvement by  $I = 21$ . The presence of points in the bottom right of the plot, at faint magnitudes and high improvement factors, is evidence that we mitigate the second, catastrophic effect in a large number of cases. By using neighbour subtraction, we bring light curves that were hopelessly contaminated down close to the photon noise envelope. The number of light curves with improvement of more than 50% on this sample night was 5205- one-seventh of the total of 35563 measured stars in the field of IC 2714. This population is marked in black in Figure 3.4, showing that most of these light curves were formerly too noisy for detection of variability, as they were at least four times noisier than the theoretical limit (an interval of 0.6 in log space). Out of a total of 6039 stars at magnitudes of  $15 < I < 21$  with light curve rms more than four times as poor as the photon noise limit, 2597 stars (or 43%) improved to under four times the photon noise limit. The median improvement in rms for these light curves was 4.52, and so they are now far more useful for variability detection.

Let us take a detailed look at a specific pair of stars. Figure 3.1 demonstrates the dramatic improvement to a real-time light curve from using neighbour subtraction on a close pair of stars. Star 20516 is an  $I = 14.6$  star in IC 2714. Less than  $2''$  (about five pixels) away lies Star 20493, with  $I = 15.3$ . These stars heavily contaminate each other's photometry apertures, even with apertures only five pixels in diameter. The light curves are shown for night 7 of the run, and they are textbook cases of the effect of neighbour

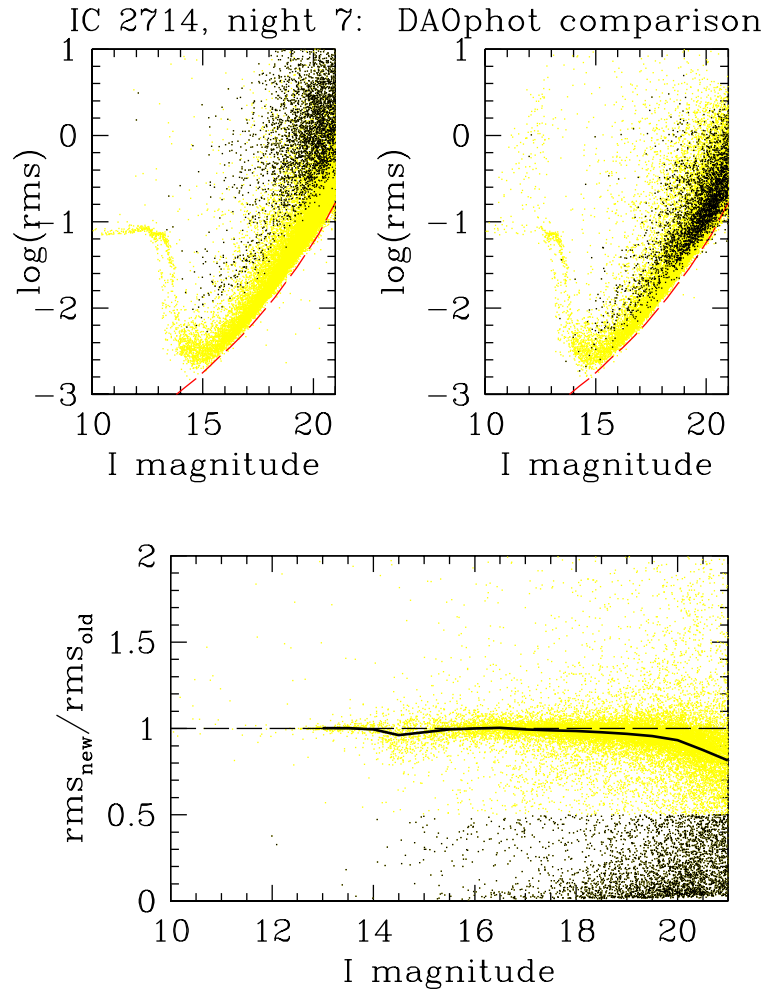


Figure 3.4: **Top left:** Light curve rms scatter about the mean as a function of  $I$ , for one sample night of IC 2714 observations, using the old relative photometry and no DA0phot subtraction. Photometry becomes poor at faint magnitudes due to photon noise, and at bright magnitudes due to saturation near  $I = 14.5$ . In all panels, yellow points represent stars with less than 50% improvement in rms scatter after DA0phot subtraction; black points represent stars with more than 50% improvement. The red dashed line is the theoretical photon noise limit. **Top right:** Quality of same sample night of IC 2714 light curves after turning on DA0phot subtraction. **Bottom:** Factor of improvement in rms; values less than one (i.e., below the dashed line) represent improvement. The median improvement is overplotted as a solid line.

contamination on photometry.

The uncorrected light curve for the fainter star 20493 shows a brief jump at the beginning of the night, and another jump at the end of the night, both up to approximately the magnitude of star 20516. These jumps occur when the telescope is pointed into high airmasses and the resultant seeing is poor. This demonstrates how the photometry program has difficulty targeting a faint star once it becomes buried inside a bright star's halo. With DAOphot correction, not only do the jumps vanish, but the seeing-dependent leakage of light into the photometry aperture is removed. As a result, the rms scatter of the light curve (even excluding the jump regions) improves by a factor of almost ten, from 0.04 to 0.005 (taken over the time range 6.6 days to 6.8 days).

The brighter star 20516 does not suffer catastrophic errors of tenths of a magnitude, but is still affected by the leakage of extra light into its aperture when the seeing worsens. At the beginning and end of the night, star 20516 appears up to 0.04 mag brighter before DAOphot correction. With DAOphot correction, the light curve appears much flatter over the night, improving by a factor of three from an rms scatter of 0.01 down to 0.0035.

Not many stars are as severely contaminated as in this case. However, it is clear that neighbour subtraction can significantly improve light curve quality for neighbouring non-saturated stars. Unfortunately, DAOphot cannot properly fit the profiles of saturated stars, and decontamination in the haloes of saturated stars is not possible at present.

DAOphot subtraction does not provide much improvement for bright, relatively isolated stars. So now, on top of the DAOphot upgrade, we implement our generalized aperture photometry. Since this pixelwise algorithm was developed specifically to address lightly saturated stars, we now expect to see improvement at the bright end of the rms-magnitude plots, around saturation,  $I \sim 14$ .

Figures 3.5 to 3.12 show how the rms scatter in the light curves computed over a single night is improved by our pixelwise relative photometry. Results from a typical full night of observations are shown for each cluster field. We quantify the quality of each light curve by the rms scatter about the mean, and plot the rmses as a function of  $I$ . Using the raw counts and sky level in ADU 5-pixel diameter aperture photometry (used as input to the old relative photometry program), we compute the theoretical photon noise for each star for one good frame from the night (the choice is somewhat arbitrary from among good seeing frames; we pick the thirtieth exposure). Since the theoretical noise varies depending on the sky background, we estimate the theoretical noise in 0.5 magnitude wide bins; in each bin, the estimated noise is the median of all computed theoretical noise values in the bin. Comparing the lower envelope of the rms scatter with

the theoretical limit, we see that our photometry performs very close to optimum. Over  $15 < I < 20$ , we generally come within 15% ( $\sim 0.05$  in log intervals) of the theoretical limit. Note the rms can sometimes be better than the representative theoretical limit, since the limit is just the median limit at a particular epoch.

In a typical individual night, we notice that the v-shaped turnover in the rms scatter at bright magnitudes (where photometry begins to go bad due to saturation) is shifted by about half a magnitude to brighter magnitudes by the implementation of pixelwise relative photometry. This corresponds to many tens of percent improvement in rms on our brightest stars (largely due to lessening of saturation systematics in the light curves)-of crucial significance because our brightest stars offer the lowest statistical noise levels and hence an increased opportunity to detect small amplitude transits. We also notice improvements in rms at the faint end, due to the SNR maximization and bad pixel clipping features in our pixelwise code.

In the bottom panels of Figures 3.5 to 3.12, we plot the factor of improvement, the ratio of the rms scatter using the new relative photometry to the rms scatter using the old relative photometry, for each light curve. We overplot the median of the distribution, calculated in 0.5 magnitude wide bins. At saturation, the median improvement in rms scatter usually reaches a factor of about two, and optimization of SNR and contaminated pixel clipping improves the light curves of the faintest objects by a similar factor. At moderately bright magnitudes where saturation is not an effect,  $16 < I < 18$ , the improvement is usually only small. Near  $I \sim 15$ , stars never saturate by very much, and the systematic bias is small. For these stars, clipping the saturated pixel reduces the SNR of the measurement by more than the small systematic bias, and the new rms scatter can appear slightly worse. However, this is a necessary trade in order to remove the bias. Remember that although we most easily quantify the removal of the bias by the improvement in rms scatter, that is not the true goal- we are removing the bias because it can be confused with a planet transit signal.

In Table 3.1, we quantify the improvements in rms scatter by the numbers of stars useful for detecting very small amplitude variations. For each of the observing nights considered in Figures 3.5 to 3.12, the table lists the number of light curves with rms scatter better than 0.5%, 1%, 1.5%, and 2%, and the fractional improvement in numbers of light curves with rms scatter better than 1% and 2%. On average, the number of 1% stars improved by 23%, and the number of 2% stars improved by 14%. While the fraction of new light curves to old light curves with rms scatter better than a given threshold can occasionally drop just below one, again we stress that rms scatter does

not always correlate perfectly with removal of systematic biases. The removal of biases is difficult to view for all stars at once, and is best viewed on an individual light curve basis.

Table 3.1: Quantities of well-measured stars yielded by relative photometry: single nights

Cluster / photometry method	Number of stars				$\frac{\text{new 1\% stars}}{\text{old 1\% stars}}$	$\frac{\text{new 2\% stars}}{\text{old 2\% stars}}$
	0.5% rms	1% rms	1.5% rms	2% rms		
IC 2714, old phot., single night	1353	3136	4463	5605		
IC 2714, new phot., single night	1569	3477	4871	6069	1.109	1.083
IC 4651, old phot., single night	1345	3558	5466	7180		
IC 4651, new phot., single night	1245	3453	5285	6945	0.9705	0.9673
NGC 2447, old phot., single night	821	1936	2689	3293		
NGC 2447, new phot., single night	2167	3551	4407	5028	1.834	1.527
NGC 2660, old phot., single night	393	2480	3964	5259		
NGC 2660, new phot., single night	1150	3354	4810	6037	1.352	1.148
NGC 5316, old phot., single night	1341	3094	4471	5582		
NGC 5316, new phot., single night	1632	3895	5397	6585	1.259	1.180
NGC 6134, old phot., single night	1025	2828	4096	5087		
NGC 6134, new phot., single night	1124	3203	4541	5649	1.133	1.110
NGC 6208, old phot., single night	1220	5286	8609	11400		
NGC 6208, new phot., single night	2463	6293	9588	12610	1.191	1.106
NGC 6253, old phot., single night	2155	5289	8034	10450		
NGC 6253, new phot., single night	1882	5262	8143	10710	0.9949	1.025

In Figure 3.2, we present a specific case of a star which becomes saturated during periods of good seeing, and demonstrate our relative photometry improvements on a real-time light curve. Light curves using the old and new relative photometry algorithms are shown for star 15398 in the field of IC 2714, for night 1 of the observing run. Both light curves include DAOphot neighbour subtraction.

Star 15398 becomes saturated midway through the night, from time  $\sim 0.64$  days to  $\sim 0.78$  days, appearing similar to a 3% deep eclipse. The light curve using the new relative photometry shows that the bad pixel clipping algorithms are able to detect and ignore the saturated pixels, and the result is a much flatter light curve. The new rms

scatter of the light curve over the night is 0.005, compared to 0.015 rms scatter using the old relative photometry. For saturated stars similar to this one, the new relative photometry commonly improves the rms scatter by a factor of about two (see Figure 3.5, bottom panel). Remember, though, that the improvement in rms scatter is only a byproduct- the main goal is elimination of eclipse-like systematic effects.

Over an entire run, a different improvement becomes clear. Figures 3.13 to 3.20 show the improvements over the entire observing run rather than a single night, for each cluster field. The old, fixed-aperture photometry code was particularly susceptible to systematics introduced by changes in observing conditions from night-to-night, which caused the baseline of the light curve to wander up and down with amplitudes up to a few percent. This is evidenced by the typically shallow bottom of our whole-run rms-magnitude plots in the top two panels in each of Figures 3.13 to 3.20. These drifts in the baseline of the light curve require any automated transit-finding algorithm to introduce an extra fitting step to remove night-to-night level shifts. Our pixelwise relative photometry is carefully normalized, so is much less sensitive to night-to-night changes. Clearly, it consistently provides better quality light curves when evaluated over the course of an entire observing run. As in previous figures, we show the theoretical photon limit computed based on a typical frame on a good night for reference, but note that we do not expect to achieve anywhere near the theoretical limit over the whole run because all nights have been included in the rms scatter computations, including nights with poor observing conditions.

The ratio of rms scatter in the new photometry to the old photometry is shown in the bottom panels of Figures 3.13 to 3.20. All the way from saturation to faint magnitudes, the new photometry in general offers huge improvements in the night-to-night stability in the light curves, with the best improvement at moderate magnitudes of  $14 < I < 17$ , where the theoretical photon noise is much less than the size of the night-to-night drifts in the old photometry. The median whole-run rms scatter improvement is typically factors of several, even reaching an order of magnitude at  $14 < I < 17$  for IC 2714, NGC 5316, and NGC 6134. The new photometry is also able to extract light curves for some stars which the old photometry could not accurately measure, for which the ratio of new rms scatter to old rms scatter is almost zero.

In Table 3.2, we show the number of stars with rms better than 0.5%, 1%, 1.5%, and 2%. The fractional improvement in numbers of light curves better than given quality thresholds is not computed, since often, the old photometry does not yield any stars at all with whole-run rms scatter better than 0.5%. The numbers of stars counted by each

threshold, as yielded by the new photometry, are generally larger than the counts from the old photometry by several hundred, and even up to 3900 for IC 2714. For the new photometry, these threshold counts are smaller than the single night threshold counts because of the inclusion of every night in the rms scatter computations.

From tens of percent improvement in rms scatter, to removal of eclipse-like systematic biases, to improving the numbers of stars useful for variable finding by thousands, DAOphot neighbour subtraction and generalized aperture photometry have made very visible differences in the performance characteristics of our pipeline. Because of the improvements introduced by neighbour subtraction and pixelwise relative photometry at both bright and faint magnitudes, as well as intranight and internight timescales, we integrate both advances in our final photometric pipeline processing.

Table 3.2: Quantities of well-measured stars yielded by relative photometry: entire runs

Cluster / photometry method	Number of stars			
	0.5% rms	1% rms	1.5% rms	2% rms
IC 2714, old phot., whole run	0	5	8	16
IC 2714, new phot., whole run	529	1989	3046	3939
IC 4651, old phot., whole run	86	1006	1979	2893
IC 4651, new phot., whole run	364	1395	2189	2992
NGC 2447, old phot., whole run	2	28	102	172
NGC 2447, new phot., whole run	1125	2274	3046	3669
NGC 2660, old phot., whole run	0	47	135	235
NGC 2660, new phot., whole run	271	1079	1979	2813
NGC 5316, old phot., whole run	0	0	0	0
NGC 5316, new phot., whole run	534	1841	2723	3480
NGC 6134, old phot., whole run	0	1	1	1
NGC 6134, new phot., whole run	208	1005	1675	2212
NGC 6208, old phot., whole run	0	0	0	0
NGC 6208, new phot., whole run	299	416	524	670
NGC 6253, old phot., whole run	0	6	15	30
NGC 6253, new phot., whole run	3	24	53	85

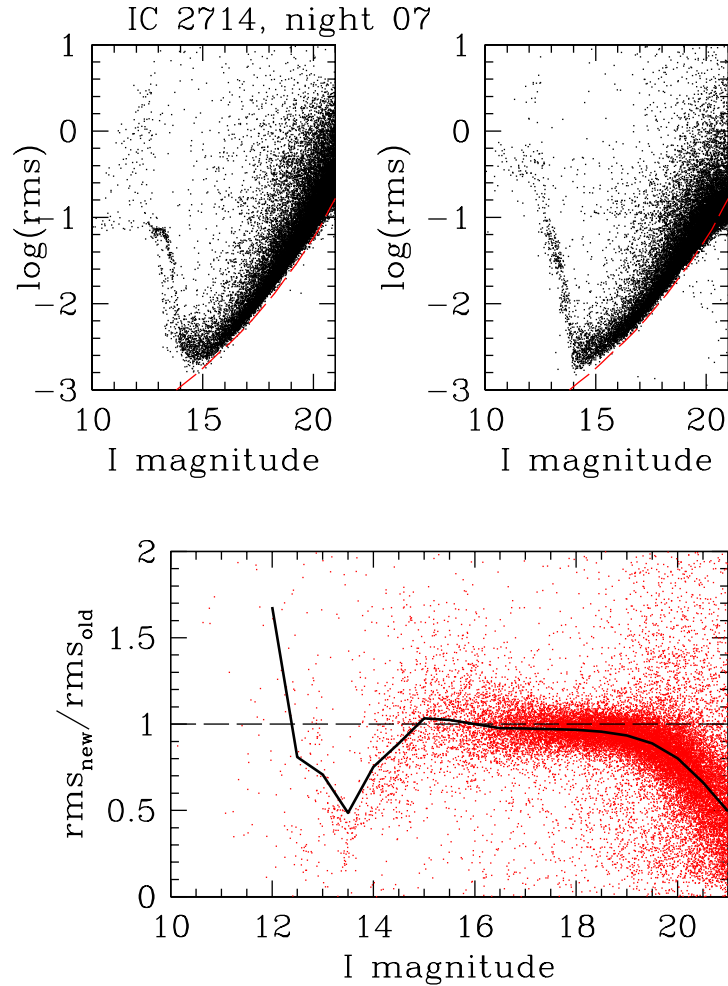


Figure 3.5: **Top left:** Quality of one sample night of IC 2714 light curves, rms as a function of  $I$ , for old relative photometry. In both this figure and the top right-hand figure, the red dashed line is the theoretical photon noise limit for a typical frame from the middle of the night. **Top right:** Quality of same sample night of IC 2714 light curves processed using new pixelwise relative photometry. **Bottom:** Factor of improvement in rms using the pixelwise relative photometry. The median improvement, calculated in 0.5 magnitude bins, is overplotted, showing up to 50% improvements in rms after saturation ( $I \sim 14$ ) and at  $I \sim 21$ , as bad pixels are clipped while the signal-to-noise ratio of the reference ensemble is optimized.



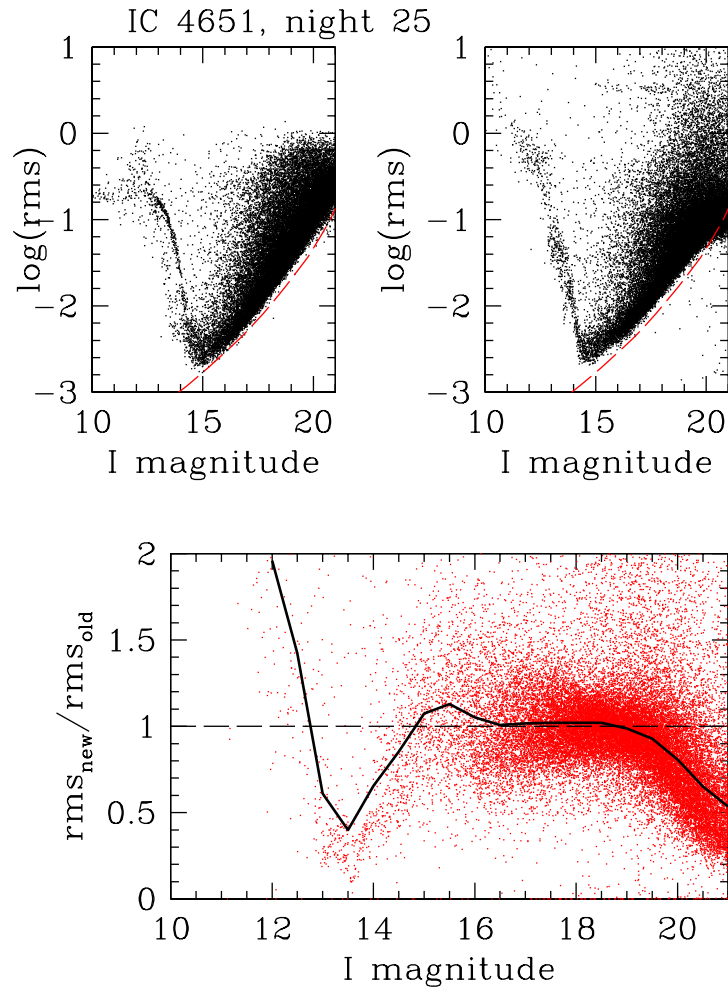


Figure 3.6: **Top left:** Quality of one sample night of IC 4651 light curves, rms as a function of  $I$ , for old relative photometry. The dashed red line in this panel and the top right panel is a single-frame median theoretical photon noise limit. **Top right:** Quality of same sample night of IC 4651 light curves processed using pixelwise relative photometry. **Bottom:** Factor of improvement in rms using the pixelwise relative photometry. The median of the distribution is overplotted in solid black. The new photometry improved the rms scatter for all light curves underneath the black dashed line.

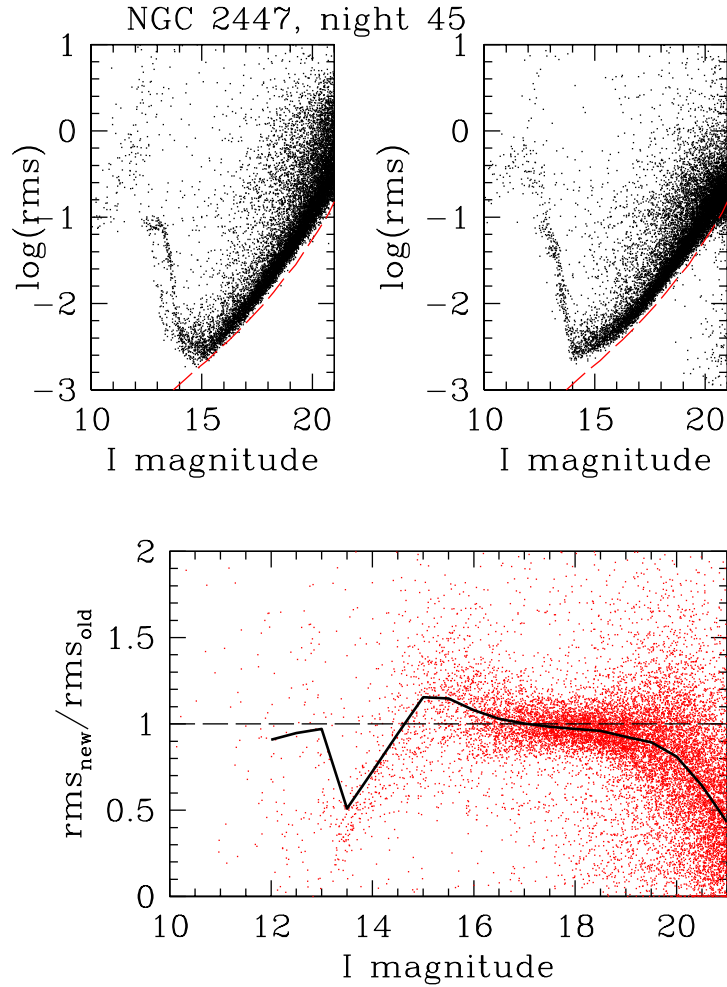


Figure 3.7: **Top left:** Quality of one sample night of NGC 2447 light curves, rms as a function of  $I$ , for old relative photometry. The dashed red line in this panel and the top right panel is a single-frame median theoretical photon noise limit. **Top right:** Quality of same sample night of NGC 2447 light curves processed using pixelwise relative photometry. **Bottom:** Factor of improvement in rms using the pixelwise relative photometry. The median of the distribution is overplotted in solid black. The new photometry improved the rms scatter for all light curves underneath the black dashed line.

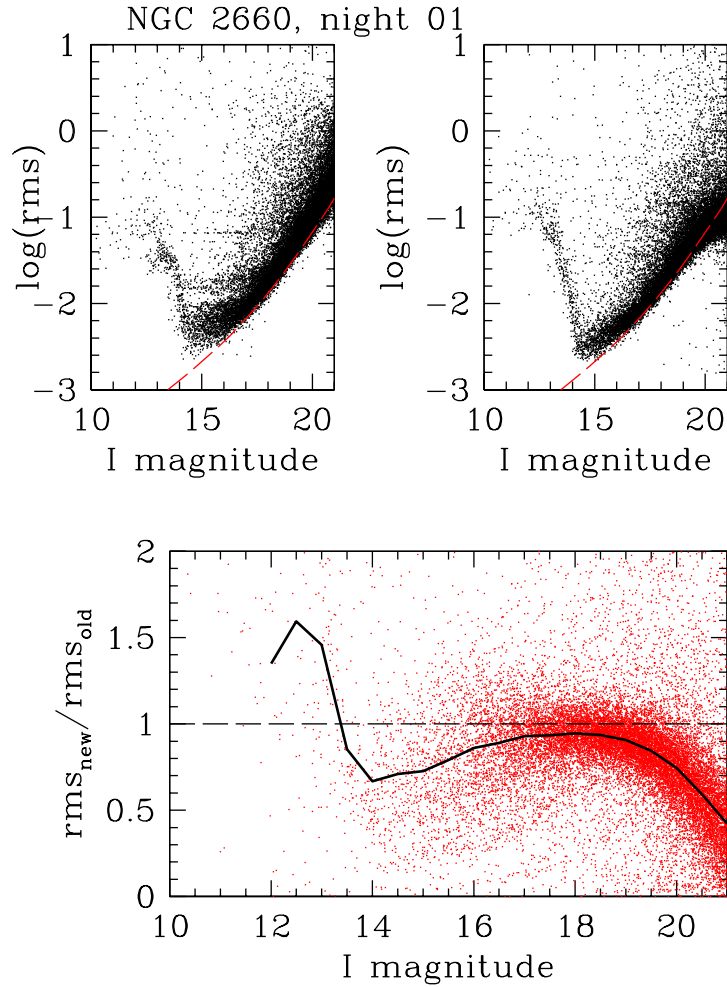


Figure 3.8: **Top left:** Quality of one sample night of NGC 2660 light curves, rms as a function of  $I$ , for old relative photometry. The dashed red line in this panel and the top right panel is a single-frame median theoretical photon noise limit. **Top right:** Quality of same sample night of NGC 2660 light curves processed using pixelwise relative photometry. **Bottom:** Factor of improvement in rms using the pixelwise relative photometry. The median of the distribution is overplotted in solid black. The new photometry improved the rms scatter for all light curves underneath the black dashed line.

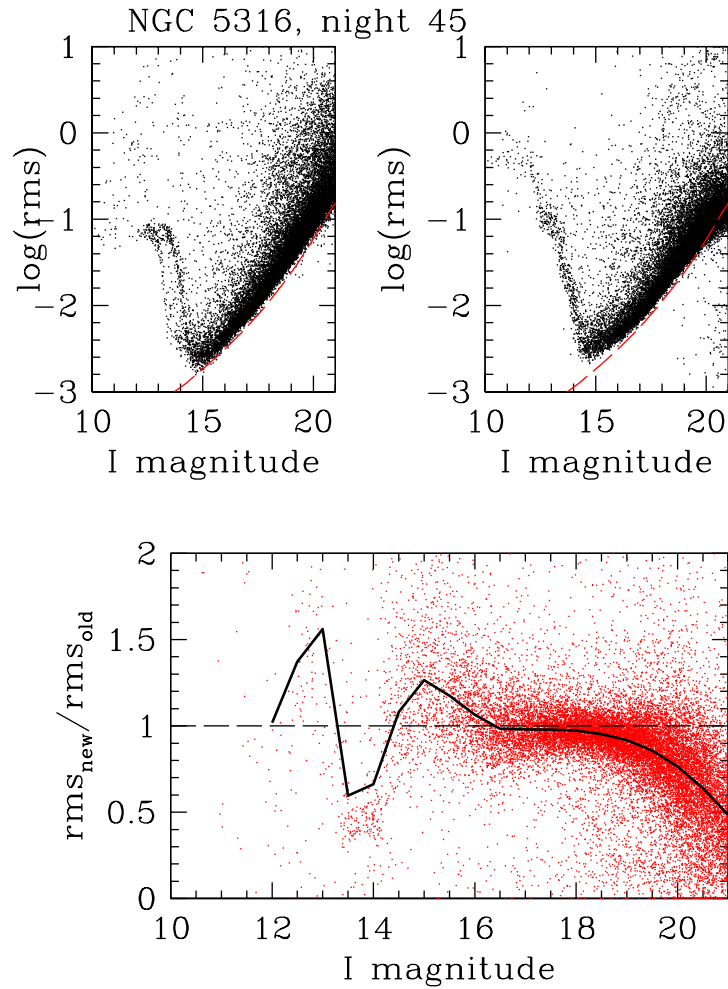


Figure 3.9: **Top left:** Quality of one sample night of NGC 5316 light curves, rms as a function of  $I$ , for old relative photometry. The dashed red line in this panel and the top right panel is a single-frame median theoretical photon noise limit. **Top right:** Quality of same sample night of NGC 5316 light curves processed using pixelwise relative photometry. **Bottom:** Factor of improvement in rms using the pixelwise relative photometry. The median of the distribution is overplotted in solid black. The new photometry improved the rms scatter for all light curves underneath the black dashed line.

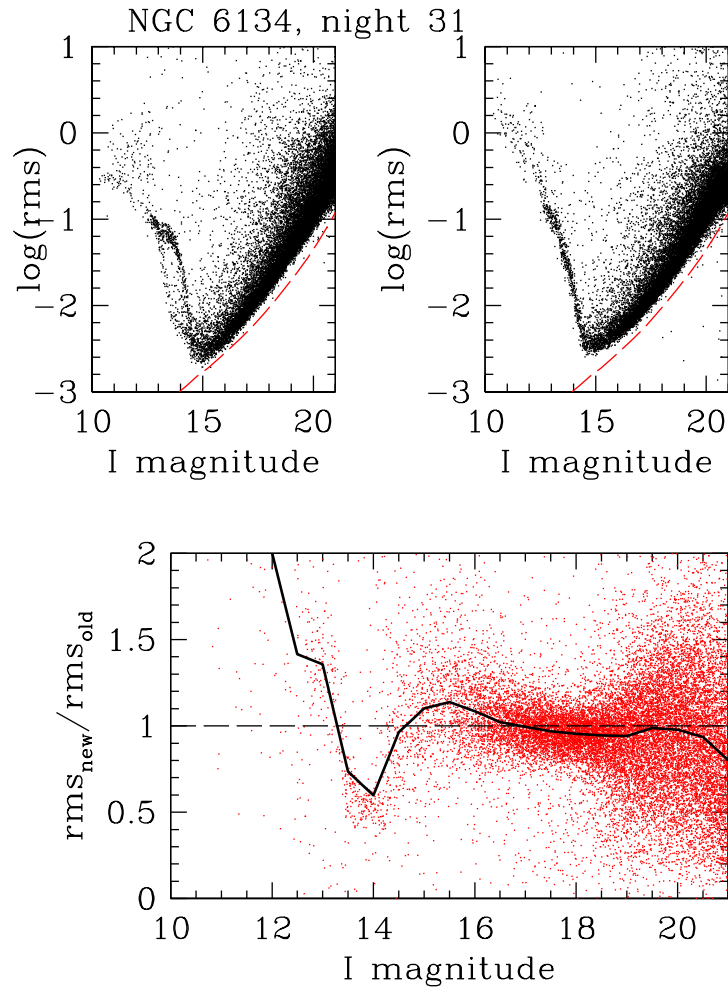


Figure 3.10: **Top left:** Quality of one sample night of NGC 6134 light curves, rms as a function of  $I$ , for old relative photometry. The dashed red line in this panel and the top right panel is a single-frame median theoretical photon noise limit. **Top right:** Quality of same sample night of NGC 6134 light curves processed using pixelwise relative photometry. **Bottom:** Factor of improvement in rms using the pixelwise relative photometry. The median of the distribution is overplotted in solid black. The new photometry improved the rms scatter for all light curves underneath the black dashed line.

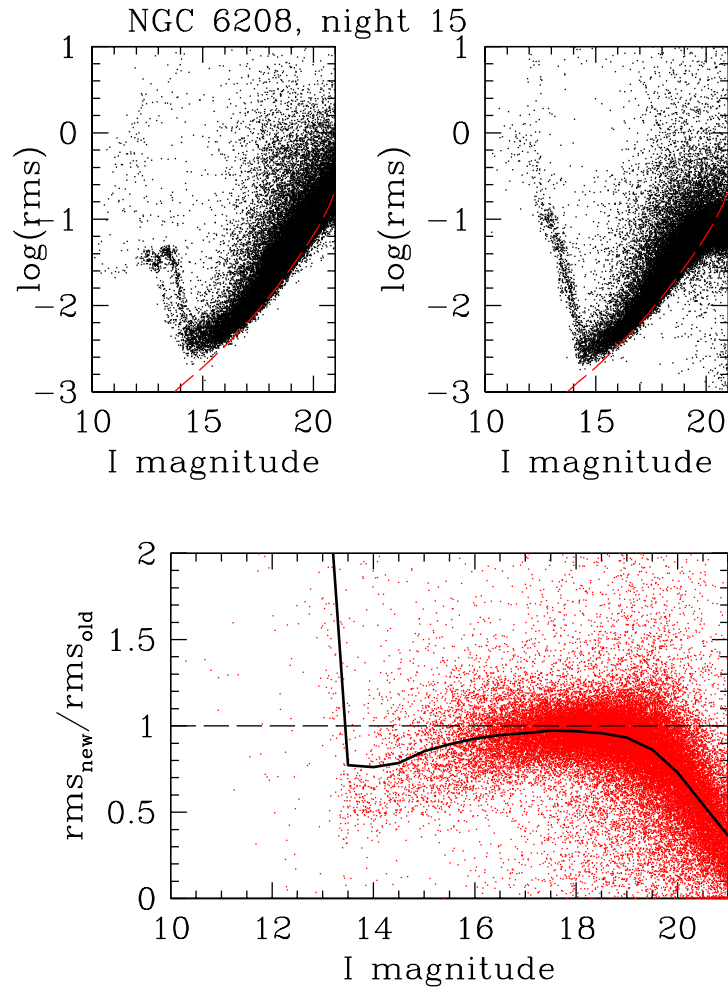


Figure 3.11: **Top left:** Quality of one sample night of NGC 6208 light curves, rms as a function of  $I$ , for old relative photometry. The dashed red line in this panel and the top right panel is a single-frame median theoretical photon noise limit. **Top right:** Quality of same sample night of NGC 6208 light curves processed using pixelwise relative photometry. **Bottom:** Factor of improvement in rms using the pixelwise relative photometry. The median of the distribution is overplotted in solid black. The new photometry improved the rms scatter for all light curves underneath the black dashed line.

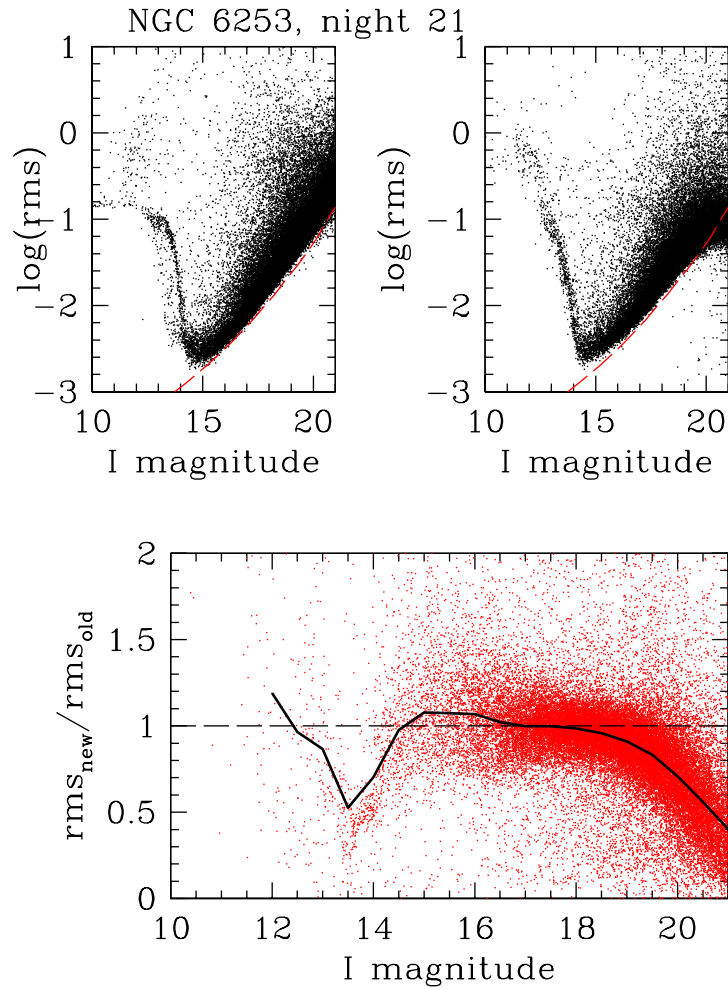


Figure 3.12: **Top left:** Quality of one sample night of NGC 6253 light curves, rms as a function of  $I$ , for old relative photometry. The dashed red line in this panel and the top right panel is a single-frame median theoretical photon noise limit. **Top right:** Quality of same sample night of NGC 6253 light curves processed using pixelwise relative photometry. **Bottom:** Factor of improvement in rms using the pixelwise relative photometry. The median of the distribution is overplotted in solid black. The new photometry improved the rms scatter for all light curves underneath the black dashed line.

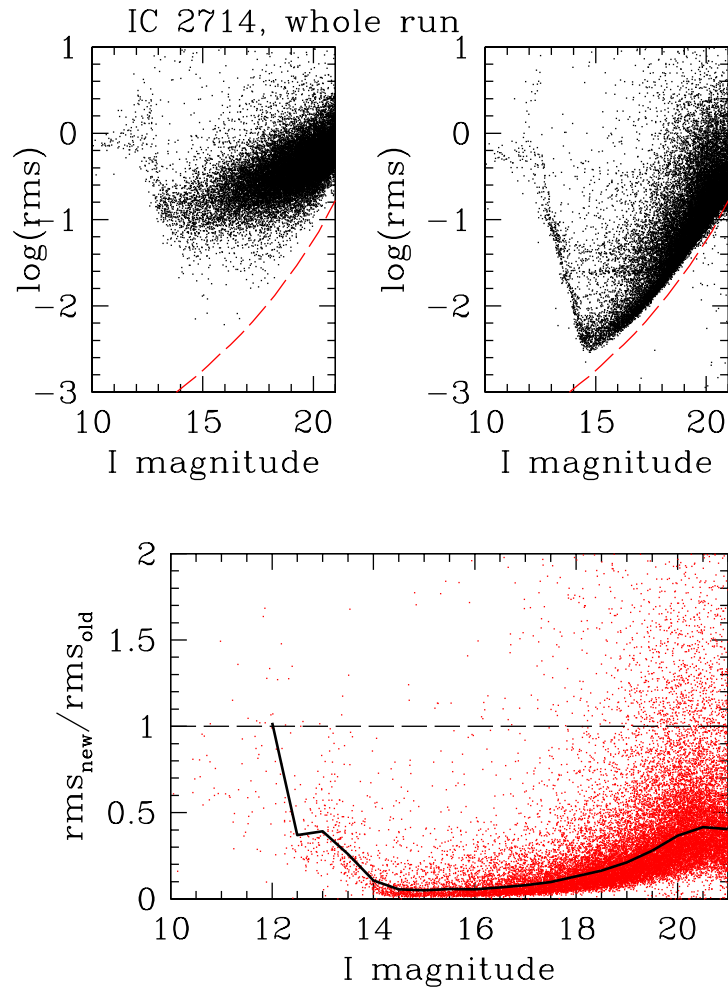


Figure 3.13: **Top left:** Quality of IC 2714 light curves over entire run, rms as a function of  $I$ , for old relative photometry. The dashed red line in this panel and the top right panel is a single-frame median theoretical photon noise limit. **Top right:** Quality of IC 2714 light curves over entire run, processed using pixelwise relative photometry. **Bottom:** Factor of improvement in rms using the pixelwise relative photometry. The median of the distribution is overplotted in solid black. The new photometry improved the rms scatter for all light curves underneath the black dashed line.



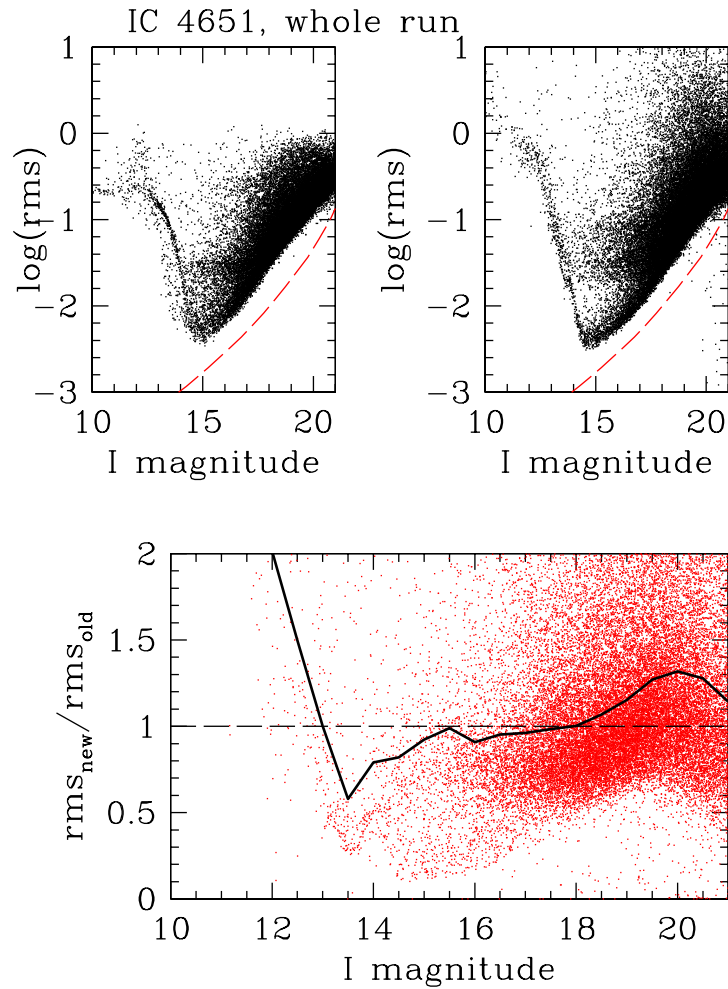


Figure 3.14: **Top left:** Quality of IC 4651 light curves over entire run, rms as a function of  $I$ , for old relative photometry. The dashed red line in this panel and the top right panel is a single-frame median theoretical photon noise limit. **Top right:** Quality of IC 4651 light curves over entire run, processed using pixelwise relative photometry. **Bottom:** Factor of improvement in rms using the pixelwise relative photometry. The median of the distribution is overplotted in solid black. The new photometry improved the rms scatter for all light curves underneath the black dashed line.

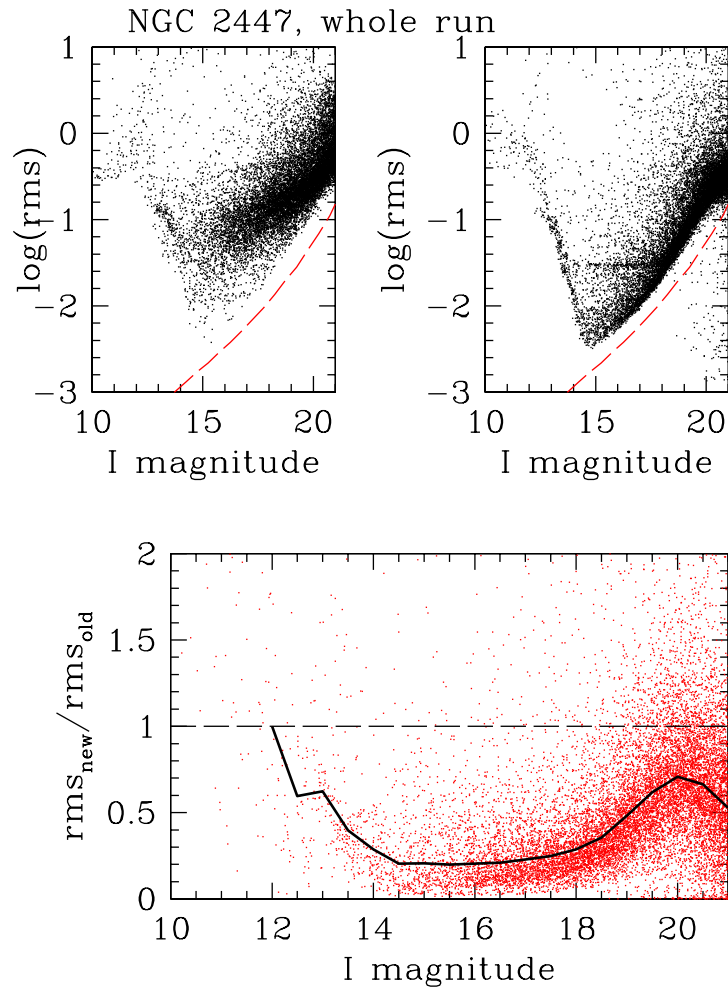


Figure 3.15: **Top left:** Quality of NGC 2447 light curves over entire run, rms as a function of  $I$ , for old relative photometry. The dashed red line in this panel and the top right panel is a single-frame median theoretical photon noise limit. **Top right:** Quality of NGC 2447 light curves over entire run, processed using pixelwise relative photometry. **Bottom:** Factor of improvement in rms using the pixelwise relative photometry. The median of the distribution is overplotted in solid black. The new photometry improved the rms scatter for all light curves underneath the black dashed line.

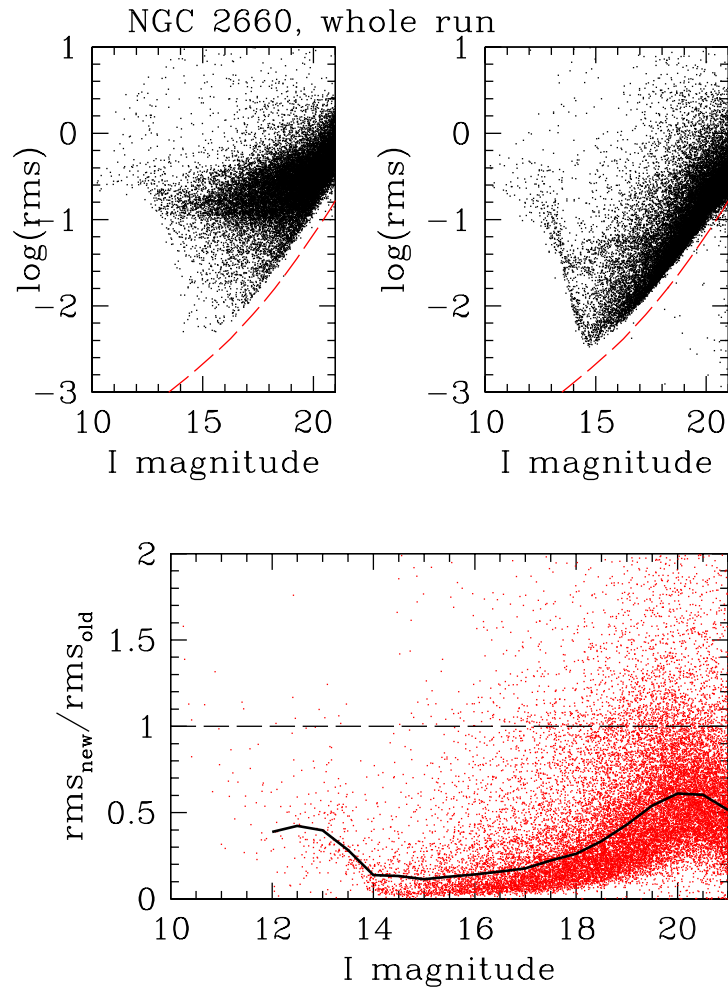


Figure 3.16: **Top left:** Quality of NGC 2660 light curves over entire run, rms as a function of  $I$ , for old relative photometry. The dashed red line in this panel and the top right panel is a single-frame median theoretical photon noise limit. **Top right:** Quality of NGC 2660 light curves over entire run, processed using pixelwise relative photometry. **Bottom:** Factor of improvement in rms using the pixelwise relative photometry. The median of the distribution is overplotted in solid black. The new photometry improved the rms scatter for all light curves underneath the black dashed line.

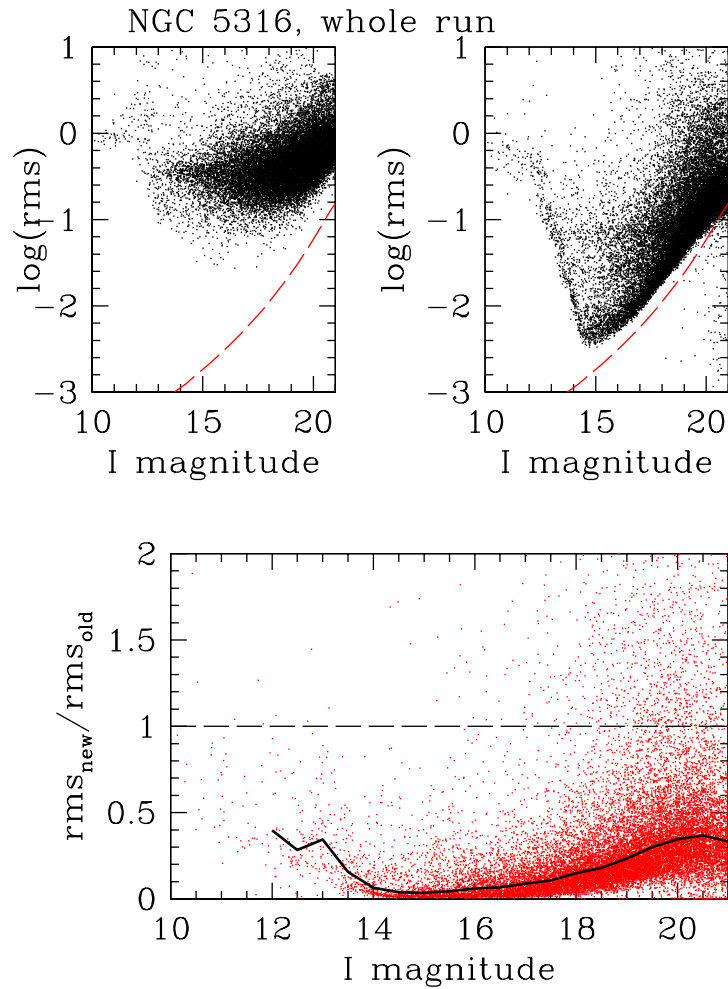


Figure 3.17: **Top left:** Quality of NGC 5316 light curves over entire run, rms as a function of  $I$ , for old relative photometry. The dashed red line in this panel and the top right panel is a single-frame median theoretical photon noise limit. **Top right:** Quality of NGC 5316 light curves over entire run, processed using pixelwise relative photometry. **Bottom:** Factor of improvement in rms using the pixelwise relative photometry. The median of the distribution is overplotted in solid black. The new photometry improved the rms scatter for all light curves underneath the black dashed line.

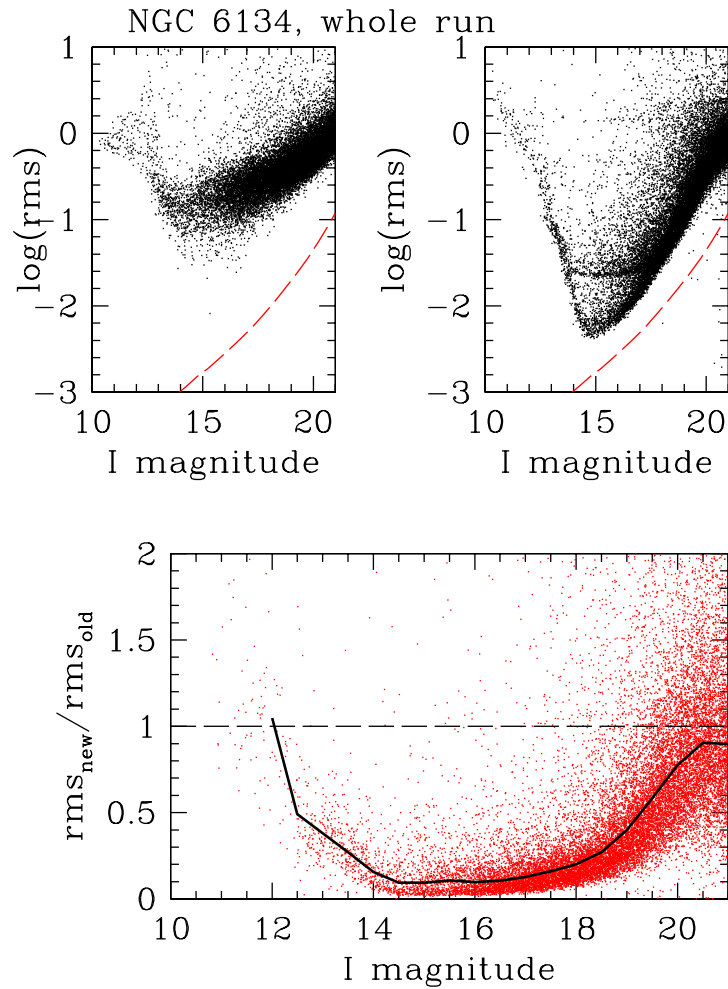


Figure 3.18: **Top left:** Quality of NGC 6134 light curves over entire run, rms as a function of  $I$ , for old relative photometry. The dashed red line in this panel and the top right panel is a single-frame median theoretical photon noise limit. **Top right:** Quality of NGC 6134 light curves over entire run, processed using pixelwise relative photometry. **Bottom:** Factor of improvement in rms using the pixelwise relative photometry. The median of the distribution is overplotted in solid black. The new photometry improved the rms scatter for all light curves underneath the black dashed line.

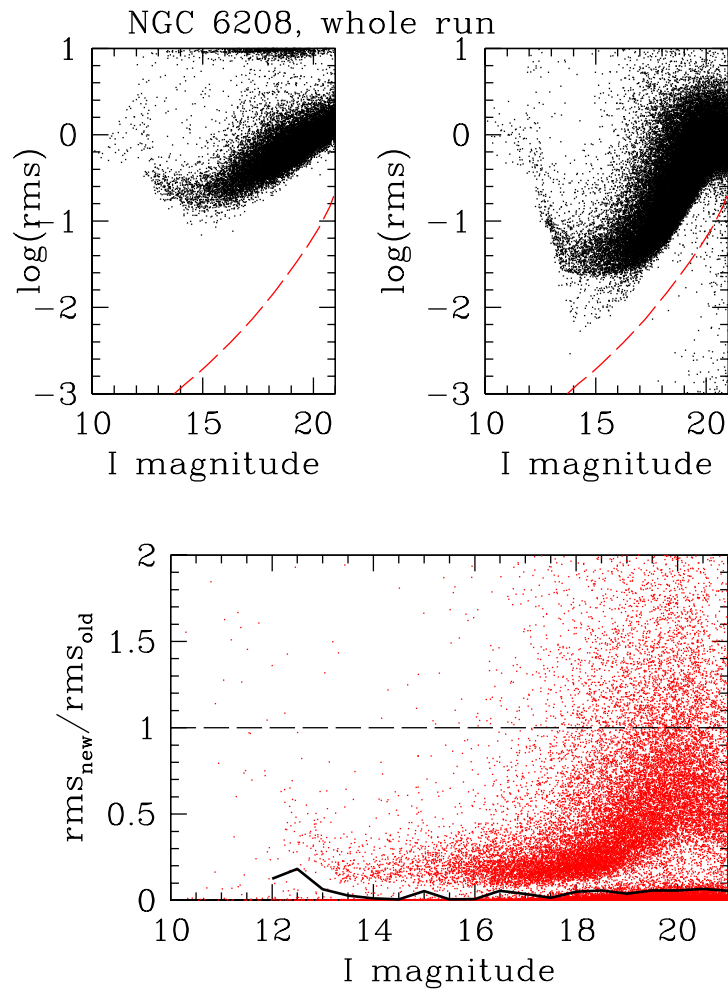


Figure 3.19: **Top left:** Quality of NGC 6208 light curves over entire run, rms as a function of  $I$ , for old relative photometry. The dashed red line in this panel and the top right panel is a single-frame median theoretical photon noise limit. This cluster has 29300 stars which the old photometry did not measure well, and appear here at  $\log(\text{rms}) \sim 1$ . **Top right:** Quality of NGC 6208 light curves over entire run, processed using pixelwise relative photometry. **Bottom:** Factor of improvement in rms using the pixelwise relative photometry. The median of the distribution is overplotted in solid black. The new photometry improved the rms scatter for all light curves underneath the black dashed line. 28775 of the stars not measured well in the old photometry but with good values in the new photometry populate the factor of improvement plot at fractions less than 0.1.

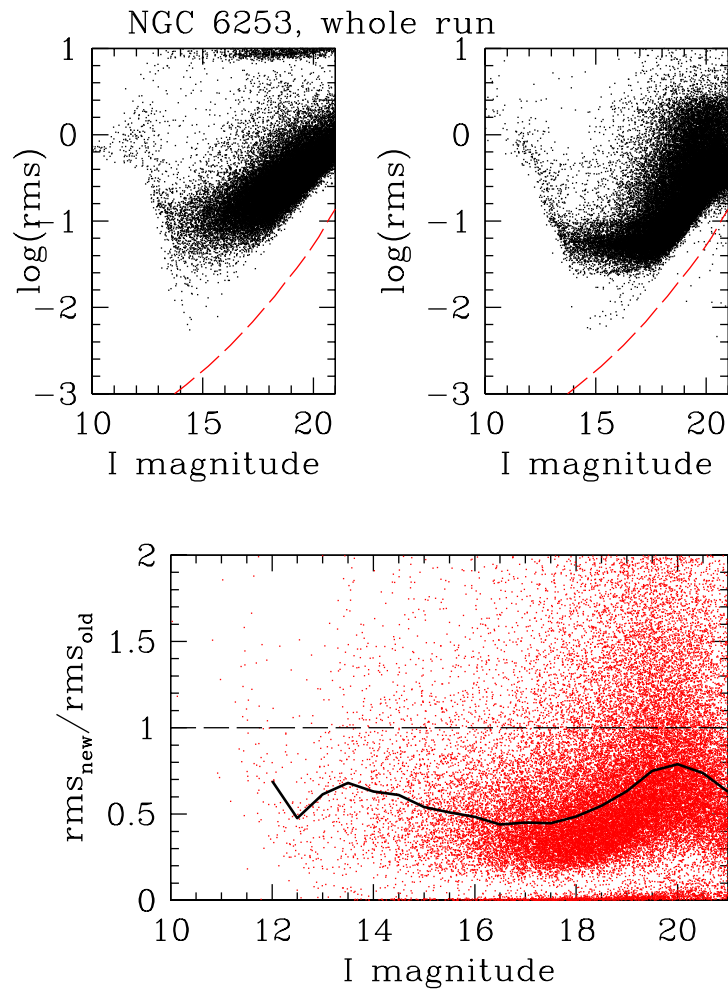


Figure 3.20: **Top left:** Quality of NGC 6253 light curves over entire run, rms as a function of  $I$ , for old relative photometry. The dashed red line in this panel and the top right panel is a single-frame median theoretical photon noise limit. This cluster has 2185 stars which the old photometry did not measure well, and appear here at  $\log(\text{rms}) \sim 1$ . **Top right:** Quality of NGC 6253 light curves over entire run, processed using pixelwise relative photometry. **Bottom:** Factor of improvement in rms using the pixelwise relative photometry. The median of the distribution is overplotted in solid black. The new photometry improved the rms scatter for all light curves underneath the black dashed line. 1976 of the stars not measured well in the old photometry but with good values in the new photometry populate the factor of improvement plot at fractions less than 0.1.

# Chapter 4

## Cluster membership analysis

### 4.1 Introduction

Our variable star detections will be most valuable when contextualized by the probability that the stars are open cluster members. If they are, then the variable stars' ages and metallicities can be assigned the well-determined values from the open cluster.

Typically, one assigns the probability of cluster membership based on proximity to the best fit isochrone, plus radial velocity and proper motion information where available. While we do not possess radial velocity and proper motion measurements in quantities or precision to assist with cluster membership determination for our variable stars, we do possess imaging in multiple filters. The availability of multiple colours allows us to estimate spectral types, and hence distances and reddenings, for a wide range of stars in our sample.

By definition, the spectral type of a star is determined by matching its spectrum within a classification library of standard spectra- the widespread standard being the MK classification system (Morgan et al. 1943; Morgan et al. 1978; Keenan & McNeil 1976). This classification system closely follows the effective temperatures and surface gravities of the stars. Therefore, the spectral energy distribution (SED) will change smoothly as a function of spectral type, both because of the shift in the blackbody peak and changes in line blanketing. Thus, the SED can be used as a coarse-precision proxy for true spectral classification. The SED will also be sensitive to the amount of interstellar reddening along the line of sight to the star.

To derive the MK spectral type, luminosity class, reddening, and distance of a star, we perform SED fitting in a subset of  $BVRIJHK$ . We ease the computation by first determining the reddening as a function of distance. We rely on MK classification spec-



troscopy of a small sample of stars as our primary method of determining distance and reddening, and bootstrap to red clump giants as a secondary distance indicator. Incorporating the run of reddening into our SED fitting code, we perform a chi-squared minimization and determine the best fitting model.

We describe our methods for calculating reddening as a function of distance in §4.2. Section 4.3 describes the makeup of our SED fitting engine. Section 4.4 tests the algorithm on both simulated and real data where spectral types are already known. Finally, §4.5 shows the application of this technique to our open clusters, in concert with background level subtraction to yield probabilities of cluster membership.

## 4.2 Reddening along the line of sight

Our primary *BVRI* imaging of each star provides four data points to use to derive the MK spectral type (temperature), luminosity class (surface gravity), reddening, and distance. However, photometric noise can cause models with significantly different parameters to overlap in this four-dimensional phase space, so it is important to simplify the problem as much as possible. This can be accomplished by reducing the dimensionality of the problem from four independent model parameters to three: reddening and distance are related all across a field of uniform extinction properties. In order to derive the equation expressing reddening as a function of distance, we require photometry of sources of known luminosity and colour. We employ two such known sources: spectroscopically classified stars, and red clump giants.

### 4.2.1 Spectroscopic Determination

Using du Pont’s WFCCD with multi-object slit masks, we have collected spectra of dozens of stars, selected randomly from the magnitude bin  $14 < I < 15.5$ , in the fields of NGC 2447, NGC 5316, NGC 6253, and IC 2714 (see §2.3.2). The final extracted spectra have  $\text{SNR} \gtrsim 10$  in the blue ( $\sim 4000 \text{ \AA}$ ), and resolution  $\sim 1.3 \text{ \AA}$ . Using WFCCD with a custom-made long slit of the same width as the multi-object slits, we collected spectra of tens of MK primary and secondary standard stars. We visually compared the cluster field spectra with the grid of standards, and classified the cluster field spectral types to within  $\pm 3$  spectral subtypes. Since the luminosity class is difficult to determine accurately at this SNR and resolution, we use our photometry and colour-magnitude diagram to assist with luminosity classification, labelling objects along the giant branch at bright *V*

magnitudes and red  $V - I$  colours (exact colour cuts varying from cluster to cluster) as class III giants.

By looking up our visually derived MK classifications in a flux-calibrated library of stellar spectra (Pickles 1998), we then find the intrinsic colours and absolute magnitudes. We compare the measured colours of these stars to the intrinsic colours and derive the chi-squared best-fit reddening based on the photometry error bars. Applying the distance modulus equation with the absolute magnitudes and reddenings then yields the distances.

We plot our reddenings as a function of distance, and considering the amount of scatter, we are only able to fit the reddening as a function of distance by eye, using a set of straight lines. In the final analysis, §4.2.2 below, we incorporate red clump methods to augment the amount of data, and fit a smooth, continuous analytic function for reddening as a function of distance. We show our spectroscopically derived reddenings as a function of distance in Fig. 4.1. The spectroscopic data, mapped out by the small square points, have relatively large error bars corresponding to our modest MK classification error bars. However, because the data are numerous, one can still trace the rise in extinction with distance, despite the scatter and outliers.

## 4.2.2 Red Clump Determination with Bootstrapping

For fields with no spectroscopic sample, it is necessary to choose an alternate method for deriving the reddening as a function of distance. Also, a complementary method can enhance the domain of distance over which measured reddenings are available. We choose the “red clump” method (Stanek et al. 1994, Paczynski et al. 1994) to fulfill these needs.

Core helium-burning giants comprise the tight “red clump” on a colour-magnitude diagram. Theory predicts (Castellani et al. 1992) that these stars have luminosities and infrared colours nearly constant as a function of age and metallicity, so are good standard candles. In the MK classification scheme they are K2III giants (López-Corredoira et al. 2002).

Therefore, adopting a single colour and absolute magnitude to represent a typical red clump star, one may use the observed colour of a red clump star to calculate its reddening. We opt to use the infrared colours, as recommended by López-Corredoira et al. (2002) and Durant & van Kerkwijk (2006). We convert the  $J - K$  excess to  $A_V$  by the standard factor of 0.168 (Cardelli et al. 1989).

Using the derived reddening and the measured absolute magnitude in the distance modulus equation yields the distance to the star. Since core helium-burning can last up

to 10% of the star’s main sequence lifetime, and since its luminosity is over ten times higher than a main sequence star of equal spectral type, the colour-magnitude diagram (CMD) of any observed field will show an obvious excess along a stripe corresponding to red clump stars at a variety of distances. The locus of the red clump stars on the CMD thus permits the determination of reddening as a function of distance.

To garner sufficient statistics, especially to sample the reddening in nearby space ( $\lesssim 3$  kpc), we require fields of view substantially larger than provided by our Swope imaging. Therefore, we have drawn from the 2MASS catalogue, and for bins one  $K$  magnitude in width, we choose fields of view with radii from 10’ for  $13 < K < 14$  up to 150’ for  $6 < K < 7$ . Our succession of bin sizes resolves the position of the red clump well, with a few hundred stars per bin. For each cluster, these “composite” CMDs, built up using data from several field sizes, allow the tight continuity of the red clump to be traced, defining the reddening-distance locus.

We determine the reddening-distance locus in a manner similar to that followed by Durant (2006). We bin the CMD into 0.5 mag bins in  $K$  and 0.05 mag bins in  $J - K$ . Then, for each  $K$  magnitude (horizontal slice through the CMD), we examine the histogram of stars as a function of  $J - K$ . There are up to three population peaks in the histogram as one traverses from blue to red: main sequence stars, the red clump, and other kinds of giants. Therefore, at each  $K$  magnitude, we determine the  $J - K$  centroid of the red clump population by modelling the histogram with a least-squares fit to the sum of three displaced Gaussians, and we record this mean  $(J - K)_{measured}$  of the Gaussian associated with the red clump.

We convert the locus thus derived from (magnitude, colour) pairs to (distance, reddening) pairs, using the conversion factors between colour excess  $(J - K)_{measured} - (J - K)_0$ , extinctions  $A_V$  and  $A_K = 0.112A_V$ , and absolute magnitude  $M_K$ , with the distance modulus equation:

$$A_V = \frac{(J - K)_{measured} - (J - K)_0}{0.168}; \text{ and} \quad (4.1)$$

$$d = 10^{0.2(K - M_K - 0.112A_V)}. \quad (4.2)$$

The intrinsic colour  $(J - K)_0$  may be subject to systematic error on the order of 0.1 mag compared to the literature value (van Kerkwijk, p. comm), so we have chosen to calibrate  $(J - K)_0$  based on our own spectroscopic data.

For fields where we have spectra, we combine the spectroscopically derived reddening-distance pairs with the red clump pairs. This produces an enhanced data set, where

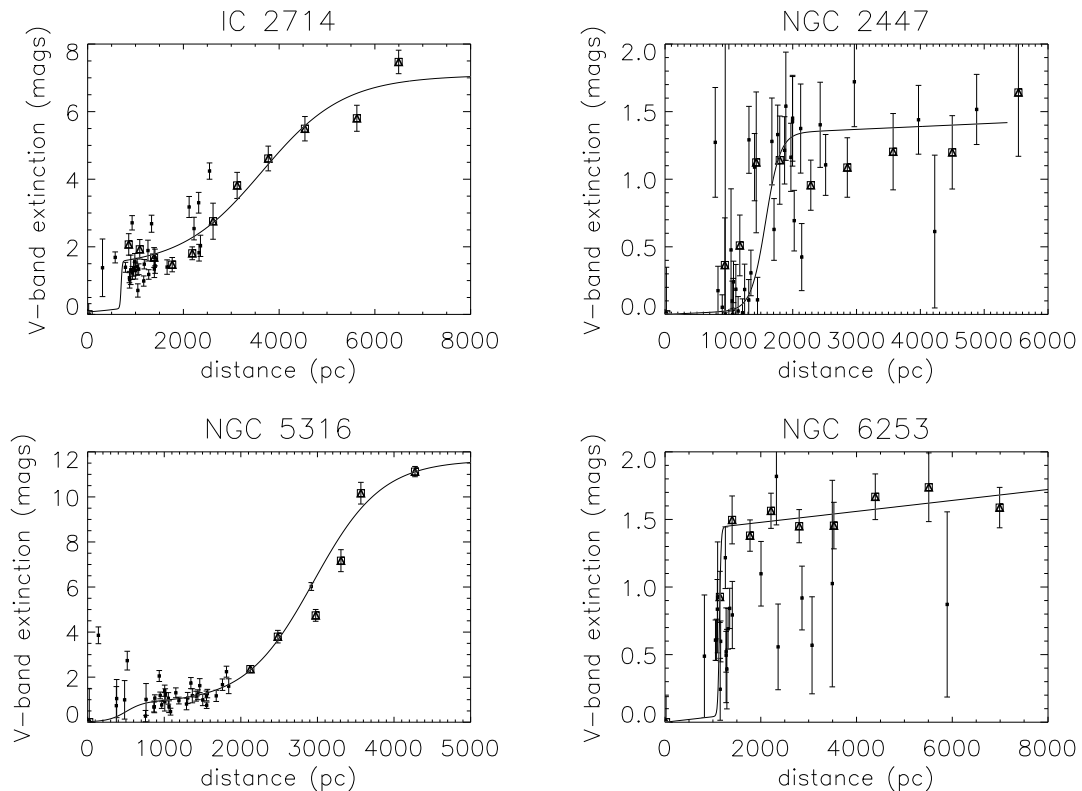


Figure 4.1: Combined spectroscopic and red clump reddening-distance relation, for the fields of IC 2714, NGC 2447, NGC 5316, and NGC 6253.

the  $A_V$  at nearby distances is covered by the spectroscopic set, and the  $A_V$  at large distances by the red clump. While no single value of  $(J - K)_0$  produces perfect  $A_V$ -distance agreement for all the overlapping regions in the datasets, a value  $(J - K)_0 = 0.55$  is adopted as a happy medium, and applied to translate all red clump colours into reddenings.

We assume a simple physical model of uniform background dust, plus dust clouds. On a plot of  $A_V$  as a function of distance, this corresponds to a linear rise broken by step steps. We represent the steps by Fermi functions, and hence fit the data using:

$$A_V = md + \sum_{i=1}^N \left[ A_i - \frac{A_i}{e^{\frac{d-d_i}{\sigma_i}} + 1} \right], \quad (4.3)$$

where  $m$  is the slope due to the uniform dust background,  $N$  is the number of steps modelled (typically one or two),  $A_i$  are the sizes of the steps, in magnitudes,  $d_i$  are the locations of the steps, and  $\sigma_i$  are the widths of the steps. We fit using a least-squares

routine for IDL, MPFIT (Markwardt 2006). Error bars on the spectroscopic data points correspond to a  $\pm 3$  subtype visual MK classification uncertainty. Error bars on the red clump data correspond to  $\frac{\sigma}{\sqrt{N}}$  where  $\sigma$  is the fitted width of the red clump and  $N$  is the area of the fitted peak. See Table 4.1 for a list of the resulting fit coefficients describing the reddening as a function of distance in our cluster fields. For IC 4651, NGC 2447, NGC 6208, and NGC 6253, the reddening is well fit by a single step. The other clusters require two step functions for a good fit.

An example of a 2MASS  $J - K$  colour-magnitude diagram for the field of NGC 2447 is shown in the left panel of Figure 4.2. We overplot the location of the red clump as found by fitting three displaced Gaussians. In the right panel of Figure 4.2, we show the equivalent path of the red clump locus translated to coordinates of distance and reddening, using Equations 4.1 and 4.2. A Fermi step function in reddening on top of a linear background is seen to provide a good analytical description of the reddening-distance relation.

Table 4.1: Reddening-distance fit coefficients.

Cluster	Number of step functions $N$	Background slope $m$	$A_1$	$d_1$	$\sigma_1$	$A_2$	$d_2$	$\sigma_2$
IC 2714	2	1.40	700	12.04	5.52	3643	845	0.000018
IC 4651	1	1.14	911	19.67	–	–	–	0.000048
NGC 2447	1	0.82	1142	105.1	–	–	–	.00012
NGC 2660	2	1.52	725	50.81	1.73	5442	722	0.000010
NGC 5316	2	1.00	986	50.00	7.64	3234	221.6	0.00065
NGC 6134	2	1.36	1536	50.00	11.56	2699	100.5	0.00098
NGC 6208	1	1.40	1108	17.45	–	–	–	0.000035
NGC 6253	1	1.40	1137	16.78	–	–	–	0.000041

### 4.3 Algorithm for Determining Photometric Spectral Types

Our SED-fitting routine, given photometry of a star in some or all of  $BVRIJHK$ , estimates spectral type, luminosity class, distance, and reddening. The ingredients that plug in to the fitting code are:

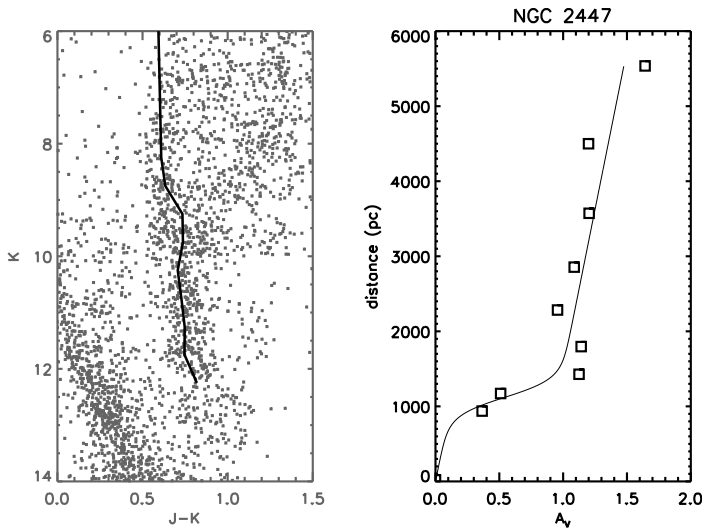


Figure 4.2: **Left:** 2MASS  $J - K$  colour-magnitude diagram for the field of NGC 2447. The location of the red clump is indicated by a line. **Right:** The reddening as a function of distance for NGC 2447, calculated from the red clump locus as located in the left panel.

1. A stellar spectral library containing flux measurements of standard spectral types
2. A relation between visual extinction  $A_V$  and extinction at any other wavelength  $A_\lambda$
3. An interpolation engine to smoothly fill the gaps in the library
4. A robust global chi-squared minimizer

For many of our target fields, we have fit based on  $BVRI$  alone in order to minimize the number of stars lost due to the shallowness of the 2MASS  $JHK$  data. However, we must be able to accommodate fits including  $JHK$  for the control fields with incomplete colour coverage. Therefore, we must use a stellar spectral library providing fluxes out to at least the end of the  $K_s$  band at  $\sim 2.4 \mu\text{m}$ . We choose the Pickles (1998) library because it is calculated from measured template spectra, rather than theoretical model atmospheres.

To compute colours from the Pickles library, we integrate the library fluxes over the standard filter transmission curves from Bessell (1979, 1988), multiplied by a polynomial interpolation of reddening as a function of wavelength taken from Cardelli, Clayton, and Mathis (1989), using the standard  $R_V = 3.1$  parametrization of dust properties. We

save a table of the colours computed in steps of  $\Delta A_V = 0.05$ , and later use interpolation between the steps to save on the computational time of repeatedly integrating the spectra in the later stages of the SED fitting routine.

The Pickles library contains 131 stellar spectra. As provided, this does not cover the chi-squared surface for SED fitting with sufficient density to pick out the correct minima. Therefore, we use interpolation to fill the phase space in three dimensions: spectral type, luminosity class, and  $A_V$ . Our interpolation is engaged on a “just-in-time” basis- when the chi-squared minimizer requires a set of model colours for a given spectral type, luminosity class, and  $A_V$ , our interpolation module performs a simple, fast, trilinear interpolation. It seeks the closest grid points in  $A_V$ , luminosity class, and spectral type. Then, it performs linear interpolations between those points, axis-by-axis, first along the  $A_V$  axis, then along the spectral type axis, and lastly along the luminosity class axis.

To perform the chi-squared fit between the measured *BVRIJHK* photometry and the library *BVRIJHK* photometry, we have tried two popular general non-linear minimization algorithms. We initially used the robust but slow downhill simplex algorithm (Nelder & Mead 1965; Press et al. 1989). Later, we used the Levenberg-Marquardt algorithm, with derivatives computed numerically using the MINPACK software (Moré et al. 1980) as ported to C (Bond 2006), which ran orders of magnitudes faster but was trapped more often within local minima. By parachuting in a sufficient density ( $\sim 10$ - $20$ ) of different, evenly spaced initial guesses for the fit parameters, then picking the solution chain with the best final chi-squared, we were able to obtain agreement between the methods. The code used publicly available algorithms subplex (Rowan 1990) for downhill simplex minimization and MINPACKC for Levenberg-Marquardt minimization. We used the speedier MINPACKC version for final computations.

## 4.4 Verification

In order to verify that we recover the correct spectral types of our stars, we employ our spectroscopic samples. For the spectroscopic samples, we previously identified the MK classifications to within  $\pm 3$  subtypes. Therefore, we check our answers simply by cross-referencing the photometrically derived spectral type estimates with the spectroscopically derived estimates.

Plots of photometrically estimated spectral type as a function of spectroscopically determined spectral type are shown in Fig. 4.3. We codify spectral types and subtypes numerically for ease of cataloguing and sorting; we use the tens digit to represent the

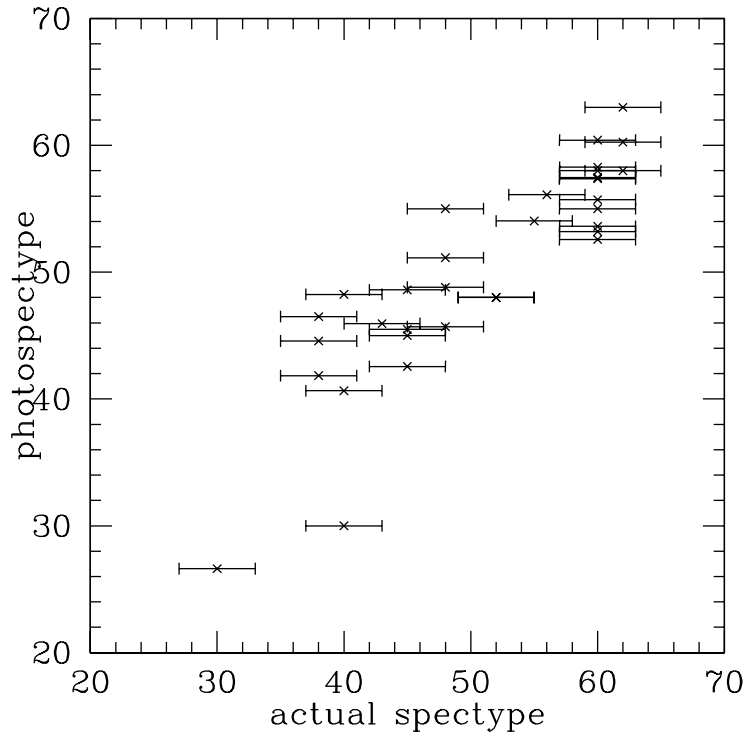


Figure 4.3: Photometric estimate of spectral type as a function of true spectroscopic MK classification, for a sample of stars in NGC 2447. The numerical spectral types 11-19 are MK types O1-O9, 20-29 are B0-B9, and similarly down to 70-79, standing for M0-M9. The two estimates lie near a 1:1 relation, indicating good performance. We estimate the error in visual MK classification at this SNR and resolution to be three spectral types.

spectral type, and the ones digit to represent the subtype, so spectral types O1-O9 translate to numeric labels 11-19, B0-B9 to labels 20-29, proceeding similarly down to M0-M9, which are labelled 70-79. The photometric estimates agree well with the spectroscopic estimates, to within less than one spectral type.

We also created simulated photometry based on colours from the library plus Gaussian random noise. We show photometrically estimated spectral type as a function of library spectral type, for several combinations of noise levels and colours fit, in Fig. 4.4. At spectral types later than about K3 (numerical type 63), catastrophic errors become common as the phase space becomes dense with both nearby red dwarfs and distant, highly reddened hot giants, and given photometric error bars, the algorithm becomes hard-pressed to pick the correct classification. Therefore, we must consider fainter potential cluster stars in a different statistical bin when calculating cluster membership probabilities.



We can improve the recovery of late type dwarfs somewhat by seeking spectral type alone using only colour information without an absolute scaling; in this case, the luminosity class could be recovered by a second stage of fitting in the vicinity of the known spectral type. However, even then, a high percentage of late type dwarfs are misidentified.

We investigated the behaviour of the spectral type analysis on binary stars by creating a grid of simulated binary photometry and attempting to recover the spectral type. There are two extremes to the problem. One extreme is the case of a binary composed of two identical stars. In this case, one might expect the spectral type algorithm to derive the temperature (spectral type) fairly accurately since the colours would be the same as a single star, but that the star might be misclassified either in luminosity class or in distance. The other extreme is the case of a binary composed of one high mass and one low mass star, in which case the low mass star contributes little flux and one expects the spectral type analysis to be fairly accurate.

In Table 4.2, we present the recovered spectral types for pairings of dwarf stars from A0 to M0. The simulated binaries were given  $A_V = 0.14$  (the reddening for NGC 2447), and recovery was attempted using the reddening-distance relation for NGC 2447. As expected, most recovered spectral types are very close to the spectral type of the primary. There is only a single catastrophic error in spectral type in the 14 simulated binaries- an F0V + G0V binary is well fit by a distant, highly reddened B giant. Between luminosity class and reddening (distance), the algorithm prefers to adjust the luminosity class to match the high flux from the binary. This is fortunate, since an accurate distance is useful for determining cluster membership.

## 4.5 The Results: Cluster Membership Probabilities

Our calculated quantities of spectral type, luminosity class, reddening, and distance effectively recast our magnitude information into a parameter space where it is easy to define simple cuts that will isolate cluster stars. Here, we show plots of several parameters which demonstrate the effects of various cuts on the colour-magnitude diagrams (CMDs) and on enhancing the visibility of the spatial structure of the clusters. In all CMDs that follow in this section, the data points' colour coding illustrates the spectral types of the stars plotted: blue data points represent B stars, cyan points are A stars, green points are F stars, yellow points are G stars, orange points are K stars, and red points are M stars.

While it is not always obvious from cursory inspection of CMDs whether the control

Table 4.2: Spectral type analysis of simulated binaries at the reddening of NGC 2447

Primary MK spectral type	Secondary MK spectral type	Recovered numerical spectral type	Recovered interpolated luminosity class	Recovered $A_V$
A0V	A0V	30.15	2.94	0.147
A0V	F0V	32.88	3.39	0.147
A0V	G0V	32.32	3.70	0.156
A0V	K0V	31.06	4.34	0.142
A0V	M0V	30.47	4.52	0.150
F0V	F0V	40.64	4.34	0.156
F0V	G0V	21.70	2.87	1.804
F0V	K0V	43.35	4.56	0.154
F0V	M0V	40.18	4.85	0.175
G0V	G0V	50.94	5.00	0.068
G0V	K0V	52.40	4.49	0.149
G0V	M0V	52.00	4.62	0.159
K0V	K0V	60.01	4.63	0.169
K0V	M0V	59.32	4.75	0.318

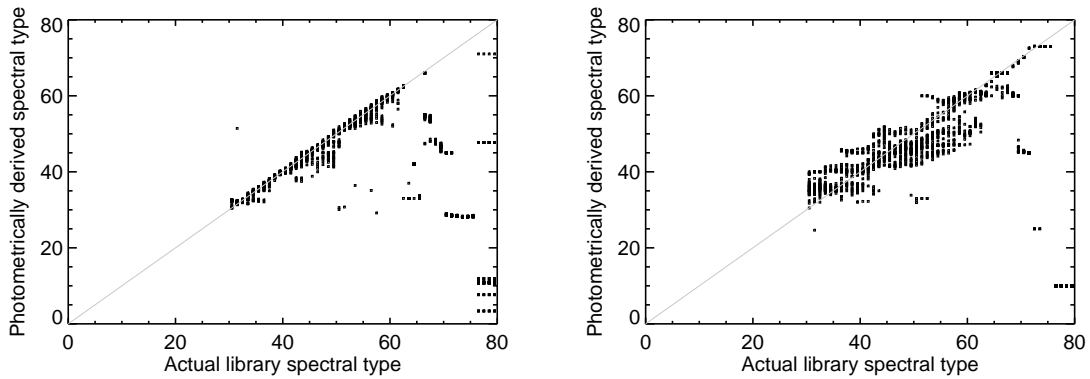


Figure 4.4: Recovery of spectral types from simulated photometry of stars inside a cluster with the properties of NGC 6253. The numerical spectral types 11-19 are MK types O1-O9, 20-29 are B0-B9, and similarly down to 70-79, standing for M0-M9. **Top:** Quality of recovery using  $BVRI$  library star photometry with 1% Gaussian noise added. Note how performance degrades at late spectral types. **Bottom:** Quality of recovery using  $B - V$ ,  $V - R$ , and  $V - I$  alone without an absolute scaling. Identification of late spectral types improves, although the overall relation is less tight.

fields are different from the main cluster fields, subtracting histograms of the population clearly reveals whether a certain cut correlates with an excess of cluster stars. We assign bins in distance, spatial radius from cluster centre, and  $V$ , and compute the overdensity as a fraction of the total number of stars in the cluster field. This number serves as the probability of cluster membership in that bin, but note that it can be negative to indicate that the cluster field is actually underdense in that bin (which can occur if the cluster field is highly reddened relative to the control field).

### 4.5.1 NGC 2447

NGC 2447 is the closest cluster to the Galactic anticentre that we observed, and as a result, the background level is relatively low. The cluster main sequence is marginally visible on a raw CMD. Control fields were available in  $VI$  only, so we used catalogue matching to augment our data with 2MASS  $JHK$ . In order to minimize mismatches between 2MASS objects and spurious sources in our catalogue, we matched only on stars  $I < 18.5$ , well within our survey completeness limit. Out of 4925 stars with  $I < 18.5$ , there were 3326 successful matches with 2MASS objects with  $JHK$  photometry.

A distance cut of  $500 < d < 1500$  pc cleans the background level for this cluster quite well and shows the profile of the cluster, as demonstrated in Figures 4.5 through 4.7.

Figure 4.8 shows that the large number of objects within a distance cut of  $1500 < d < 2500$  pc do not cluster strongly, and so our method does a good job of separating the background.

Figure 4.9 compares the level of background objects (defined by the average of the control fields) to the level of cluster objects. While the distributions share similar morphologies, the cluster field does contain an excess of stars at the cluster distance.

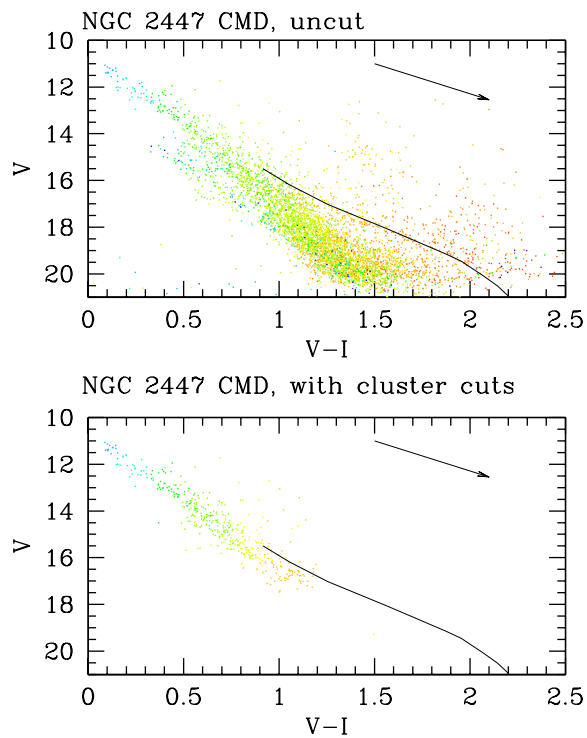


Figure 4.5: **Top:** CMD of NGC 2447, with no cuts on objects reported. The curved line overlaid at bottom is the predicted location of the lower main sequence (less than  $1 M_{\odot}$ ), using the BCAH98 models and the WEBDA properties of NGC 2447. The vector in the top right is the direction in which a source moves away from its intrinsic colour and magnitude, when it is reddened by standard dust (with  $\frac{A_V}{E_{B-V}} = 3.1$ ). **Bottom:** CMD of NGC 2447, with distance cut of  $500 < d < 1500$  pc to isolate cluster stars relative to background stars, and only spectral types earlier than K3 displayed. The Galactic background stars are removed particularly well from this cluster.

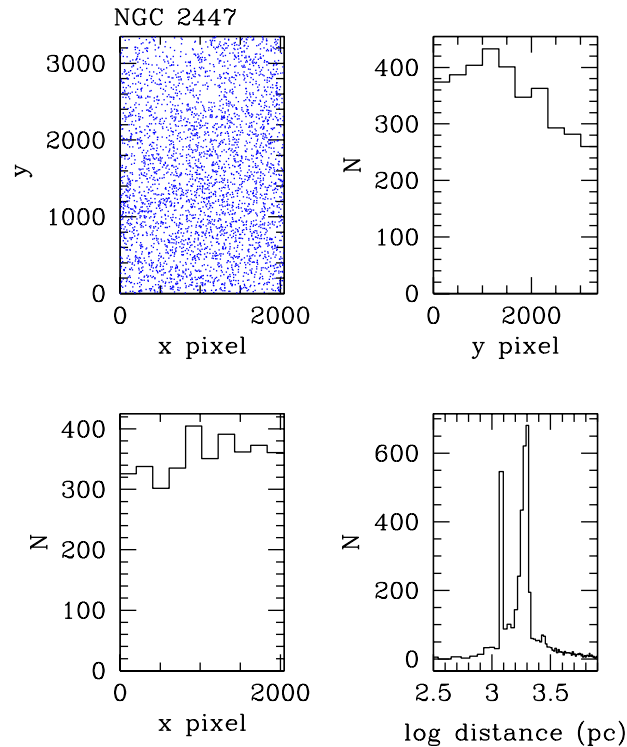


Figure 4.6: **Top left:** Spatial clustering in the field of NGC 2447, for all objects brighter than  $I = 18$ . **Top right:** y-axis histogram of objects detected in top left panel. A gradient is visible due to small amounts of dust. **Bottom left:** x-axis histogram of objects detected in top left panel. **Bottom right:** Histogram of distances reported by photometric estimation of spectral types.

### 4.5.2 NGC 2660

NGC 2660 was our pilot cluster, and has different properties from the remainder of the sample. In particular, it is the most distant cluster we monitored, at 3 kpc. Because of its distance, it has a small angular size and is very prominent on each exposure. On the CMD, the cluster main sequence is not obviously separated from the background main sequences. NGC 2660 has control field images in full  $BVRI$ , so no supplementary  $JHK$  from 2MASS was required, and all stars with  $BVRI$  were classified.

Although this cluster is so concentrated that it is clearly visible on Figure 4.11 without any cuts, the profile of this cluster is enhanced by a distance cut of  $2000 < d < 4000$  pc, as demonstrated in Figures 4.10 through 4.12. Figure 4.13 shows that while the objects in a distance cut of  $500 < d < 1500$  pc are clustered, the fraction of cluster stars landing in that distance bin is only perhaps a tenth of the total.

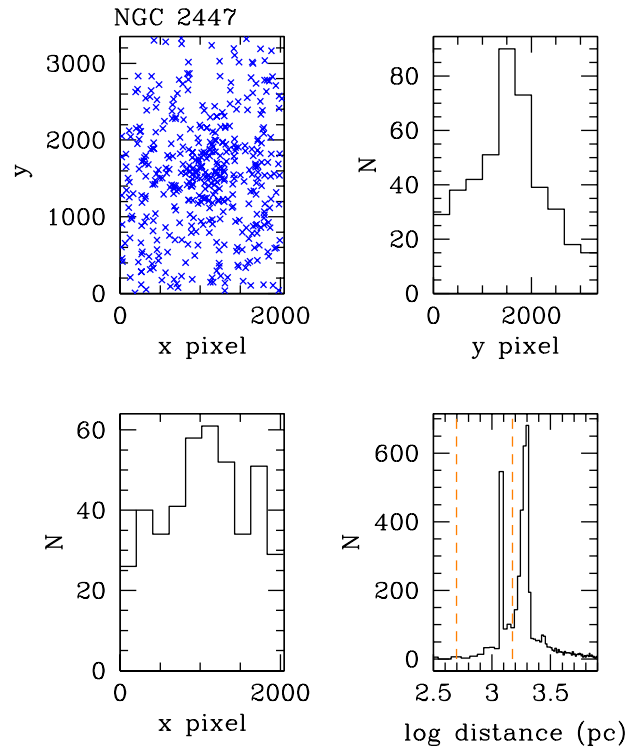


Figure 4.7: **Top left:** Spatial clustering in the field of NGC 2447, with distance cut of  $500 < d < 1500$  pc to isolate cluster stars relative to background stars. There is also a spectral type cut discarding stars later than K3. Prominent central clustering is visible. **Top right:** y-axis histogram of objects detected in top left panel. **Bottom left:** x-axis histogram of objects detected in top left panel. **Bottom right:** Histogram of distances reported by photometric estimation of spectral types. Dotted lines show the distance cut made.

Figure 4.14 compares the level of background objects (defined by the average of the control fields) to the level of cluster objects. While the distributions share similar morphologies, the cluster field does contain an excess of stars at the cluster distance.

### 4.5.3 NGC 5316

NGC 5316 is one of a few possible cluster choices observable in the southern autumn (April). Although the field contains dust lanes, it was also rich in stars in our desired magnitude range. Perhaps because of the dust, the cluster does not appear very centrally concentrated, even after making a relatively tight distance cut of  $900 < d < 1300$  pc. On the CMD, Figure 4.15, the cluster main sequence lies directly on top of the background

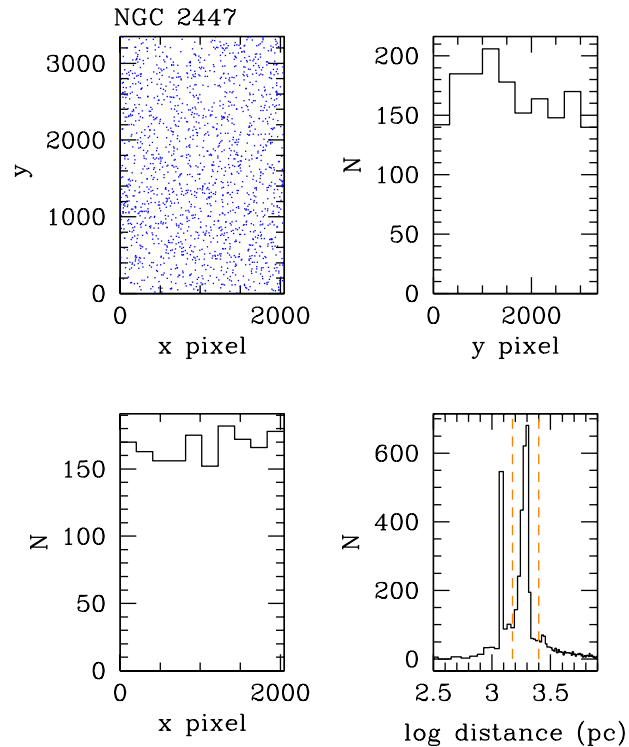


Figure 4.8: **Top left:** Spatial clustering in the field of NGC 2447, with distance cut of  $1500 < d < 2500$  pc to demonstrate that not many cluster stars are misclassified at distances farther than expected. There is also a spectral type cut discarding stars later than K3. **Top right:** y-axis histogram of objects detected in top left panel. **Bottom left:** x-axis histogram of objects detected in top left panel. **Bottom right:** Histogram of distances reported by photometric estimation of spectral types. Dotted lines show the distance cut made.

main sequences. NGC 5316 has control field images in *BVI*, so we included supplementary *JHK* from 2MASS. Catalogue matching yielded 5940 stars with both *BVI* and *JHK* colours, out of 7320 stars with *BVI*.

The cluster is not highly concentrated and is not visible in the uncut diagram in Figure 4.16. The cluster’s amorphous morphology shows as a very broad peak along the x direction and a much sharper peak along y, as seen in Figure 4.17, with the cluster-isolating distance cut  $900 < d < 1300$  pc. Figure 4.18 shows that the objects in a distance cut of  $1500 < d < 4000$  pc do not comprise many cluster stars.

Figure 4.19 compares the level of background objects (defined by the average of the control fields) to the level of cluster objects. The subtraction is not very clean because

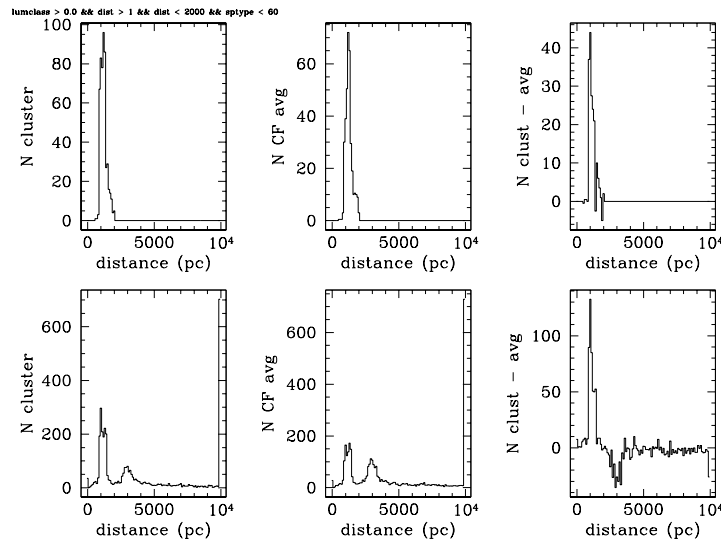


Figure 4.9: **Bottom left:** Histogram of distances from photometric spectral typing of all stars in the field of NGC 2447. **Bottom middle:** Average of the histograms of distances from photometric spectral typing of the two control fields for NGC 2447. **Bottom right:** Cluster histogram minus control field histogram, showing a peak of cluster stars. The trough is caused by misclassifications due to non-uniform reddening across the field. **Top left, middle, and right:** As their respective bottom panels, but considering only spectral types earlier than K0 and distances less than 2000 pc.

of the variable reddening throughout the field.

#### 4.5.4 NGC 6134

NGC 6134 has even higher levels of extinction than NGC 5316, but is also quite rich. Control fields are available in complete *BVRI*, so no catalogue matching with 2MASS *JHK* was needed. The CMD, as can be seen in Figure 4.20, contains a main sequence separated slightly to the blue of the background main sequence population. One might expect the clean cluster sequence to equate to good cluster definition, which appears to be the case for a distance cut of  $500 < d < 1500$  pc in Figures 4.20 and 4.22. However, this may be due in part to strategic placement of the dust lanes, as seen by the rather non-uniform sky distribution of sources in in Figures 4.21 and 4.23.

Subtracting off the control fields (which also appear dusty), we see that the cluster peak is small compared to the trough due to the highly variable reddening. Figure 4.24 compares the level of background objects to the level of cluster objects.



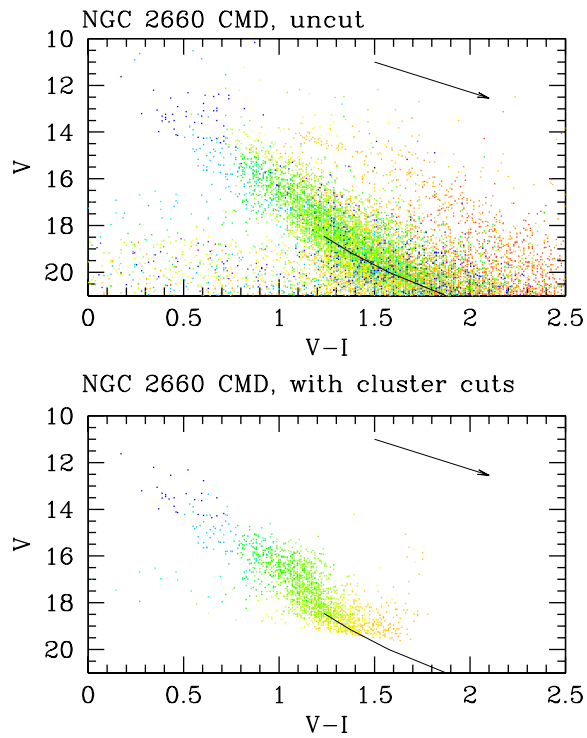


Figure 4.10: **Top:** CMD of NGC 2660, with no cuts on objects reported. The curved line overlaid at bottom is the predicted location of the lower main sequence (less than  $1 M_{\odot}$ ), using the BCAH98 models and the WEBDA properties of NGC 2660. **Bottom:** CMD of NGC 2660, with distance cut of  $2000 < d < 4000$  pc to isolate cluster stars relative to background stars, and a spectral type cut discarding stars later than K3.

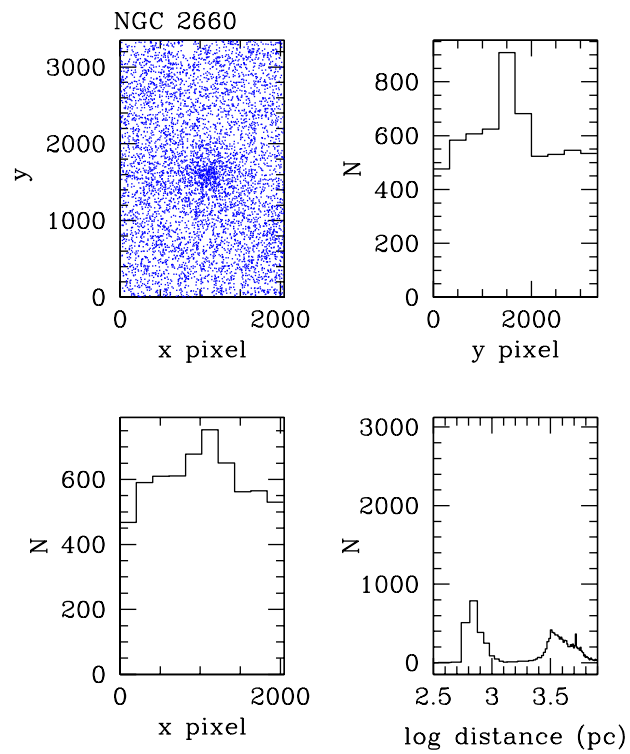


Figure 4.11: **Top left:** Spatial clustering in the field of NGC 2660, for all objects brighter than  $I = 18$ . **Top right:** y-axis histogram of objects detected in top left panel. **Bottom left:** x-axis histogram of objects detected in top left panel. **Bottom right:** Histogram of distances reported by photometric estimation of spectral types.

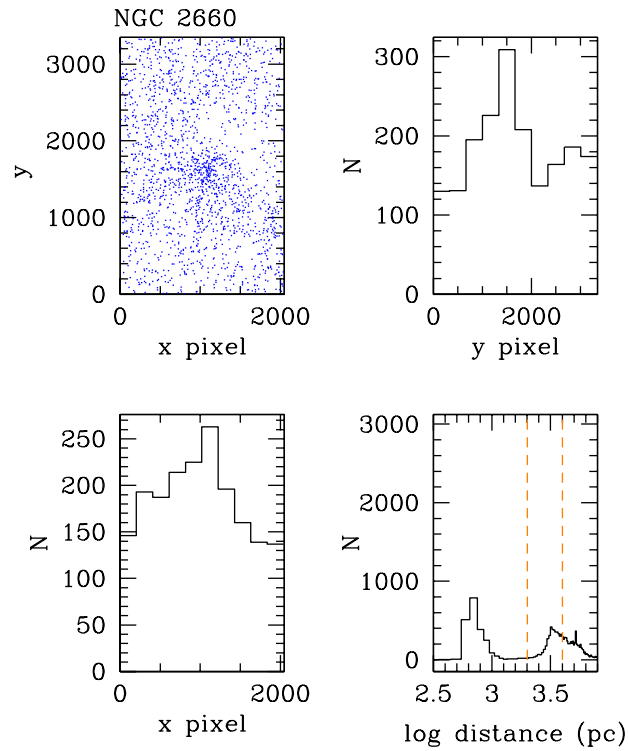


Figure 4.12: **Top left:** Spatial clustering in the field of NGC 2660, with distance cut of  $2000 < d < 4000$  pc to isolate cluster stars relative to background stars. There is also a spectral type cut discarding stars later than K3. Prominent central clustering is visible. **Top right:** y-axis histogram of objects detected in top left panel. **Bottom left:** x-axis histogram of objects detected in top left panel. **Bottom right:** Histogram of distances reported by photometric estimation of spectral types. Dotted lines show the distance cut made.

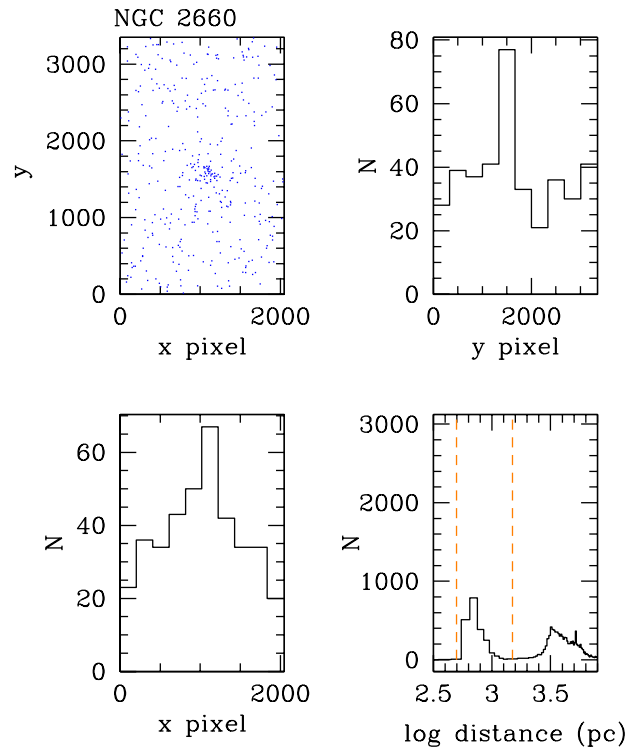


Figure 4.13: **Top left:** Spatial clustering in the field of NGC 2660, with distance cut of  $1500 < d < 2500$  pc to demonstrate that not too many cluster stars are misclassified at distances closer than expected. There is also a spectral type cut discarding stars later than K3. **Top right:** y-axis histogram of objects detected in top left panel. **Bottom left:** x-axis histogram of objects detected in top left panel. **Bottom right:** Histogram of distances reported by photometric estimation of spectral types. Dotted lines show the distance cut made.

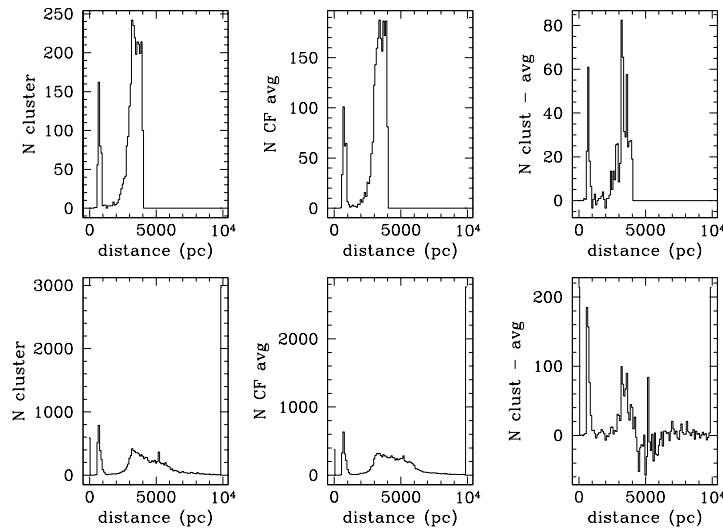


Figure 4.14: **Bottom left:** Histogram of distances from photometric spectral typing of all stars in the field of NGC 2660. **Bottom middle:** Average of the histograms of distances from photometric spectral typing of the two control fields for NGC 2660. **Bottom right:** Cluster histogram minus control field histogram, showing a peak of cluster stars at around 3000-4000 pc. The trough is caused by misclassifications due to non-uniform reddening across the field. Also, since the photometry for this cluster was best suited for relatively bright, distant stars, a number of distant early type stars were misclassified as late nearby dwarfs (as expected from the simulations in §4.4) **Top left, middle, and right:** As their respective bottom panels, but considering only spectral types earlier than K3 and distances less than 4000 pc.

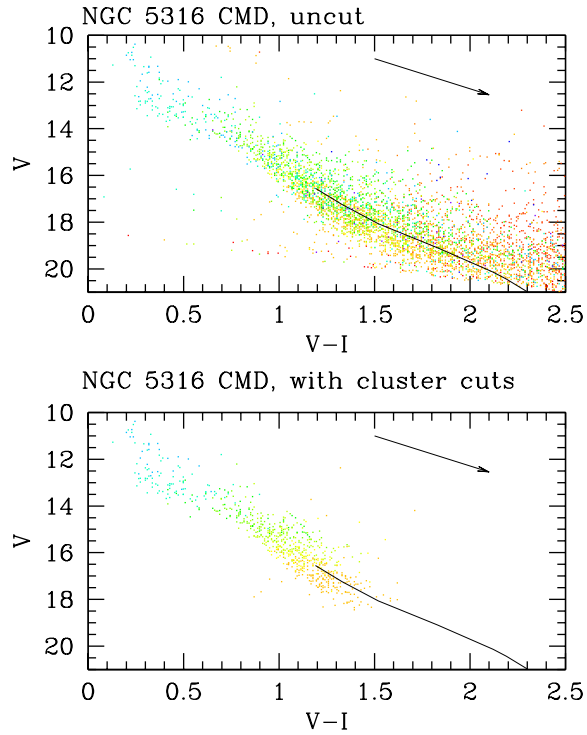


Figure 4.15: **Top:** CMD of NGC 5316, with no cuts on objects reported, other than a limit at  $I = 18$ . The curved line overlaid at bottom is the predicted location of the lower main sequence (less than  $1 M_{\odot}$ ), using the BCAH98 models and the WEBDA properties of NGC 5316. **Bottom:** CMD of NGC 5316, with distance cut of  $900 < d < 1300$  pc to isolate cluster stars relative to background stars. There is also a spectral type cut discarding stars later than K3. The Galactic background stars are removed particularly well from this cluster.

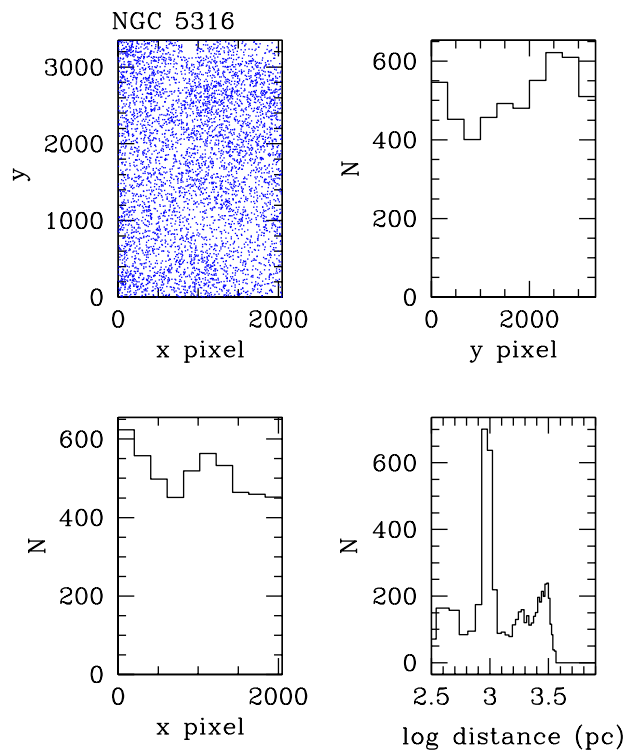


Figure 4.16: **Top left:** Spatial clustering in the field of NGC 5316, for all objects brighter than  $I = 18$ . **Top right:** y-axis histogram of objects detected in top left panel. **Bottom left:** x-axis histogram of objects detected in top left panel. **Bottom right:** Histogram of distances reported by photometric estimation of spectral types.

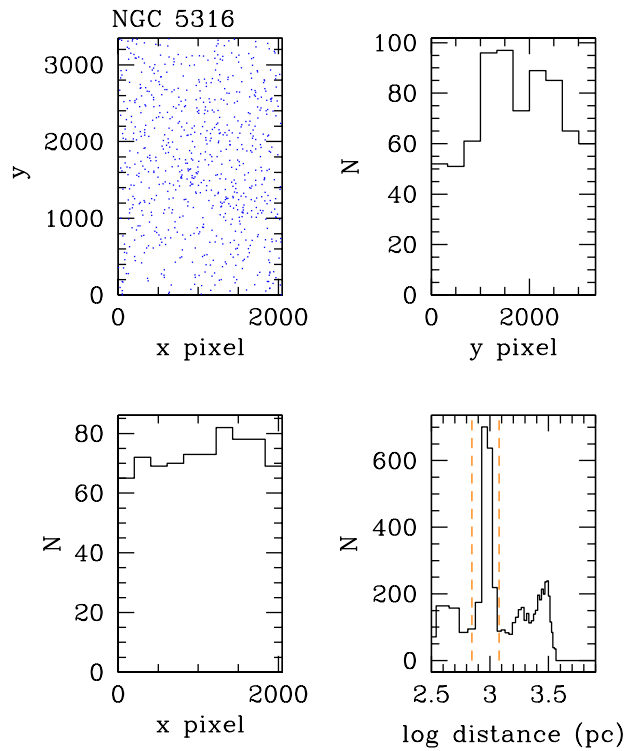


Figure 4.17: **Top left:** Spatial clustering in the field of NGC 5316, with distance cut of  $900 < d < 1300$  pc to isolate cluster stars relative to background stars. There is also a spectral type cut discarding stars later than K3. **Top right:** y-axis histogram of objects detected in top left panel. **Bottom left:** x-axis histogram of objects detected in top left panel. **Bottom right:** Histogram of distances reported by photometric estimation of spectral types. Dotted lines show the distance cut made.



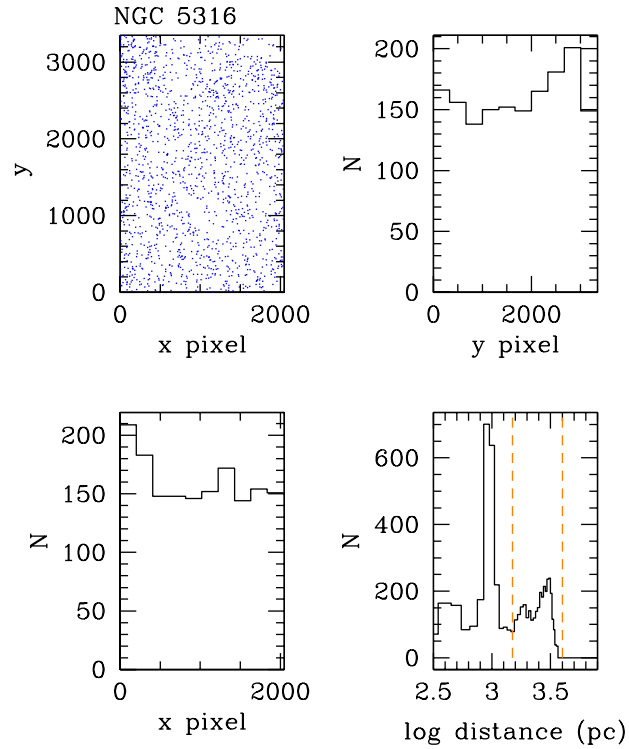


Figure 4.18: **Top left:** Spatial clustering in the field of NGC 5316, with distance cut of  $1500 < d < 4000$  pc to demonstrate that not many cluster stars are misclassified at distances farther than expected. There is also a spectral type cut discarding stars later than K3. **Top right:** y-axis histogram of objects detected in top left panel. **Bottom left:** x-axis histogram of objects detected in top left panel. **Bottom right:** Histogram of distances reported by photometric estimation of spectral types. Dotted lines show the distance cut made.

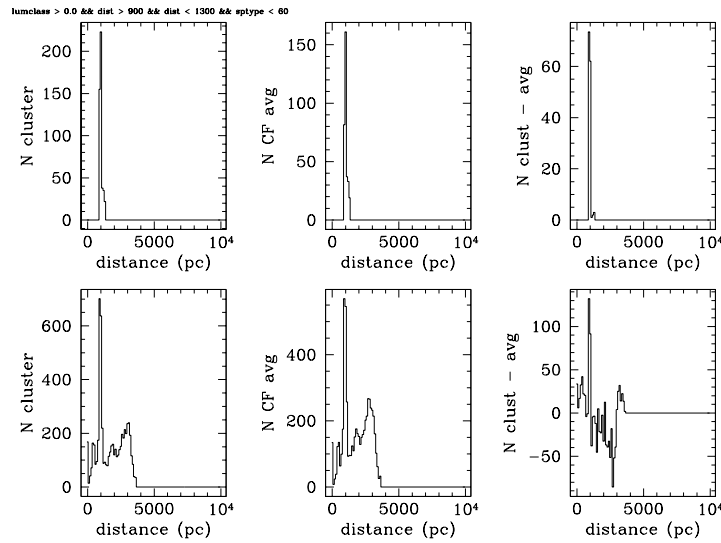


Figure 4.19: **Bottom left:** Histogram of distances from photometric spectral typing of all stars in the field of NGC 5316. **Bottom middle:** Average of the histograms of distances from photometric spectral typing of the two control fields for NGC 5316. **Bottom right:** Cluster histogram minus control field histogram, showing a peak of cluster stars. The trough is caused by misclassifications due to non-uniform reddening across the field. **Top left, middle, and right:** As their respective bottom panels, but considering only spectral types earlier than K0 and distances of  $900 < d < 1300$  pc.

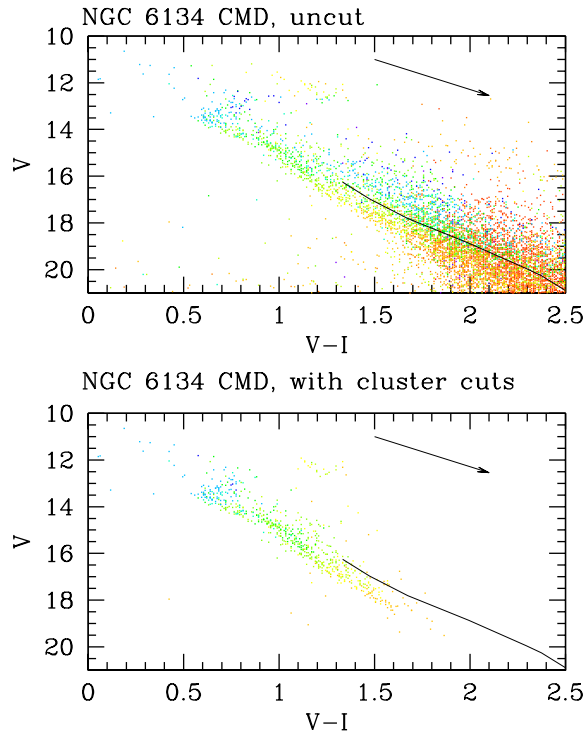


Figure 4.20: **Top:** CMD of NGC 6134, with no cuts on objects reported. The curved line overlaid at bottom is the predicted location of the lower main sequence (less than  $1 M_{\odot}$ ), using the BCAH98 models and the WEBDA properties of NGC 6134. **Bottom:** CMD of NGC 6134, with distance cut of  $500 < d < 1500$  pc to isolate cluster stars relative to background stars. There is also a spectral type cut discarding stars later than K3. The main sequence appears to be nicely cleaned by this cut.

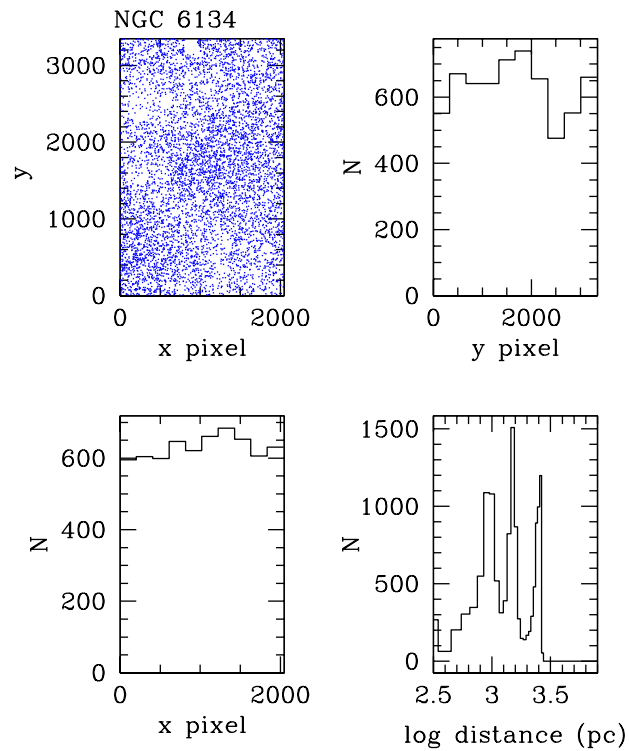


Figure 4.21: **Top left:** Spatial clustering in the field of NGC 6134, for all objects brighter than  $I = 18$ . **Top right:** y-axis histogram of objects detected in top left panel. **Bottom left:** x-axis histogram of objects detected in top left panel. **Bottom right:** Histogram of distances reported by photometric estimation of spectral types. Note the non-uniform distribution due to heavy dust lanes.

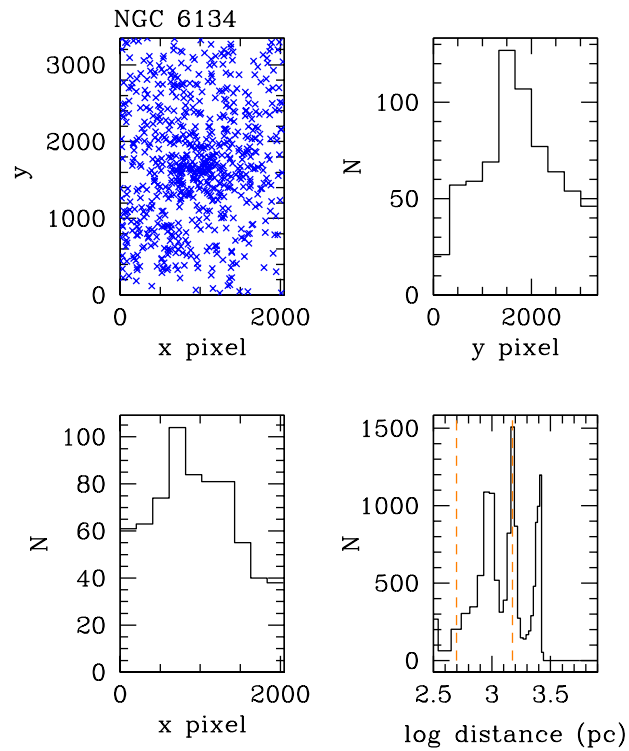


Figure 4.22: **Top left:** Spatial clustering in the field of NGC 6134, with distance cut of  $500 < d < 1500$  pc to isolate cluster stars relative to background stars. There is also a spectral type cut discarding stars later than K3. **Top right:** y-axis histogram of objects detected in top left panel. **Bottom left:** x-axis histogram of objects detected in top left panel. **Bottom right:** Histogram of distances reported by photometric estimation of spectral types. Dotted lines show the distance cut made.

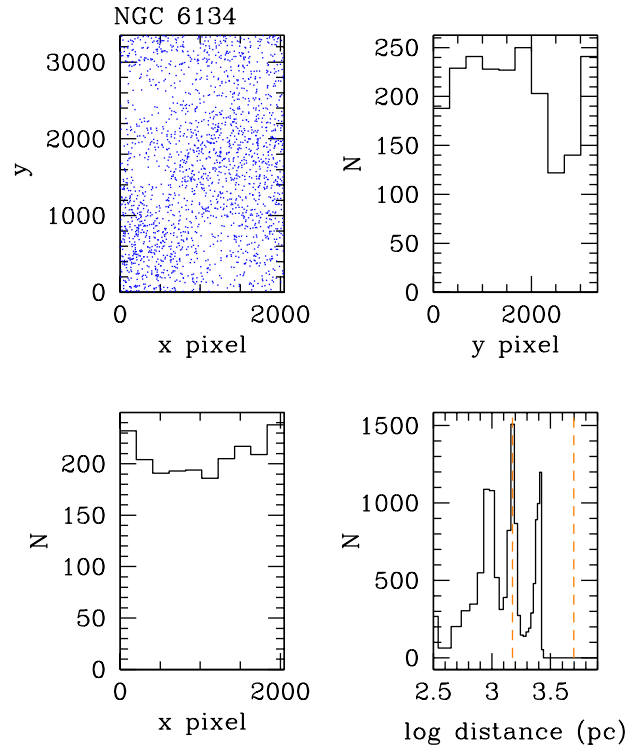


Figure 4.23: **Top left:** Spatial clustering in the field of NGC 6134, with distance cut of  $1500 < d < 5000$  pc to demonstrate that not many cluster stars are misclassified at distances farther than expected. There is also a spectral type cut discarding stars later than K3. **Top right:** y-axis histogram of objects detected in top left panel. **Bottom left:** x-axis histogram of objects detected in top left panel. **Bottom right:** Histogram of distances reported by photometric estimation of spectral types. Dotted lines show the distance cut made.

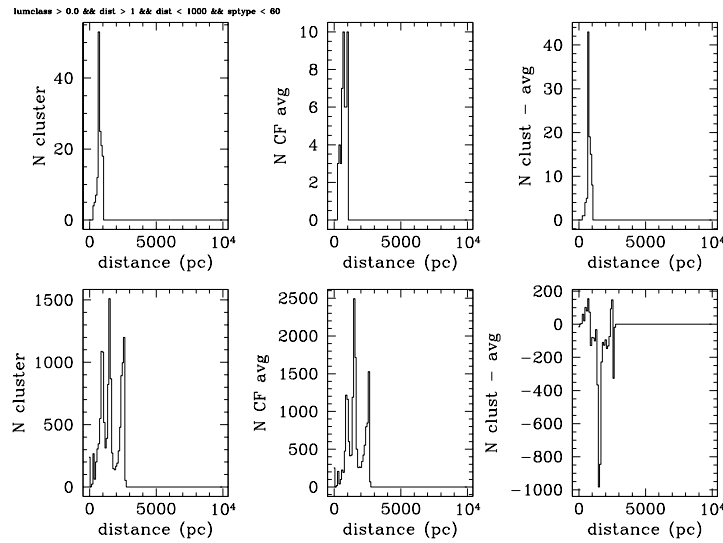


Figure 4.24: **Bottom left:** Histogram of distances from photometric spectral typing of all stars in the field of NGC 6134. **Bottom middle:** Average of the histograms of distances from photometric spectral typing of the two control fields for NGC 6134. **Bottom right:** Cluster histogram minus control field histogram, showing a peak of cluster stars. The trough is caused by misclassifications due to non-uniform reddening across the field. **Top left, middle, and right:** As their respective bottom panels, but considering only spectral types earlier than K0 and distances less than 1000 pc.

### 4.5.5 NGC 6208

NGC 6208 was our second observed cluster- the first for which we took control fields (NGC 2660 control fields were done the next season). We have full *BVRI* control fields for NGC 6208. This cluster is located in a very rich Galactic field, and the CMD exhibits one of the most prominent red clump populations of all the cluster fields. Unfortunately, this feature crosses over the expected main sequence, causing heavy contamination. Figure 4.25 shows the CMD with and without a  $500 < d < 1200$  pc distance cut, which does not clean the CMD quite as well as for other clusters.

Figure 4.26 shows the dense source count without any cuts. Figure 4.27 shows a central excess emerging after applying the  $500 < d < 1200$  pc distance cut. Figure 4.28 shows that the objects in a distance cut away from the cluster,  $1200 < d < 15000$  pc, are negligibly clustered.

Figure 4.29 compares the level of background objects (defined by the average of the control fields) to the level of cluster objects, for bright stars of  $V_{14}$ . However, because of the heavy Galactic domination of this field, we find that the control fields actually contain larger numbers of objects at any fainter  $V$  magnitudes.

### 4.5.6 NGC 6253

NGC 6253 also has a prominent Galactic red clump feature and strong Galactic main sequence. However, the cluster is more concentrated than NGC 6208, and clearly shows up once a distance cut is applied. Figure 4.30 shows how a fair amount of the Galactic background remains after a fairly tight distance cut of  $700 < d < 1300$ . Yet, this is offset by clustering which is even slightly visible in the uncut spatial position information seen in Figure 4.31. The clustering is obvious once the distance cut is applied in Figure 4.32. Figure 4.33 shows a relatively uniform field of objects at derived distances  $1300 < d < 15000$  pc.

Figure 4.34 compares the level of background objects (defined by the average of the control fields) to the level of cluster objects. Of all eight clusters presented here, NGC 6253 has the strongest clustering signal, at several hundred stars, after background subtraction.



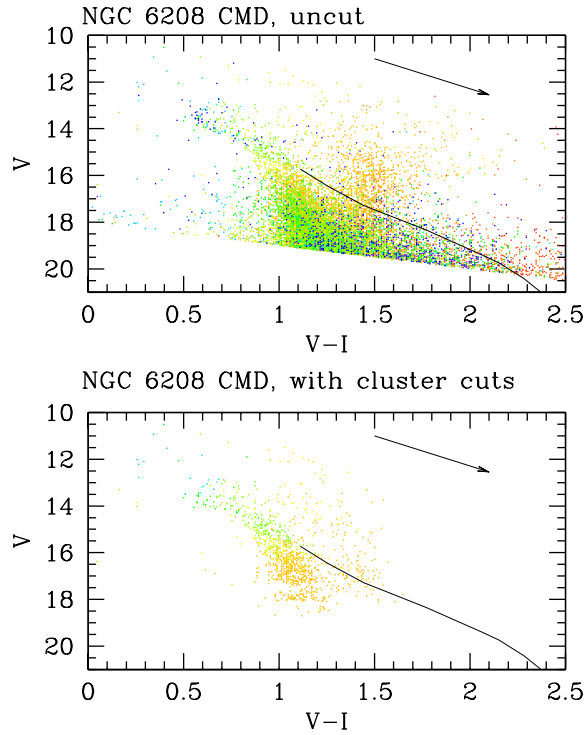


Figure 4.25: **Top:** CMD of NGC 6208, with no cuts on objects reported other than an  $I = 18$  limit. The curved line overlaid at bottom is the predicted location of the lower main sequence (less than  $1 M_{\odot}$ ), using the BCAH98 models and the WEBDA properties of NGC 6208. **Bottom:** CMD of NGC 6208, with distance cut of  $500 < d < 1200$  pc to isolate cluster stars relative to background stars. There is also a spectral type cut discarding stars later than K3. The Galactic background is very prominent in this cluster.

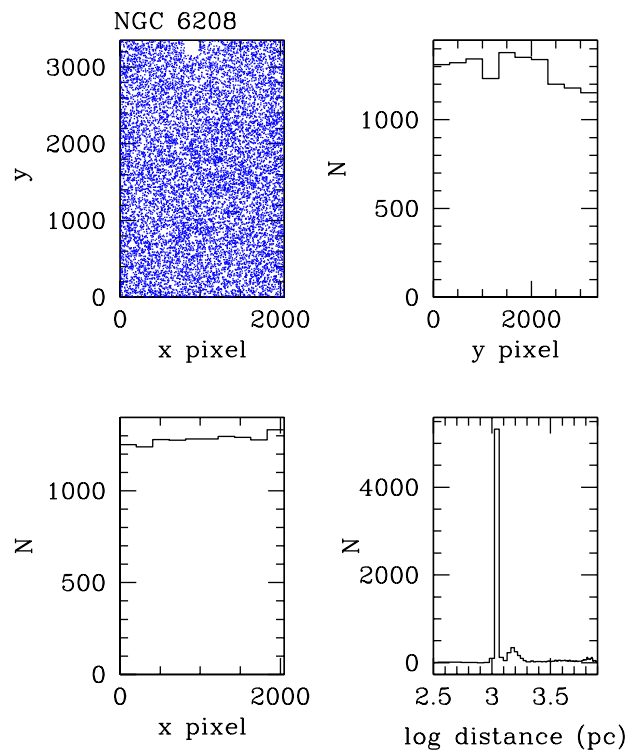


Figure 4.26: **Top left:** Spatial clustering in the field of NGC 6208, for all objects brighter than  $I = 18$ . **Top right:** y-axis histogram of objects detected in top left panel. **Bottom left:** x-axis histogram of objects detected in top left panel. **Bottom right:** Histogram of distances reported by photometric estimation of spectral types.

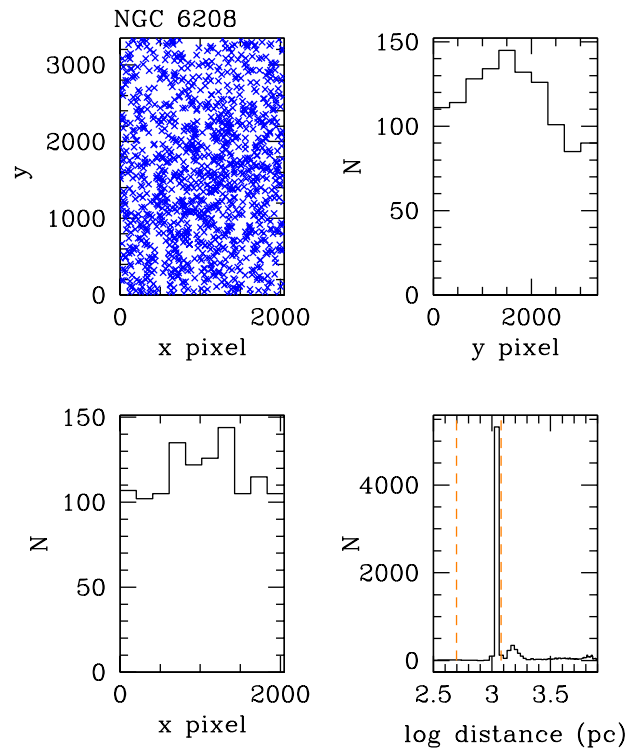


Figure 4.27: **Top left:** Spatial clustering in the field of NGC 6208, with distance cut of  $500 < d < 1200$  pc to isolate cluster stars relative to background stars. There is also a spectral type cut discarding stars later than K3. **Top right:** y-axis histogram of objects detected in top left panel. **Bottom left:** x-axis histogram of objects detected in top left panel. **Bottom right:** Histogram of distances reported by photometric estimation of spectral types. Dotted lines show the distance cut made.

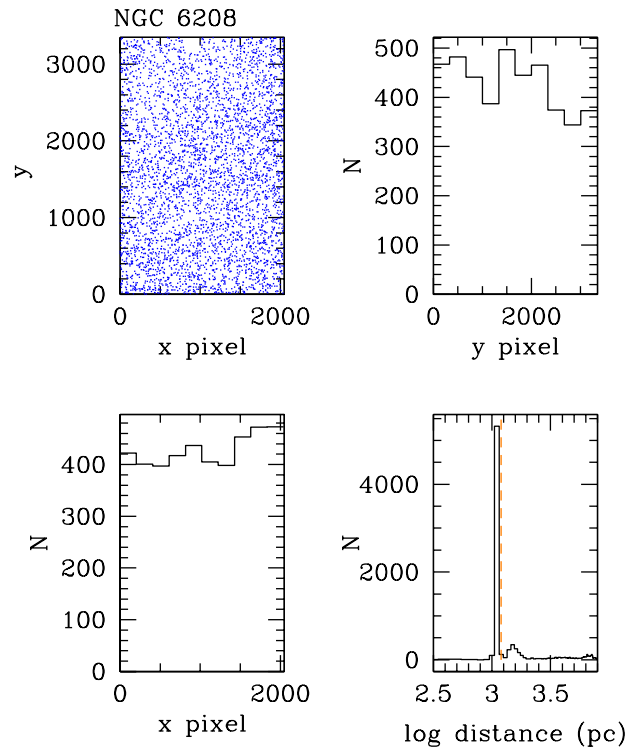


Figure 4.28: **Top left:** Spatial clustering in the field of NGC 6208, with distance cut of  $1200 < d < 15000$  pc to demonstrate that not many cluster stars are misclassified at distances farther than expected. There is also a spectral type cut discarding stars later than K3. **Top right:** y-axis histogram of objects detected in top left panel. **Bottom left:** x-axis histogram of objects detected in top left panel. **Bottom right:** Histogram of distances reported by photometric estimation of spectral types. Dotted lines show the distance cut made.

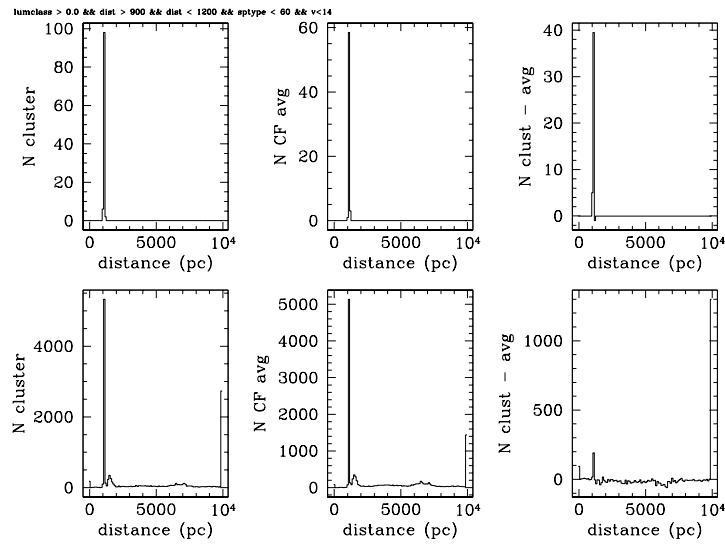


Figure 4.29: **Bottom left:** Histogram of distances from photometric spectral typing of all stars in the field of NGC 6208. **Bottom middle:** Average of the histograms of distances from photometric spectral typing of the two control fields for NGC 6208. **Bottom right:** Cluster histogram minus control field histogram, showing a small peak of cluster stars. **Top left, middle, and right:** As their respective bottom panels, but considering only spectral types earlier than K3 and distances  $900 < d < 1200$ .

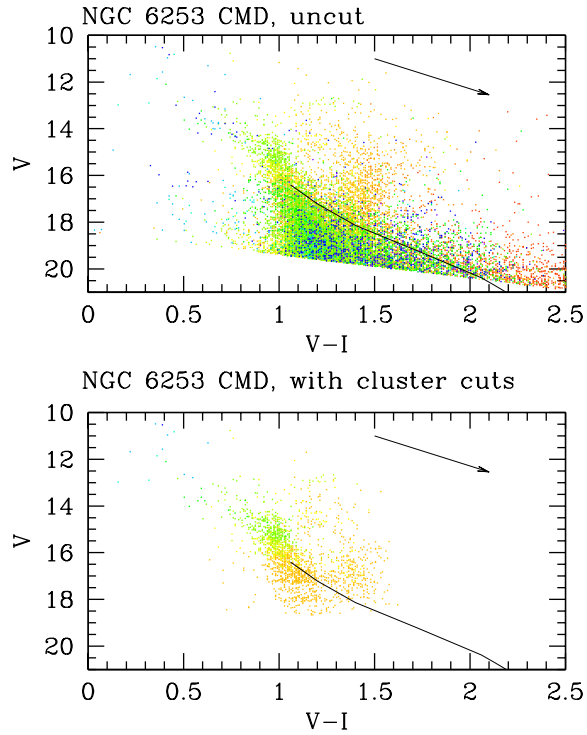


Figure 4.30: **Top:** CMD of NGC 6253, with no cuts on objects reported, other than a limit at  $I = 18$ . The curved line overlaid at bottom is the predicted location of the lower main sequence (less than  $1 M_{\odot}$ ), using the BCAH98 models and the WEBDA properties of NGC 6253. **Bottom:** CMD of NGC 6253, with distance cut of  $700 < d < 1300$  pc to isolate cluster stars relative to background stars. There is also a spectral type cut discarding stars later than K3. The Galactic background stars are removed particularly well from this cluster.

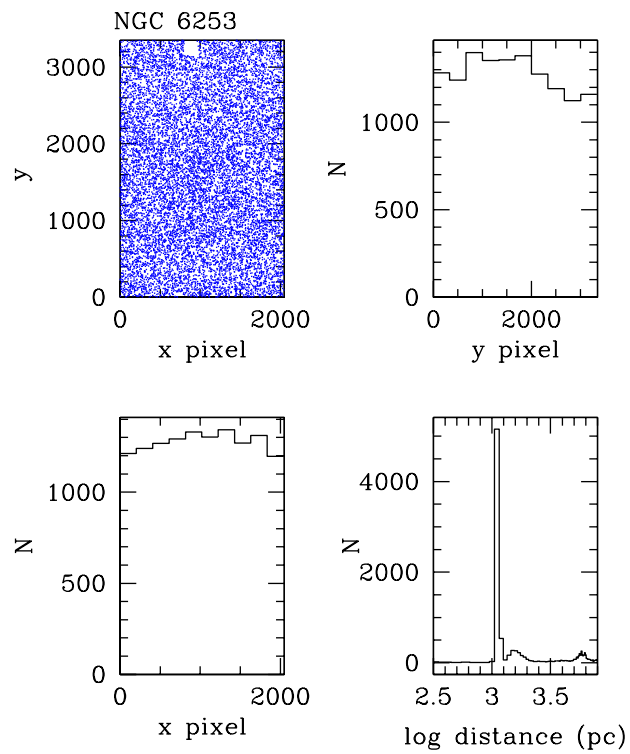


Figure 4.31: **Top left:** Spatial clustering in the field of NGC 6253, for all objects brighter than  $I = 18$ . **Top right:** y-axis histogram of objects detected in top left panel. **Bottom left:** x-axis histogram of objects detected in top left panel. **Bottom right:** Histogram of distances reported by photometric estimation of spectral types.

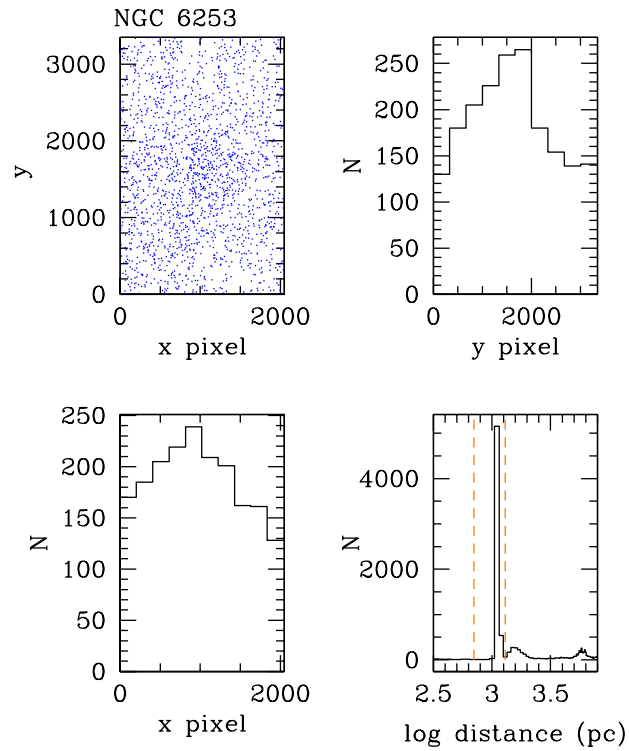


Figure 4.32: **Top left:** Spatial clustering in the field of NGC 6253, with distance cut of  $700 < d < 1300$  pc to isolate cluster stars relative to background stars. There is also a spectral type cut discarding stars later than K3. Central clustering is quite visible. **Top right:** y-axis histogram of objects detected in top left panel. **Bottom left:** x-axis histogram of objects detected in top left panel. **Bottom right:** Histogram of distances reported by photometric estimation of spectral types. Dotted lines show the distance cut made.



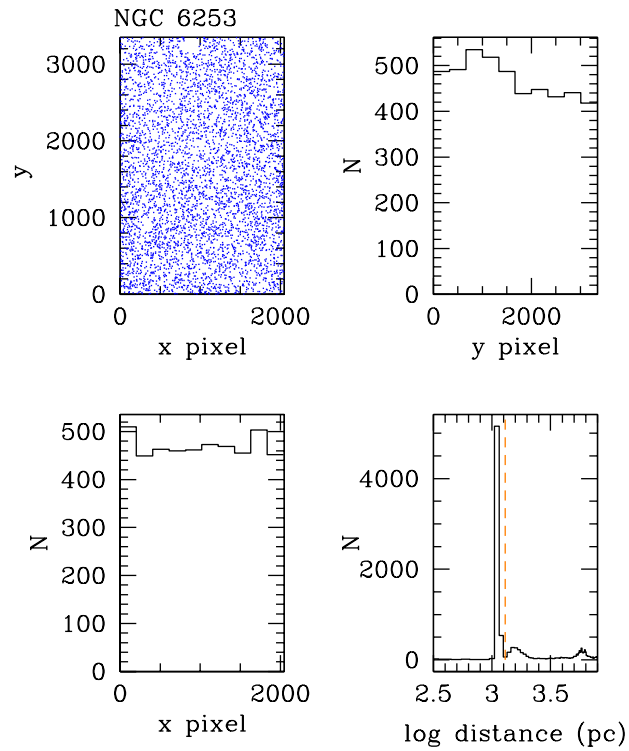


Figure 4.33: **Top left:** Spatial clustering in the field of NGC 6253, with distance cut of  $1300 < d < 15000$  pc to demonstrate that not many cluster stars are misclassified at distances farther than expected. There is also a spectral type cut discarding stars later than K3. **Top right:** y-axis histogram of objects detected in top left panel. **Bottom left:** x-axis histogram of objects detected in top left panel. **Bottom right:** Histogram of distances reported by photometric estimation of spectral types. Dotted lines show the distance cut made.

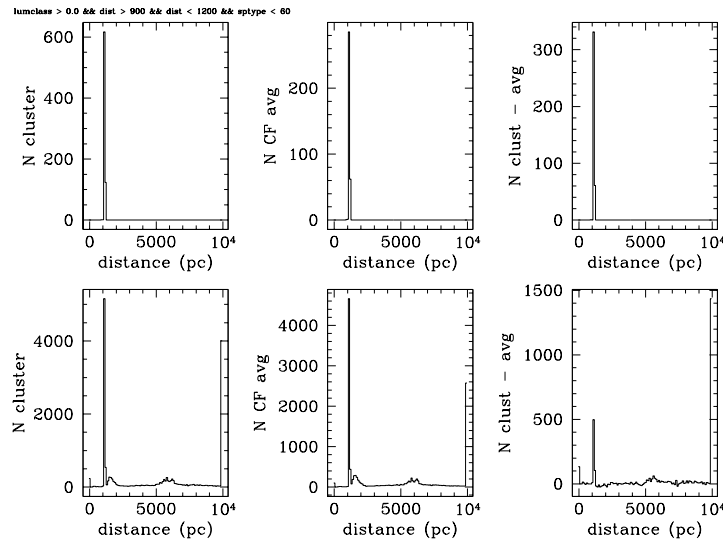


Figure 4.34: **Bottom left:** Histogram of distances from photometric spectral typing of all stars in the field of NGC 6253. **Bottom middle:** Average of the histograms of distances from photometric spectral typing of the two control fields for NGC 6253. **Bottom right:** Cluster histogram minus control field histogram, showing a peak of cluster stars. A very clear cluster peak is visible after subtraction. **Top left, middle, and right:** As their respective bottom panels, but considering only spectral types earlier than K3 and distances  $900 < d < 1200$  pc.

### 4.5.7 IC 2714

IC 2714 was another one of the few target choices available in March and April. As it only has control field images in full  $VI$ , we augmented our photometry with 2MASS  $JHK$ . Catalogue matching yielded 6290 objects with  $VIJHK$ , out of 7464 objects in the brighter than  $I = 18.5$ . The cluster is on a sight line 70 degrees away in longitude from the Galactic Centre, so Galactic background is not as severe as for NGC 6208 and NGC 6253. However, the cluster main sequence does lie on top of the background main sequence, as seen in Figure 4.35.

Figure 4.36, a map of the field with no cuts, shows no clustering in the centre of the field. A distance cut  $500 < d < 1000$  pc selects objects which are preferentially clustered towards the centre, seen in Figure 4.37. A distance cut to investigate objects beyond the cluster,  $1000 < d < 5000$  pc (Figure 4.38), reveals no visible clustering.

Figure 4.39 compares the level of background objects (defined by the average of the control fields) to the level of cluster objects. A solid cluster overdensity is visible.

### 4.5.8 IC 4651

IC 4651 shows Galactic background contamination, though with less density than NGC 6208 and NGC 6253, as seen in the CMDs in Figure 4.40. Although none of Figure 4.41 (no cuts), Figure 4.42 (cluster distance cut  $d < 1000$  pc), or Figure 4.43 show obvious clustering, subtracting off the background measured by the control fields (Figure 4.44) does show a cluster peak near 1000 pc.

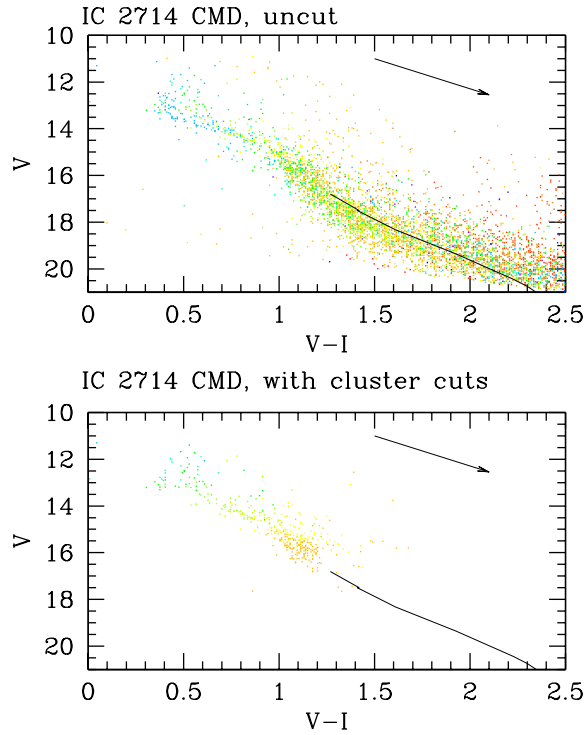


Figure 4.35: **Top:** CMD of IC 2714, with no cuts on objects reported, other than a limit at  $I = 18$ . The curved line overlaid at bottom is the predicted location of the lower main sequence (less than  $1 M_{\odot}$ ), using the BCAH98 models and the WEBDA properties of IC 2714. **Bottom:** CMD of IC 2714, with distance cut of  $500 < d < 1000$  pc to isolate cluster stars relative to background stars. There is also a spectral type cut discarding stars later than K3. The Galactic background stars are removed particularly well from this cluster.

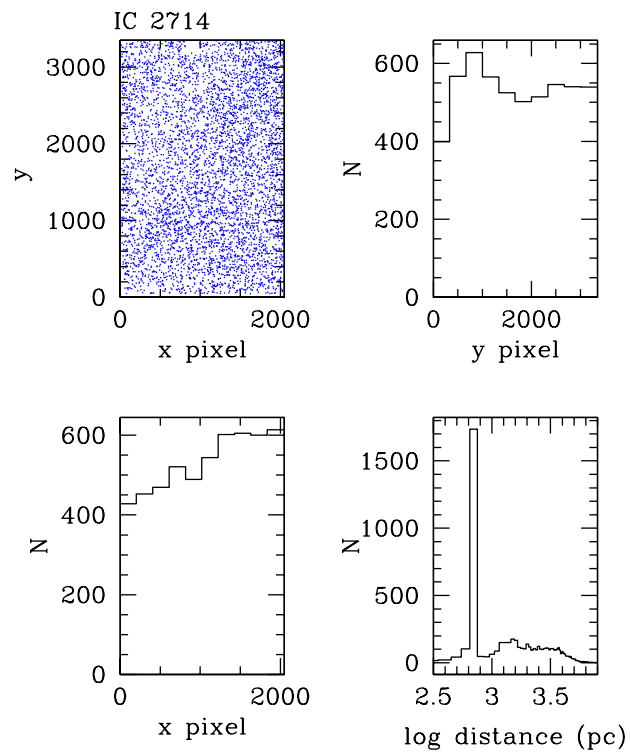


Figure 4.36: **Top left:** Spatial clustering in the field of IC 2714, for all objects brighter than  $I = 18$ . **Top right:** y-axis histogram of objects detected in top left panel. **Bottom left:** x-axis histogram of objects detected in top left panel. **Bottom right:** Histogram of distances reported by photometric estimation of spectral types.

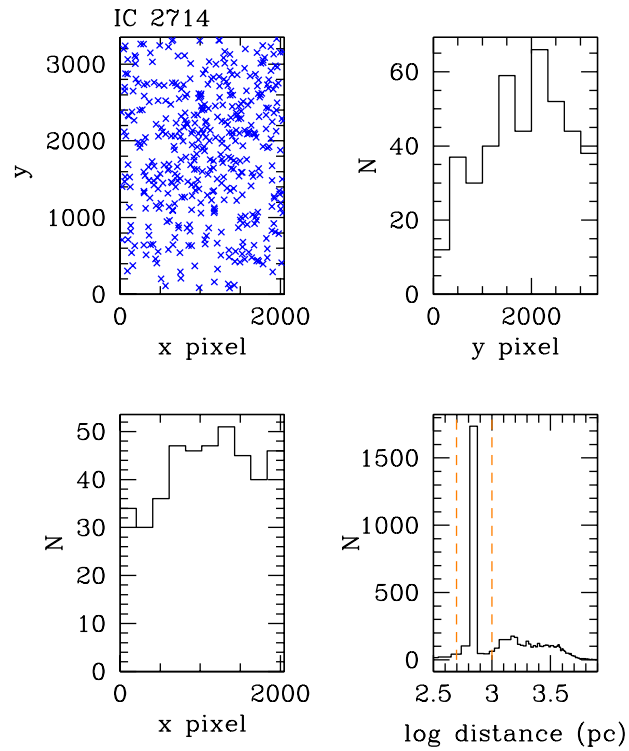


Figure 4.37: **Top left:** Spatial clustering in the field of IC 2714, with distance cut of  $500 < d < 1000$  pc to isolate cluster stars relative to background stars. There is also a spectral type cut discarding stars later than K3. Light central clustering is visible. **Top right:** y-axis histogram of objects detected in top left panel. **Bottom left:** x-axis histogram of objects detected in top left panel. **Bottom right:** Histogram of distances reported by photometric estimation of spectral types. Dotted lines show the distance cut made.

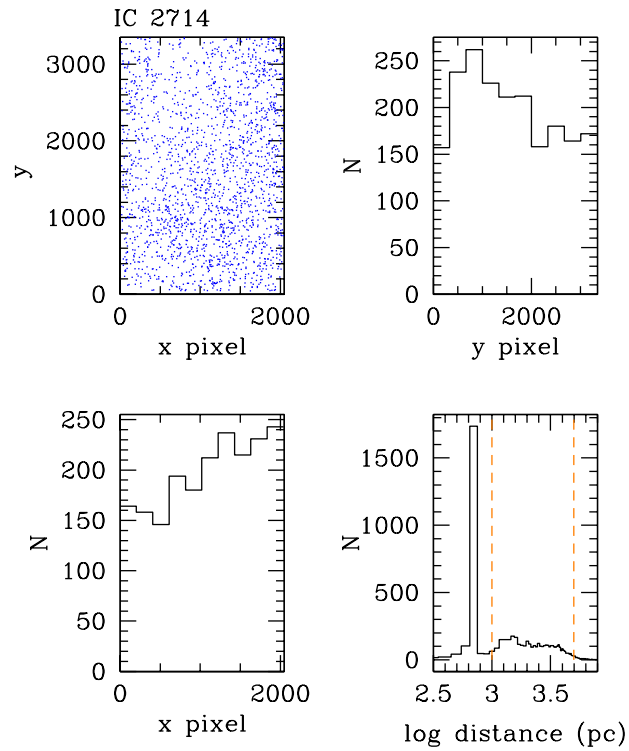


Figure 4.38: **Top left:** Spatial clustering in the field of IC 2714, with distance cut of  $1000 < d < 5000$  pc to demonstrate that not many cluster stars are misclassified at distances farther than expected. There is also a spectral type cut discarding stars later than K3. **Top right:** y-axis histogram of objects detected in top left panel. **Bottom left:** x-axis histogram of objects detected in top left panel. **Bottom right:** Histogram of distances reported by photometric estimation of spectral types. Dotted lines show the distance cut made.

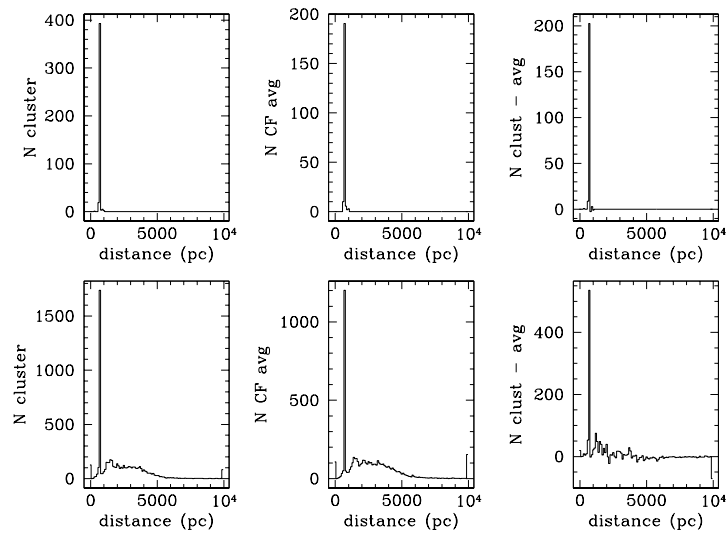


Figure 4.39: **Bottom left:** Histogram of distances from photometric spectral typing of all stars in the field of IC 2714. **Bottom middle:** Average of the histograms of distances from photometric spectral typing of the two control fields for IC 2714. **Bottom right:** Cluster histogram minus control field histogram, showing a peak of cluster stars. **Top left, middle, and right:** As their respective bottom panels, but considering only spectral types earlier than K3 and distances less than 1000 pc.



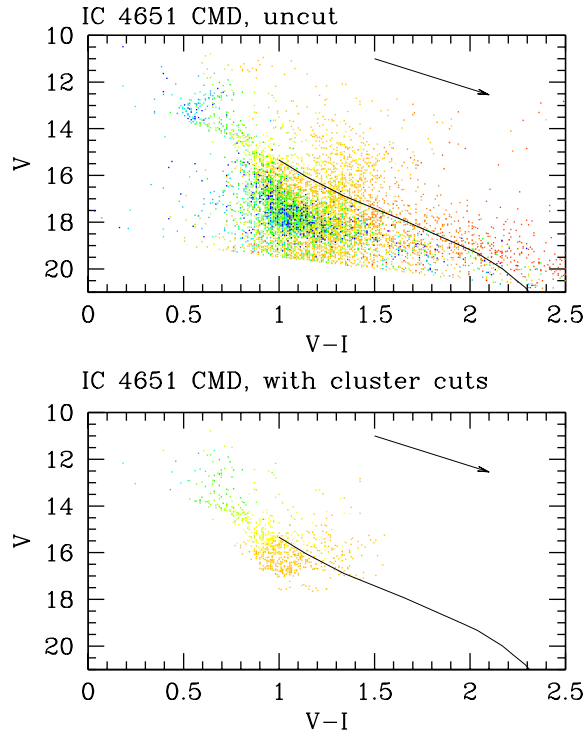


Figure 4.40: **Top:** CMD of IC 4651, with no cuts on objects reported, other than a limit at  $I = 18$ . The curved line overlaid at bottom is the predicted location of the lower main sequence (less than  $1 M_{\odot}$ ), using the BCAH98 models and the WEBDA properties of IC 4651. **Bottom:** CMD of IC 4651, with distance cut of  $d < 1000$  pc to isolate cluster stars relative to background stars. There is also a spectral type cut discarding stars later than K3. The Galactic background stars are removed particularly well from this cluster.

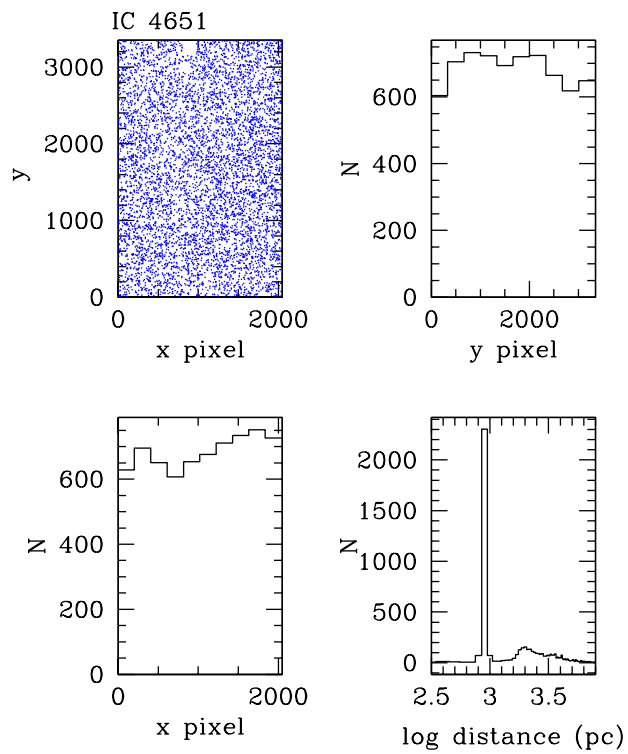


Figure 4.41: **Top left:** Spatial clustering in the field of IC 4651, for all objects brighter than  $I = 18$ . **Top right:** y-axis histogram of objects detected in top left panel. **Bottom left:** x-axis histogram of objects detected in top left panel. **Bottom right:** Histogram of distances reported by photometric estimation of spectral types.

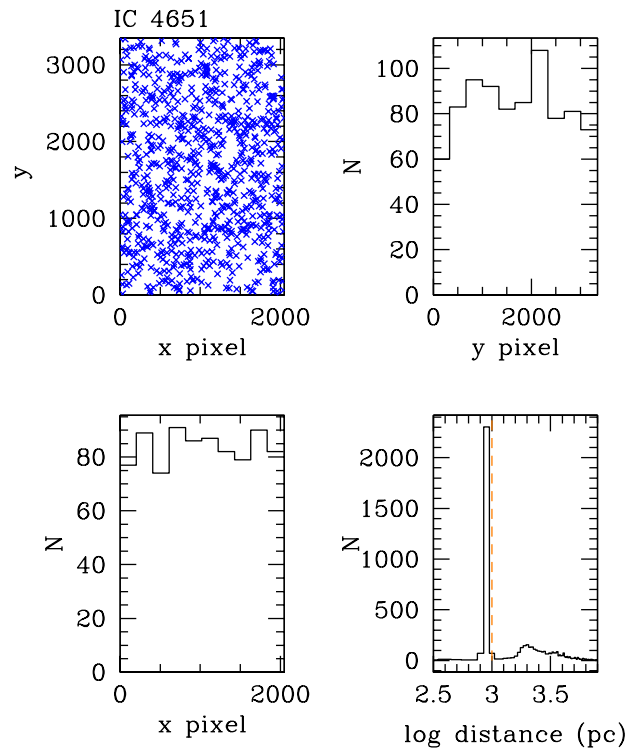


Figure 4.42: **Top left:** Spatial clustering in the field of IC 4651, with distance cut of  $d < 1000$  pc to isolate cluster stars relative to background stars. There is also a spectral type cut discarding stars later than K3. Still, no obvious clustering is visible. **Top right:** y-axis histogram of objects detected in top left panel. **Bottom left:** x-axis histogram of objects detected in top left panel. **Bottom right:** Histogram of distances reported by photometric estimation of spectral types. Dotted lines show the distance cut made.

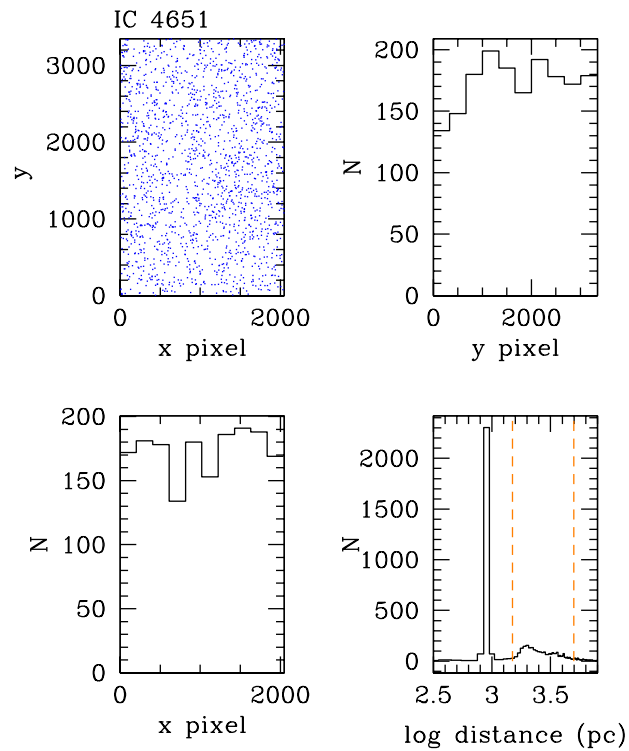


Figure 4.43: **Top left:** Spatial clustering in the field of IC 4651, with distance cut of  $1500 < d < 5000$  pc to search for cluster stars misclassified to large distances. **Top right:** y-axis histogram of objects detected in top left panel. **Bottom left:** x-axis histogram of objects detected in top left panel. **Bottom right:** Histogram of distances reported by photometric estimation of spectral types. Dotted lines show the distance cut made.

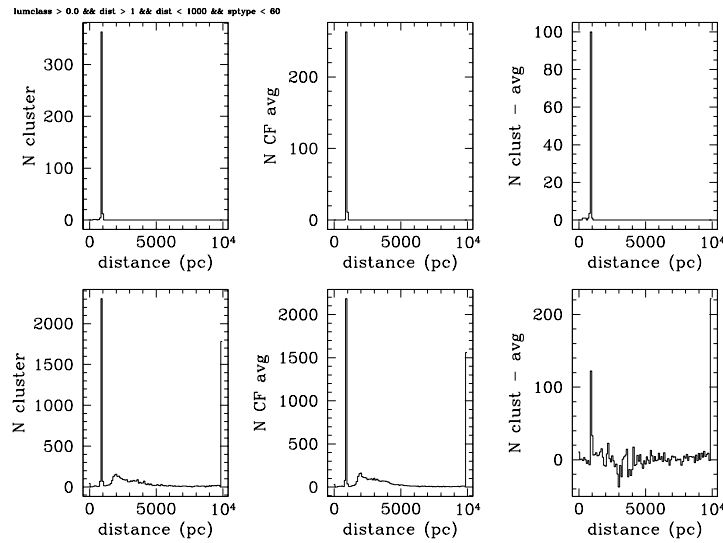


Figure 4.44: **Bottom left:** Histogram of distances from photometric spectral typing of all stars in the field of IC 4651. **Bottom middle:** Average of the histograms of distances from photometric spectral typing of the two control fields for IC 4651. **Bottom right:** Cluster histogram minus control field histogram, showing a peak of cluster stars. The trough is caused by misclassifications due to non-uniform reddening across the field. **Top left, middle, and right:** As their respective bottom panels, but considering only spectral types earlier than K0 and distances less than 1000 pc.

# Chapter 5

## Planet Transit Candidates and Statistics

### 5.1 Introduction

In this chapter, we extract planet transit-like light curves from the high-precision light curves we derived, as described in Chapter 3, for stars in our observed fields. The precision and consecutive time-sampling strategy we employ, as detailed in Chapter 2, makes interesting variability events clear even in unphased plots of our light curves. The variability time scales for planet transit events are of order hours- an order of magnitude greater than our observing cadence.

Armed with such a high level of detail, it is easy to visually examine the quality of our light curves. We observe that there can be non-periodic small-amplitude (of order 1%) flux decrements, often asymmetric, and often inconsistent with the typical shapes of eclipses or stellar pulsations. These correlated systematic uncertainties surely affect the performance of various options for finding variability, which are in general tested only on light curves free of correlated systematic uncertainties. In the process of extracting our planet transit candidates and other interesting variables, we investigate the relative performance of various automated variable-finding techniques. We use these automated finding techniques to rank our light curves by the strength of their variability detection figures of merit. Then, we verify by eye whether they are robust variables.

Finally, we examine our low-amplitude eclipsing systems, and discuss which are the most robust planet candidates, using the unique solution equations of (Seager & Mallén-Ornelas 2003). We show that this number of candidates is consistent with the expecta-

tions established from radial velocity planet searches.

## 5.2 Algorithms for variable finding

### 5.2.1 Lomb-Scargle periodogram

The Lomb-Scargle periodogram (Lomb 1976; Scargle 1982) is used to perform a Fourier analysis of the frequencies present in a time series when the data are unevenly sampled. Appropriate modifications to the classical periodogram (which is the square of the Discrete Fourier Transform of the time series, divided by the number of data points) in order to give the periodogram a straightforward statistical interpretation are described in Scargle 1982. A peak in the periodogram at some frequency then indicates a periodic signal in the time series at that frequency, and the height of the peak represents the significance of the detection. We use an implementation of the Lomb-Scargle periodogram by D. Nguyen (private communication).

### 5.2.2 Phase Dispersion Minimization

Phase Dispersion Minimization (PDM; Stellingwerf 1978) is a trial-and-error method which steps through a set of possible values for the period and discovers which period yields the highest quality phase-folded light curve. The quality of the light curve is defined as the variance of the data with respect to the mean light curve, where the mean light curve is calculated piecewise by splitting the light curve into a number of bins. The figure of merit for detection of the correct period is the sum of the variances in the individual bins (normalized according to the number of data points and the number of bins) divided by the variance of the light curve as a whole. If the trial period is not a true period, then the variances in the individual bins will be the same as the variance of the light curve as a whole, and the figure of merit evaluates to 1. Lower values for the figure of merit correspond to more significant detections of a periodicity in the time series. We use an implementation of PDM by D. Nguyen (private communication).

### 5.2.3 Box-fitting Least Squares

The Box-fitting Least Squares (BLS) algorithm (Kovacs et al. 2002) is designed to use the *a priori* knowledge that the best planet transit signals are box-shaped flux decrements with a low duty cycle. The algorithm assumes the light curve takes on only two levels, and

performs a least-squares fit for the period, length of eclipse, epoch of eclipse, and depth of eclipse. The figure of merit is related to the improvement in the fit when assuming a transit has occurred. The BLS algorithm is suited for picking up small planet transit signals in light curves with white noise, but may not perform as well in detecting other kinds of variability which are not box-shaped.

### 5.2.4 Correlation

Tingley (2002) finds that a simple correlation is highly competitive relative to other planet transit detection methods. We slightly modify the technique to increase its robustness. Similar to a matched-filter implementation (which cross-correlates a set of model templates with the data, attempting to find the best match template at the best temporal lag), our new method operates by using a time-reversed, resampled version of the original light curve as the model template to be matched with the data (mathematically, this is precisely an autoconvolution). Thus this method automatically correlates the correct template for any form of symmetric variability, eliminating the usual time-consuming search over variability parameters for the template (which, if too coarse or restricted, may not even yield a good match). Also, since photometry systematics are, in general, quite asymmetric and aperiodic, they tend not to correlate with time-reversed versions of themselves, and are significantly filtered by this scheme. The tradeoff compared with a matched-filter implementation is that our “template” is noisy, rather than a perfect model- in the case of infinite CPU resources, a matched-filter should outperform a correlation.

Note that a flat light curve does correlate well with itself. Therefore, the basic metric of the correlation must use the scatter of the light curve to help decide whether a good match between the time-forward and time-backward series indicates variability. Essentially, one wishes to compare the goodness of the model fit to the goodness of fitting a non-varying light curve. We implement this comparison by including a denominator that will correct for flat light curve detection. Equation 5.1 gives the figure of merit used,

$$M = \frac{\sum_{i=1}^N [(y_{data_i}) - (y_{model_i}(\text{lag} = \tau))]^2}{N \frac{\sigma_{data}^2 + \sigma_{model}^2}{2}}. \quad (5.1)$$

where the  $y$  values are the deviations from the light curve mean or median (the median is a cleaner choice in the presence of systematics) for the data light curve and time-reversed



model light curve,  $N$  is the number of points being compared between the data and model,  $\sigma$  is the rms scatter of a light curve about the mean or median, and  $\tau$  is a trial offset in time between the data and the model. Note that the best trial offset does not indicate where in the light curve the variability occurs- this method is purely a variability detector, not a parameter estimator.

Experimentation showed that the power of the statistic could be washed out by poor quality nights if calculated over the whole run at once. In our final implementation, we calculate our correlation statistic for each possible pair of nights, rather than over the whole run, in order to restrict the noise to outliers. We can then rank the light curves for repeating signals, based on the lowest correlation statistic achieved on any pair of nights.

### 5.3 Visual examination

We examined light curves by eye to detect all forms of variability. In each cluster, we searched all stars with rms scatter better than 2%, and also all stars with magnitudes  $I < 18$ . This magnitude criterion was chosen because stars of that magnitude or brighter should yield better than 2% photometric precision in the absence of systematic errors. One must include these bright stars because there may be high quality light curves with large amplitude, high duty cycle variability, and the rms scatter on these variable star light curves would be high.

Typically, this sample consisted of order  $\sim 10000$  light curves per cluster. We plotted the light curves on a real-time axis, and with an initial vertical scale typically 0.14 relative flux units wide. The vertical scale was adjusted after viewing the range of variation of the light curve, since contact binaries and large amplitude detached eclipsing binaries typically had amplitudes of tens of percent.

In order to maximize our efficiency in scanning through light curves, we ranked them using one of our automated statistics. We chose to use the correlation statistic. This brought most of the contact binary light curves to the top of the ranked list, as a Lomb-Scargle analysis would do, but also ranked highly many of the short period, highest amplitude eclipsing binaries which a Lomb-Scargle algorithm would have more difficulty detecting. By examining a ranked list, we minimize the possibility of missing variable objects due to fatigue.

For each variable object detected, its type is noted in a file for later automated reading during catalogue sorting and extraction operations. We use three broad classifications: detached (or semi-detached) eclipsing binaries, contact binaries, and other

variables. Contact binaries were picked out by looking for very smooth, rounded maxima with no discontinuity in slope marking the outer contact during ingress and egress.  $\delta$  Scuti pulsators are easy to recognize in real-time light curves because their multi-periodic pulsations give rise to beat frequencies (but such a multiperiodic light curve is difficult to identify by automated methods). Large amplitude RR Lyrae stars were easily recognized from their asymmetric light curve shapes. Light curves with short maxima and long minima, such as  $\alpha^2$  Canum Venaticorum stars, were generally distinguishable from contact binary light curves, but when in doubt, any noisy sinusoidal variable with a period of around half a day would generally be classified as a contact binary. If there was asymmetry in the light curve, it would be classified as a miscellaneous variable.

## 5.4 Detection threshold

Lee et al. (2003) tested the detectability by eye of transit signals in EXPLORE data. Simulated transits were injected into real data from the EXPLORE project for the test. The simulations were inserted at the image level, to ensure that all systematic errors introduced by the photometric pipeline would appear in the simulated light curves. 990 simulated light curves containing 288 transits were used to test three visual examiners. The result was that 100% detection completeness is reached for signals  $\sim 2.5$  times deeper than the rms scatter in the light curve (specifically, a light curve with rms scatter 0.004 mag was required to be 100% sure of recovering a 1% deep transit).

## 5.5 Relative performance of automated algorithms

In this section, we test our various algorithms against the variable star detections and classifications we gleaned from visual inspection. As our test sample, we use  $\sim 13000$  light curves from NGC 6208. The light curves either have rms scatter about the mean less than 2%, or come from stars with magnitudes  $14 < I < 18$ , which are expected to show better than 2% precision. Figures 5.1, 5.2, and 5.3 show the relative performances of our different variability detection measures. These figures of merit were derived from running the four variable finding programs presently in the EXPLORE arsenal, as described in §5.2.

Lomb-Scargle and PDM are two of the most common general-purpose variability detection methods in use, so we compare them together in Figure 5.1. We see that Lomb-Scargle performs similarly to PDM. The PDM statistic decreases nearly linearly as

the Lomb-Scargle statistic increases (low PDM statistic and high Lomb-Scargle power indicating variability). Contact binaries, in particular, are quite well detected by both algorithms. Lomb-Scargle does discard some chaff that PDM rates as variable, so we compare the remainder of our variable-finding techniques with Lomb-Scargle.

We compare the Lomb-Scargle power to the SDE figure of merit for the BLS algorithm in Figure 5.2. The figure shows that BLS does not do a good job of separating out the non-boxy contact binaries, in contrast to Lomb-Scargle, but does sort detached binaries to significant figures of merit. The recommended threshold in Kovacs (2002) for considering an object to be variable is 6. However, the contamination by non-variables in the BLS variability ranking scheme is high, with a very large cloud of non-variable data points well above the recommended threshold.

Finally, we compare the Lomb-Scargle power to the correlation figure of merit in Figure 5.3. Low values of the correlation statistic indicate variability, with a statistic of 1 indicating that the variability detection is no better than a straight line. Low-amplitude ( $< 10\%$  deep eclipse) objects are not well detected by either Lomb-Scargle or correlation, but correlation in general manages to pull more variables out from the non-variable population. Note how the combination of more than one detection method here has the potential to provide more variable detections than either one, with a reduced false positive rate.

We show the performance of each statistic separately in Figures 5.4, 5.5, 5.6, and 5.7, and show some performance metrics derived from the histograms in Tables 5.1, 5.2, and 5.3. We plot histograms that show how well the different statistics differentiate between variable objects and non-variable objects. We investigate three kinds of variable objects: contact binaries, detached eclipsing binaries, and small-amplitude eclipsing objects.

Figure 5.4 shows the performance of the Lomb-Scargle algorithm. It does a fairly good job of separating the contact binaries from the non-varying light curves. It is unable to separate half of the detached eclipsing binaries from the bulk of the flat light curves, and loses four out of five low amplitude objects.

Figure 5.5 shows the performance of the PDM algorithm. As noted from the plot of PDM statistic together with the Lomb-Scargle statistic, it performs only slightly worse than Lomb-Scargle. Many contact binaries are well-separated from flat light curves, while over half of the detached binaries have PDM values similar to flat light curves.

BLS performance quantified by the SDE statistic is shown in Figure 5.6. BLS has a very difficult time separating contact binaries to any useful degree from flat light curves. Detached eclipsing binaries are better separated, but about half of detached eclipsing

binary population overlaps with the flat light curve population.

Figure 5.7 shows the performance of the correlation algorithm. Contact binaries are exceptionally well distinguished from flat light curves compared to all other techniques. Detached eclipsing binaries still suffer overlap with the flat light curve distribution, although one low amplitude object is relatively cleanly detected.

None of our methods, then, are perfectly clean, and visual examination outperformed the automated detectors. What is of interest is therefore by what level we can use these algorithms to at least reduce the work required for visual examination. One can envision making a threshold cutoff at some value of the statistic which will limit the amount of contamination from flat light curves while retaining a large fraction the truly variable objects. This balance between the tolerable percentage of false positives and the detection completeness can only be picked according to one's own data, depending on how crucial completeness is, and how many objects would have to be visually examined at a given false positive rate. Tables 5.1, 5.2, and 5.3 show this balance numerically. For statistic thresholds giving 10% false positives, 50% false positives, and 99% false positives (based on the data from the histograms in Figures 5.4 to 5.7, the costs of achieving sample cleanliness are quantified by the fraction of variable stars cut out when the thresholds are stringent. Entries of “–” in Tables 5.1 to 5.3 mean that it was not possible to reach such a good false positive threshold.

Table 5.1 evaluates the performance of our four algorithms in detecting contact binaries. BLS fares the worst, with any given threshold sample always being contaminated by at least 10% false positives. Even accepting 99% false positives, BLS still does not detect 71% of contact binaries. This poor performance on contact binary light curves is expected since BLS is designed to fit square-well signals. Correlation performs the best, rejecting just over half the contact binaries when including only 10% false positives, so it is our method of choice for sifting light curves for contact binaries.

Table 5.2 evaluates our algorithms' performance in finding detached eclipsing binaries. Here, Lomb-Scargle and PDM have a difficult time detecting any of the variables cleanly, finally detecting up to 50% of variables with a 99% false positive rate. BLS and correlation perform better, surpassing 50% completeness by the time false positives reach 99%.

Table 5.3 shows how our algorithms fare on the main target of this survey- low amplitude eclipses. Some examples of light curves with low amplitude eclipses are shown later, in §5.6. We find that none of the algorithms perform well in detecting the low amplitude eclipses, with all methods finally detecting a single low amplitude eclipse light curve by the time the threshold is pushed up to give 99% false positives.

Our results underscore the power of human pattern recognition, showing how difficult it is to program a computer to detect variable star light curves as well as a visual examination can. As a consequence, we emphasize that we only use computer algorithms to increase the efficiency of our visual examination- in the end, every variable star and planet candidate catalogued in this thesis was found by visual inspection.

Table 5.1: Performance of automated detection algorithms for contact binaries in NGC 6208

Algorithm	Fraction of true variables rejected at:		
	10% False positive threshold	50% False positive threshold	99% False positive threshold
Lomb-Scargle	0.74	0.53	0.29
Phase Dispersion Minimization	0.90	0.80	0.46
Box Least-Squares	–	0.98	0.71
Correlation	0.54	0.15	0.06

Table 5.2: Performance of automated detection algorithms for detached eclipsing binaries in NGC 6208

Algorithm	Fraction of true variables rejected at:		
	10% False positive threshold	50% False positive threshold	99% False positive threshold
Lomb-Scargle	–	–	0.50
Phase Dispersion Minimization	–	–	0.625
Box Least-Squares	0.94	0.75	0.44
Correlation	0.92	0.92	0.38

## 5.6 Planet Transit Candidates

Our planet transit candidates are drawn from within the  $< 2\%$  rms photometric precision sample, including all stars at  $14 < I < 18$ , amounting to  $\sim 10000$  stars per field. We used the correlation algorithm of §5.2 to rank all the light curves by likelihood of being

Table 5.3: Performance of automated detection algorithms for low-amplitude eclipsing objects in NGC 6208

Algorithm	Fraction of true variables rejected at:		
	10% False positive threshold	50% False positive threshold	99% False positive threshold
Lomb-Scargle	-	-	0.80
Phase Dispersion Minimization	-	-	0.80
Box Least-Squares	-	-	0.80
Correlation	-	-	0.80

variable stars. We selected by eye all light curves with low amplitude eclipses,  $< 10\%$  in depth. To make our initial planet transit candidate list from these low amplitude eclipse light curves, we discarded light curves that were clearly binary stars on visual inspection. Thus, we discarded all light curves with secondary eclipses and all light curves with clear sinusoidal modulation. We also discarded all light curves with only one eclipse, because we cannot analyze whether they are due to planets or binaries from one eclipse.

In this section, we evaluate how well a planet transit hypothesis fits in with these visually selected low amplitude eclipsing systems, and indicate which ones are most in need of follow-up observations. As mentioned in §2.3.1, our survey is designed with high time-sampling in order to provide power to rank the quality of planet candidates by their light curves alone, before expending resources on follow-up. The prescription in Seager & Mallén-Ornelas (2003), hereafter SM03, for the unique solution of planet and star parameters from a planet transit light curve parametrizes the light curve shape by the time spent in totality ( $t_{flat}$ ) and the total duration of eclipse ( $t_{total}$ ). Our time-sampling on a scale of minutes gives us sufficient epochs to fit the ingress and egress, and apply the unique solution equations.

We use Equations 7-14 and their associated assumptions from SM03 to derive the planetary radius, under the assumption that the eclipses in the light curve are due to a transiting planet. If it is not, then the equations will either be unsolvable, or the solutions will be physically inconsistent with the planet hypothesis. The equation from SM03 giving the planetary radius,  $R_p$ , is Equation 14,

$$\frac{R_p}{R_\odot} = \left( k^{1/x} \frac{\rho_*}{\rho_\odot} \right)^{x/(1-3x)} \sqrt{\Delta F}, \quad (5.2)$$

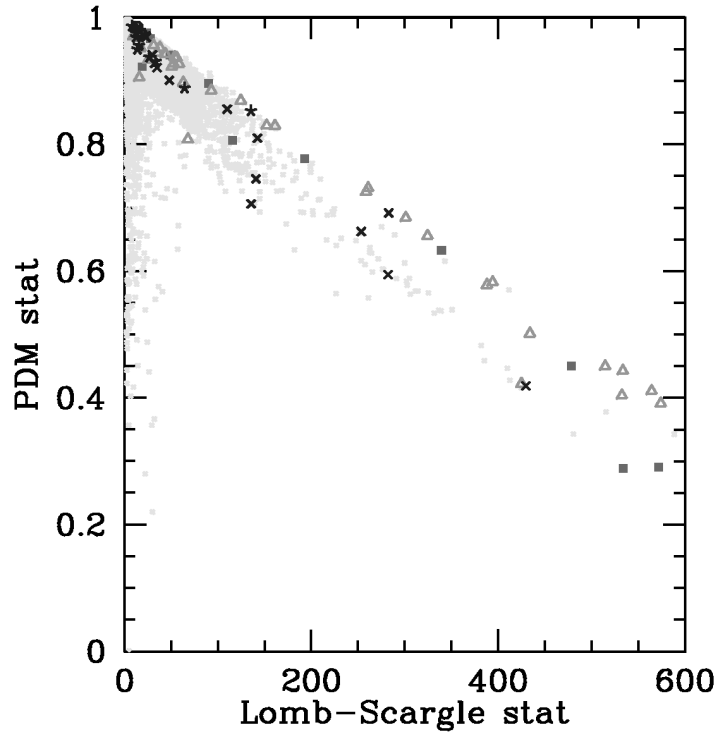


Figure 5.1: Variable finding by Lomb-Scargle and PDM. The techniques track each other well (low PDM value and high Lomb-Scargle power indicating variability), indicating that the techniques are not very different, although Lomb-Scargle discards some chaff that PDM rates as variable. The different symbols represent the results of visual classification: open triangles are contact binary or other short-period sinusoidally varying light curves, large black x's are detached eclipsing binaries with at least two primary eclipses showing, five-pointed stars are detached eclipsing binaries with only single transits, open octagons are transit-like or very small amplitude eclipses, solid squares are other variables such as RR Lyrae or  $\delta$  Scuti stars, and small light grey x's are stars with no variability obvious by eye.

where  $\Delta F$  is the transit depth, and for main-sequence stars,  $k = 1$ ,  $x \approx 0.8$ . The stellar density  $\rho_*$  is given by SM03, Equation 9,

$$\rho_* = \left( \frac{4\pi^2}{P^2 G} \right) \left[ \frac{(1 + \sqrt{\Delta F})^2 - b^2 [1 - \sin^2(t_{total}\pi/P)]}{\sin^2(t_{total}\pi/P)} \right]^{3/2}, \quad (5.3)$$

where  $P$  is the orbital period,  $G$  is the universal gravitational constant, and  $b$  is the impact parameter given by SM03, Equation 7,

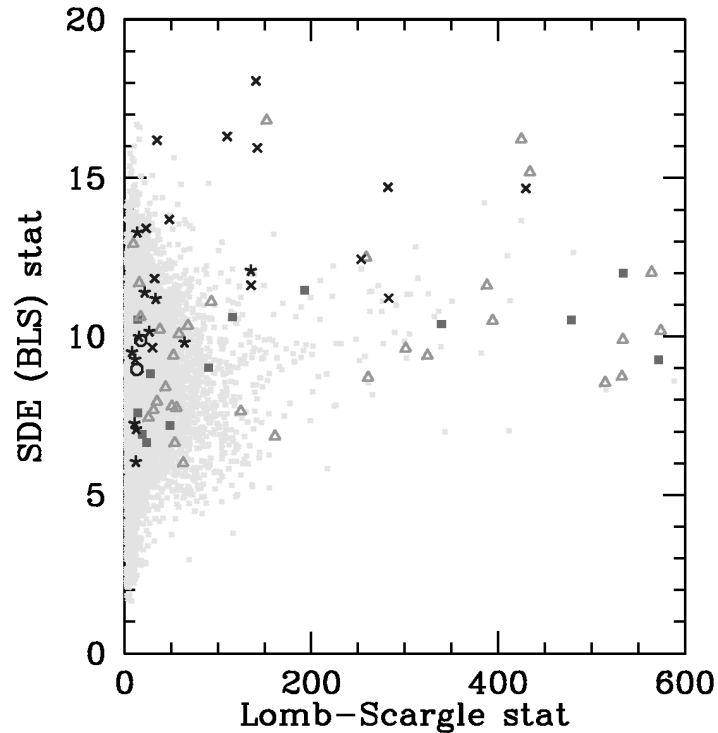


Figure 5.2: Variable finding by Lomb-Scargle and BLS box-fitting. High SDE is supposed to indicate transit detections. Contact binaries are not well separated by BLS. The different symbols represent the results of visual classification: open triangles are contact binary or other short-period sinusoidally varying light curves, large black x's are detached eclipsing binaries with at least two primary eclipses showing, five-pointed stars are detached eclipsing binaries with only single transits, open octagons are transit-like or very small amplitude eclipses, solid squares are other variables such as RR Lyrae or  $\delta$  Scuti stars, and small light grey x's are stars with no variability obvious by eye.

$$b = \left[ \frac{(1 - \sqrt{\Delta F})^2 - [\sin^2(t_{flat}\pi/P) / \sin^2(t_{total}\pi/P)](1 + \sqrt{\Delta F})^2}{1 - [\sin^2(t_{flat}\pi/P) / \sin^2(t_{total}\pi/P)]} \right]^{1/2}. \quad (5.4)$$

We derive  $t_{flat}$  and  $t_{total}$  using a simple grid-search chi-squared fit program written by K. von Braun. This program is CPU-intensive and is only run on the handful of light curves with eclipses that might indicate small mass companions (any light curve which, when examined by eye, has at least two eclipses visible, primary eclipse depth  $< 0.1$ , no visible secondary eclipse, and no sinusoidal light curve modulations). The program uses the BLS algorithm (Kovacs et al. 2002) as a front-end that evaluates the period



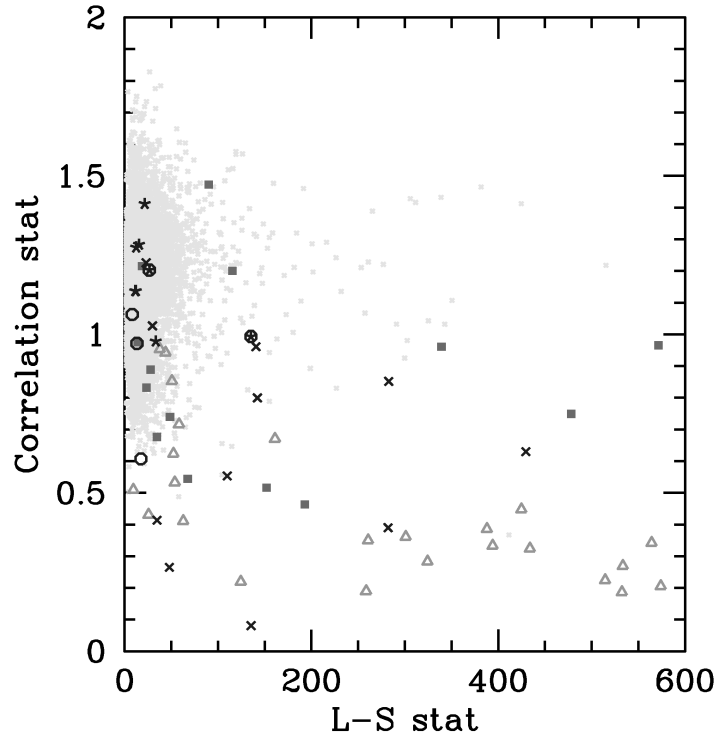


Figure 5.3: Variable finding by Lomb-Scargle and correlation. Note how the combination of more than one detection method has the potential to provide more variable detections with a reduced false positive rate. The different symbols represent the results of visual classification: open triangles are contact binary or other short-period sinusoidally varying light curves, large black x's are detached eclipsing binaries with at least two primary eclipses showing, five-pointed stars are detached eclipsing binaries with only single transits, open octagons are transit-like or very small amplitude eclipses, solid squares are other variables such as RR Lyrae or  $\delta$  Scuti stars, and small light grey x's are stars with no variability obvious by eye.

$P$  and depth  $\Delta F$  of the transit candidate, and outputs a light curve as a function of phase. To ensure that the correct period and depth are returned, the periods and depths searched by BLS are restricted based on prior inspections of the light curve. This phased light curve is then fit by minimizing the chi-squared for a simple three-parameter model, where the parameters are phase at start of eclipse, and the  $t_{flat}$  and the  $t_{total}$  of the eclipse. The eclipse is assumed to be symmetric, and the light curve is fit with four line segments. 1-sigma upper and lower error bars on  $t_{flat}$  and  $t_{total}$  are calculated by finding the maximum and minimum parameter values for which the chi-squared for the fit does

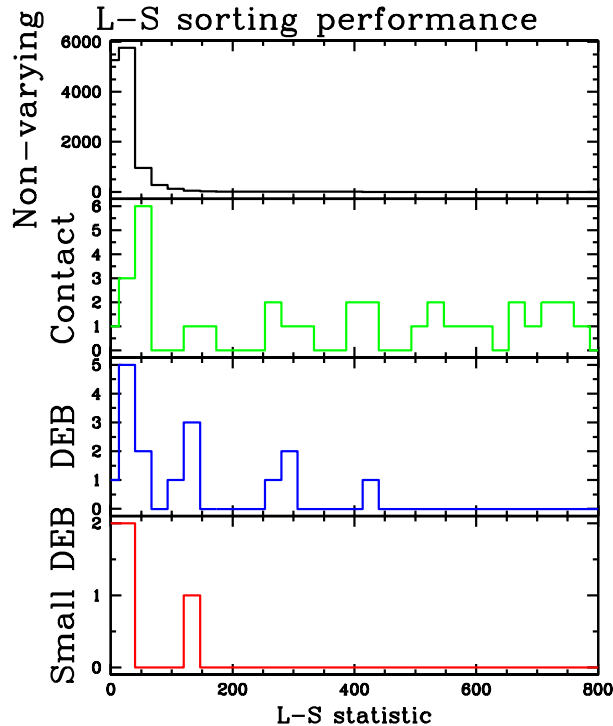


Figure 5.4: Histograms of the Lomb-Scargle statistic for various types of light curves with  $< 2\%$  rms, in NGC 6208. The types were assigned by visual inspection. From top to bottom, the samples are: non-varying light curves, contact binary light curves, detached eclipsing binary light curves, and light curves with low-amplitude eclipses.

not exceed 3.5 above the minimum, as recommended in Press et al. (1992). If only the minimum chi-squared cell in the grid search satisfies this criterion, then the error bar is set to the resolution of the grid.

We insert the fit values for  $P$ ,  $\Delta F$ ,  $t_{flat}$ , and  $t_{total}$  in Equations 5.2 to 5.4 and compute  $R_p$ . SM03 points out a monotonic relation between  $b$  and  $t_{flat}/t_{total}$ , implying that for a given  $\Delta F$ , the minimum  $R_p$  within our error bars will correspond to a maximum  $t_{flat}/t_{total}$ , and conversely, the maximum  $R_p$  will correspond to a minimum  $t_{flat}/t_{total}$ . So, we also compute extreme  $R_p$  values allowed by the 1-sigma error bars in  $t_{flat}$  and  $t_{total}$ . For this illustration, we do not add the complexity of also varying  $P$  and  $\Delta F$ , since experimentation (SM03) showed that for boxy planetary transits the error was dominated by uncertainties in  $t_{flat}/t_{total}$ .

The results of our  $R_p$  calculations for light curves with low-amplitude eclipses are presented in Tables 5.4 to 5.6. The stellar density and stellar mass are byproducts

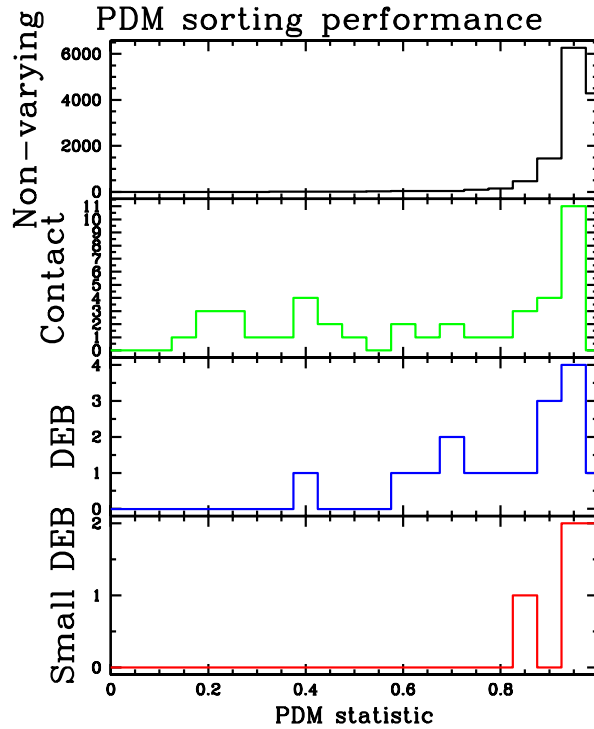


Figure 5.5: Histograms of the Phase Dispersion Minimization statistic for various types of light curves with  $< 2\%$  rms, in NGC 6208. The types were assigned by visual inspection. From top to bottom, the samples are: non-varying light curves, contact binary light curves, detached eclipsing binary light curves, and light curves with low-amplitude eclipses.

of the calculations in SM03, and are also shown in the tables. Note that for some combinations of  $P$ ,  $\Delta F$ ,  $t_{flat}$ , and  $t_{total}$ , the SM03 equations were unsolvable (yielding imaginary numbers), indicating that those combinations were unphysical. For example, no combinations at all of parameters within the error bars permit star 46192 in the field of NGC 6253 to satisfy the equations. One or more of the assumptions must be broken in order for these unphysical combinations to be measured: perhaps the companion is bright, one or both of the stars is not on the main sequence, or the system is blended with light from a third star.

The largest radius transiting planet currently known is WASP-1b (Charbonneau et al. 2006), at  $R_p = 1.44 \pm 0.08 R_{Jupiter}$ . We note that in most cases, the lower limits on  $R_p$  from the unique solution results greatly exceed this radius, and so the majority of light curves with  $\Delta F < 0.1$  are probably not due to planet transits. As can be seen

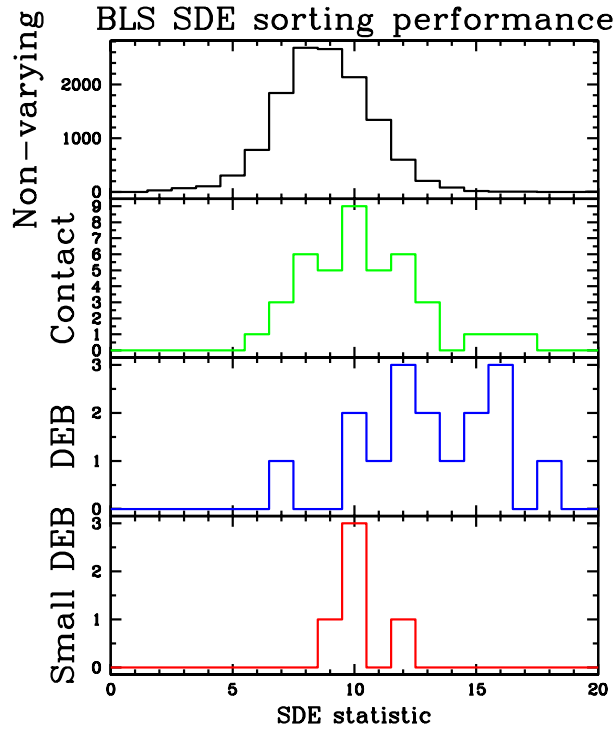


Figure 5.6: Histograms of the SDE statistic, from the BLS algorithm, for various types of light curves with  $< 2\%$  rms, in NGC 6208. The types were assigned by visual inspection. From top to bottom, the samples are: non-varying light curves, contact binary light curves, detached eclipsing binary light curves, and light curves with low-amplitude eclipses.

from Figure 5.8, a histogram of the inferred companion radii, there are a few objects clustered at high radii, and a larger group of low-amplitude eclipsing objects centred near  $2 R_{Jupiter}$ . Since the low-radius clump may constitute a different population, and since that population would be the one to contain any planets, we ensure we include the peak in the list of interesting objects. Even though it is high compared to the largest known planetary radius, we wish to have a small buffer in our candidate definition, to cover any systematic effects in the unique solution equations which might scatter planets to the  $2R_{Jupiter}$ . Therefore, we define a planet candidate as an object with a 2-sigma  $t_{flat}$  and  $t_{total}$  consistent with  $R_p = 1.44R_{Jupiter}$ .

There are five objects which satisfy this criterion: NGC 6134-star 18882, NGC 2447-star 11724, NGC 2447-star 17417, NGC 6208-star 12407, and NGC 6253-star 13404. These are planet candidates based on only the relative photometry; further tests based

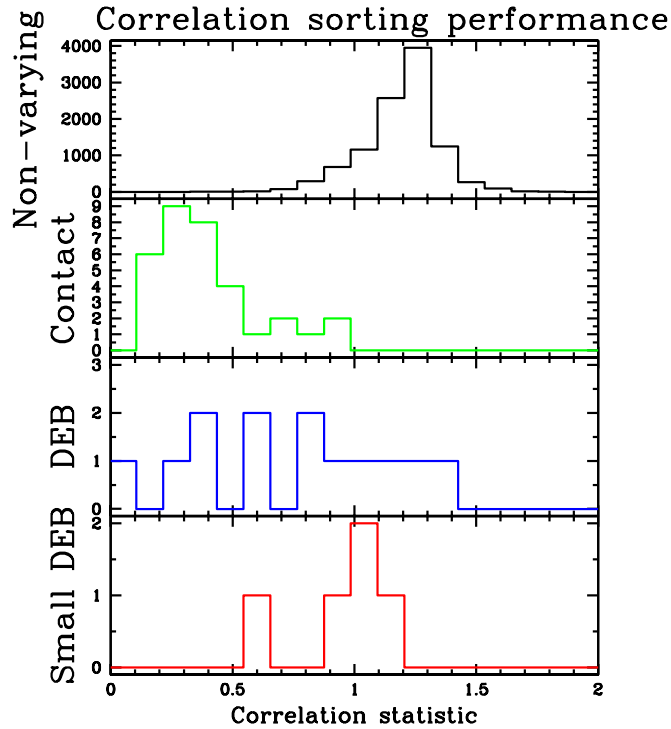


Figure 5.7: Histograms of our correlation statistic for various types of light curves with  $< 2\%$  rms, in NGC 6208. The types were assigned by visual inspection. From top to bottom, the samples are: non-varying light curves, contact binary light curves, detached eclipsing binary light curves, and light curves with low-amplitude eclipses.

on other measurements may rule them out as planets. Let us take a closer look at these objects.

### 5.6.1 NGC 6134, star 18882

The phased light curve for star 18882 in the field of NGC 6134 is shown in Figure 5.9. Both an overall view (with a repetition over 1.5 cycles in phase) and a close-up of the eclipse are plotted. The fit values,  $P = 1.5452$  days,  $\Delta F = 0.033$ ,  $t_{total} = 0.0761$  days, and  $t_{flat} = 0.0305$  days, give  $R_p = 1.5 \pm 0.3 R_{Jupiter}$ , consistent with the radius of a transiting planet. The fit gives the mass of the host star equal to that of a K0V dwarf,  $0.84 \pm 0.18 M_{\odot}$ .

Photometric spectral type estimation on this star, with  $I = 17.14$ ,  $B - V = 1.42$ ,  $V - R = 0.88$ , and  $V - I = 1.90$ , gives a best fit of an F6V star at distance 2140 pc

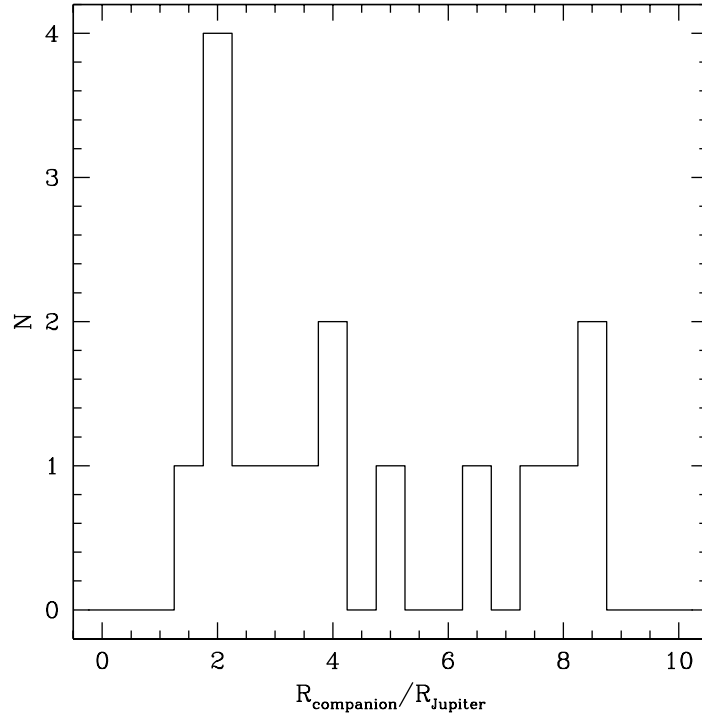


Figure 5.8: Histogram of the inferred radii of companions to host stars showing low-amplitude eclipses. The companion radii were derived using the SM03 unique solution equations. Note the conspicuous peak in the distribution at 2 Jupiter radii. This peak represents our most interesting objects- small companions, or special situations such as blends that mimic small companions. The small peak of objects at 8 Jupiter radii is very unlikely to correspond to transiting planets.

and  $A_V = 3.51$ . This best-fit model has  $I = 17.08$ ,  $B - V = 1.49$ ,  $V - R = 0.91$ , and  $V - I = 1.92$ . However, note that, for example, one may obtain almost as good a fit with a K0V star at distance 1580 pc and  $A_V = 2.45$ , which would have colours  $I = 17.20$ ,  $B - V = 1.46$ ,  $V - R = 0.89$ , and  $V - I = 1.81$ . This star lies in the portion of the CMD where fitted models of nearby low mass dwarfs become similar to models of more distant hot stars. Therefore, photometric spectral type estimation is unable to conclusively rule out this star as a candidate, and an MK classification spectrum shall have to be obtained at a later date.

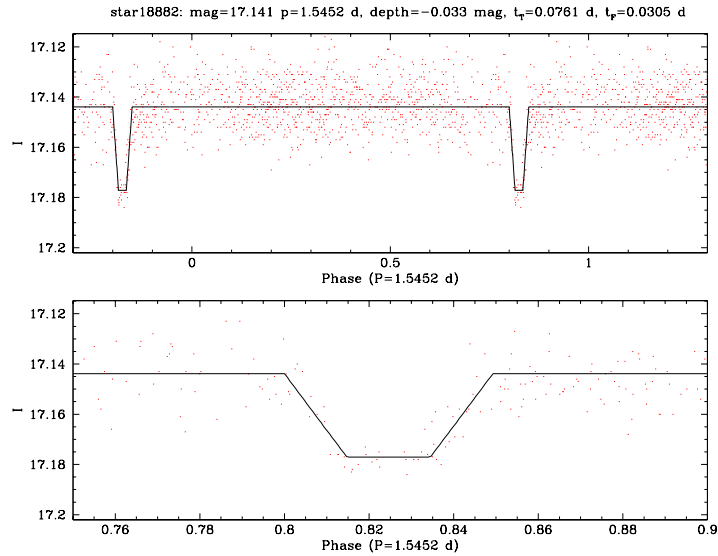


Figure 5.9: The phased light curve of star 18882 in the field of NGC 6134. The top panel shows 1.5 cycles of the light curve, while the bottom panel shows a close-up of the eclipse. The solid line shows the best chi-squared fit model. Applying the unique solution equations implies a companion radius  $R_p = 1.5 \pm 0.3 R_{Jupiter}$ , consistent with the radii of the largest known transiting planets.

### 5.6.2 NGC 2447, star 11724

The phased light curve for star 11724 in the field of NGC 2447 is shown in Figure 5.10, repeated over 1.5 cycles for a large scale view, and also zoomed in to 0.2 cycles around the transit. The noise level of this light curve is typical for its magnitude, but is significant compared to the eclipse depth. The eclipse is recovered because it repeats multiple times over the course of the observing run. Further photometric observations are required to refine the shape parameters. The best fit using the data at hand gives  $P = 1.5792$  days,  $\Delta F = 0.008$ ,  $t_{total} = 0.0633$  days, and  $t_{flat} = 0.0612$  days. The best fit values are actually unphysical, but the values at the lower limit on  $t_{flat}/t_{total}$  do admit the possibility of a transiting planet of radius  $R_p = 0.81$  around a G5V star of mass  $0.91 M_{\odot}$ .

The best fit photometric spectral type for this star is K4V, at a distance 1090 pc and  $A_V = 0.45$ . The best fit photometry is  $I = 16.44$ ,  $B - V = 1.21$ ,  $V - R = 0.74$ , and  $V - I = 1.40$ , compared to measured photometry  $I = 16.46$ ,  $B - V = 1.07$ ,  $V - R = 0.59$ , and  $V - I = 1.41$ . The photometry is not consistent with the G5V star implied by the unique solution. The best fit colours from our photometric spectral type estimate are not very close to the measured values, so this object is possibly a blend.

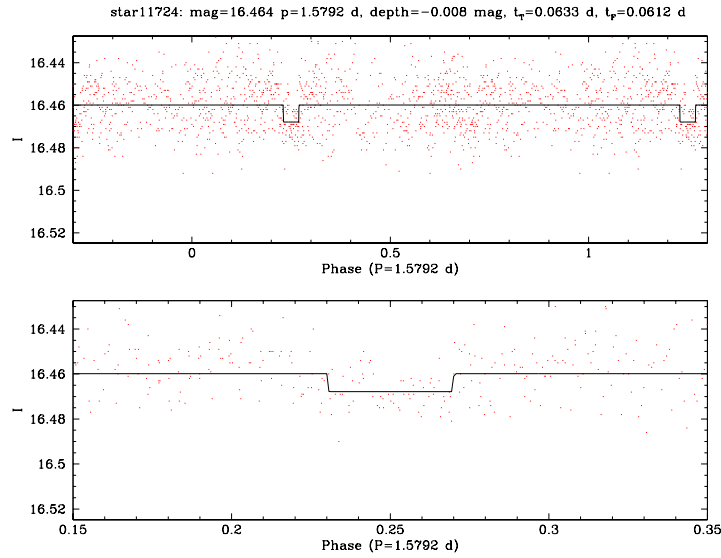


Figure 5.10: The phased light curve of star 11724 in the field of NGC 2447. The top panel shows 1.5 cycles of the light curve, while the bottom panel shows a close-up of the eclipse. Applying the unique solution equations for the lower 1-sigma limit on  $t_{flat}/t_{total}$  implies a companion radius  $R_p = 0.81R_{Jupiter}$ , but the upper limit on  $t_{flat}/t_{total}$  is unphysical.

### 5.6.3 NGC 2447, star 17417

Star 17417 in NGC 2447 is shown in Figure 5.12. Again, there are two views: 1.5 cycles and 0.35 cycles. The best fit to the data gives  $P = 0.7126$  days,  $\Delta F = 0.015$ ,  $t_{total} = 0.0758$  days, and  $t_{flat} = 0.0161$  days. The high 1-sigma limit on  $t_{flat}/t_{total}$  gives a companion of radius  $1.54R_{Jupiter}$ , orbiting an F5V star.

The best fit photometric spectral type for this star is B5V, at a distance 15970 pc and  $A_V = 2.71$ . The best fit photometry is  $I = 15.22$ ,  $B - V = 0.69$ ,  $V - R = 0.41$ , and  $V - I = 0.97$ , compared to measured photometry  $I = 15.24$ ,  $B - V = 0.79$ ,  $V - R = 0.47$ , and  $V - I = 0.97$ . The photometry is not consistent with the F5V star mentioned above for the 1-sigma limit of the unique solution; this object could be a binary star with an early-type primary.

### 5.6.4 NGC 6208, star 12407

Star 12407 in NGC 6208 is shown in Figure 5.12. The two views of the light curve span 1.5 cycles and 0.35 cycles. The best fit to the data gives  $P = 0.4907$  days,  $\Delta F = 0.012$ ,



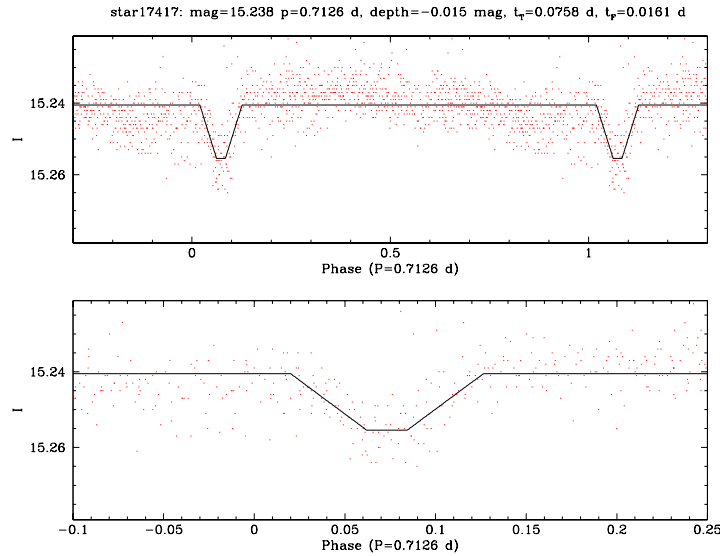


Figure 5.11: The phased light curve of star 17417 in the field of NGC 2447. The top panel shows 1.5 cycles of the light curve, while the bottom panel shows a close-up of the eclipse.

$t_{total} = 0.0690$  days, and  $t_{flat} = 0.0097$  days. At such a small  $t_{flat}$ , the light curve may not even be truly flat-bottomed, in which case the unique solution equations are not valid. However, the lower 1-sigma limit on  $t_{flat}$  is still 0.008, so we try out the unique solution anyways. The high 1-sigma limit on  $t_{flat}/t_{total}$  gives a companion of radius  $1.64R_{Jupiter}$ , orbiting an F2V star.

The best fit photometric spectral type for this star is K0V, at a distance 1113 pc and  $A_V = 0.85$ . The best fit photometry is  $I = 15.47$ ,  $B - V = 1.02$ ,  $V - R = 0.60$ , and  $V - I = 1.20$ , compared to measured photometry  $I = 15.61$ ,  $B - V = 1.01$ ,  $V - R = 0.55$ , and  $V - I = 1.12$ . The photometry is not at all consistent with the F2V star mentioned above for the 1-sigma limit of the unique solution; this is possibly a grazing binary system.

### 5.6.5 NGC 6253, star 13404

Star 13404 in NGC 6253 is shown in Figure 5.13. The two views of the light curve span 1.5 cycles and 0.35 cycles. The best fit to the data gives  $P = 5.9323$  days,  $\Delta F = 0.043$ ,  $t_{total} = 0.1418$  days, and  $t_{flat} = 0.0297$  days. The high 1-sigma limit on  $t_{flat}/t_{total}$  gives a rather large companion of radius  $1.86R_{Jupiter}$ , orbiting an G5V star. This object has the largest inferred radius of the five robust candidates picked from the photometry.

The best fit photometric spectral type for this star is K3V, at a distance 1147 pc and

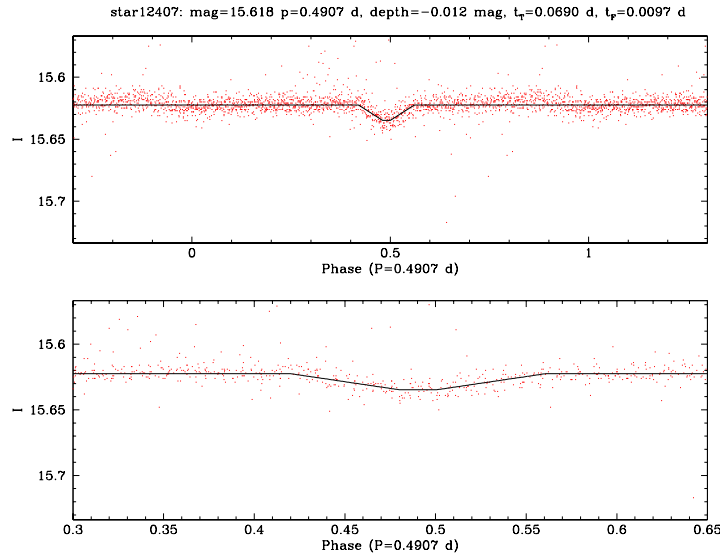


Figure 5.12: The phased light curve of star 12407 in the field of NGC 6208. The top panel shows 1.5 cycles of the light curve, while the bottom panel shows a close-up of the eclipse.

$A_V = 0.95$ . The best fit photometry is  $I = 16.57$ ,  $B - V = 1.20$ ,  $V - R = 0.76$ , and  $V - I = 1.47$ , compared to measured photometry  $I = 17.41$ ,  $B - V = 1.07$ ,  $V - R = 0.63$ , and  $V - I = 1.14$ . The photometry is not consistent with the G5V star mentioned above for the 1-sigma limit of the unique solution, and the strange colours giving a rather poor photometric spectral type fit indicate that this is possibly a blend.

## 5.7 Statistical significance

*A posteriori*, we can calculate how many transiting planets we expect to find, and compare to the number of robust candidates we extracted, using various cuts on the data to define the parent sample. Because of our ability to find cluster membership probabilities, we have the ability to define the parent sample in a number of different ways. Here, we investigate the statistics of several different choices for the parent sample cuts. We consider the statistics of the following subsets of our data.

1. Objects with photometrically estimated spectral types and rms light curve scatter less than 1.5%. Setting the bar at this level of precision allows us to compare our quantity of stars with the OGLE-III survey, which found 5 transiting planets in 155 000 stars measured to better than 1.5% photometric precision.

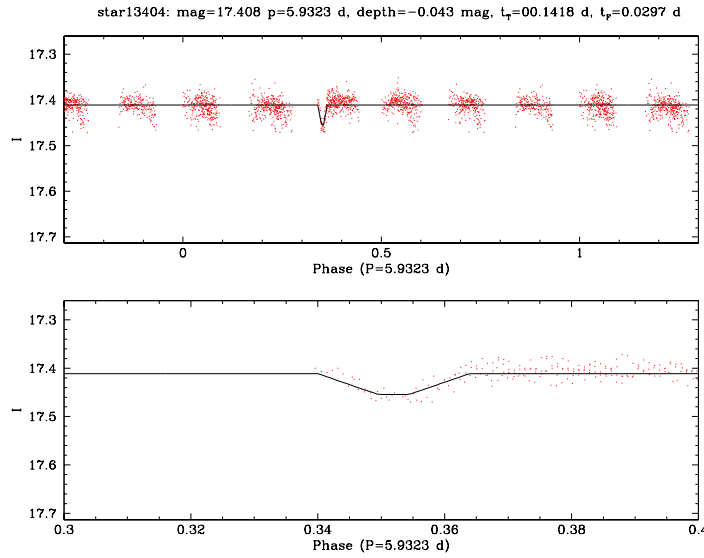


Figure 5.13: The phased light curve of star 13404 in the field of NGC 6253. The top panel shows 1.5 cycles of the light curve, while the bottom panel shows a close-up of the eclipse.

2. Objects with photometrically estimated spectral types and either rms light curve scatter less than 2%.
3. Objects within the SNR-optimized cluster cuts described in Chapter 4. These objects have spectral type estimates, since the spectral types are a prerequisite for consideration as cluster members. We derive multiple statistics from within this cut, using the following quantities for the definition of the parent sample::
  - (a) the number of cluster stars with rms light curve scatter less than 1.5% (computed as the sum of the cluster membership probabilities of all objects in the cut),
  - (b) the number of non-cluster stars with rms light curve scatter less than 1.5% (computed as the sum of all objects in the cut, minus the sum of the cluster membership probabilities of all objects in the cut),
  - (c) the number of cluster stars with rms light curve scatter less than 2%, and,
  - (d) the number of non-cluster stars with rms light curve scatter less than 2%.

We also considered each of the above subsets but with an added cut removing all stars classified as earlier than F0. By removing the early-type stars, we better match the

Table 5.4: Application of unique solution equations to low-amplitude eclipses in IC 2714, IC 4651, and NGC 2447

Star ID	Period (d)	Fractional depth	Mean $\frac{t_{flat}}{t_{total}}$ , and $1\sigma$ limits	$t_{flat}$	$t_{total}$	$\log \frac{\rho_*}{\rho_\odot}$	$\frac{M_*}{M_\odot}$	$\frac{R_{companion}}{R_{Jupiter}}$
IC2714-star31296	5.146	0.131	lower $\frac{t_{flat}}{t_{total}} = 0.000 :$	0.000	0.238	-0.534	2.407	7.110
			$\frac{t_{flat}}{t_{total}} = 0.115 :$	0.026	0.223	-0.441	2.064	6.289
			upper $\frac{t_{flat}}{t_{total}} = 0.197 :$	0.041	0.208	-0.333	1.729	5.458
IC4651-star41072	0.890	0.021	lower $\frac{t_{flat}}{t_{total}} = 0.169 :$	0.015	0.088	-0.504	2.290	2.716
			$\frac{t_{flat}}{t_{total}} = 0.205 :$	0.018	0.086	-0.462	2.138	2.570
			upper $\frac{t_{flat}}{t_{total}} = 0.243 :$	0.020	0.083	-0.416	1.983	2.421
NGC2447-star11724	1.579	0.008	lower $\frac{t_{flat}}{t_{total}} = 0.753 :$	0.058	0.078	0.055	0.914	0.809
			$\frac{t_{flat}}{t_{total}} = 0.966 :$	0.061	0.063	—	—	—
			upper $\frac{t_{flat}}{t_{total}} = 1.253 :$	0.078	0.062	—	—	—
NGC2447-star17417	0.713	0.015	lower $\frac{t_{flat}}{t_{total}} = 0.172 :$	0.013	0.077	-0.495	2.258	2.277
			$\frac{t_{flat}}{t_{total}} = 0.212 :$	0.016	0.076	-0.467	2.157	2.196
			upper $\frac{t_{flat}}{t_{total}} = 0.386 :$	0.024	0.063	-0.202	1.395	1.549
NGC2447-star8847	1.122	0.073	lower $\frac{t_{flat}}{t_{total}} = 0.000 :$	0.000	0.115	-0.389	1.896	4.389
			$\frac{t_{flat}}{t_{total}} = 0.050 :$	0.006	0.111	-0.352	1.785	4.183
			upper $\frac{t_{flat}}{t_{total}} = 0.206 :$	0.019	0.092	-0.088	1.156	2.955

sample to the radial velocity search sample. For the cluster cuts 3abcd, we find the early-type cut rejects no stars for all fields except NGC 2660, where fewer than 10 stars are rejected. Therefore, we only show results for removal of early-type stars for cuts 1 and 2.

Without considering cluster membership (cuts 1 and 2), the yield is around 40000 stars, with individual fields each contributing a few thousand stars to the sample. With the fairly restrictive membership cuts in place, the yield is around 2000 stars, with each cluster contributing tens to hundreds of stars to the sample. As shown in Table 5.7, the early-type cut does not affect the raw numbers of stars very much even in the data without cluster membership considerations. NGC 6134 in particular has a particularly low yield because of the complications of heavy and non-uniform reddening in the field. The numbers of cluster stars reported here are much lower than the totals in Chapter 4 because of the high precision rms cut we have imposed here.

Table 5.5: Application of unique solution equations to low-amplitude eclipses in NGC 2660, NGC 5316, and NGC 6134

Star ID	Period (d)	Fractional depth	Mean $\frac{t_{flat}}{t_{total}}$ , and $1\sigma$ limits	$t_{flat}$	$t_{total}$	$\log \frac{\rho_*}{\rho_{\odot}}$	$\frac{M_*}{M_{\odot}}$	$\frac{R_{companion}}{R_{Jupiter}}$
NGC2660-star15800	7.140	0.051	lower $\frac{t_{flat}}{t_{total}} = 0.000 :$	0.000	0.204	-0.499	2.272	4.253
			$\frac{t_{flat}}{t_{total}} = 0.195 :$	0.036	0.183	-0.333	1.730	3.419
			upper $\frac{t_{flat}}{t_{total}} = 0.350 :$	0.057	0.162	-0.115	1.208	2.566
NGC2660-star24794	4.931	0.054	lower $\frac{t_{flat}}{t_{total}} = 0.299 :$	0.068	0.228	-0.718	3.260	5.829
			$\frac{t_{flat}}{t_{total}} = 0.388 :$	0.083	0.213	-0.590	2.639	4.923
			upper $\frac{t_{flat}}{t_{total}} = 0.489 :$	0.097	0.199	-0.429	2.024	3.982
NGC5316-star10469	1.286	0.036	lower $\frac{t_{flat}}{t_{total}} = 0.050 :$	0.006	0.128	-0.684	3.078	4.512
			$\frac{t_{flat}}{t_{total}} = 0.144 :$	0.014	0.097	-0.349	1.775	2.905
			upper $\frac{t_{flat}}{t_{total}} = 0.240 :$	0.022	0.090	-0.226	1.450	2.471
NGC5316-star13437	2.115	0.057	lower $\frac{t_{flat}}{t_{total}} = 0.453 :$	0.054	0.120	-0.146	1.271	2.801
			$\frac{t_{flat}}{t_{total}} = 0.655 :$	0.074	0.113	—	—	—
			upper $\frac{t_{flat}}{t_{total}} = 0.855 :$	0.086	0.101	—	—	—
NGC6134-star18882	1.545	0.033	lower $\frac{t_{flat}}{t_{total}} = 0.322 :$	0.026	0.081	-0.013	1.022	1.798
			$\frac{t_{flat}}{t_{total}} = 0.401 :$	0.031	0.076	0.102	0.845	1.544
			upper $\frac{t_{flat}}{t_{total}} = 0.491 :$	0.035	0.071	0.244	0.669	1.281
NGC6134-star20577	3.241	0.060	lower $\frac{t_{flat}}{t_{total}} = 0.231 :$	0.054	0.236	-0.923	4.563	8.013
			$\frac{t_{flat}}{t_{total}} = 0.283 :$	0.064	0.227	-0.854	4.072	7.316
			upper $\frac{t_{flat}}{t_{total}} = 0.339 :$	0.074	0.217	-0.775	3.580	6.600
NGC6134-star3952	2.099	0.036	lower $\frac{t_{flat}}{t_{total}} = 0.155 :$	0.035	0.227	-1.190	7.079	8.871
			$\frac{t_{flat}}{t_{total}} = 0.188 :$	0.041	0.221	-1.152	6.648	8.437
			upper $\frac{t_{flat}}{t_{total}} = 0.222 :$	0.048	0.215	-1.111	6.213	7.991
NGC6134-star8950	5.376	0.036	lower $\frac{t_{flat}}{t_{total}} = 0.091 :$	0.027	0.297	-1.198	7.178	8.971
			$\frac{t_{flat}}{t_{total}} = 0.152 :$	0.043	0.281	-1.120	6.306	8.087
			upper $\frac{t_{flat}}{t_{total}} = 0.221 :$	0.059	0.265	-1.029	5.434	7.180

Table 5.6: Application of unique solution equations to low-amplitude eclipses in NGC 6208 and NGC 6253

Star ID	Period (d)	Fractional depth	Mean $\frac{t_{flat}}{t_{total}}$ , and $1\sigma$ limits	$t_{flat}$	$t_{total}$	$\log \frac{\rho_*}{\rho_\odot}$	$\frac{M_*}{M_\odot}$	$\frac{R_{companion}}{R_{Jupiter}}$
NGC6208-star12407	0.491	0.014	lower $\frac{t_{flat}}{t_{total}} = 0.117 :$	0.008	0.070	-0.472	2.175	2.166
			$\frac{t_{flat}}{t_{total}} = 0.140 :$	0.010	0.069	-0.450	2.097	2.104
			upper $\frac{t_{flat}}{t_{total}} = 0.287 :$	0.017	0.059	-0.262	1.538	1.641
NGC6208-star22341	1.394	0.041	lower $\frac{t_{flat}}{t_{total}} = 0.141 :$	0.032	0.225	-1.236	7.642	10.037
			$\frac{t_{flat}}{t_{total}} = 0.240 :$	0.048	0.200	-1.097	6.070	8.349
			upper $\frac{t_{flat}}{t_{total}} = 0.266 :$	0.052	0.196	-1.067	5.784	8.032
NGC6253-star13404	5.932	0.043	lower $\frac{t_{flat}}{t_{total}} = 0.000 :$	0.000	0.147	-0.209	1.411	2.665
			$\frac{t_{flat}}{t_{total}} = 0.217 :$	0.030	0.136	-0.080	1.141	2.249
			upper $\frac{t_{flat}}{t_{total}} = 0.321 :$	0.040	0.126	0.064	0.899	1.860
NGC6253-star37511	1.575	0.029	lower $\frac{t_{flat}}{t_{total}} = 0.340 :$	0.031	0.092	-0.200	1.390	2.145
			$\frac{t_{flat}}{t_{total}} = 0.412 :$	0.036	0.087	-0.096	1.170	1.869
			upper $\frac{t_{flat}}{t_{total}} = 0.782 :$	0.050	0.064	—	—	—
NGC6253-star46192	6.979	0.058	lower $\frac{t_{flat}}{t_{total}} = 0.655 :$	0.117	0.179	—	—	—
			$\frac{t_{flat}}{t_{total}} = 0.870 :$	0.138	0.158	—	—	—
			upper $\frac{t_{flat}}{t_{total}} = 1.150 :$	0.158	0.138	—	—	—

We shall use the solar neighbourhood radial velocity search statistics from Chapter 1 to calculate the probability  $P(M)$  that our survey should detect  $M$  transiting planets, where  $M$  is the sum of the detections  $X_i$  expected in each of the eight cluster fields  $i$ .

In each individual field, we assume there is a probability  $p_i$  of any given star hosting a transiting Hot Jupiter. Then the probability of seeing  $X_i$  detections in each field is given by a binomial distribution  $B(x = X_i; N_i, p_i)$  where  $N_i$  is the number of objects in the parent sample.

Recall Equation 1.2 from Chapter 1. The probability  $p_i$  is calculated from the raw astrophysical probability of a star hosting a Hot Jupiter, the  $P_{vis}$  for the observations (cf. Chapter 2), and the geometrical probability  $\frac{R_*}{a} \approx 0.1$  that the orbit will lie along the line of sight. We further assume [Fe/H] dictates the raw frequency of occurrence as laid out for four 0.5 dex wide bins in Fischer, Valenti, and Marcy (2004), that the 0.7% HJ fraction of Marcy et al. (2005) is valid in the  $0.0 < [\text{Fe}/\text{H}] < 0.25$  bin, and that

this fraction  $f_{HJ} = 0.7\%$  obeys exactly the same metallicity scaling as the total planet fraction,  $f([\text{Fe}/\text{H}])$ . So, we use  $p_i = (0.7\%) \frac{f([\text{Fe}/\text{H}]_{\text{target}})}{f([\text{Fe}/\text{H}]_{=0.125})} \langle P_{\text{vis}} \rangle \langle \frac{R_*}{a} \rangle$ . When dealing with stars from the Galactic field, we adopt an average  $[\text{Fe}/\text{H}] = -0.1$  (Prantzos 1998).

In order to calculate the  $P(M)$ , we consider all possible joint probabilities,

$$J_j = \left[ \prod_{i=1}^8 B(x = X_i; N_i, p_i) \right]_j, \quad (5.5)$$

such that for each  $j$ ,  $M$  is the sum of the set of  $X_i$ 's. Suppose that there are  $W$  ways to choose the set of  $X_i$ 's. Then  $P(M)$  is just the sum of all the possible joint probabilities:

$$P(M) = \sum_{j=1}^W \left[ \prod_{i=1}^8 B(x = X_i; N_i, p_i) \right]_j. \quad (5.6)$$

In practice, the  $p_i$  are very small, and the product  $N_i p_i < 10$  so we use the Poisson distribution approximation to the binomial distribution to simplify the calculations.

In Figure 5.14, we show the function  $P(M)$  for  $M < 10$ , calculated for cuts 1 and 2. We see the most likely number of planets present in the 1.5% rms sample without cuts is 6, with probability 0.15, for a 39000 star parent sample. The most likely number for the 2% rms sample is 8, with probability 0.14, out of a 47000 star parent sample. Our number of robust planet candidates from the light curves alone for these samples is fairly consistent at 5 (see discussion of Table 5.8 below). Cutting early spectral types makes very little difference in the distribution.

In Figures 5.15 and 5.16, we show the function  $P(M)$  for  $M < 10$ , calculated for the various cluster cut samples derived from cut 3. We also illustrate the additional effect of removing the few early-type stars in the samples, and see that it indeed has a negligible effect. The most likely number of planets for all of these small statistics samples is 0, with relatively high probability, between about 0.4 and 0.7 depending on the specific cut. Our numbers of robust planet candidates for these samples are around 0.5, consistent with the expected null detection using the cluster cut.

In Table 5.8, we show the number of planet candidates detected in each of the various subsets, the expectation values computed based on  $N_i$  from Table 5.7 and  $p_i$  from Equation 1.2, and the cumulative probability that the number of transiting planets would be less than or equal to the number of robust candidates detected (a summation of the  $P(M)$  from Equation 5.6). The number of robust candidates detected in the sample without cluster cuts, 4 or 5, is relatively consistent with expectations of 6 to 8 detections. There is no significant evidence to reject the hypothesis that the frequency of occurrence of HJ in

our fields is the same as that derived from radial velocity searches in the solar neighbourhood. The lowest probability event was a detection of 4 robust candidates (in the 2% rms sample with early spectral types cut) when the expectation was 7.4 transiting planets. In that case, the probability of detecting 4 or fewer was 8.9%. The highest consistency achieved without diminishing the number statistics by the cluster cuts is a 31.1% chance of detecting 5 or fewer planets in the 1.5% rms sample without any additional cuts. For this sample, 6.2 planets were expected compared to the 5 robust candidates detected.

Turning to the smaller statistics offered by the cluster cut, we find the number of robust candidates present after cluster cuts, 0.4-0.6, is quite consistent with expectations of 0.3-0.8 detections. There is no evidence to support the hypothesis that the frequency of occurrence of HJ in open clusters is different from that derived from radial velocity searches in the solar neighbourhood. However, the number of cluster stars surviving the cuts was small, making consistency between the prediction and number of detections easy to achieve (since zero detections was the most likely outcome).

Note, however, that in the possible case (especially considering the colour information for our candidates) that, after follow-up work, all of our candidates turn out to be blends or low-mass stars, and if there are no further HJ candidates hidden below the systematics noise levels, then we have a highly significant ( $3\sigma$ ) rejection of the hypothesis of similar frequencies of occurrence of HJ between our sample and the radial velocity searches, and we strongly accept the alternative that the frequency of occurrence of HJ in our sample is lower than in the radial velocity searches. For example, for the 1.5% rms sample without any additional cuts, there is only a 0.1% chance that a null detection would occur if the frequency of occurrence was at the radial velocity search value. This would imply that either the solar neighbourhood is unusually planet rich, or that rv surveys have an observational bias towards selecting systems with high HJ frequencies (since they are more sensitive at longer periods, and search slightly larger stars than we do).

Note also that all the expectation values we calculated assumed 100% detectability of planet transits at these rms thresholds. In practice, the detectability may currently not be at 100%, but for transit detection by visual examination, could be closer to 28%. This estimate is calculated as follows, using NGC 2447 as a specific example. We start with the distribution of spectral types derived for all the stars in the 1.5% rms sample of NGC 2447. For each of those stars, we calculate the transit depth that would be created by a  $1R_{Jupiter}$  planet. We know the rms photometric precision of each of those stars, so we compare the hypothetical transit depth to the photometric precision. If a star's transit depth is smaller than 2.5 times the photometric precision, we assume it would



not be picked up by visual examination. The fraction of stars that would be picked up by a visual examination sensitive down to  $2.5\sigma$  is 28% for NGC 2447.

This factor of almost 4 reduction in probability would make a null detection much more probable- for the case of the 1.5% rms sample without any additional cuts, the chance of null detection would actually rise to 17.7%, and the most likely number of planet transits to be found would be 1 (with 31% probability). However, there should still be room for improvement in the detectability factor and consequent tightening of limits if one implements post-processing systematics removal algorithms. One of the most common remaining systematics is a gradual parabolic-shaped trend in a light curve over the course of a night, which could be due to a second-order, colour-related atmospheric extinction term, and hence can recur on multiple nights. This should be easy to remove in post-processing.

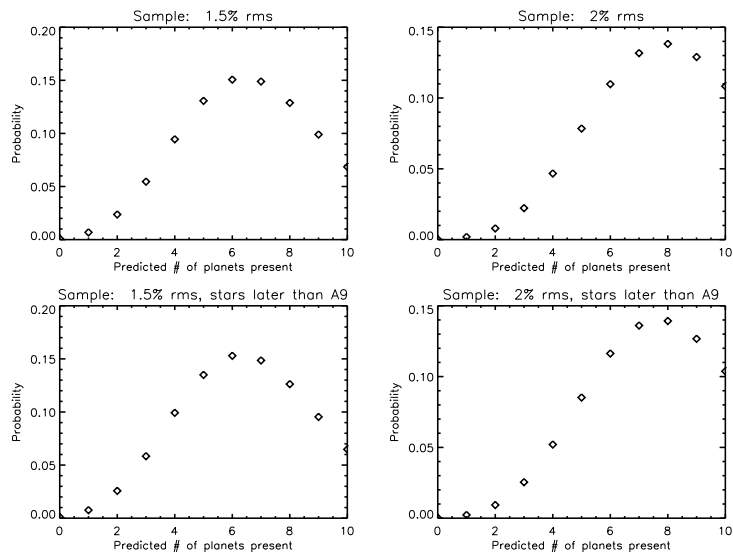


Figure 5.14: The summed joint probabilities over all eight fields of all ways of finding 0-10 planets, including all stars with rms better than 1.5% (top left), all stars with rms better than 2% or with  $I < 18$  (top right), all stars with rms better than 1.5% and photometric spectral types later than A9 (bottom left), and all stars with photometric spectral types later than A9, and rms better than 2% or  $I < 18$  (bottom right). Since the probabilities are small, we have used a Poisson approximation for each binomial probability distribution.

Table 5.7: Star yields after applying cuts 1, 2, and 3abcd, outlined in §5.7, with and without additional early-type cuts.

Cluster name	Stars in cut 1	Stars in cut 1	Stars in cut 2	Stars in cut 2	Stars in cut 3a	Stars in cut 3b	Stars in cut 3c	Stars in cut 3d
	All types	No early-types	All types	No early-types				
IC 2714	3987	3961	4661	4620	237.29	139.71	246.75	143.25
IC 4651	4089	3841	4616	4332	40.03	125.97	46.92	137.08
NGC 2447	2459	2253	2745	2512	641.25	462.74	686.63	491.37
NGC 2660	4320	4216	5467	5321	451.40	513.60	462.69	521.31
NGC 5316	3720	3705	4319	4298	489.63	595.37	525.85	634.15
NGC 6134	4025	3949	5047	4964	22.33	20.67	27.57	23.43
NGC 6208	8195	7980	9683	9384	54.15	193.85	64.07	205.93
NGC 6253	7799	7591	10236	9910	328.05	134.96	356.46	146.54
Totals:	38594	37496	46774	45341	2264.12	2186.87	2416.94	2303.06

Table 5.8: Planet candidate yields in cuts 1, 2, and 3abcd, as outlined in §5.7, with and without additional early-type cuts.

Cut	Number of low-amplitude eclipsing objects	Number of robust candidates	Probability of finding this number of robust candidates or fewer	Expected number of transiting planets	Total stars in cut
Cut 1: < 1.5% rms	16	5	31.1%	6.2	38594
Cut 1 without early-types	13	4	15.8%	6.1	37496
Cut 2: < 2% rms	18	5	19.2%	7.6	46774
Cut 2 without early-types	15	4	8.9%	7.4	45341
Cut 3a: < 1.5% rms, cluster	1.03	0.40	45.9%	0.71	2264.12
Cut 3b: < 1.5% rms, non-cluster	0.96	0.60	71.4%	0.30	2186.87
Cut 3c: < 2% rms, cluster	1.03	0.40	43.3%	0.76	2416.94
Cut 3d: < 2% rms, non-cluster	0.96	0.60	70.0%	0.32	2303.06

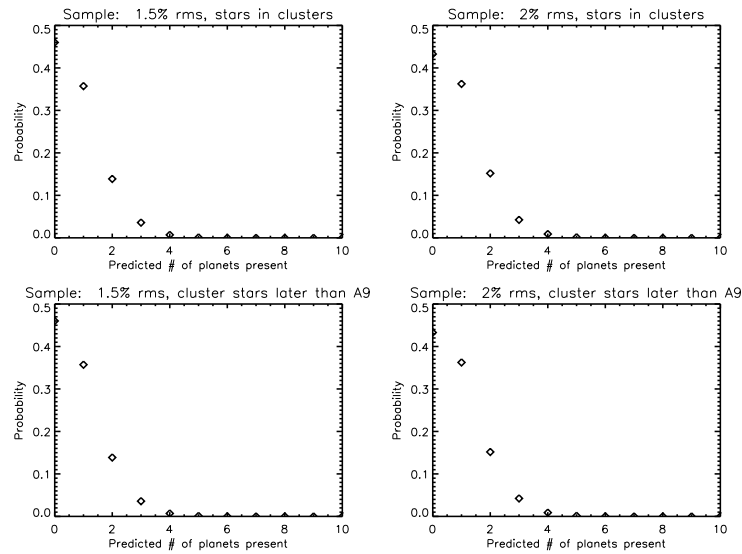


Figure 5.15: The summed joint probabilities over all eight fields of all ways of finding 0-10 planets, including cluster stars with rms better than 1.5% (top left), cluster stars with rms better than 2% or with  $I < 18$  (top right), cluster stars with rms better than 1.5% and photometric spectral types later than A9 (bottom left), and cluster stars with photometric spectral types later than A9, and rms better than 2% or  $I < 18$  (bottom right). Since the probabilities are small, we have used a Poisson approximation for each binomial probability distribution. Our statistics based on our cluster cuts are not great enough to yield a very high probability that we should have observed a transiting planet inside an open cluster.

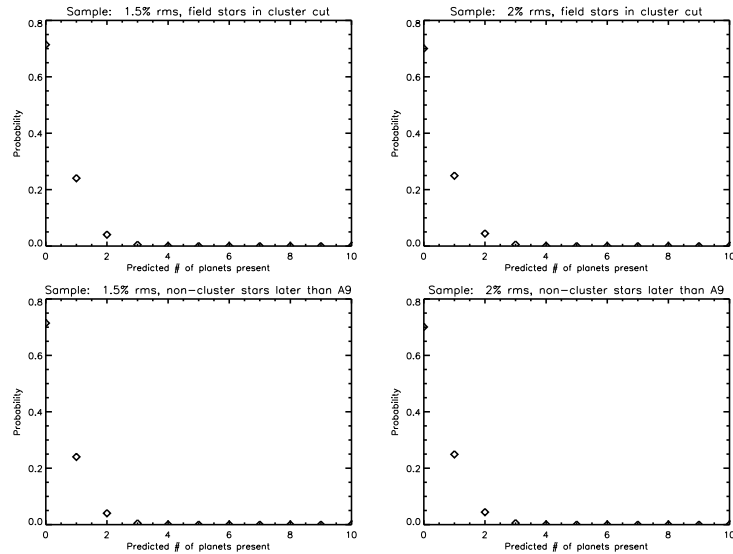


Figure 5.16: The summed joint probabilities over all eight fields of all ways of finding 0-10 planets, including field stars in the cluster cut with rms better than 1.5% (top left), field stars in the cluster cut with rms better than 2% or with  $I < 18$  (top right), field stars in the cluster cut with rms better than 1.5% and photometric spectral types later than A9 (bottom left), and field stars in the cluster cut with photometric spectral types later than A9, and rms better than 2% or  $I < 18$  (bottom right). Since the probabilities are small, we have used a Poisson approximation for each binomial probability distribution. The number statistics are very similar to those for the cluster members, and the field metallicity is subsolar, so the probability of a null detection for field stars in the cluster cut is higher than 50%.

# Chapter 6

## Binary Star Statistics

### 6.1 Introduction

A compilation of contact eclipsing binaries in old open clusters (age > 0.7Gyr) was been given in Rucinski (1998; hereafter R98). This is the largest existing dataset on the properties of contact binaries in cluster fields. Here, we show our dataset, which is  $1.3 \times$  larger than the Rucinski sample, and compare the distributions of the properties of the two samples. Further, we extend to and contrast the distributions of detached eclipsing binaries, which outnumber our contact binary detections by almost 2:1.

### 6.2 The sample

#### 6.2.1 Variable star properties

In Chapter 5, we ranked all light curves with photometric precision better than 2% or magnitudes  $14 < I < 18$  for variability according to a correlation statistic. We then searched the light curves by eye. Typically, the number of light curves searched was of order 10000. Most of the variables, particularly large amplitude, short period variables, were sorted to high figures of merit and easily verified. As the light curves were being searched, they were classified as detached binaries (including semi-detached binaries and low amplitude objects that could be planet candidates), contact binaries, or other variables. Contact binaries were picked out by looking for very smooth, rounded maxima with no kinks between maximum and minimum except at the start and end of the flat bottom of a total eclipse. The numerous  $\delta$  Scuti pulsators were easily classified because of the beat frequencies in the light curve. High signal-to-noise ratio RR Lyrae stars were easily

identified because of their highly asymmetric shape. Light curves with short maxima and long minima, such as  $\alpha^2$  Canum Venaticorum stars, were generally distinguishable from contact binary light curves, but when in doubt, any noisy  $\sim$ sinusoidal variable with a period of around half a day would generally be classified as a contact binary. If there was asymmetry in the light curve, it would be classified as a miscellaneous variable.

We used automated scripts to assist with the determination of periods and eclipse depths. Periods for all binaries were calculated by using a Lomb-Scargle periodogram routine in IDL maintained by Wilms (2006), followed by a sine fit with a starting guess from the peak frequency from the periodogram. The sine fit was performed using the MPFIT package (Markwardt 2006). The light curve was automatically phased according to the fitted frequency, and the result checked by eye. If the automatic phasing did not find the correct period, in particular because of aliasing in the case of detached binaries, the phasing period was manually adjusted, typically in steps no finer than 0.1% of the automatically found period. After the period was verified by eye, the phased light curve was binned by a factor  $\sim 40 - 100$ , depending on the duty cycle of the variability and the noise level of the light curve. The primary amplitude was estimated as the difference between the maximum value and the minimum value on the binned light curve, and in the case of an eclipsing binary, the secondary amplitude was estimated by searching for the local minimum binned value in the light curve at  $0.50 \pm 0.25$  in phase away from the absolute minimum. Refined depths and periods for planet transit candidates were later found using the BLS algorithm plus chi-squared fitting, as described in Chapter 5.

### 6.2.2 Catalogue of binaries: properties and light curves

We have detected 98 contact binaries and 175 detached binaries in our sample. In Tables 6.1 to 6.7, we present a catalogue of the observed properties of the contact binaries. In Tables 6.8 to 6.20, we present a catalogue of the observed properties of the detached binaries.

Figure 6.1 shows typical light curves of binary stars in our sample. In the top panel, star 8297 in NGC 6134, a contact binary with period 0.3 days is shown. In the middle panel, star 13412 in IC 2714, an eclipsing binary which may be either detached or semi-detached (with exact determination requiring in-depth modelling), is shown. In the bottom panel, star 34689, a detached binary with a secondary eclipse, is shown. Note that all classifications are tentative, and require in-depth parameter modelling (possibly in concert with radial velocity curves) at a later date in order to be validated.

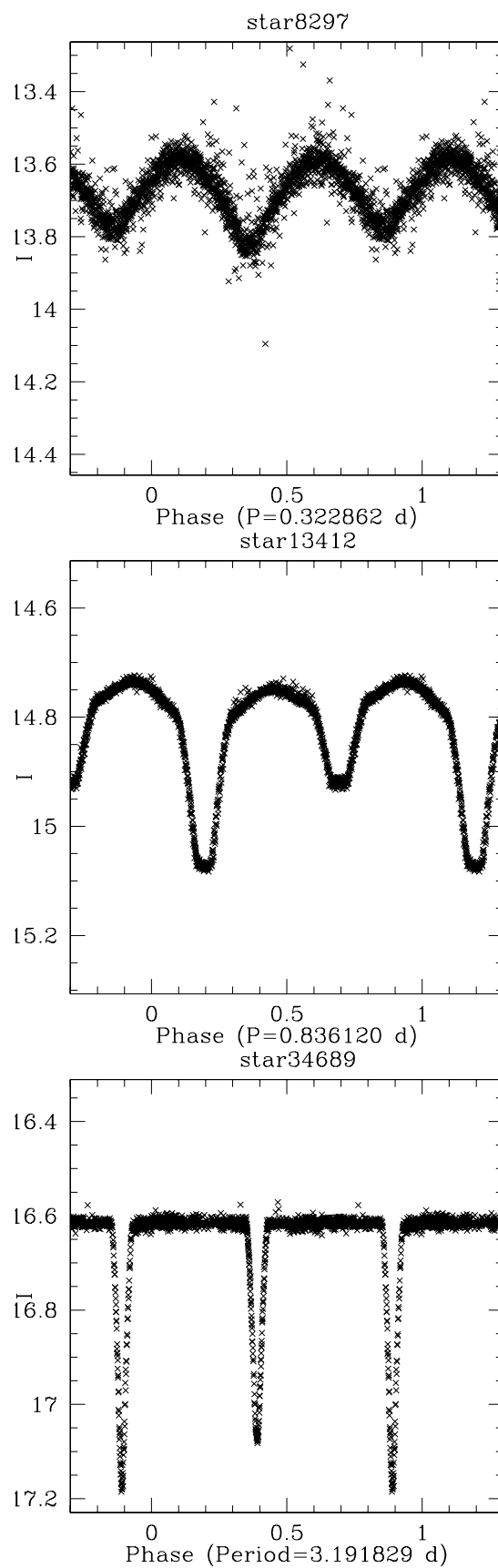


Figure 6.1: Sample light curves of contact (top), possibly semi-detached or detached (middle), and detached (bottom) binaries



Table 6.1: Properties of the contact binaries (part 1)

ID	Cluster	V	B-V	V-R	V-I	Distance	$A_V$	Numerical	Luminosity	Cluster membership	Period	Primary	Secondary	In cluster
						(pc)		spectral type	class	probability	(d)	amplitude	amplitude	aperture?
28463	IC 2714	18.10	1.52	0.91	1.82	2423	2.50	63	3.911	$0.57 \pm 0.04$	0.3434	0.10	0.10	n
8839	IC 2714	17.12	1.18	0.67	1.34	681	0.43	64	5.000	$0.71 \pm 0.10$	0.3305	0.45	0.41	n
27326	IC 2714	15.68	0.81	0.51	1.05	1093	1.68	45	5.000	$0.75 \pm 0.17$	0.5070	0.12	0.12	y
33972	IC 2714	19.28	1.17	0.93	1.82	1535	1.85	63	4.890	$0.69 \pm 0.06$	0.3807	0.44	0.41	n
25668	IC 4651	16.80	0.67	0.43	0.90	2692	1.28	50	4.094	$0.26 \pm 0.15$	0.3821	0.18	0.18	n
17930	IC 4651	15.18	0.78	0.47	0.95	889	0.32	57	4.994	$0.41 \pm 0.18$	0.3621	0.49	0.45	y
27299	IC 4651	16.30	0.56	0.33	0.73	1989	1.25	45	5.000	$-0.08 \pm 0.13$	0.4834	0.31	0.12	n
16709	IC 4651	17.23	0.64	0.39	0.67	12119	1.73	29	4.003	$0.14 \pm 0.07$	0.4510	0.12	0.07	n
7921	IC 4651	16.55	0.94	0.58	1.17	891	0.36	62	5.000	$-0.21 \pm 0.08$	1.1265	0.15	0.10	n
17806	NGC 2447	16.83	0.74	0.41	0.88	1285	0.81	59	5.000	$0.57 \pm 0.16$	0.3002	0.10	0.09	y
4231	NGC 2447	18.59	1.00	0.62	1.23	1406	0.93	63	5.000	$0.40 \pm 0.13$	0.3125	0.70	0.67	y
9531	NGC 2447	17.90	1.14	0.72	1.43	1186	0.64	63	4.954	$0.40 \pm 0.18$	0.2435	0.20	0.19	y
21369	NGC 2447	14.38	0.41	0.25	0.60	1256	0.77	40	5.000	$0.74 \pm 0.14$	0.6124	0.75	0.46	y
12059	NGC 2447	15.00	0.65	0.49	0.95	886	0.17	59	4.816	$0.62 \pm 0.49$	0.2793	0.66	0.63	y

Table 6.2: Properties of the contact binaries (part 2)

ID	Cluster	V	B-V	V-R	V-I	Distance	$A_V$	Numerical	Luminosity	Cluster membership	Period	Primary	Secondary	In cluster
						(pc)		spectral type	class	probability	(d)	amplitude	amplitude	aperture?
9300	NGC 2660	18.09	1.08	0.67	1.29	885	1.48	62	5.000	$0.26 \pm 0.07$	0.3472	0.11	0.11	n
9170	NGC 2660	15.63	0.76	0.47	1.01	2410	1.57	45	3.649	$0.55 \pm 0.13$	0.9733	0.11	0.10	y
7032	NGC 2660	17.47	1.00	0.67	1.25	856	1.43	62	5.000	$0.63 \pm 0.10$	0.3780	0.36	0.35	n
15325	NGC 2660	17.33	1.15	0.88	1.45	742	0.90	63	5.000	$0.47 \pm 0.16$	0.3891	0.37	0.30	n
3520	NGC 2660	18.10	1.22	0.73	1.47	2875	1.60	60	4.431	$0.63 \pm 0.03$	0.4087	0.08	0.06	n
7544	NGC 2660	17.84	1.04	0.79	1.50	5660	2.58	45	2.967	$0.61 \pm 0.08$	0.3204	0.05	0.05	n
2056	NGC 2660	18.70	1.28	0.73	1.46	3162	1.63	59	4.616	$0.66 \pm 0.06$	1.3444	0.05	0.05	y
15201	NGC 2660	19.08	1.76	1.02	1.85	4558	1.96	62	4.222	$0.30 \pm 0.10$	0.3547	0.20	0.19	n
336	NGC 2660	17.42	1.71	0.04	0.72	4272	1.85	37	5.000	$0.61 \pm 0.08$	0.3076	0.08	0.06	n
113	NGC 2660	18.83	1.54	0.55	1.97	141759	4.67	28	0.419	$0.59 \pm 0.02$	0.6315	0.16	0.13	n
16935	NGC 2660	18.55	0.98	0.79	1.40	944	1.52	63	5.000	$0.26 \pm 0.07$	0.2977	0.10	0.07	n
12785	NGC 2660	17.98	1.74	1.05	2.13	788	1.20	69	4.734	$-0.14 \pm 0.18$	0.3637	0.02	0.02	n
20794	NGC 2660	20.39	1.72	1.26	2.91	642	0.26	74	4.904	$0.26 \pm 0.07$	2.1261	0.06	0.06	n
6641	NGC 2660	15.72	0.97	0.62	1.27	4514	1.95	45	2.725	$0.04 \pm 0.32$	3.6367	0.02	0.02	n
8274	NGC 2660	16.35	0.70	0.47	0.94	3233	1.64	45	3.668	$0.20 \pm 0.12$	1.3932	0.02	0.01	y
3293	NGC 2660	17.32	1.21	0.77	1.52	770	1.09	63	4.999	$0.63 \pm 0.10$	4.7557	0.06	0.06	n

Table 6.3: Properties of the contact binaries (part 3)

ID	Cluster	V	B-V	V-R	V-I	Distance	$A_V$	Numerical	Luminosity	Cluster membership	Period	Primary	Secondary	In cluster
						(pc)		spectral type	class	probability	(d)	amplitude	amplitude	aperture?
16443	NGC 5316	16.48	1.07	0.63	1.24	931	0.86	60	4.997	$0.24 \pm 0.25$	0.4062	0.21	0.20	y
18672	NGC 5316	15.68	0.88	0.53	1.06	966	1.04	52	5.000	$0.69 \pm 0.12$	0.3764	0.22	0.22	y
17113	NGC 5316	20.62	4.13	0.78	2.17	1767	2.17	65	4.900	$0.05 \pm 0.08$	0.3605	0.36	0.31	n
24422	NGC 5316	19.11	1.40	0.96	2.00	758	0.51	71	4.923	$0.65 \pm 0.06$	1.7928	0.08	0.08	n
8708	NGC 5316	19.81	2.88	1.04	2.25	2284	2.60	64	4.480	$0.63 \pm 0.04$	1.1847	0.08	0.07	n
3739	NGC 6134	17.07	1.89	1.00	2.13	1414	1.50	66	4.223	$0.59 \pm 0.21$	1.1278	0.18	0.09	n
9349	NGC 6134	17.36	1.38	0.77	1.75	2355	4.04	34	4.702	$0.24 \pm 0.07$	0.4880	0.41	0.38	n
12486	NGC 6134	20.94	2.52	1.79	3.40	2560	6.21	61	3.833	$-0.24 \pm 0.07$	0.4350	0.30	0.15	n
10648	NGC 6134	16.56	1.26	0.79	1.70	1761	3.07	44	4.000	$-0.69 \pm 0.16$	0.7506	0.22	0.18	n
8297	NGC 6134	21.14	1.87	1.18	2.76	968	0.95	73	4.842	$0.04 \pm 0.04$	0.3229	0.18	0.15	n
745	NGC 6134	21.88	1.97	2.50	4.41	1480	1.79	75	4.305	$0.53 \pm 0.02$	0.5452	0.16	0.15	n
8341	NGC 6134	19.44	1.81	1.07	2.39	2534	5.72	34	5.000	$0.56 \pm 0.03$	0.6415	0.30	0.29	n
20244	NGC 6134	18.03	1.29	0.81	1.90	2347	4.00	38	4.739	$-0.15 \pm 0.05$	0.2384	0.70	0.64	n

Table 6.4: Properties of the contact binaries (part 4)

ID	Cluster	V	B-V	V-R	V-I	Distance	$A_V$	Numerical	Luminosity	Cluster membership	Period	Primary	Secondary	In cluster
						(pc)		spectral type	class	probability	(d)	amplitude	amplitude	aperture?
50465	NGC 6208	17.03	0.71	0.45	0.95	6159	1.61	40	3.752	$0.50 \pm 0.05$	0.5460	0.16	0.16	n
48918	NGC 6208	17.05	1.11	0.62	1.47	47764	3.07	39	1.549	$0.50 \pm 0.05$	0.3912	0.29	0.25	n
46693	NGC 6208	17.89	0.77	0.46	1.03	8065	1.68	40	4.000	$0.50 \pm 0.05$	0.5001	0.16	0.14	n
3970	NGC 6208	18.54	0.85	0.69	1.42	9753	1.74	47	2.997	$0.64 \pm 0.03$	0.2939	0.36	0.31	n
38526	NGC 6208	18.19	0.94	0.58	1.01	1116	0.91	63	5.000	$0.18 \pm 0.05$	0.4004	0.35	0.34	n
11972	NGC 6208	17.42	1.20	0.79	1.04	3463	1.52	53	4.011	$0.50 \pm 0.05$	0.3620	0.43	0.37	n
24921	NGC 6208	15.26	0.88	0.56	1.00	1067	0.17	60	4.709	$0.05 \pm 0.26$	0.3174	0.46	0.44	n
55186	NGC 6208	17.01	0.94	0.63	1.07	1075	0.22	63	4.922	$0.61 \pm 0.04$	0.3965	0.16	0.16	n
45367	NGC 6208	17.20	1.00	0.61	1.23	4345	1.55	48	3.530	$0.50 \pm 0.05$	0.3722	0.24	0.21	n
25307	NGC 6208	17.03	1.19	0.80	1.04	1081	0.29	62	4.967	$0.02 \pm 0.08$	0.3156	0.55	0.44	n
5998	NGC 6208	16.84	1.12	0.69	1.15	1083	0.32	63	4.826	$0.55 \pm 0.05$	0.3534	0.36	0.34	n
43146	NGC 6208	17.62	0.68	0.46	1.02	40315	2.81	25	2.526	$0.50 \pm 0.05$	0.4070	0.21	0.20	n
53496	NGC 6208	17.70	0.92	0.69	1.17	1076	0.24	64	5.000	$0.61 \pm 0.04$	0.3867	0.41	0.35	n
33318	NGC 6208	17.80	0.72	0.55	1.07	6781	1.63	45	3.505	$-0.15 \pm 0.07$	0.4135	0.24	0.21	n

Table 6.5: Properties of the contact binaries (part 5)

ID	Cluster	V	B-V	V-R	V-I	Distance	$A_V$	Numerical	Luminosity	Cluster membership	Period	Primary	Secondary	In cluster
						(pc)		spectral type	class	probability	(d)	amplitude	amplitude	aperture?
4325	NGC 6208	19.17	1.30	0.80	1.42	1092	0.44	69	5.000	$0.69 \pm 0.03$	0.3683	0.36	0.23	n
19167	NGC 6208	17.08	0.70	0.48	0.89	4930	1.57	44	3.577	$-0.11 \pm 0.09$	0.4823	0.16	0.14	n
18199	NGC 6208	18.07	1.09	0.70	1.20	1076	0.25	64	5.000	$0.69 \pm 0.03$	0.4123	0.41	0.40	n
37525	NGC 6208	17.58	0.88	0.51	1.03	2525	1.48	52	4.564	$0.50 \pm 0.05$	0.3345	0.09	0.07	n
50029	NGC 6208	17.74	0.75	0.46	1.07	44751	2.96	24	2.424	$0.50 \pm 0.05$	0.3880	0.21	0.14	n
19570	NGC 6208	18.89	1.21	0.70	1.15	6365	1.62	58	4.006	$0.64 \pm 0.03$	0.3234	0.25	0.23	n
7147	NGC 6208	17.51	0.73	0.42	1.29	6001	1.61	42	4.000	$0.50 \pm 0.05$	0.4208	0.38	0.37	n
55610	NGC 6208	17.69	0.74	0.49	1.03	6635	1.63	45	3.448	$0.50 \pm 0.05$	0.6320	0.16	0.08	n
48590	NGC 6208	18.94	1.16	0.82	1.46	4348	1.55	60	4.427	$0.61 \pm 0.04$	0.3191	0.19	0.18	n
23848	NGC 6208	18.95	2.33	1.23	1.73	1174	1.41	65	4.891	$0.18 \pm 0.05$	0.3438	0.32	0.28	n
12269	NGC 6208	19.09	1.05	0.58	1.35	71770	3.91	22	2.323	$0.64 \pm 0.03$	0.3538	0.17	0.15	n
10436	NGC 6208	15.74	0.82	0.43	1.17	44708	2.96	25	1.377	$0.61 \pm 0.23$	0.7883	0.51	0.33	n
4548	NGC 6208	17.95	1.29	0.82	1.88	89330	4.53	30	1.051	$0.50 \pm 0.05$	0.2452	0.31	0.27	n
11429	NGC 6208	18.48	1.24	0.55	1.29	3804	1.53	53	4.556	$0.10 \pm 0.04$	0.5325	0.10	0.09	n
45005	NGC 6208	17.74	0.99	0.70	1.22	1076	0.23	64	5.000	$0.61 \pm 0.04$	0.2842	0.06	0.03	n
18574	NGC 6208	18.74	1.01	0.74	1.46	26675	2.33	45	2.427	$0.15 \pm 0.05$	0.9494	0.04	0.02	n
36704	NGC 6208	17.05	0.90	0.61	1.16	8313	1.69	45	2.790	$-0.15 \pm 0.07$	0.4155	0.02	0.02	n

Table 6.6: Properties of the contact binaries (part 6)

ID	Cluster	V	B-V	V-R	V-I	Distance	$A_V$	Numerical	Luminosity	Cluster membership	Period	Primary	Secondary	In cluster
						(pc)		spectral type	class	probability	(d)	amplitude	amplitude	aperture?
9999	NGC 6253	18.36	1.01	0.74	1.44	24614	2.40	45	2.359	$0.71 \pm 0.02$	0.2940	0.32	0.30	n
6461	NGC 6253	15.76	1.02	0.23	0.68	1102	0.20	58	4.999	$0.78 \pm 0.10$	0.7738	0.24	0.19	y
20743	NGC 6253	18.60	1.17	0.82	1.31	1147	0.95	64	4.998	$0.17 \pm 0.10$	0.3709	0.55	0.52	n
34411	NGC 6253	17.82	0.99	0.63	1.12	1106	0.24	64	5.000	$-0.20 \pm 0.07$	0.3635	0.33	0.32	n
40310	NGC 6253	16.47	0.76	0.54	1.02	3708	1.55	45	3.596	$0.78 \pm 0.08$	0.4363	0.32	0.31	n
38662	NGC 6253	18.30	0.77	0.57	1.06	6163	1.65	45	4.311	$0.71 \pm 0.02$	0.5330	0.29	0.28	n
38102	NGC 6253	17.39	1.07	0.71	1.36	1123	0.47	63	4.916	$0.57 \pm 0.04$	0.2911	0.25	0.19	n
47785	NGC 6253	16.67	0.72	0.48	1.04	4301	1.57	44	3.370	$0.78 \pm 0.08$	0.3598	0.31	0.29	n
33417	NGC 6253	15.00	0.58	0.42	0.87	1099	0.18	51	5.000	$0.55 \pm 0.15$	0.4273	0.41	0.25	y
44635	NGC 6253	18.83	0.83	0.61	1.26	9069	1.76	45	3.790	$0.71 \pm 0.02$	0.3179	0.30	0.25	n
4462	NGC 6253	16.80	0.51	0.36	0.74	8794	1.75	31	4.000	$0.78 \pm 0.08$	0.5173	0.25	0.24	n

Table 6.7: Properties of the contact binaries (part 7)

ID	Cluster	V	B-V	V-R	V-I	Distance	$A_V$	Numerical	Luminosity	Cluster membership	Period	Primary	Secondary	In cluster
						(pc)		spectral type	class	probability	(d)	amplitude	amplitude	aperture?
14346	NGC 6253	14.88	0.71	0.45	0.92	1144	0.93	45	4.887	$0.72 \pm 0.12$	0.4968	0.32	0.32	y
24738	NGC 6253	18.49	1.17	0.59	1.35	5338	1.61	52	4.052	$0.22 \pm 0.03$	0.3378	0.21	0.18	n
13647	NGC 6253	15.69	0.54	0.39	0.77	3411	1.54	40	3.713	$0.68 \pm 0.21$	0.4789	0.08	0.06	n
23857	NGC 6253	18.86	0.49	-0.08	1.14	20651	2.23	29	4.000	$0.26 \pm 0.04$	0.3827	0.23	0.23	n
20204	NGC 6253	16.07	0.64	0.42	0.85	3302	1.53	40	4.210	$0.51 \pm 0.12$	0.6097	0.10	0.09	n
16019	NGC 6253	18.28	1.19	0.70	1.31	1107	0.25	65	5.000	$0.62 \pm 0.03$	0.2731	0.35	0.33	n
38417	NGC 6253	17.59	0.86	0.60	1.15	6174	1.65	45	3.508	$0.79 \pm 0.05$	0.3204	0.07	0.07	n
19531	NGC 6253	18.70	1.15	0.68	1.42	18710	2.16	47	2.618	$0.71 \pm 0.02$	0.2866	0.17	0.14	n
33482	NGC 6253	18.01	0.86	0.64	1.17	1106	0.24	64	5.000	$0.62 \pm 0.03$	0.3335	0.10	0.09	n
44870	NGC 6253	18.00	1.07	0.68	1.41	20016	2.21	46	2.417	$0.79 \pm 0.05$	0.4122	0.09	0.08	n
37661	NGC 6253	17.52	0.60	0.47	0.90	5925	1.64	45	3.505	$0.79 \pm 0.05$	0.9156	0.44	0.27	n
29142	NGC 6253	18.11	0.94	0.56	1.04	3664	1.55	57	4.221	$0.22 \pm 0.03$	0.3953	0.10	0.08	n

Table 6.8: Properties of the detached binaries (part 1)

ID	Cluster	V	B-V	V-R	V-I	Distance (pc)	$A_V$	Numerical spectral type	Luminosity class	Cluster membership probability	Period (d)	Primary amplitude	Secondary amplitude	In cluster aperture?
13412	IC 2714	16.11	0.97	0.65	1.31	2791	2.93	34	4.097	$-0.23 \pm 0.32$	0.8370	0.28	0.17	n
22405	IC 2714	14.91	0.68	0.47	0.96	1175	1.70	40	4.805	$0.73 \pm 0.21$	0.7116	0.32	0.18	y
8511	IC 2714	16.89	0.97	0.64	1.33	2075	2.19	43	4.768	$0.58 \pm 0.18$	4.6853	0.17	0.07	n
19575	IC 2714	20.82	1.52	1.16	2.57	1296	1.75	73	4.618	$0.24 \pm 0.09$	1.1875	0.29	0.27	n
34689	IC 2714	18.93	1.92	1.05	2.32	640	0.18	72	4.910	$0.73 \pm 0.05$	3.2071	0.37	0.29	n
30825	IC 2714	17.66	1.13	0.82	1.59	1110	1.68	61	4.868	$0.80 \pm 0.20$	1.2397	0.08	0.06	n
12590	IC 2714	16.98	1.10	0.72	1.47	1167	1.70	57	4.885	$-0.03 \pm 0.26$	2.9347	0.04	0.03	y
24209	IC 2714	18.68	1.46	0.89	1.82	2008	2.13	62	4.637	$-0.16 \pm 0.07$	0.3908	0.10	0.02	n
28923	IC 2714	14.94	0.80	0.55	1.10	687	0.52	59	4.861	$0.74 \pm 0.14$	8.0320	0.13	0.08	y
16891	IC 2714	19.45	1.69	1.30	2.54	3236	3.57	62	4.099	$-0.15 \pm 0.15$	2.6469	0.33	0.02	n
1489	IC 2714	19.21	2.33	1.21	2.50	5128	6.21	33	2.781	$0.66 \pm 0.04$	2.4245	0.09	0.04	n
4781	IC 2714	18.88	1.91	1.25	2.46	5973	6.70	25	5.000	$0.66 \pm 0.04$	3.7667	0.04	0.02	n
31296	IC 2714	17.67	1.09	0.76	1.72	2907	3.08	45	3.920	$0.55 \pm 0.11$	3.9967	0.05	0.05	n
34753	IC 2714	20.83	2.99	1.55	2.83	3533	4.05	62	4.285	$0.57 \pm 0.04$	1.8919	0.27	0.04	n
11667	IC 2714	19.43	2.65	1.08	2.29	3279	3.64	58	4.000	$0.15 \pm 0.07$	2.2552	0.04	0.02	n
11759	IC 2714	21.44	1.22	1.61	3.37	9377	7.09	42	2.469	$0.15 \pm 0.07$	0.8933	0.20	0.04	n
4987	IC 2714	17.75	1.50	0.86	1.89	708	1.11	66	4.872	$0.71 \pm 0.10$	12.4348	0.07	0.03	n
811	IC 2714	18.08	1.21	0.67	1.39	2512	2.59	45	4.970	$0.66 \pm 0.04$	7.0679	0.02	0.02	n
30288	IC 2714	21.03	1.17	1.69	3.19	660	0.22	75	4.675	$0.73 \pm 0.05$	1.6191	0.03	0.03	n



Table 6.9: Properties of the detached binaries (part 2)

ID	Cluster	V	B-V	V-R	V-I	Distance	$A_V$	Numerical	Luminosity	Cluster membership	Period	Primary	Secondary	In cluster
						(pc)		spectral type	class	probability	(d)	amplitude	amplitude	aperture?
34041	IC 4651	17.02	0.86	0.54	1.02	889	0.33	63	5.000	$0.04 \pm 0.08$	5.6909	0.31	0.02	n
41072	IC 4651	17.37	0.84	0.52	1.10	3328	1.31	49	4.209	$0.14 \pm 0.16$	0.8883	0.02	0.01	n
11821	IC 4651	18.82	1.05	0.69	1.40	2267	1.26	63	4.634	$0.10 \pm 0.06$	0.6701	0.11	0.09	n
29899	IC 4651	17.20	0.82	0.57	0.99	9970	1.63	40	2.811	$0.14 \pm 0.07$	0.5027	0.01	0.01	n
26780	IC 4651	16.03	0.91	0.59	1.10	868	0.16	62	4.914	$-0.21 \pm 0.08$	1.9866	0.03	0.02	n
32244	IC 4651	17.54	0.91	0.56	1.08	3331	1.31	56	4.200	$-0.15 \pm 0.07$	0.9271	0.02	0.01	n
7985	IC 4651	18.51	0.96	0.62	1.16	2021	1.25	63	4.622	$0.04 \pm 0.07$	1.7424	0.07	0.03	n
18318	IC 4651	18.37	1.01	0.65	1.16	1974	1.24	63	4.592	$-0.10 \pm 0.10$	2.7173	0.25	0.13	n
22925	IC 4651	16.90	1.11	0.77	1.33	880	0.24	64	4.901	$-0.25 \pm 0.12$	4.2711	0.36	0.32	n

Table 6.10: Properties of the detached binaries (part 3)

ID	Cluster	V	B-V	V-R	V-I	Distance	$A_V$	Numerical	Luminosity	Cluster membership	Period	Primary	Secondary	In cluster
						(pc)		spectral type	class	probability	(d)	amplitude	amplitude	aperture?
3735	NGC 2447	17.65	1.05	0.61	1.30	1128	0.52	63	5.000	$0.76 \pm 0.12$	0.8420	0.63	0.45	y
11462	NGC 2447	16.43	0.66	0.40	0.88	1014	0.31	61	5.000	$-0.07 \pm 0.30$	1.1625	0.17	0.08	y
9021	NGC 2447	17.61	1.16	0.72	1.45	937	0.21	65	4.970	$0.34 \pm 0.35$	1.5690	0.24	0.18	y
15760	NGC 2447	19.20	1.11	0.67	1.33	13315	2.39	63	3.016	$0.73 \pm 0.09$	1.6349	0.16	0.00	n
212	NGC 2447	16.21	0.92	0.49	1.19	1306	0.83	59	4.719	$0.57 \pm 0.16$	1.3722	0.03	0.02	y
19573	NGC 2447	20.35	1.63	1.03	2.62	782	0.12	73	4.943	$0.72 \pm 0.13$	0.7777	0.12	0.00	y
6119	NGC 2447	17.68	0.77	0.40	0.99	3052	1.18	51	4.591	$-0.28 \pm 0.11$	6.7681	0.06	0.04	n
3935	NGC 2447	18.66	0.91	0.62	1.40	3167	1.20	61	4.609	$0.73 \pm 0.09$	2.2044	0.29	0.27	n
4439	NGC 2447	17.91	0.63	0.47	1.19	14086	2.48	37	2.659	$0.41 \pm 0.07$	0.4969	0.13	0.00	n
8847	NGC 2447	18.69	0.92	0.52	1.23	10241	2.03	42	3.049	$-0.01 \pm 0.11$	0.9845	0.02	0.00	n
3520	NGC 2447	17.45	1.02	0.58	1.31	1060	0.39	63	4.984	$0.76 \pm 0.12$	0.4991	0.04	0.00	y
11724	NGC 2447	17.87	1.07	0.59	1.41	1092	0.45	64	5.000	$0.40 \pm 0.18$	0.3354	0.01	0.00	y
17417	NGC 2447	16.21	0.79	0.47	0.97	15969	2.71	25	2.945	$0.43 \pm 0.09$	0.7127	0.01	0.00	n
6932	NGC 2447	18.06	1.02	0.59	1.23	5319	1.45	50	3.754	$-0.01 \pm 0.11$	0.9041	0.02	0.02	n
4346	NGC 2447	15.47	0.56	0.30	0.65	8166	1.79	29	3.011	$0.39 \pm 0.14$	5.9598	0.04	0.02	n
6341	NGC 2447	16.01	0.69	0.19	0.63	6658	1.61	30	4.427	$0.43 \pm 0.09$	4.4228	0.18	0.14	n

Table 6.11: Properties of the detached binaries (part 4)

ID	Cluster	V	B-V	V-R	V-I	Distance	$A_V$	Numerical	Luminosity	Cluster membership	Period	Primary	Secondary	In cluster
						(pc)		spectral type	class	probability	(d)	amplitude	amplitude	aperture?
14704	NGC 2660	15.25	0.64	0.53	0.88	628	0.21	61	5.000	$0.72 \pm 0.37$	1.4593	0.29	0.29	n
21269	NGC 2660	18.59	1.24	0.73	1.55	5524	2.50	47	3.695	$-0.05 \pm 0.03$	2.2338	0.19	0.17	n
1281	NGC 2660	16.73	0.83	0.53	1.13	2878	1.60	45	4.426	$0.64 \pm 0.09$	0.9466	0.77	0.25	y
28342	NGC 2660	17.73	0.75	0.53	1.16	6007	2.77	32	4.809	$0.61 \pm 0.08$	1.2686	0.55	0.16	n
6750	NGC 2660	18.73	0.88	0.72	1.38	4779	2.07	46	4.584	$0.59 \pm 0.02$	1.4826	0.09	0.05	n
9974	NGC 2660	19.02	0.96	0.70	1.57	7277	3.20	38	4.082	$-0.05 \pm 0.03$	0.3783	0.10	0.00	n
19223	NGC 2660	18.49	1.30	0.95	1.78	2742	1.59	62	4.452	$0.28 \pm 0.06$	2.0999	0.28	0.11	n
22861	NGC 2660	18.17	1.02	0.58	1.21	3131	1.62	49	4.912	$0.66 \pm 0.06$	0.1837	1.11	0.00	y
28904	NGC 2660	18.99	1.10	0.53	1.41	36074	3.62	29	2.412	$0.59 \pm 0.02$	1.5919	0.28	0.18	n
9987	NGC 2660	18.65	1.13	0.71	1.29	942	1.52	63	4.992	$0.32 \pm 0.08$	0.6294	0.29	0.11	n
16339	NGC 2660	18.35	1.26	0.74	1.49	2946	1.61	59	4.521	$0.65 \pm 0.14$	1.7105	0.27	0.27	y

Table 6.12: Properties of the detached binaries (part 5)

ID	Cluster	V	B-V	V-R	V-I	Distance	$A_V$	Numerical	Luminosity	Cluster membership	Period	Primary	Secondary	In cluster
						(pc)		spectral type	class	probability	(d)	amplitude	amplitude	aperture?
24794	NGC 2660	16.44	0.91	0.57	1.14	3325	1.65	46	3.559	$0.64 \pm 0.09$	4.9308	0.05	0.00	y
3989	NGC 2660	18.53	0.98	0.77	1.56	5489	2.47	45	4.028	$0.59 \pm 0.02$	1.6826	0.46	0.41	n
13720	NGC 2660	17.46	0.83	0.57	1.18	3424	1.66	45	4.549	$-0.24 \pm 0.14$	1.7157	0.09	0.09	y
3244	NGC 2660	19.50	0.94	0.90	1.75	6400	2.96	45	4.154	$0.59 \pm 0.02$	1.5759	0.27	0.26	n
5398	NGC 2660	16.93	0.90	0.73	1.51	5211	2.31	45	2.855	$0.51 \pm 0.13$	1.3932	0.14	0.03	n
15800	NGC 2660	18.70	1.47	0.73	1.72	33511	3.59	41	2.000	$-0.01 \pm 0.07$	7.1510	0.05	0.00	n
14494	NGC 2660	15.40	0.69	0.44	0.89	4140	1.81	39	2.835	$0.83 \pm 0.35$	2.9193	0.12	0.04	n
26373	NGC 2660	17.70	0.83	0.65	1.24	4354	1.88	45	4.254	$0.61 \pm 0.08$	3.3386	0.23	0.09	n
9149	NGC 2660	19.32	0.68	0.83	1.46	5098	2.24	46	4.782	$0.59 \pm 0.02$	8.1647	0.12	0.00	n
23893	NGC 2660	16.28	0.96	0.59	1.23	4219	1.84	45	2.925	$0.51 \pm 0.13$	4.8686	0.04	0.02	n
26730	NGC 2660	18.97	1.00	0.69	1.48	6155	2.85	39	4.431	$0.59 \pm 0.02$	4.1919	0.12	0.06	n

Table 6.13: Properties of the detached binaries (part 6)

ID	Cluster	V	B-V	V-R	V-I	Distance	$A_V$	Numerical	Luminosity	Cluster membership	Period	Primary	Secondary	In cluster
						(pc)		spectral type	class	probability	(d)	amplitude	amplitude	aperture?
2054	NGC 5316	15.51	0.72	0.46	1.00	973	1.07	50	5.000	$0.69 \pm 0.12$	3.1837	0.18	0.07	y
5450	NGC 5316	18.39	1.80	1.14	2.35	388	0.26	72	5.000	$0.65 \pm 0.06$	4.3706	0.17	0.14	n
22841	NGC 5316	17.86	1.48	1.08	2.07	2864	4.09	42	2.978	$0.54 \pm 0.07$	5.9340	0.25	0.23	n
2474	NGC 5316	21.46	0.67	2.81	4.86	2523	2.95	75	3.985	$0.63 \pm 0.04$	3.7992	0.10	0.09	n
548	NGC 5316	18.74	2.24	1.13	2.57	374	0.25	73	4.999	$0.65 \pm 0.06$	0.6524	0.14	0.13	n
15542	NGC 5316	15.49	0.96	0.55	1.07	934	0.88	55	4.984	$0.41 \pm 0.21$	0.7792	0.22	0.14	y
8888	NGC 5316	17.74	1.28	0.91	1.76	2068	2.39	55	4.365	$0.54 \pm 0.07$	2.7508	0.10	0.09	n
22353	NGC 5316	21.04	2.04	0.88	3.05	901	0.74	76	4.500	$0.59 \pm 0.06$	7.2191	0.51	0.43	y
1926	NGC 5316	21.41	2.20	2.30	3.84	1006	1.25	73	4.839	$0.59 \pm 0.06$	6.8979	0.19	0.00	y
8382	NGC 5316	21.39	1.53	3.23	5.95	3591	9.72	42	2.530	$-0.31 \pm 0.09$	3.0944	0.09	0.04	n
23815	NGC 5316	18.84	2.20	1.11	2.32	511	0.34	72	5.000	$0.65 \pm 0.06$	4.1605	0.16	0.08	n
8566	NGC 5316	15.13	0.75	0.48	1.01	1185	1.76	40	4.993	$0.69 \pm 0.12$	1.2976	0.05	0.03	y
20128	NGC 5316	19.23	2.31	1.38	2.65	1107	1.64	72	4.558	$0.59 \pm 0.06$	7.1844	0.61	0.25	y
10326	NGC 5316	19.67	2.58	1.45	3.00	457	0.30	74	4.856	$0.20 \pm 0.09$	2.6325	0.14	0.13	n
7625	NGC 5316	21.04	2.01	1.94	3.91	3340	7.92	33	3.054	$0.50 \pm 0.05$	1.5314	0.40	0.33	n

Table 6.14: Properties of the detached binaries (part 7)

ID	Cluster	V	B-V	V-R	V-I	Distance	$A_V$	Numerical	Luminosity	Cluster membership	Period	Primary	Secondary	In cluster
						(pc)		spectral type	class	probability	(d)	amplitude	amplitude	aperture?
19826	NGC 5316	17.04	1.18	0.65	1.37	1259	1.82	52	5.000	$0.79 \pm 0.46$	2.7350	0.37	0.09	y
22352	NGC 5316	20.60	3.18	1.50	3.29	2488	2.89	72	4.145	$0.63 \pm 0.04$	2.7996	0.11	0.06	n
19654	NGC 5316	20.11	1.93	1.07	2.04	1446	1.95	65	4.935	$0.01 \pm 0.07$	1.7069	0.17	0.00	n
139	NGC 5316	21.29	0.98	2.14	4.28	1001	1.23	76	4.405	$0.59 \pm 0.06$	3.2570	0.27	0.22	y
26123	NGC 5316	18.92	1.60	1.18	2.68	402	0.26	73	5.000	$0.65 \pm 0.06$	3.9239	0.31	0.25	n
26169	NGC 5316	19.15	2.69	1.75	3.49	381	0.25	73	5.000	$0.65 \pm 0.06$	3.1353	0.26	0.17	n
21643	NGC 5316	19.39	1.82	1.14	2.16	3055	5.38	63	3.202	$0.63 \pm 0.04$	2.6954	0.13	0.08	n
17478	NGC 5316	19.97	2.78	2.03	3.29	902	0.75	75	4.438	$0.02 \pm 0.11$	4.1080	0.05	0.00	y
20416	NGC 5316	17.77	2.22	1.16	2.36	290	0.19	72	4.999	$0.69 \pm 0.14$	2.6673	0.04	0.02	n
946	NGC 5316	17.22	1.80	1.13	2.33	232	0.15	72	5.000	$0.69 \pm 0.14$	9.6192	0.05	0.03	n
13437	NGC 5316	16.29	1.00	0.69	1.60	2310	2.63	47	3.000	$-0.13 \pm 0.16$	2.1177	0.06	0.00	n
17072	NGC 5316	16.34	1.05	0.59	1.15	639	0.42	63	5.000	$0.04 \pm 0.40$	4.3808	0.31	0.00	n
20959	NGC 5316	16.52	0.95	0.59	1.20	1612	2.06	45	4.907	$0.61 \pm 0.09$	3.7140	0.03	0.00	n
25865	NGC 5316	16.43	0.98	0.57	1.22	963	1.02	59	5.000	$0.68 \pm 0.15$	2.6907	0.31	0.24	y
10469	NGC 5316	19.62	2.73	1.48	2.97	1503	1.99	72	4.341	$0.63 \pm 0.04$	1.2735	0.04	0.00	n

Table 6.15: Properties of the detached binaries (part 8)

ID	Cluster	V	B-V	V-R	V-I	Distance	$A_V$	Numerical	Luminosity	Cluster membership	Period	Primary	Secondary	In cluster
						(pc)		spectral type	class	probability	(d)	amplitude	amplitude	aperture?
17840	NGC 6134	17.82	1.27	1.09	2.13	2360	4.06	45	3.400	$-0.98 \pm 0.15$	1.6805	0.24	0.00	n
3342	NGC 6134	16.93	1.22	0.75	1.59	1602	2.65	46	4.570	$0.39 \pm 0.08$	4.1779	0.20	0.19	n
22149	NGC 6134	19.02	1.54	1.08	2.40	541	0.53	72	4.921	$0.79 \pm 0.07$	1.0729	0.42	0.00	n
10295	NGC 6134	21.56	4.62	2.06	3.97	2574	6.47	66	3.844	$-0.17 \pm 0.04$	5.3318	0.10	0.03	n
3952	NGC 6134	15.82	1.15	0.69	1.50	2126	3.49	34	3.818	$0.57 \pm 0.10$	2.0977	0.04	0.01	n
9447	NGC 6134	19.93	2.09	0.95	2.13	1306	1.29	68	4.933	$0.53 \pm 0.02$	2.4319	0.23	0.11	n
19175	NGC 6134	15.88	1.19	0.69	1.46	1549	2.29	47	3.986	$0.57 \pm 0.10$	0.3715	0.18	0.00	n
4563	NGC 6134	16.47	1.34	0.81	1.75	1853	3.18	45	3.472	$0.39 \pm 0.08$	4.2156	0.43	0.41	n
3222	NGC 6134	19.24	1.62	1.06	2.29	528	0.52	72	5.000	$0.79 \pm 0.07$	2.0585	0.13	0.03	n
5891	NGC 6134	18.07	1.68	0.94	2.00	880	0.86	68	4.786	$0.65 \pm 0.03$	0.4684	0.57	0.53	n
19567	NGC 6134	18.16	1.56	1.02	2.38	285	0.28	73	4.924	$0.34 \pm 0.11$	1.8539	0.19	0.16	n
16610	NGC 6134	19.29	2.03	1.08	2.46	840	0.82	72	4.676	$0.04 \pm 0.04$	0.4352	0.04	0.04	n
6892	NGC 6134	18.64	1.83	1.14	2.43	2513	5.43	40	3.298	$-0.15 \pm 0.05$	2.4514	0.05	0.04	n
7783	NGC 6134	18.09	1.49	1.01	2.15	442	0.44	71	5.000	$0.34 \pm 0.11$	2.6033	0.07	0.04	n

Table 6.16: Properties of the detached binaries (part 9)

ID	Cluster	V	B-V	V-R	V-I	Distance	$A_V$	Numerical	Luminosity	Cluster membership	Period	Primary	Secondary	In cluster
						(pc)		spectral type	class	probability	(d)	amplitude	amplitude	aperture?
20577	NGC 6134	18.68	1.58	0.98	2.20	787	0.77	72	4.633	$0.04 \pm 0.04$	3.2428	0.06	0.00	n
12626	NGC 6134	19.27	1.39	0.91	2.01	2211	3.62	46	5.000	$-0.15 \pm 0.05$	1.1568	0.09	0.00	n
1479	NGC 6134	18.13	2.03	0.89	3.98	224	0.22	75	4.582	$0.79 \pm 0.07$	2.6403	0.29	0.00	n
13985	NGC 6134	17.88	1.64	0.76	1.80	883	0.87	66	4.838	$0.46 \pm 0.20$	0.8007	0.05	0.03	n
23262	NGC 6134	20.75	1.90	1.37	2.74	1511	2.00	72	4.671	$0.53 \pm 0.02$	8.0216	0.12	0.00	n
12913	NGC 6134	21.44	7.90	2.08	4.39	2216	3.63	75	3.970	$-0.25 \pm 0.04$	16.8009	0.42	0.00	n
18882	NGC 6134	19.04	1.42	0.88	1.90	2141	3.51	46	5.000	$-0.15 \pm 0.05$	1.5457	0.04	0.00	n
4634	NGC 6134	18.72	1.40	0.90	1.77	1443	1.60	63	4.808	$0.53 \pm 0.02$	5.9745	0.01	0.00	n
17859	NGC 6134	17.71	1.97	1.23	2.57	1512	2.00	70	4.141	$0.47 \pm 0.30$	17.9677	0.15	0.00	n
6200	NGC 6134	17.18	1.27	0.72	1.69	2375	4.14	31	5.000	$0.24 \pm 0.07$	3.7249	0.17	0.04	n
8950	NGC 6134	16.92	1.23	0.75	1.70	2381	4.16	32	4.562	$0.39 \pm 0.08$	5.3547	0.04	0.00	n
21571	NGC 6134	19.16	1.95	0.95	2.10	802	0.79	70	5.000	$0.65 \pm 0.03$	10.3101	0.15	0.07	n
23319	NGC 6134	18.55	1.60	1.10	2.28	662	0.65	72	4.837	$0.65 \pm 0.03$	27.9953	0.08	0.00	n



Table 6.17: Properties of the detached binaries (part 10)

ID	Cluster	V	B-V	V-R	V-I	Distance	$A_V$	Numerical	Luminosity	Cluster membership	Period	Primary	Secondary	In cluster
						(pc)		spectral type	class	probability	(d)	amplitude	amplitude	aperture?
31274	NGC 6208	15.18	1.24	0.70	1.34	1081	0.29	63	4.277	$0.16 \pm 0.15$	4.6483	0.11	0.00	n
6543	NGC 6208	15.60	1.09	0.71	1.31	1062	0.14	64	4.477	$0.53 \pm 0.09$	3.0421	0.19	0.16	n
8644	NGC 6208	17.13	0.67	0.59	1.07	4860	1.57	45	3.608	$0.50 \pm 0.05$	3.2203	0.37	0.18	n
14193	NGC 6208	15.68	0.80	0.53	0.98	1114	0.90	51	5.000	$-0.36 \pm 0.20$	4.4456	0.30	0.19	y
34878	NGC 6208	18.32	1.68	1.04	2.03	1132	1.16	67	4.686	$0.18 \pm 0.05$	1.3303	0.27	0.26	n
42815	NGC 6208	18.63	0.53	0.38	1.32	13053	1.85	37	3.999	$0.64 \pm 0.03$	1.0873	0.65	0.16	n
40797	NGC 6208	16.66	0.96	0.61	1.24	11706	1.81	45	2.479	$0.57 \pm 0.08$	4.6245	0.19	0.16	n
22341	NGC 6208	17.70	1.01	0.64	1.13	1076	0.24	63	5.000	$0.12 \pm 0.06$	1.3941	0.05	0.00	n
23038	NGC 6208	17.86	1.18	0.70	1.37	1095	0.54	63	5.000	$0.61 \pm 0.04$	1.8513	0.98	0.39	n
9377	NGC 6208	16.70	0.95	0.62	1.13	1072	0.20	63	4.784	$0.55 \pm 0.05$	0.9875	0.10	0.08	n
10256	NGC 6208	17.26	0.51	0.32	0.72	11201	1.79	30	4.017	$0.50 \pm 0.05$	2.4924	0.14	0.08	n
39457	NGC 6208	18.52	1.47	0.99	2.02	1055	0.11	71	4.758	$0.69 \pm 0.03$	0.8958	0.49	0.41	n
12407	NGC 6208	16.74	1.01	0.55	1.12	1113	0.85	60	5.000	$-0.06 \pm 0.08$	0.4913	0.01	0.00	n

Table 6.18: Properties of the detached binaries (part 11)

ID	Cluster	V	B-V	V-R	V-I	Distance	$A_V$	Numerical	Luminosity	Cluster membership	Period	Primary	Secondary	In cluster
						(pc)		spectral type	class	probability	(d)	amplitude	amplitude	aperture?
31238	NGC 6208	18.19	1.05	0.78	1.50	23000	2.20	47	2.376	$0.64 \pm 0.03$	13.2731	0.01	0.00	n
23211	NGC 6208	16.49	0.85	0.85	1.33	3907	1.53	48	3.000	$0.57 \pm 0.08$	4.5804	0.10	0.08	n
27834	NGC 6208	16.92	0.86	0.53	1.02	2074	1.47	50	4.518	$0.15 \pm 0.24$	7.4260	0.19	0.04	n
28082	NGC 6208	16.64	1.35	0.79	1.45	1085	0.34	64	4.637	$0.02 \pm 0.10$	0.5005	0.01	0.00	n
31691	NGC 6208	16.79	1.04	0.64	1.20	1072	0.21	63	4.810	$0.02 \pm 0.10$	47.9818	0.03	0.00	n
40597	NGC 6208	17.35	0.84	0.52	1.01	4633	1.56	47	3.604	$0.50 \pm 0.05$	37.1772	0.01	0.00	n
51146	NGC 6208	17.20	1.50	1.24	1.86	1153	1.35	65	4.477	$0.61 \pm 0.04$	10.5069	0.11	0.04	n
21800	NGC 6208	17.68	1.34	0.53	1.30	1134	1.21	61	5.000	$0.12 \pm 0.06$	38.0203	0.12	0.00	n
49312	NGC 6208	19.06	1.06	0.90	2.07	1070	0.20	71	4.884	$0.69 \pm 0.03$	3.2349	0.25	0.00	n
29403	NGC 6208	16.21	0.92	0.57	1.22	3580	1.52	46	3.131	$-0.18 \pm 0.17$	6.6811	0.07	0.00	n
31171	NGC 6208	16.80	1.32	0.73	1.36	1073	0.20	64	4.730	$0.02 \pm 0.10$	7.9993	0.03	0.00	n
43157	NGC 6208	18.71	1.11	0.72	1.41	9330	1.72	49	3.006	$0.64 \pm 0.03$	38.7786	0.03	0.00	n
53118	NGC 6208	16.16	0.81	0.53	1.37	31789	2.51	40	1.687	$0.57 \pm 0.08$	7.8000	0.01	0.00	n

Table 6.19: Properties of the detached binaries (part 12)

ID	Cluster	V	B-V	V-R	V-I	Distance	$A_V$	Numerical	Luminosity	Cluster membership	Period	Primary	Secondary	In cluster
						(pc)		spectral type	class	probability	(d)	amplitude	amplitude	aperture?
43651	NGC 6253	15.24	0.76	0.49	0.97	1145	0.91	47	5.000	$0.78 \pm 0.10$	1.9797	0.12	0.05	y
1183	NGC 6253	18.03	0.53	0.29	0.77	15015	2.01	30	4.026	$0.71 \pm 0.02$	2.2160	0.35	0.15	n
35495	NGC 6253	16.51	0.88	0.63	1.12	1077	0.09	62	4.915	$0.61 \pm 0.06$	0.8514	0.45	0.27	n
1284	NGC 6253	17.58	1.04	0.59	1.10	1141	0.84	63	4.856	$0.57 \pm 0.04$	4.2555	0.08	0.04	n
1388	NGC 6253	20.21	1.71	1.18	1.84	16841	2.08	62	3.468	$0.56 \pm 0.03$	0.5001	0.53	0.43	n
20122	NGC 6253	17.97	0.94	0.70	1.21	1106	0.24	64	5.000	$0.07 \pm 0.08$	3.0824	0.30	0.18	n
16195	NGC 6253	17.01	0.95	0.55	1.08	1138	0.77	61	5.000	$-0.20 \pm 0.07$	6.5812	0.29	0.24	n
4220	NGC 6253	16.70	0.79	0.46	0.97	1116	0.36	61	4.999	$0.61 \pm 0.06$	1.7052	0.06	0.03	n
21658	NGC 6253	16.36	0.92	0.58	1.15	1099	0.18	62	4.870	$0.36 \pm 0.10$	1.7339	0.03	0.01	n
46192	NGC 6253	17.10	0.95	0.68	1.31	1115	0.36	62	4.926	$0.57 \pm 0.04$	6.9679	0.06	0.00	n
23353	NGC 6253	20.85	0.99	1.30	2.78	1150	1.01	73	4.806	$0.17 \pm 0.10$	0.5060	0.79	0.62	n
18298	NGC 6253	18.39	0.72	0.37	1.73	39830	3.01	40	1.983	$0.26 \pm 0.04$	0.6817	0.45	0.15	n
37511	NGC 6253	18.14	1.19	0.68	1.47	36068	2.86	41	1.994	$0.71 \pm 0.02$	1.5751	0.04	0.00	n

Table 6.20: Properties of the detached binaries (part 13)

ID	Cluster	V	B-V	V-R	V-I	Distance	$A_V$	Numerical	Luminosity	Cluster membership	Period	Primary	Secondary	In cluster
						(pc)		spectral type	class	probability	(d)	amplitude	amplitude	aperture?
35325	NGC 6253	17.12	1.07	0.74	1.34	1132	0.68	62	4.873	$-0.20 \pm 0.07$	1.3433	0.16	0.07	n
27945	NGC 6253	18.37	1.17	0.71	1.52	29540	2.59	45	2.217	$0.22 \pm 0.03$	0.6825	0.26	0.18	n
3453	NGC 6253	16.13	0.74	0.53	1.04	3548	1.54	45	3.247	$0.78 \pm 0.08$	20.2346	0.22	0.00	n
46235	NGC 6253	15.24	0.88	0.53	1.04	1145	0.96	50	4.648	$0.78 \pm 0.10$	40.0000	0.03	0.00	y
1720	NGC 6253	17.17	1.00	0.61	1.34	5628	1.63	48	2.952	$0.79 \pm 0.05$	0.9322	0.03	0.03	n
26822	NGC 6253	16.55	0.71	0.53	1.13	9169	1.77	45	2.588	$0.51 \pm 0.12$	6.2417	0.06	0.00	n
13294	NGC 6253	15.85	0.89	0.56	1.07	1096	0.16	61	4.831	$0.10 \pm 0.15$	5.6282	0.20	0.00	n
13404	NGC 6253	18.55	1.07	0.63	1.14	1147	0.95	63	5.000	$0.06 \pm 0.05$	10.1243	0.01	0.00	n
42346	NGC 6253	18.31	0.81	0.65	1.14	7662	1.71	45	3.791	$0.71 \pm 0.02$	5.5959	0.11	0.00	n
9183	NGC 6253	18.64	0.81	0.57	1.17	7923	1.72	45	4.085	$0.71 \pm 0.02$	4.3267	0.11	0.00	n
42178	NGC 6253	17.70	0.89	0.60	1.16	6391	1.66	45	3.516	$0.79 \pm 0.05$	7.4629	0.05	0.00	n
40969	NGC 6253	17.32	0.95	0.61	1.16	1105	0.23	63	4.997	$0.57 \pm 0.04$	8.4706	0.14	0.09	n

## 6.3 Results

### 6.3.1 Period distribution

In Figure 6.2, we show a histogram of the periods of contact binary periods in the EXPLORE/OC sample. The distribution is peaked at in the period bin  $0.30 < P < 0.35$  days, with the lowest period system at 0.238 days. This is close to the short-period cutoff of 0.225 days in the R98 period distribution for contact binaries in old open cluster fields. Since our time-sampling is  $\sim 7$  min., we are sensitive to lower periods, and agree with Rucinski (2002) that short period contact binaries are very rare or absent. Since we have 98 contact binary systems compared to the R98 cluster sample of 63 contact binary systems, we expect to find a few more systems at longer periods. In fact, we find 15 systems at  $P > 0.7$  days, providing number statistics larger than in R98, but still with large error bars and numerous empty period bins.

Figure 6.2 also shows the R98 distribution, normalized up to 19 counts at the  $0.30 < P < 0.35$ d central bin of the three-bin wide peak, and overplotted. Although the number statistics and error bars for the R98 distribution are not too different from the EXPLORE/OC distribution, we also normalize the Poisson error bars on the R98 distribution and plot them. With this normalization, we see that the two distributions are consistent to within Poisson errors (estimated using the approximation in Gehrels 1986). A two-distribution K-S test gives a 99.8% probability that the samples were drawn from the same underlying distribution.

We do not apply a volume correction to derive the period function of R98, because these are cluster samples: the volume sampled will not necessarily be well-correlated with the number of contact binaries detected. We note that since all of our clusters were observed with the same exposure time with the same instrument on the same telescope, the depth of the survey should be approximately uniform across all the clusters, and so no per-cluster volume correction should be needed for the population of Galactic field stars in the sample.

Figure 6.3 shows the period distribution of detached eclipsing binaries in EXPLORE/OC. The decrease in number of detected systems at long periods is not astrophysical, but rather, is due to the difficulty of detecting two (or even one) eclipses at periods at large fractions of the observing run length (as illustrated by  $P_{vis}$  in Chapter 2). As a demonstration, dividing out the window function (by adopting the window function for the typical three-week observing run on IC 2714) renders the distribution quite consistent with flat

or slowly rising with period, in agreement with the peak in the distribution occurring at much wider binary separations (peaking beyond 10000 days) found by Duquennoy and Mayor (1991).

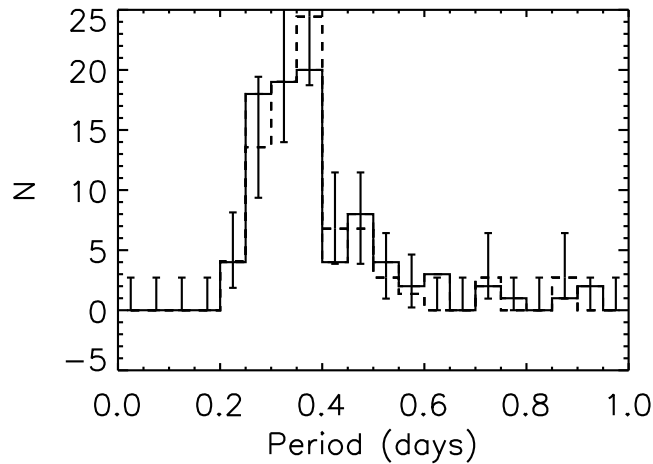


Figure 6.2: The period distribution of contact eclipsing binaries in EXPLORE/OC is shown as a solid line histogram. Overlaid as a dashed line is the period distribution in the cluster sample of R98, which has been normalized to the same value at the  $0.30 < P < 0.35$ d bin. The Poisson error bars for the Rucinski distribution were estimated using the approximations recommended in Gehrels (1986). The period distributions are consistent.

### 6.3.2 Colour distribution

Figure 6.4 shows dereddened  $B-V$  colours for contact eclipsing binaries in EXPLORE/OC and R98. Our dereddening was performed based on the photometric spectral type estimation- the intrinsic colour,  $(B-V)_0$ , could simply be looked up from the interpolated model values. The R98 distribution is normalized up to 8 counts in the  $0.5 < (B-V)_0 < 0.6$ d bin, and the approximate Poisson error bars for R98 are scaled up accordingly. The EXPLORE/OC distribution forms a broad peak over  $0.3 < (B-V)_0 < 0.8$ , consistent with the rescaled R98 colour distribution, although slightly bluer and lacking the spike at  $(B-V)_0 = 0.75$ . A two-distribution K-S test gives a 80.0% probability that the samples were drawn from the same underlying distribution.

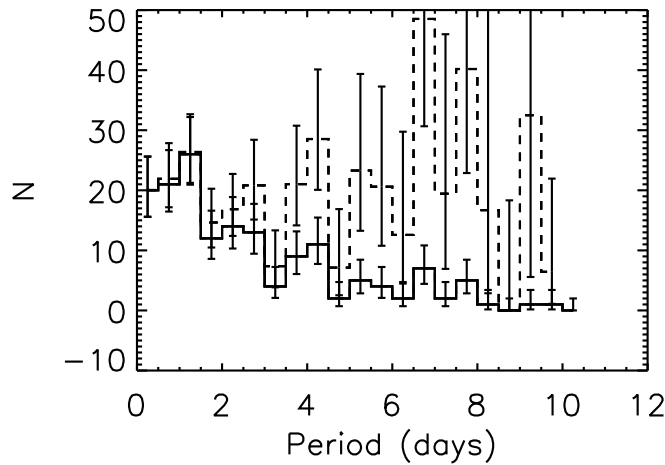


Figure 6.3: The period distribution of detached eclipsing binaries in EXPLORE/OC. The raw distribution is the solid line. The distribution, corrected for a typical observing window function ( $P_{vis}$  for the IC 2714 observing run) is the dashed line. We show the distribution out to 10 day periods, beyond which it becomes difficult to detect more than one eclipse over a typical observing run of three weeks.

Figure 6.5 shows dereddened  $B - V$  colours for detached eclipsing binaries in EXPLORE/OC. Dereddening was performed as for the contact binaries, which are overplotted the detached eclipsing binary colour distribution in the figure. The two distributions are somewhat similar, with different shapes for the peak of the distribution. The top of the contact binary distribution is wider, and could potentially be double-peaked, whereas the detached binary colour distribution is single-peaked. A two-distribution K-S test gives a 55.3% probability that the samples were drawn from the same underlying distribution.

### 6.3.3 Estimated spectral type and $M_V$ distribution

In Figures 6.6 and 6.7, we show histograms of the best-fit models'  $M_V$ . Unfortunately,  $M_V \sim 2$  is contaminated by a number of cool dwarfs mistaken for highly reddened distant giants (cf. Chapter 4). The peak near  $M_V \sim 2$  corresponds to the peak at spectral types F5 in the plots of the spectral type distribution in Figures 6.8 and 6.9. The contamination of the  $M_V$  histogram by these misclassified stars means we are unable to reliably estimate the luminosity function, so do not perform a scaled comparison with R98. The main effect of the misclassification is to scatter stars mistakenly to very large distances, which means

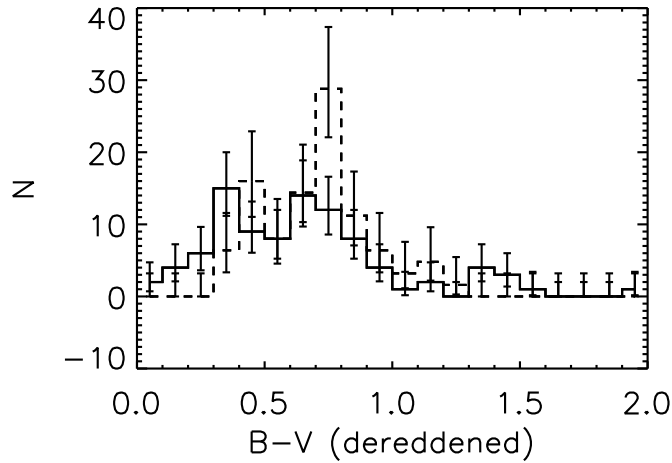


Figure 6.4: The dereddened,  $(B - V)_0$  colour distribution of contact eclipsing binaries in EXPLORE/OC is shown as a solid line histogram. Overlaid as a dashed line is the  $(B - V)_0$  colour distribution in the cluster sample of R98, which has been normalized to the same value at the  $0.5 < (B - V)_0 < 0.6$  bin. The Poisson error bars for both distributions were estimated using the approximations recommended in Gehrels (1986). The colour distributions are mostly consistent except for the R98 peak at  $(B - V)_0 = 0.75$ , a peak which was also high when compared with the Galactic field contact eclipsing binary colour distribution in R98.

we do not include them in the cluster sample and we lose cluster stars. Also, when we consider spectral types of individual stars, such as planet candidates, we should remember that a classification as a hot, distant F star by no means excludes the possibility that the star under consideration is actually a nearby K0 dwarf. The misclassification will cause the calculated intrinsic colour of some stars to be too blue, and may be responsible for the slight blueward skew of the colour distribution in Figure 6.4

### 6.3.4 Primary eclipse amplitude distribution

The distribution of the contact binary primary eclipse depths is shown in Figure 6.10. The distribution from R98 is overplotted, scaled by  $98/74$  to match the EXPLORE/OC histogram in area. The depths are shown in magnitudes, out to 1.2, in order to match our binning to that of R98. The two-distribution K-S test gives a 64.6% probability that the samples were drawn from the same underlying distribution. Most of the difference



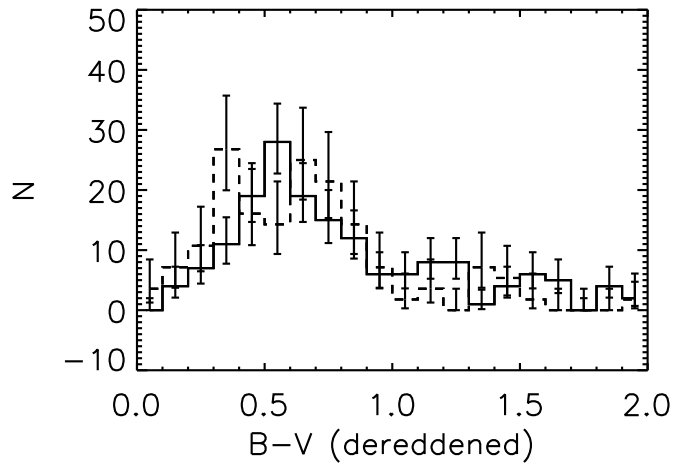


Figure 6.5: The dereddened,  $(B-V)_0$  colour distribution of detached eclipsing binaries in EXPLORE/OC is shown as a solid line histogram. The distribution for EXPLORE/OC contact binaries from Figure 6.4 is overlaid (dashed line), normalized up to the same histogram area. The Poisson error bars for both distributions were estimated using the approximations recommended in Gehrels (1986). The colour distributions are somewhat consistent, where a two-distribution K-S test yields a 55% probability that both samples are drawn from the same distribution.

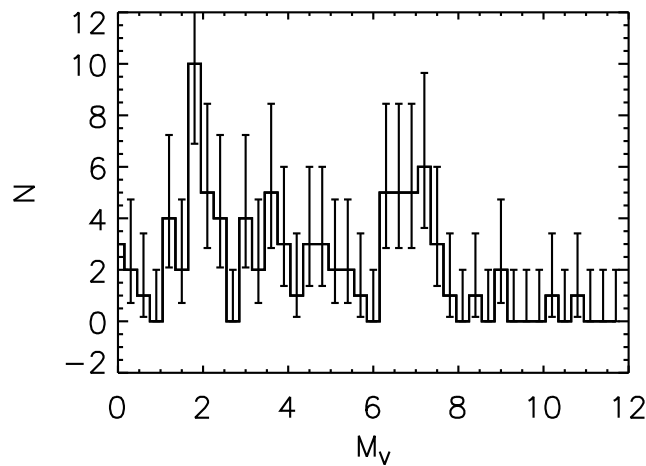


Figure 6.6: The  $M_V$  distribution for contact binaries. Peaks exist near  $M_V = 2$  and  $M_V = 6$ , which are due to spectral type misclassifications.

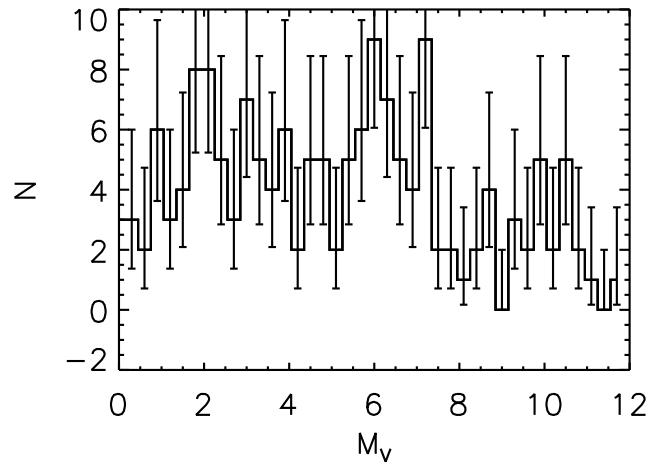


Figure 6.7: The  $M_V$  distribution for detached eclipsing binaries. Peaks exist near  $M_V = 2$  and  $M_V = 6$ , which are due to spectral type misclassifications.

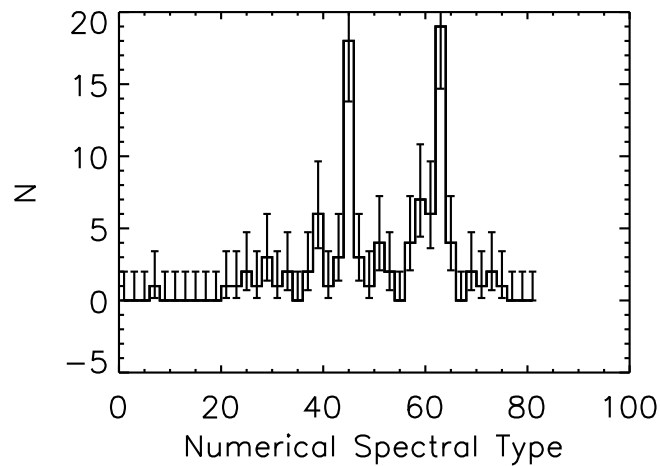


Figure 6.8: The numerical spectral type distribution for contact binaries. Tens digits represent full MK classes, and ones digits, subtypes. Thus, spectral type 11 is MK spectral type O1, 12 is O2, 20 is B0, 30 is A0, and similarly out to 79, which is M9. Models which are capable of matching nearby cool dwarfs lie around 45 (F5) and 60 (K0), which translate to peaks in the  $M_V$  distribution.

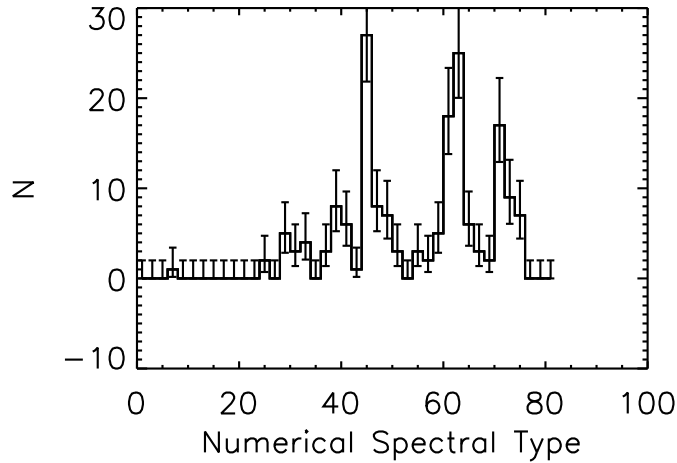


Figure 6.9: The numerical spectral type distribution for detached eclipsing binaries. Tens digits represent full MK classes, and ones digits, subtypes. Thus, spectral type 11 is MK spectral type O1, 12 is O2, 20 is B0, 30 is A0, and similarly out to 79, which is M9. Models which are capable of matching nearby cool dwarfs lie around 45 (F5) and 60 (K0), which translate to peaks in the  $M_V$  distribution.

between the two histograms is in the first bin, where the R98 histogram turns over, whereas the EXPLORE/OC histogram continues to rise. This may be partially due to the high precision, hence better completeness, of the EXPLORE/OC photometry, which can find eclipses to smaller amplitudes than the R98 sample of  $> 5\%$  deep eclipses. As mentioned in R98, the large number of small depth eclipses may be indicative of a relatively large number of small mass ratio systems, but the mass ratio distribution is difficult to extract from the distribution of primary depths.

In Figure 6.11, we show the distribution of detached binary primary eclipse depths. The EXPLORE/OC contact binary distribution is overplotted, normalized up to 28 counts in the bin  $0.1 < \text{depth} < 0.2$ . Here, the distribution is shown on a relative flux scale, rather than a magnitude scale, so the bins are different from Figure 6.10. While the two-distribution K-S test gives a 99.6% probability that the samples were drawn from the same underlying distribution, the detached sample does show an excess in the smallest amplitude bin.

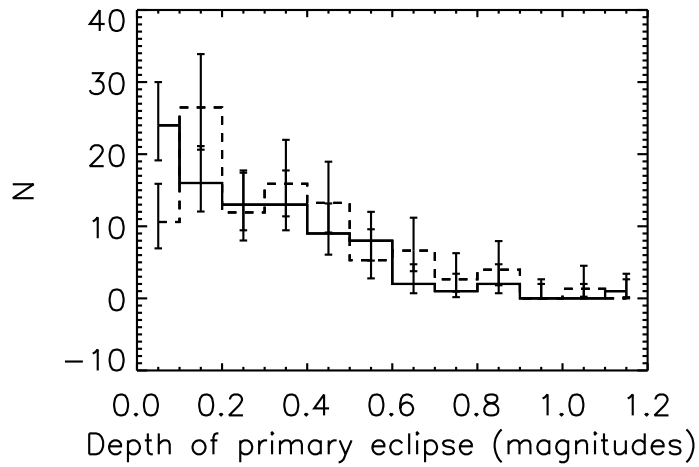


Figure 6.10: The primary eclipse depth distribution for contact binaries, in magnitudes. The solid line is the EXPLORE/OC distribution, and the dashed line is for the cluster sample in R98, normalized up to equal histogram areas. The depth is shown in magnitudes for ease of comparison with R98. The distributions appear consistent.

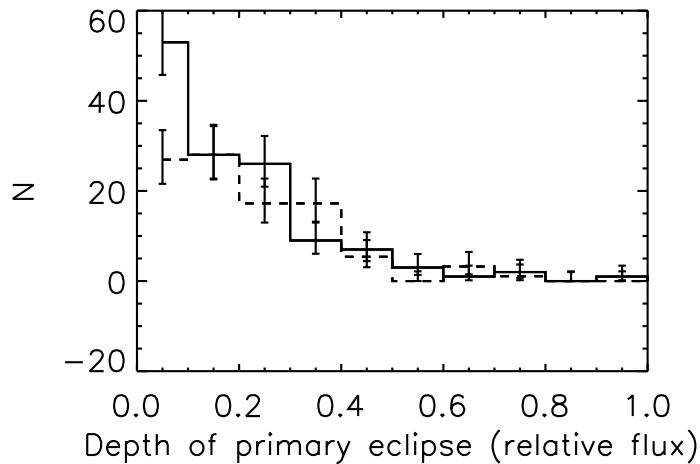


Figure 6.11: The solid line shows the primary eclipse depth distribution for detached eclipsing binaries. The contact binary distribution from Figure 6.10 is overplotted (dashed line), normalized up to 28 counts in the bin  $0.1 < \text{depth} < 0.2$ . The depth is shown in relative flux units. The distributions appear consistent.

### 6.3.5 Secondary eclipses and the mass ratio distribution

Due to the high photometric precision and long time baseline of our survey, we are able to observe the secondary eclipses of most of our short-period binary stars. The secondary depth combined with the primary depth provides a way of extracting information on the relative properties of the two components. We outline the result of some simple assumptions below.

Consider a short period ( $< 10\text{d}$ ) circularized eclipsing main sequence binary similar to the binaries we are capable of finding in EXPLORE/OC. Let the flux from the primary be  $F_1$  and the flux from the secondary,  $F_2$ . Let us assume quite a general case: that there is a non-variable background star or companion adding flux  $F_0$  to the system, and that the eclipses are not necessarily total eclipses, but that a maximal fraction  $A$  of area of the secondary is superposed. Assume spherical stars, a primary with radius  $r_1$ , a smaller radius  $r_2$  for the secondary, and no limb darkening.

The flux level of the system outside of eclipse is  $F_0 + F_1 + F_2$ . The loss of flux at the primary eclipse minimum is just the light from the primary blocked by the (smaller) secondary,

$$E_p = AF_1 \left( \frac{r_2}{r_1} \right)^2. \quad (6.1)$$

Because of symmetry in the case of a circular orbit, the loss of flux at the secondary eclipse minimum is just:

$$E_s = AF_2. \quad (6.2)$$

When we perform relative photometry, then the actual quantities we measure from the light curve are  $D_p = E_p/(F_0 + F_1 + F_2)$  and  $D_s = E_s/(F_0 + F_1 + F_2)$ . We can eliminate  $F_0$  and  $A$  by considering the easily measurable ratio  $D_s/D_p$ , and the result after simplification is:

$$\frac{D_s}{D_p} = \frac{F_2}{F_1} \left( \frac{r_1}{r_2} \right)^2. \quad (6.3)$$

Assume that the stars are in the lower-middle main sequence and that the average mass-luminosity and mass-radius relations apply:  $L \propto M^{3.5}$  and  $M \propto r^{0.8}$ . Introduce a bolometric correction factor  $b$  between  $I$ -band fluxes and the stellar luminosities such that  $F_i = b_i L_i$ . Define the mass ratio  $q = \frac{M_2}{M_1}$ . Then,

$$\frac{D_s}{D_p} = \frac{b_2}{b_1} \left( \frac{M_2}{M_1} \right)^{3.5} \left[ \left( \frac{M_1}{M_2} \right)^{1.25} \right]^2 = \frac{b_2}{b_1} q. \quad (6.4)$$

For the lower main sequence, G and K dwarfs should not have very different bolometric corrections. From Cox (2000), the  $V$ -band bolometric correction is -0.18 magnitudes for a G0V star, and -0.72 for a K5V star, and because the K5V star is much redder, the  $I$ -band bolometric corrections are much closer together: -0.63 for the G0V star and -0.90 for the K5V star. The difference of .27 magnitudes is only 28% on a linear scale. So,  $\frac{b_2}{b_1} \sim 1$  is not a bad approximation, even for a binary made up of fairly unequal mass lower main sequence dwarfs. Therefore, to first order under these particular simplifying assumptions, the mass ratio of a detached eclipsing binary is simply the ratio of secondary eclipse depth to primary eclipse depth.

The ratio of depths for a contact binary will not obey this simple relation because the common envelope does not obey the main sequence relations. However, information does come from putting the bolometric correction alone into Equation 6.3 and assuming the stars are spherical blackbodies,  $L_i = 4\pi r_i^2 \sigma T_i^4$ , then simplification yields:

$$\frac{D_s}{D_p} = \frac{b_2 T_2^4}{b_1 T_1^4}. \quad (6.5)$$

Since the bolometric corrections are functions of temperature, this shows how to first order, the ratio of eclipse depths in contact binaries is a measure of the relative temperatures. So, for binaries in good thermal contact, the eclipse depths will be equal. To second order, the ratio is a measure of the system geometry.

We show the distribution of secondary to primary eclipse depth ratios for the EXPLORE/OC contact binary sample in Figure 6.12. The distribution is highly peaked towards equal ratios, as expected for contact binary systems. Over two-thirds of the systems occur at ratios  $> 0.8$ , but there is a long, low-level tail of systems which may include interloping semi-detached binaries..

The distribution of secondary to primary eclipse depth ratios, for the EXPLORE/OC detached binary sample is shown in Figure 6.13. The distribution is highly peaked near ratios of zero, where no secondary eclipse was visible above the noise, which would suggest a large number of unequal mass systems. However, it is possible that some of the systems with ratio 0 are actually ratio 1.0.

Assuming that for our detached binary sample, the depth ratio is a good proxy for the mass ratio (cf. Equation 6.4), we note that the error bars on our distribution do not agree with a distribution strongly peaked at 1.0, as has been recently suggested by

Lucy (2006). Rather, the distribution looks relatively flat, as suggested by Mazeh et al. (2003).

Note that the closer binaries in our detached sample can be subject to reflection and ellipsoidal variability effects, which change the eclipse depth measurements. The primary effect this sinusoidal modulation can have is to greatly magnify the apparent size of a secondary eclipse, located at the minimum of the sine wave. If this effect is present, it will have caused us to measure higher secondary-to-primary depth ratios than in the complete absence of sinusoidal modulations. This bias moves the distribution away from unequal masses, yet still we see no peak at equal mass ratios.

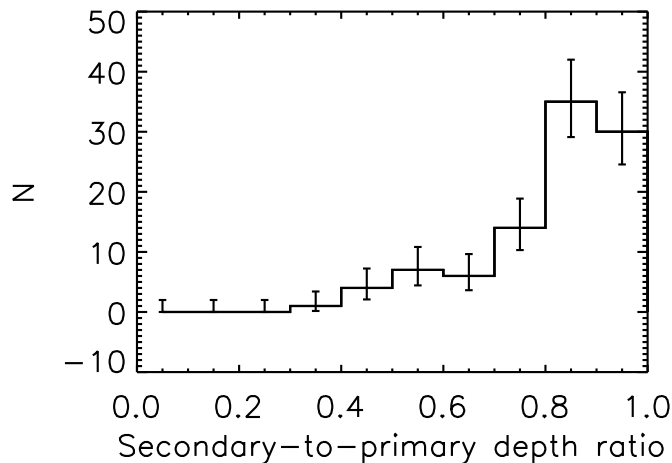


Figure 6.12: The distribution of ratios of secondary eclipse depths to primary eclipse depths for contact eclipsing binaries. The distribution is peaked towards equal depths as expected for common-envelope contact binary stars.

### 6.3.6 Evolution of contact and detached binaries in clusters

Here, we leverage the age range of our open cluster sample. Cluster members count as stars with the properties of the cluster. So, summing the cluster membership probabilities of variable stars in each of our cluster fields gives a statistical estimate of the number of cluster variables. In most of our clusters, a number of our eclipsing binary detections fall within the magnitude, distance, and spatial limits that maximize the ratio of cluster stars detected (again, statistically speaking, the sum of the cluster membership probabilities) to the uncertainty in the number of cluster stars detected. It turns out that there are

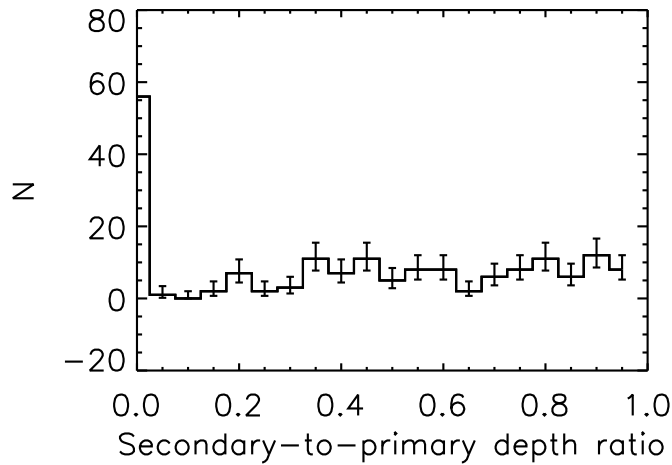


Figure 6.13: The distribution of ratios of secondary eclipse depths to primary eclipse depths for detached eclipsing binaries. For typical simplifying main-sequence assumptions and no limb darkening, this ratio is equal to the mass ratio. We see that there is no convincing support for a mass ratio peaked at equal masses.

sufficient statistics to compute the contact and detached binary fractions (the number of binary cluster stars divided by the total number of cluster stars) as a function of cluster age.

R98 was able to compute the contact binary fraction (the precise definition in R98 being the frequency of occurrence of contact binaries relative to all main sequence stars) in open clusters directly, using confirmed cluster members. He found that the contact binary fraction increased as a function of age, from between 1 in 1000 to 1 in 500 for his youngest open clusters, up to 1 in 275 for his oldest open clusters. We verify these findings, and furthermore, we extend the discussion of binary fraction evolution to detached binaries.

The last column of Tables 6.8 to 6.20 indicates the detached eclipsing binary systems which survive the cluster aperture cut in distance, sky position, magnitude, and spectral type; similarly, the contact eclipsing binary systems are in Tables 6.1 to 6.7. Note that in some clusters, the derived cluster aperture cuts were restrictive and did not yield large numbers of cluster stars; in turn, those cuts admitted no binary detections. The cuts give no detections for detached eclipsing binaries in both NGC 6208 and IC 4651, and no detections for contact eclipsing binaries in both NGC 6134 and NGC 6208. These null detections are not very useful on their own, but they still carry useful information.



Therefore, we calculate the cluster binary fractions in age bins, 0.5 wide in  $\log(\text{age})$ , rather than on a strictly individual cluster basis (some age bins are still only populated by one cluster, though). For each age bin, the binary fraction is defined as the sum of the cluster membership probabilities of the binaries, divided by the sum of cluster membership probabilities of all stars in that bin.

In order to compare directly with R98, we compute only the apparent contact eclipsing binary fraction; as in R98, we do not correct for undetected ellipsoidal variables, or for misclassified pulsators. Because of the short, mostly  $< 1$  day periods and continuous light variation of contact binaries, our long observing runs should pick up all contact eclipsing binaries with sufficient signal-to-noise ratio. Our binary fractions are signal-to-noise limited, rather than strictly magnitude-limited, similar to R98. The apparent contact eclipsing binary fraction should be close to the true contact binary fraction because of the near 100% visibility of contact binaries' short periods, as well as their visibility as ellipsoidal variables even when the orbital plane is not along the line of sight. We present our resulting contact binary fractions in Figure 6.14.

For detached eclipsing binaries, we introduce two average correction factors in the calculation, in order to derive the total fraction of detached binaries. In order to correct for non-detection of systems with long periods, we divide each binary's cluster membership probability by the average  $P_{vis}$  (cf. Chapter 2) for that run; the average is computed over the range 0.4 to 10 days. We also divide each binary's cluster membership probability by the fraction of detached binaries we expect to be eclipsing. This number is difficult to compute accurately, but we make a ballpark estimate by computing the average probability of eclipse for a test mass orbiting a  $1M_{\odot}$  star, for an even period distribution from 0.4 to 10 days. This geometric probability of eclipse, 0.1053, should be a reasonable estimate for our sample of lower main-sequence stars and unequal mass ratios, probably to a factor better than 2. For example, even in the case of an equal mass binary of  $2M_{\odot}$  stars and a period of 10 days, the geometric probability of eclipse would be 0.0547. The raw, uncorrected detached binary fractions are shown in Figure 6.15. After applying the two corrections, we present our resulting detached binary fractions in Figure 6.16. To check whether the fraction is affected by massive stars having evolved out of the sample in the older clusters, we also present the corrected detached binary fractions for only stars classified as G0 or later in Figure 6.17.

In Figure 6.14, we see that our apparent contact binary fraction increases from  $\sim 1/700$  at age 200 Myr to  $\sim 1/250$  at age 5 Gyr, with a low-lying outlier near 1 Gyr (where two fields had no detections). We thus span an age range similar to that covered

in the R98 open cluster sample, and our rise in contact binary fraction is consistent with the expectations from R98. Kendall's rank correlation test on the EXPLORE/OC data indicate a positive correlation value of 0.667, with 0.174 two-sided significance value of deviation from zero. Spearman's rank correlation test yields a positive correlation value of 0.800, with 0.200 two-sided significance.

In Figure 6.16, the detached binary fraction drops from a level of  $\sim 1/3$  at 200 Myr to  $\sim 1/10$  at 5 Gyr (and a similar trend is observed for late type stars, in Figure 6.17). Kendall's rank correlation test indicates detached binary fraction and  $\log(\text{age})$  are anticorrelated, with a correlation value -1.000 and 0.0415 two-sided significance value of deviation from zero. Spearman's rank correlation test also yields a correlation value -1.000, and a 0.0000 two-sided significance. This destruction of detached binaries over time is likely due to dynamical effects, as the apparent contact binary fraction does not rise as quickly as the detached fraction falls. Until now, destruction of detached binaries has mainly been observed in globular cluster simulations (see, e.g., Ivanova 2005), and theoretical work on simulating the open cluster M67 (Hurley et al. 2005) found very little evolution in the binary fraction. Our result from Figure 6.16 contrasts with the M67 theoretical work, and gives ballpark estimates to test the outcomes of more general theoretical cluster evolution simulations.

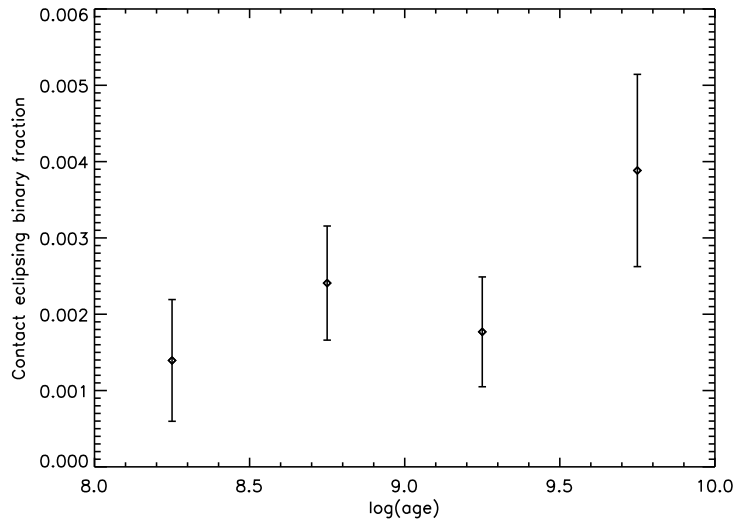


Figure 6.14: The contact binary fractions, computed in four equal  $\log(\text{age})$  bins. These fractions are uncorrected, for direct comparison with R98. The binary fraction rises from a level of  $\sim 1/700$  at 200 Myr to  $\sim 1/250$  at 5 Gyr, consistent with expectations from R98. Kendalls' rank correlation gives a 0.667 correlation between contact binary fraction and  $\log(\text{age})$ .

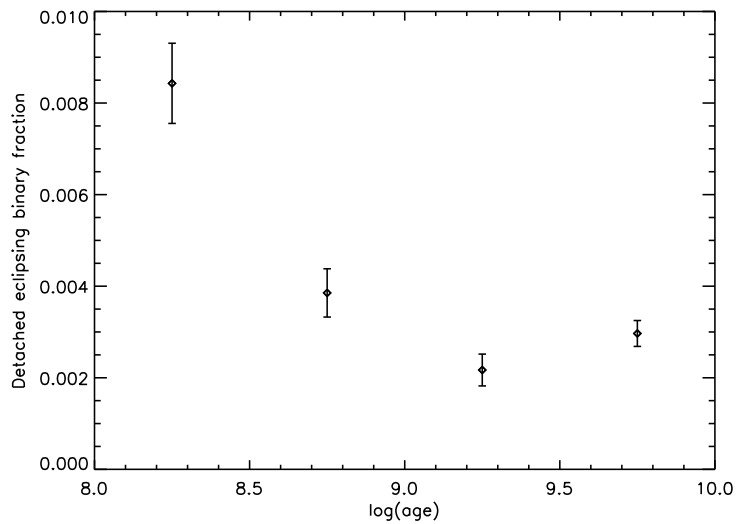


Figure 6.15: The detached binary fractions of stars, computed in four equal  $\log(\text{age})$  bins. These are the raw fractions, uncorrected for geometry and the observing window.

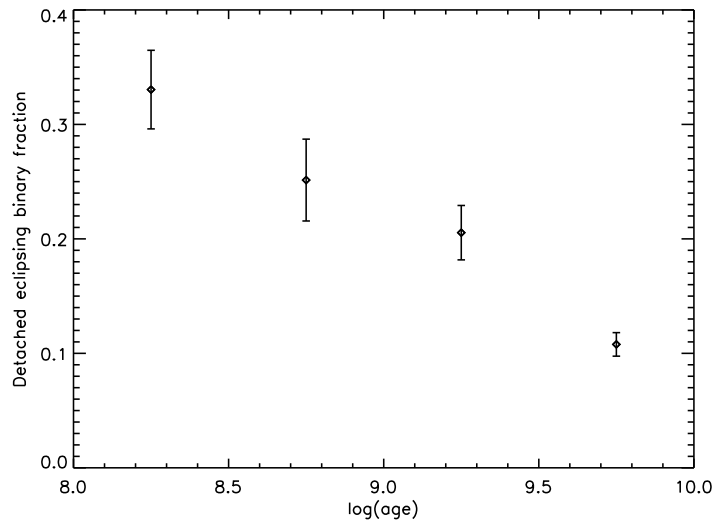


Figure 6.16: The detached binary fractions, computed in four equal  $\log(\text{age})$  bins. These fractions have been corrected for systems missed due to the observing window, and for systems missed due to orbital inclination not along the line of sight. The binary fraction drops from a level of  $\sim 1/3$  at 200 Myr to  $\sim 1/10$  at 5 Gyr. The Kendalls' rank correlation gives a -1.000 correlation between detached binary fraction and  $\log(\text{age})$ .

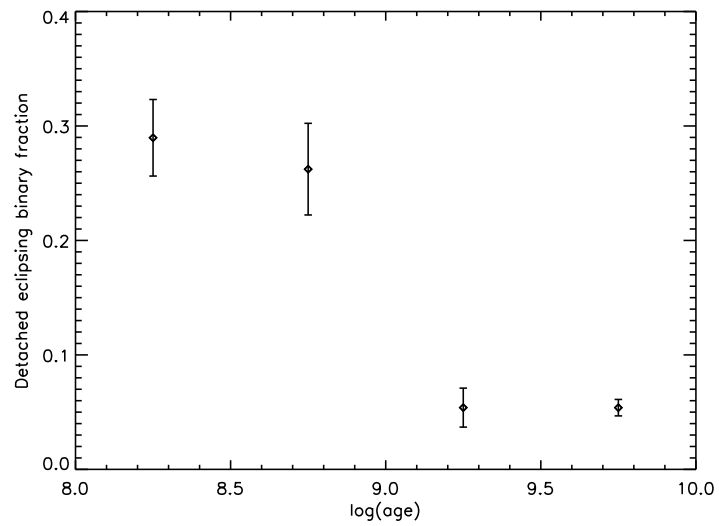


Figure 6.17: The detached binary fractions of stars classified as G0 or later, computed in four equal  $\log(\text{age})$  bins. These fractions have been corrected for systems missed due to the observing window, and for systems missed due to orbital inclination not along the line of sight. Similar to Fig. 6.16, the detached binary fraction decreases with time.

# Chapter 7

## Conclusion

Extrasolar planet searches have produced over 200 planet discoveries in a decade of operation. A link between the frequency of occurrence of planets and the metallicities of the host systems has been established, with higher metallicities corresponding to sizable enhancements in the probability of planet occurrence.

More recent successful detections of *transiting* planets have provided the first look at the exact masses and radii of extrasolar planetary bodies, confirming their planetary natures and challenging theorists to explore in detail the mass-radius relationship for low mass objects. For the brightest transiting planet host stars, it is already possible to analyze atmospheric composition from transmission spectroscopy of the planet, and to infer the temperature of the planet from infrared detection of the secondary eclipse. These physical characterizations, available because of a planet's transiting nature, are one reason why transit searches are highly complementary to radial velocity searches. They are also complementary in search space. A transit of a Jupiter-like planet around a Sun-like star can be discovered around a much fainter star than is feasible using today's radial velocity instruments.

Each open cluster in our galaxy offers a convenient sample of stars of uniform  $[\text{Fe}/\text{H}]$  and age packed in one location on the sky. Transit searches in open clusters provide a relatively direct and independent method of probing the occurrence of planets as a function of  $[\text{Fe}/\text{H}]$ . They also permit the investigation of any other trends in the properties of planet-bearing cluster stars or variable cluster stars.

## 7.1 The Survey

In this thesis, we monitored an unprecedented eight open clusters for transiting extrasolar planets. Chapter 2 presented our observations conducted at Las Campanas Observatory with the Swope 1-m Telescope. The survey was conducted using high time-sampling, and to a depth designed to capture cluster GKM dwarfs. Our clusters ranged over metallicities from  $[\text{Fe}/\text{H}]=-0.18$  to  $[\text{Fe}/\text{H}]=+0.36$ , and over ages 150 Myr to 5 Gyr.

We used a data reduction pipeline from the EXPLORE Galactic field search, and upgraded it as described in Chapter 3. The upgrades of neighbour subtraction and a generalized aperture technique reduced systematic and catastrophic photometry errors, while on average improving photometric precision. The resulting catalogue of light curves contains  $\sim 39000$  stars with rms photometric precision better than 1.5%.

In Chapter 4, we used broadband colour photometry, spectroscopy, and the red clump method together with a chi-squared spectral energy distribution fit to estimate spectral types, distances, and reddenings of stars in our catalogue. The distances were used along with RA and DEC, magnitude, and estimated spectral type to compute cluster membership probabilities, and to define an aperture in parameter space which contained a high ratio of cluster stars to Galactic field stars. The background level was estimated using off-cluster control fields.

Our final object catalogues thus include colour photometry, spectral types, distances, reddenings, and cluster membership probabilities.

## 7.2 Results

### 7.2.1 Planets

#### Transiting Planet Candidates

We recovered 18 objects with low-amplitude ( $< 10\%$ ) eclipses from light curves with photometric precision  $< 1.5\%$  and with photometrically estimated spectral types. These 18 objects exclude those showing only a single eclipse (hence without a period measurement), those which show a secondary eclipse (binary stars), and those with clear sinusoidal modulations outside of transit (also binary stars).

We tested the assumption that all of these objects were planets transiting main sequence stars, using the unique solution method of Seager & Mallén-Ornelas (2003). We found that 5 of the 18 objects had companions of sufficiently low radii to bring them

within 2-sigma of  $1.44R_{Jupiter}$ , the radius of the largest currently known transiting planet, WASP-1b. We call these objects robust candidates, based on the light curve information. Colour photometry suggests other astrophysical explanations are possibilities for four of the five robust candidates.

Our best robust planet candidate, with period 1.545 days, has predicted radius  $1.5 \pm 0.3R_{Jupiter}$ , consistent with the radii of several known planets, and is predicted to orbit a K0V host star. The colour photometry is not able to constrain the likelihood of the planet hypothesis much further, and spectroscopic follow-up is called for. This star lies in a dusty region of the field of NGC 6134, and its cluster membership is therefore uncertain, as the control field contains more stars than the cluster in the bin of parameter space where this star falls.

### Frequency of Occurrence

The five robust candidates we detected, out of a parent sample of  $\sim 39000$  stars measured to better than 1.5% photometric precision, are consistent with radial velocity searches. Assuming the radial velocity search fraction of 0.7% (Marcy et al. 2004), scaled by the [Fe/H] dependence seen in Fischer et al. (2004), is correct, and assuming the average metallicity of the sample is [Fe/H]=-0.1, then the probability of detecting five or fewer transiting planets in this parent sample is 31.1%. The expectation value for number of planets that should be discovered is 6.2. We conclude that there is no evidence to reject the hypothesis that the frequency of occurrence of HJ in our fields is any different from that in the solar neighbourhood FGKM dwarfs searched by radial velocity techniques.

One of the robust candidates lies within the sample of probable cluster stars defined by statistically optimizing the error bars on the count of cluster stars within the sample. It has a cluster membership probability of  $0.4 \pm 0.2$ . For the total number of cluster stars sampled with 1.5% photometric precision, this number of candidates is reasonably consistent with the expectation of 0.70 planets in the cluster sample. Although the number statistics of the cluster subset are over ten times poorer than for the entire sample of field plus cluster, the significance of the cluster subset is that the metallicities are known from literature. Thus, we find that our frequency of detected candidates is consistent with an [Fe/H] scaling following the trend in Fischer et al. (2004).



## 7.3 Binary Stars

### 7.3.1 Global Properties

#### Contact Eclipsing Binaries

We catalogued the periods, colours, and amplitude of primary eclipses of the 98 contact binaries detected among stars with  $< 2\%$  photometric precision and with estimated spectral types. We compare with existing work in R98. We find our period, colours, and primary eclipse amplitudes are all distributed in a manner consistent with R98, with probabilities 99.8%, 80.0%, and 64.6% according to two-sided K-S tests.

The lowest contact binary period we find is 0.238 days, just slightly higher than the lowest period in R98 of 0.225 days. Because of our high time-sampling of  $\sim 7$  minutes, we are highly sensitive to short periods down to a quarter of an hour. Thus our results are consistent with contact binaries at periods less than .22 days being absent (Rucinski 2002).

#### Detached Eclipsing Binaries

We also catalogued the periods, colours, and amplitudes of primary eclipses for the 175 detached or semi-detached eclipsing binaries among stars with  $< 2\%$  photometric precision and with estimated spectral types. We find the colour and primary eclipse depth distributions are consistent with those we derived for contact binaries, with respective two-sided K-S probabilities of 55.3% and 99.6%.

The period distribution is consistent with the overall trend from Duquennoy & Mayor (1991), although their period bins are rather large and their period range extends out to years. We find our data are consistent with a period distribution which is flat or slightly rising out to 10 day periods.

### 7.3.2 Mass Ratios

Lucy (2006) has recently argued that the distribution of binary mass ratios is peaked towards equal masses, contrary to the previously accepted result of Hogeveen (1992) that the mass ratio distribution favours unequal masses, with a probability density function decreasing towards equal masses as  $q^{-2}$ . Mazeh et al. (2003) find a relatively flat mass ratio distribution, adding to a similar previous work, Goldberg et al. (2003).

We constructed the ratio of secondary to primary eclipse depths and used the ratio as

a proxy for the mass ratio distribution, since for some simple assumptions, this ratio in detached eclipsing binaries is even equal to the mass ratio. Our distribution is consistent to within Poisson error bars with being flat, not sharply peaked. A number of objects show no secondary eclipse and evaluate to mass ratios of zero. However, this peak is probably not real, as it contains objects where the secondary eclipse was up to 0.2 of the depth of the primary (but undetectable because of the noise level of the light curve), as well as equal mass ratio objects, which cannot be told apart from systems with very small secondaries from the light curve alone. Note that our determination is independent of Hogeveen, Mazeh et al., and Lucy, since they use samples of spectroscopic binaries to derive mass ratios.

### 7.3.3 Evolution of the Binary Fraction

We found an increase in the apparent relative frequency of occurrence of cluster contact binary systems as a function of age, from  $0.0014 \pm 0.0008$  at 180 Myr, to  $0.004 \pm 0.001$  at the 6 Gyr bin, in agreement with R98, which gives evolution of the fraction from  $\sim 0.001$  at 0.8 Gyr up to  $\sim 0.004$  at 5-7 Gyr. This supports the theory that contact binaries form out of detached binaries that spiral in towards each other over time.

We also find a decrease in the frequency of occurrence of cluster detached eclipsing binaries as a function of age, from  $0.33 \pm 0.03$  at 180 Myr, to  $0.11 \pm 0.01$  at 6 Gyr, after corrections for geometric effects and the observing window function. The destruction of binaries at such a rate is higher than the rate of creation of contact binaries, which probably indicates cluster dynamics play a role in destroying binaries. Such destruction has been seen in simulations of globular cluster evolution (Ivanova et al. 2005), but has not been seen in open cluster simulations (Hurley et al. 2005).

## 7.4 Future Work

One of the immediate priorities for work building on the observations collected for this thesis is to conduct spectroscopic classification reconnaissance on all candidates detected, to check the spectral types and compare with the unique solution and photometrically estimates results. This can be done efficiently using a multi-object spectrograph on a telescope of modest aperture, such as the 2.5-m du Pont, used in this thesis for calibrating the red clump technique.

We also want to perform radial velocity follow up any candidates for which spectro-

scopic reconnaissance agrees with the unique solution and photometry, to radial velocity precision of  $\sim 100$  m/s or better, in order to verify the existence of any planets. This can be done with a multi-object spectrograph on an 8-m class telescope. For example, Bouchy et al. (2005a) have performed  $\sim 100$  m/s radial velocity follow-up of relatively faint OGLE planet candidates of  $14 < V < 18$  using VLT+FLAMES. Since we have numerous binaries per field, we can also include binary targets in any multi-object radial velocity follow-ups, to acquire radial velocity orbits, complementing the eclipse data to yield masses, and correctly identify the natures of systems that had no visible secondary eclipses.

The cluster membership analysis can be improved in two ways. First, for all fields including control fields, deeper *BVR IJHK* imaging (to statistical SNR at least 100 for stars of  $I = 18$  would be desirable, as our colour coverage is not complete over all fields. This would allow every star of interest to have a photometrically estimated spectral type, whereas at present, thousands of stars are lost as dropouts in several bands (particularly in control fields with only *VI* imaging). Second, for all fields, small spectroscopic samples should be taken to improve the distance-reddening calibrations. In particular, fields with patchy reddening would benefit from a distance-reddening relation computed as a function of RA and DEC on our fields (there are insufficient red clump stars to provide such a fine spatial scale computation using the red clump method).

The variable star collection in this sample remains relatively unmined. Many peculiar light curves exist within this data set, and may be of interest to pulsating star researchers. There are dozens of  $\delta$  Scuti stars and RR Lyrae in the data available for statistical studies.

Theorists should take note of the decrease we observe in the detached eclipsing binary fraction in clusters as a function of age. Further simulations of the evolution of open clusters, with tracking of the binary fraction, should be carried out.

As we move into the follow-up stage of this survey, we note that planet transit searches have begun to pay off with discoveries of extrasolar planets. Careful work using large-format, wide field CCDs on both small and moderate sized telescopes has produced outstanding ground-based photometry with precisions in the millimagnitudes. The timely analysis of the data has been facilitated by increases in computer power. The discoveries of very large planets continue to challenge theorists to refine the details of planet evolution calculations. Yet, technology is making possible detections of ever smaller planets. Upcoming transit searches to be conducted from space will have the precision to detect much smaller bodies, even as small as terrestrial planets. We very much anticipate the many exciting discoveries to be made in the coming decade.

# References

- Adams, F. C., Hollenbach, D., Laughlin, G., & Gorti, U. 2004, *ApJ*, 611, 360
- Adams, F. C., Proszkow, E. M., Fatuzzo, M., & Myers, P. C. 2006, *ApJ*, 641, 504
- Alonso, R., Brown, T. M., Torres, G., Latham, D. W., Sozzetti, A., Mandushev, G., Belmonte, J. A., Charbonneau, D., Deeg, H. J., Dunham, E. W., O'Donovan, F. T., & Stefanik, R. P. 2004, *ApJ*, 613, L153
- Bakos, G., Noyes, R. W., Kovács, G., Stanek, K. Z., Sasselov, D. D., & Domsa, I. 2004, *PASP*, 116, 266
- Bakos, G. A., Noyes, R. W., Kovacs, G., Latham, D. W., Sasselov, D. D., Torres, G., Fischer, D. A., Stefanik, R. P., Sato, B., Johnson, J. A., Pal, A., Marcy, G. W., Butler, R. P., Esquerdo, G. A., Stanek, K. Z., Lazar, J., Papp, I., Sari, P., & Sipocz, B. 2006, *ArXiv Astrophysics e-prints*
- Baraffe, I., Chabrier, G., Barman, T. S., Allard, F., & Hauschildt, P. H. 2003, *A&A*, 402, 701
- Bond, C. R. 2006, *Software for Scientific Applications*, <http://www.crbond.com/scientific.htm>
- Bouchy, F., Pont, F., Melo, C., Santos, N. C., Mayor, M., Queloz, D., & Udry, S. 2005a, *A&A*, 431, 1105
- Bouchy, F., Pont, F., Santos, N. C., Melo, C., Mayor, M., Queloz, D., & Udry, S. 2004, *A&A*, 421, L13
- Bouchy, F., Udry, S., Mayor, M., Moutou, C., Pont, F., Iribarne, N., da Silva, R., Illovaisky, S., Queloz, D., Santos, N. C., Ségransan, D., & Zucker, S. 2005b, *A&A*, 444, L15

- Bramich, D. M., Horne, K. D., & Bond, I. A. 2004, in ASP Conf. Ser. 321: Extrasolar Planets: Today and Tomorrow, ed. J. Beaulieu, A. Lecavelier Des Etangs, & C. Terquem, 68
- Burke, C. J., Depoy, D. L., Gaudi, B. S., & Marshall, J. L. 2003, in ASP Conf. Ser. 294: Scientific Frontiers in Research on Extrasolar Planets, ed. D. Deming & S. Seager, 379–382
- Burke, C. J., Gaudi, B. S., DePoy, D. L., Pogge, R. W., & Pinsonneault, M. H. 2004, *AJ*, 127, 2382
- Burrows, A., Guillot, T., Hubbard, W. B., Marley, M. S., Saumon, D., Lunine, J. I., & Sudarsky, D. 2000, *ApJ*, 534, L97
- Butler, R. P., Wright, J. T., Marcy, G. W., Fischer, D. A., Vogt, S. S., Tinney, C. G., Jones, H. R. A., Carter, B. D., Johnson, J. A., McCarthy, C., & Penny, A. J. 2006, *ApJ*, 646, 505
- Campbell, B., Walker, G. A. H., & Yang, S. 1988, *ApJ*, 331, 902
- Cardelli, J. A., Clayton, G. C., & Mathis, J. S. 1989, *ApJ*, 345, 245
- Castellani, V., Chieffi, A., & Straniero, O. 1992, *ApJS*, 78, 517
- Charbonneau, D., Brown, T. M., Latham, D. W., & Mayor, M. 2000, *ApJ*, 529, L45
- Collier Cameron, A., Bouchy, F., Hebrard, G., Maxted, P., Pollacco, D., Pont, F., Skillen, I., Smalley, B., Street, R. A., West, R. G., Wilson, D. M., Aigrain, S., Christian, D. J., Clarkson, W. I., Enoch, B., Evans, A., Fitzsimmons, A., Fleenor, M., Gillon, M., Haswell, C. A., Hebb, L., Hellier, C., Hodgkin, S. T., Horne, K., Irwin, J., Kane, S. R., Keenan, F. P., Loeillet, B., Lister, T. A., Mayor, M., Moutou, C., Norton, A. J., Osborne, J., Parley, N., Queloz, D., Ryans, R., Triaud, A. H. M. J., Udry, S., & Wheatley, P. J. 2006, ArXiv Astrophysics e-prints
- Duquennoy, A. & Mayor, M. 1991, *A&A*, 248, 485
- Durant, M. & van Kerkwijk, M. H. 2006, *ApJ*, 650, 1070
- Fischer, D., Valenti, J. A., & Marcy, G. 2004, in IAU Symposium, ed. A. K. Dupree & A. O. Benz

- Fischer, D. A. & Valenti, J. 2005, *ApJ*, 622, 1102
- Gaudi, B. S., Burke, C. J., DePoy, D. L., Marshall, J. L., Pogge, R. W., & STEPSS Collaboration. 2002, in *Bulletin of the American Astronomical Society*, 1264
- Gilliland, R. L., Brown, T. M., Guhathakurta, P., Sarajedini, A., Milone, E. F., Albrow, M. D., Baliber, N. R., Bruntt, H., Burrows, A., Charbonneau, D., Choi, P., Cochran, W. D., Edmonds, P. D., Frandsen, S., Howell, J. H., Lin, D. N. C., Marcy, G. W., Mayor, M., Naef, D., Sigurdsson, S., Stagg, C. R., Vandenberg, D. A., Vogt, S. S., & Williams, M. D. 2000, *ApJ*, 545, L47
- Goldberg, D., Mazeh, T., & Latham, D. W. 2003, *ApJ*, 591, 397
- Gonzalez, G. 2006, *PASP*, 118, 1494
- Guillot, T. & Showman, A. P. 2002, *A&A*, 385, 156
- Heacox, W. D. 1996, *J. Geophys. Res.*, 101, 14815
- Hogeveen, S. J. 1992, *Ap&SS*, 196, 299
- Horne, K. 2003, in *ASP Conf. Ser. 294: Scientific Frontiers in Research on Extrasolar Planets*, ed. D. Deming & S. Seager, 361–370
- Hurley, J. R., Pols, O. R., Aarseth, S. J., & Tout, C. A. 2005, *MNRAS*, 363, 293
- Ivanova, N., Belczynski, K., Fregeau, J. M., & Rasio, F. A. 2005, *MNRAS*, 358, 572
- Janes, K. 1996, *J. Geophys. Res.*, 101, 14853
- Keenan, P. C. & McNeil, R. C. 1976, *An atlas of spectra of the cooler stars: Types G,K,M,S, and C. Part 1: Introduction and tables* (Columbus: Ohio State University Press, 1976)
- Konacki, M., Torres, G., Jha, S., & Sasselov, D. D. 2003, *Nature*, 421, 507
- Konacki, M., Torres, G., Sasselov, D. D., Pietrzyński, G., Udalski, A., Jha, S., Ruiz, M. T., Gieren, W., & Minniti, D. 2004, *ApJ*, 609, L37
- Lee, B. L., von Braun, K., Mallén-Ornelas, G., Yee, H. K. C., Seager, S., & Gladders, M. D. 2004, in *AIP Conf. Proc. 713: The Search for Other Worlds*, ed. S. S. Holt & D. Deming, 177–180

- López-Corredoira, M., Cabrera-Lavers, A., Garzón, F., & Hammersley, P. L. 2002, *A&A*, 394, 883
- Lucy, L. B. 2006, *A&A*, 457, 629
- Mallén-Ornelas, G., Seager, S., Yee, H. K. C., Minniti, D., Gladders, M. D., Mallén-Fullerton, G. M., & Brown, T. M. 2003, *ApJ*, 582, 1123
- Marcy, G. W., Butler, R. P., Fischer, D. A., & Vogt, S. S. 2004, in *ASP Conf. Ser. 321: Extrasolar Planets: Today and Tomorrow*, ed. J. Beaulieu, A. Lecavelier Des Etangs, & C. Terquem
- Markwardt, C. 2006, The Markwardt IDL Library, <http://cow.physics.wisc.edu/~craigm/idl/>
- Mayor, M. & Queloz, D. 1995, *Nature*, 378, 355
- Mazeh, T., Simon, M., Prato, L., Markus, B., & Zucker, S. 2003, *ApJ*, 599, 1344
- McCullough, P. R., Stys, J. E., Valenti, J. A., Johns-Krull, C. M., Janes, K. A., Heasley, J. N., Bye, B. A., Dodd, C., Fleming, S. W., Pinnick, A., Bissinger, R., Gary, B. L., Howell, P. J., & Vanmunster, T. 2006, *ApJ*, 648, 1228
- Mermilliod, J.-C. 1996, in *ASP Conf. Ser. 90: The Origins, Evolution, and Destinies of Binary Stars in Clusters*, ed. E. F. Milone & J.-C. Mermilliod, 475
- Mochejska, B. J., Stanek, K. Z., Sasselov, D. D., & Szentgyorgyi, A. H. 2002, *AJ*, 123, 3460
- Mochejska, B. J., Stanek, K. Z., Sasselov, D. D., Szentgyorgyi, A. H., Westover, M., & Winn, J. N. 2004, *AJ*, 128, 312
- Moré, J. J., Garbow, B. S., & Hillstom, K. E. 1980, *User Guide for MINPACK-1*, Tech. Rep. ANL-80-74, Argonne National Laboratory, Argonne, IL, USA
- Morgan, W. W., Abt, H. A., & Tapscott, J. W. 1978, *Revised MK Spectral Atlas for stars earlier than the sun* (Williams Bay: Yerkes Observatory, and Tucson: Kitt Peak National Observatory, 1978)
- Morgan, W. W., Keenan, P. C., & Kellman, E. 1943, *An atlas of stellar spectra, with an outline of spectral classification* (Chicago, Ill., The University of Chicago press [1943])

- Murray, N. & Chaboyer, B. 2002, *ApJ*, 566, 442
- Nelder, J. A. & Mead, R. A. 1965, *Computer Journal*, 7, 308
- O'Donovan, F. T., Charbonneau, D., Mandushev, G., Dunham, E. W., Latham, D. W., Torres, G., Sozzetti, A., Brown, T. M., Trauger, J. T., Belmonte, J. A., Rabus, M., Almenara, J. M., Alonso, R., Deeg, H. J., Esquerdo, G. A., Falco, E. E., Hillenbrand, L. A., Roussanova, A., Stefanik, R. P., & Winn, J. N. 2006, *ApJ*, 651, L61
- Paczynski, B., Stanek, K. Z., Udalski, A., Szymanski, M., Kaluzny, J., Kubiak, M., & Mateo, M. 1994, *AJ*, 107, 2060
- Pojmanski, G. 2002, *Acta Astronomica*, 52, 397
- Pollacco, D., Skillen, I., Cameron, A., Christian, D., Irwin, J., Lister, T., Street, R., West, R., Clarkson, W., Evans, N., Fitzsimmons, A., Haswell, C., Hellier, C., Hodgkin, S., Horne, K., Jones, B., Kane, S., Keenan, F., Norton, A., Osborne, J., Ryans, R., & Wheatley, P. 2006, *Ap&SS*, 107
- Pont, F., Bouchy, F., Queloz, D., Santos, N. C., Melo, C., Mayor, M., & Udry, S. 2004, *A&A*, 426, L15
- Press, W. H., Flannery, B. P., Teukolsky, S. A., & Vetterling, W. T. 1989, *Numerical recipes in Pascal. The art of scientific computing* (Cambridge: University Press, 1989)
- Raymond, S. N., Mandell, A. M., & Sigurdsson, S. 2006, *Science*, 313, 1413
- Rivera, E. J., Lissauer, J. J., Butler, R. P., Marcy, G. W., Vogt, S. S., Fischer, D. A., Brown, T. M., Laughlin, G., & Henry, G. W. 2005, *ApJ*, 634, 625
- Rowan, T. 1990, PhD thesis, Department of Computer Sciences, University of Texas at Austin
- Rucinski, S. M. 1998, *AJ*, 116, 2998
- Sahu, K. C., Casertano, S., Bond, H. E., Valenti, J., Ed Smith, T., Minniti, D., Zoccali, M., Livio, M., Panagia, N., Piskunov, N., Brown, T. M., Brown, T., Renzini, A., Rich, R. M., Clarkson, W., & Lubow, S. 2006, *Nature*, 443, 534
- Santos, N. C., Israelian, G., & Mayor, M. 2004, *A&A*, 415, 1153



- Sato, B., Fischer, D. A., Henry, G. W., Laughlin, G., Butler, R. P., Marcy, G. W., Vogt, S. S., Bodenheimer, P., Ida, S., Toyota, E., Wolf, A., Valenti, J. A., Boyd, L. J., Johnson, J. A., Wright, J. T., Ammons, M., Robinson, S., Strader, J., McCarthy, C., Tah, K. L., & Minniti, D. 2005, *ApJ*, 633, 465
- Schneider, J. 2006, *The Extrasolar Planets Encyclopaedia*, <http://exoplanet.eu/>
- Seager, S. & Mallén-Ornelas, G. 2003, *ApJ*, 585, 1038
- Stanek, K. Z., Mateo, M., Udalski, A., Szymanski, M., Kaluzny, J., & Kubiak, M. 1994, *ApJ*, 429, L73
- Street, R. A., Horne, K., Lister, T. A., Penny, A., Tsapras, Y., Quirrenbach, A., Safizadeh, N., Cooke, J., Mitchell, D., & Collier Cameron, A. 2002, *MNRAS*, 330, 737
- Struve, O. 1952, *The Observatory*, 72, 199
- Tody, D. 1986, in *Instrumentation in astronomy VI; Proceedings of the Meeting, Tucson, AZ, Mar. 4-8, 1986. Part 2 (A87-36376 15-35)*. Bellingham, WA, Society of Photo-Optical Instrumentation Engineers, 1986, p. 733., ed. D. L. Crawford, 733
- von Braun, K., Lee, B. L., Mallén-Ornelas, G., Yee, H. K. C., Seager, S., & Gladders, M. D. 2004, in *AIP Conf. Proc. 713: The Search for Other Worlds*, ed. S. S. Holt & D. Deming, 181–184
- von Braun, K., Lee, B. L., Seager, S., Yee, H. K. C., Mallén-Ornelas, G., & Gladders, M. D. 2005, *PASP*, 117, 141
- Walker, G. A. H., Walker, A. R., Irwin, A. W., Larson, A. M., Yang, S. L. S., & Richardson, D. C. 1995, *Icarus*, 116, 359
- Weldrake, D. T. F., Sackett, P. D., Bridges, T. J., & Freeman, K. C. 2005, *ApJ*, 620, 1043
- Wilms, J. 2006, *Documentation of IDL Functions*, <http://astro.uni-tuebingen.de/software/idl/aitlib/timing/>
- Wolszczan, A. & Frail, D. A. 1992, *Nature*, 355, 145
- Wozniak, P. R., Udalski, A., Szymanski, M., Kubiak, M., Pietrzynski, G., Soszynski, I., & Zebrun, K. 2002, *Acta Astronomica*, 52, 129

Yee, H. K. C. 1991, PASP, 103, 396